

Dielectric Confinement, Structure, and Luminescence of 2D Layered Hybrid Lead Halide Perovskites

A thesis

Submitted in partial fulfilment of the requirements

for the degree of

Doctor of Philosophy

By

Rayan Chakraborty

20152025



Department of Chemistry

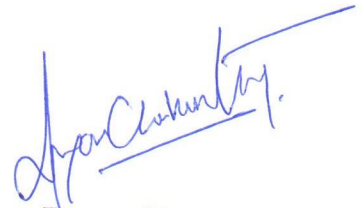
INDIAN INSTITUTE OF SCIENCE EDUCATION AND RESEARCH PUNE

2021

To my parents, and Prof. Ashish Kumar Nag,
this thesis is dedicated.

Declaration

I declare that this written submission represents my ideas in my own words and where others' ideas have been included, I have adequately cited and referenced the original sources. I also declare that I have adhered to all principles of academic honesty and integrity and have not misrepresented or fabricated or falsified any idea/data/fact/source in my submission. I understand that violation of the above will be cause for disciplinary action by the Institute and can also evoke penal action from the sources which have thus not been properly cited or from whom proper permission has not been taken when needed.



Rayan Chakraborty

ID No. 20152025

Date: 09/11/2021

Certificate

Certified that the work incorporated in the thesis entitled “**Dielectric Confinement, Structure, and Luminescence of 2D Layered Hybrid Lead Halide Perovskites**” Submitted by Rayan Chakraborty was carried out by the candidate, under our supervision. The work presented here or any part of it has not been included in any other thesis submitted previously for the award of any degree or diploma from any other University or institution.

Prasenjit Ghosh.

Dr. Prasenjit Ghosh

(Thesis co-supervisor)

Date: 09/11/2021

Angshuman Nag

Dr. Angshuman Nag

(Thesis supervisor)

Date: 09/11/2021

Acknowledgements

The popular theory of “*six degrees of separation*” suggests that any two human beings on this planet can be connected by at most six in-between people who are socially connected. What are the chances that I got connected to a specific set of random people that have led to this moment when I am writing a Ph.D. thesis to be submitted at IISER Pune? I do not know the answer, but I do think about this a lot. There have been probably hundreds of people with whom I have somehow interacted in the last twenty-seven years. Even if I let go the first five years of my childhood, twenty-two years is still a lot; there must have been at least a hundred people who have, in some way, pushed me towards this moment. This includes my teachers, friends, batchmates, labmates, department colleagues, office staff, and many more people, even people I do not know the names of. I sincerely thank all of them. It would probably take an entire book to cover all of their names and how they have contributed to this thesis; I wish to write that book someday.

While it is not possible to name everyone in this small acknowledgement section, there are some people without naming whom the thesis would remain incomplete. First and foremost, my Ph.D. thesis supervisor Dr. Angshuman Nag. Apart from being a good scientist and advisor, he has been an excellent human being throughout my Ph.D. I can easily write a thirty-page chapter only on what I have learned from him, but perhaps this is not the time. I want to thank my co-supervisor, Dr. Prasenjit Ghosh, for giving me the required knowledge and resources for venturing into the field of computational chemistry. Computational techniques were something I wanted to learn without leaving the familiarity of experimental work. From the beginning, Dr. Ghosh has been very supportive and welcoming towards my goal. I will forever be thankful to him for that. Also, thanks to my research advisory committee (RAC) members, Dr. Nirmalya Ballav and Dr. Shouvik Dutta, for their valuable comments during RAC meetings.

I was fortunate to have two sets of labmates at the two labs. I cannot thank them enough for all the memories I have made with them. Sadly, our time for interaction got shortened due to the pandemic. Nevertheless, it was a great privilege to come in contact with these beautiful people. All of them have taught something at some point through group meetings or daily interactions. It gives me great pleasure to see all of my senior labmates are flourishing in their chosen fields, and I wish the same for my junior ones. In particular, I should thank Dr. Vikash Kumar Ravi for teaching me the basics of nanocrystal synthesis and characterization, Dr. M.

Jagadeeswararao for teaching me photoluminescence measurements, Dr. Niharika Joshi for teaching the basics of density functional theory calculations, and Tariq Sheikh for teaching the single-crystal structure refinements. These techniques have been used extensively in this thesis work. I would also like to thank undergraduate students Satya Prakash Panda and Ovie Soman for their contributions to my chalcogenide work, even though the work could not be included in this thesis.

I want to thank IISER Pune and the department of chemistry for the experimental and computational facilities that have been made available for research and thanks to all the technicians and staff who keep the facilities operational. In particular, thanks to Mr. Ravinder Malothu of the single-crystal X-ray diffraction facility for helping with some of the data acquisitions, Dr. Partha Hazra's lab for TCSPC measurements, Dr. Pramod Pillai's lab for the diffused reflectance measurements, CDAC Pune for access to PARAM Yuva, CDAC and IISER Pune for access to PARAM Brahma, and CMS, Tohoku University for access to the computational facility. Also, thanks to the department of chemistry, IISER Pune, for the integrated Ph.D. fellowship.

I would also like to thank my integrated-PhD 2015 batchmates. The six-year-long journey has never been tiresome because of their presence. Among them, I should particularly thank Unmesh Mondal and Meghamala Sarkar. They have helped me out with different aspects of computational and single-crystal X-ray diffraction techniques, respectively. I would also like to thank the CLM-101 team and the people involved in Chemsymphoria-2019's organizing committee. Organizing these events was a great experience that enhanced my leadership and management skills, which I believe have improved the way I conduct scientific research as well. I am also thankful to my friends who have been a constant source of support and motivation throughout these years – Shubhajit, Sayan, Suvadeep, Suman, Farhan, Rinku, and Isha. Also, thanks to the creators of Spotify, Coffee, and Harry Potter.

And finally, I would like to thank my parents, who have gone above and beyond their capabilities to help me with my studies and work.

2D: two-dimensional	FTIR: Fourier transform infrared spectroscopy
3D: three-dimensional	FWHM: Full-width at half-maxima
BA: Butylammonium	GGA: Generalized gradient approximation
BZ: Brillouin zone	HDA: Hexadecylammonium
CBM: Conduction band minima	HER: Hydrogen evolution reaction
CBTS: Copper barium tin sulfide (Cu ₂ BaSnS ₄)	HTL: Hole transport layer
CHA: Cyclohexylammonium	IRF: Instrument response function
CN: Coordination number	LED: Light-emitting diode
DDT: Dodecanethiol	MP: Monkhorst-Pack
DFT: Density functional theory	NC: Nanocrystals
DJ: Dion-Jacobsen	NIR: Near infra-red
DMF: N,N-dimethylformamide	NMR: Nuclear magnetic resonance
DMSO: Dimethyl sulfoxide	OCT: Octylammonium
DNN: Deep neural network	OER: Oxygen evolution reaction
DOS: Density of states	OPD: Organic photodiode
EA: Ethanolammonium	PBE: Perdew–Burke–Ernzerhof
EDT: Ethanedithiol	PEA: Phenylethylammonium
EN: Ethylenediamine	PEC: Photoelectrochemical
EQE: External quantum efficiency	PL: Photoluminescence
FA: Formamide	PLE: Photoluminescence excitation
FESEM: Field effect scanning electron microscopy	PXRD: Powder X-ray diffraction
	QLED: Quantum-dot light Emitting diode
	RB: Round-bottomed flask

RHE: Reversible hydrogen electrode

RP: Ruddlesden-Popper

SAED: Selected area electron diffraction

SCXRD: Single-crystal X-ray diffraction

STE: Self-trapped exciton

TAA: Thioacetamide

TCSPC: Time-correlated single-photon counting

TEM: Transmission electron microscopy

TOP: Trioctylphosphine

UPS: Ultraviolet photoelectron spectroscopy

UV: Ultraviolet

VBM: Valence band maxima

Synopsis:

The primary focus of this thesis is optical properties of 2D hybrid lead halide perovskite semiconductors, $A_n\text{PbX}_4$ (A: organic ammonium cation, $n = 1$ or 2 , $X = \text{Cl, Br, I}$). The materials have received intense interest in the recent years because of unique optical properties originating from confined excitons in self-assembled repeated quantum-well like structure. Also, in these materials, the exciton's behaviour is strongly modulated by the organic/inorganic interfaces, giving rise to novel properties. They are easy to prepare at laboratory conditions, and their properties can be varied by the choice of composition. Thousands of compositions of these materials can be synthesized by modifying the A-site organic cation or changing the halogen (X). This tunability allows composition design to cater for targeted applications like photovoltaics (PVs), light emitting diodes (LEDs), lasing, and photodetectors. In this rapidly emerging field, the understanding about how the composition tunes optical properties was found to be inadequate in the literature. Therefore, experimental results presented in the current thesis attempts to correlate the composition and properties of 2D hybrid perovskites.

This thesis starts by giving an introduction on the halide perovskites with attention to the 2D layered hybrid perovskites. The standing challenges in understanding the optical properties of these materials are discussed. Knowledge of the exciton binding energy is an important parameter for understanding luminescence behaviour, and for application in any optoelectronic devices. The exciton binding energy is correlated with A- and X-site ions. Similarly, structural distortions in these materials significantly alter excitonic behaviour on changing compositions. The role of the A-site cations on these structural distortions have been elucidated, and the same has been connected with photoluminescence (PL). Many compositions of these materials show broadband emission spanning the entire visible range. These emissions are technologically very appealing for LED applications. The sensitization mechanism of these broadband emission is investigated using temperature-dependent excited state spectroscopy. Temperature-dependent

PL measurement is an important technique for obtaining excitonic information like binding energy, and exciton-lattice coupling. A method utilizing machine-learning is developed to decrease the time required for these experiments.

The thesis also contains an appendix section where a different kind of material, namely earth-abundant chalcogenide $\text{Cu}_2\text{BaSnS}_4$ (CBTS) is investigated for optoelectronic and catalytic applications.

A brief overview of each of the chapter is given below:

Chapter 1: Introduction

Introduction of this thesis starts with a brief history of the transition from oxide perovskites to halide perovskites. The history is followed by a discussion on the modern research directions in layered hybrid perovskite semiconductors, which is the chosen material for this thesis work. Briefly exciton photophysics and impact of spatial confinement are discussed in the context of the layered hybrid perovskite structure. A section is dedicated to discuss the typical synthesis method of these materials. Subsequently, a few optical properties originating from the layered structure are highlighted where the impact of composition is not adequately understood. The properties are exciton binding energy, exciton emission energy, and exciton trapping behaviour. Finally, the scope of this thesis work is discussed.

Chapter 2: Correlation of Dielectric Confinement and Exciton Binding Energy in 2D Hybrid Lead Halide Perovskites

This chapter discusses how the A-site and X-site ions bring change in the exciton binding energy through dielectric confinement effect. Different compositions are prepared by varying A and X in the A_2PbX_4 composition. The exciton binding energy is qualitatively estimated by radiative lifetime of PL, and further, quantitatively estimated by temperature-dependent steady-state PL. The exciton binding energy is found to increase on replacing Cl by Br by I. The trend is opposite to that observed for 3D halide perovskites like CsPbX_3 . The contrast of the high

frequency dielectric constants between A and Pb-X layers are found to be correlated with the observed exciton binding energy trend. The dependency allows tuning of exciton binding energy in the range 50-450 meV by the choice of the composition.

Chapter 3: Non-covalent Iodine-Iodine Interactions and Exciton Emission in $(\text{I}-(\text{CH}_2)_n\text{-NH}_3)_2\text{PbI}_4$ ($n = 2-6$)

In this chapter, the focus is on a new non-covalent interaction, namely halogen-halogen interaction, between the I-tail of organic A-site cation with the iodine of inorganic Pb-I layer. Typically, A-site cation does not have -I tail group, and the interactions are between ammonium ($-\text{NH}_3^+$) group of the organic cations and iodide (I^-) ions of the inorganic layer. By functionalizing the organic A-site cation with -I group, it becomes possible to introduce new iodine-iodine interaction between A-site cation and the Pb-I layer. These interactions are characterized by single crystal X-ray diffraction performed at multiple temperatures and their influence on optical properties are analysed by temperature-dependent PL spectroscopy. Presence of these iodine-iodine interactions are found to restrict temperature-dependent structural phase transitions of these materials, giving stable exciton emission energy in a large temperature window of 10 – 300 K.

Chapter 4: Two Self-Trapped Excitonic Emission in 2D Hybrid Lead Iodide Perovskite Single Crystals

In this chapter, the broadband emissions from hexylammonium lead iodide ($(\text{CH}_3-(\text{CH}_2)_5\text{-NH}_3)_2\text{PbI}_4$), and 4-aminomethylpyridinium lead iodide ($(\text{4-AMP})\text{PbI}_4$) layered hybrid lead iodide perovskite crystals are discussed. The emissions are expected to be originating from excitons trapped in transient crystal deformations, also known as, self-trapped excitons (STEs). Using temperature-dependent steady-state PL, two distinct STE emissive centres are identified at low temperatures. The excitation mechanism of these emissions is probed by PL excitation

spectroscopy. The results suggest two different channels of energy transfer from the excitonic state to these broadband emissive states.

Chapter 5: Neural Networks for Analysis of Optical Properties in 2D Layered Hybrid Lead Halide Perovskites

Employment of machine learning in spectroscopic data acquisition and analysis has been discussed in this chapter. Temperature-dependent PL experiments take a significantly long time for data acquisition owing to slow thermal equilibration of the samples at each temperature points. Also, a large number of data points are usually required for any meaningful analysis. Generative machine learning methods can find trends in sparsely collected datasets and can interpolate them. The method is employed to estimate exciton properties like emission energy and exciton binding energy. Both of these properties show non-linear changes with temperature. Near accurate quantitative estimation of the measured quantities are obtained using the machine learning method.

Appendix-A: Colloidal Synthesis, Optical Properties and Hole Transport Layer Applications of $\text{Cu}_2\text{BaSnS}_4$ (CBTS) Nanocrystals

This chapter introduces a synthesis method for CBTS nanocrystals. A ligand exchange protocol is also developed to stabilize the nanocrystals in a range of solvents with different dielectric constants. The nanocrystals are then utilized as the hole transporting layer in an organic photodiode.

Appendix-B: Mechanistic Insights of Hydrogen Evolution Reaction on $\text{Cu}_2\text{BaSnS}_4$ (CBTS) from First Principles

In this chapter, the thermodynamics of photocatalytic hydrogen evolution reaction (HER) on multiple CBTS surfaces is explored by DFT-based calculations. The metal rich (110) surface is found to have very favourable energetics and electronic properties for HER photocatalysis, which are comparable to technologically successful chalcogenide semiconductor, MoS_2 .

Thesis Summary and Future Directions

The major findings of this thesis work are summarized leading to possible future research direction. In Chapter 2 of this thesis, we showed the influence of the organic medium's dielectric constant of the exciton residing in the inorganic layer. The exciton's behaviour can be manipulated to a greater extent by the presence of ferroelectric domains in its near vicinity. The domains contain electric charges at length scale comparable to exciton Bohr radius. Tailoring the size and shape of the ferroelectric domains can elevate or suppress exciton recombination, potentially paving the way for application of these materials as high-efficiency photovoltaic absorber, high-speed photodetectors or laser sources, and in the field of quantum photonics.

Table of Contents**Chapter 1: Introduction**

1.1 Halide perovskites.....	2
1.2 Two-dimensional (2D) layered hybrid perovskites	4
1.3 A brief review of photoluminescence, excitons, and quantum wells	6
1.4 Synthetic methods for 2D layered hybrid perovskites	12
1.5 Challenges.....	13
1.6 Scope of this thesis.....	23
1.7 References.....	25

Chapter 2: Correlation of Dielectric Confinement and Exciton Binding Energy in 2D Hybrid Lead Halide Perovskites

Abstract.....	37
2.1 Introduction.....	38
2.2 Experimental Section	40
2.2.1. Chemicals.....	40
2.2.2 Preparation of caesium oleate (Cs-oleate) precursor solution.	40
2.2.3 Synthesis of colloidal CsPbX ₃ (X = Cl, Br, I) nanocrystals.	41
2.2.4 Preparing 2D layered halide perovskite films.....	41
2.2.5 Characterization and optical properties.	42
2.3 Results and Discussion	43
2.4 Conclusions.....	57
2.5 References.....	58

Chapter 3: Non-covalent Iodine-Iodine Interactions and Exciton Emission in (I-(CH₂)_n-NH₃)₂PbI₄ (n = 2-6)

Abstract.....	68
3.1 Introduction.....	69
3.2 Experimental Section	71
3.2.1 Chemicals.....	71
3.2.2 Synthesis of (I-(CH ₂) _n -NH ₃) ₂ PbI ₄ (n = 2-6) single crystals.....	71
3.2.3 Structural characterization.	71
3.2.4 Optical properties.....	72
3.3 Results and Discussion	72
3.3.1 Iodine-Iodine interaction suppressing temperature-dependent phase transitions of (I-(CH ₂) ₄ -NH ₃) ₂ PbI ₄	72

3.3.2 The generic $(I-(CH_2)_n-NH_3)_2PbI_4$ series with $n = 2-6$	77
3.3.3 Pb-I-Pb bond angle influences PL peak position (band gap) of $(I-(CH_2)_n-NH_3)_2PbI_4$ ($n = 2-6$).....	83
3.3.4 Structural parameters controlling hydrogen bonding and Pb-I-Pb bond angle.....	84
3.4 Conclusions.....	88
3.5 References.....	94

Chapter 4: Two Self-Trapped Excitonic Emission in 2D Hybrid Lead Iodide Perovskite Single Crystals

Abstract.....	100
4.1 Introduction.....	101
4.2 Experimental Section.....	103
4.2.1 Chemicals.....	103
4.2.2 Synthesis of $(CH_3-(CH_2)_5-NH_3)_2PbI_4$ and $(4-AMP)PbI_4$ single crystals.....	103
4.2.3 Characterization.....	103
4.3 Results and Discussion.....	104
4.4 Conclusions.....	111
4.5 References.....	112

Chapter 5: Neural Networks for Analysis of Optical Properties in 2D Layered Hybrid Lead Halide Perovskites

Abstract.....	118
5.1 Introduction.....	119
5.2 Experimental Section.....	121
5.2.1 Chemicals.....	121
5.2.2 Preparation of $(PEA)_2PbI_4$ and $(CHA)_2Pb(Br_{1-x}I_x)_4$ single crystals.....	121
5.2.3 Thin film of $(EA)_2PbI_4$	121
5.2.4 Characterization and optical properties.....	122
5.2.5 Neural network models.....	122
5.3 Results and Discussion.....	123
5.4 Conclusions.....	135
5.5 References.....	136

Appendix

Appendix-A: Colloidal Synthesis, Optical Properties and Hole Transport Layer Applications of Cu_2BaSnS_4 (CBTS) Nanocrystals

Abstract.....	145
---------------	-----

A.1 Introduction.....	146
A.2 Experimental Section	147
A.2.1 Chemicals.....	147
A.2.2 Synthesis of Cu ₂ BaSnS ₄ (CBTS) nanocrystals (NCs)	147
A.2.3 S ²⁻ Ligand Exchange	148
A.2.4 Characterization	148
A.2.5 Calculation of excitonic Bohr diameter	149
A.2.6 Application of CBTS NCs in organic photodiode (OPD).....	149
A.3 Results and Discussion.....	152
A.3.1 Synthesis, characterization and surface modifications of colloidal CBTS NCs	152
A.3.2 HTL application of CBTS NCs film in a OPD	158
A.4 Conclusions.....	162
A.5 References.....	162
 Appendix-B: Mechanistic Insights of Hydrogen Evolution Reaction on Cu₂BaSnS₄ (CBTS) from First Principles	
Abstract.....	169
B.1 Introduction	170
B.2 Computational Details.....	172
B.2.1 Details of DFT calculations.....	172
B.2.2 Bulk crystal	173
B.2.3 The surface models.....	176
B.3 Results and Discussion.....	179
B.3.1 Surface structures and electronic properties.....	179
B.3.2 Thermodynamics of H-adsorption on the surfaces	187
B.3.3 HER mechanism.....	192
B.4 Conclusions	195
B.5 References	196
 Thesis Summary and Future Directions	
Thesis Summary.....	203
Future Directions	205
References.....	206
List of Publications	210
Copyrights and Permissions.....	212

1.1 Halide perovskites

What is a *perovskite*?¹

This apparently simple question has kept on changing its answer since the inception of the name "*perovskite*." Gustav Rose, a German mineralogist, coined the term to report the existence of a new mineral in the Ural mountains in 1840.² The reported mineral was composed of calcium titanate (CaTiO₃). About eighty-five years later (1925), after the invention of X-ray crystallography, Victor Goldschmidt, with help from T. Barth, showed that similar composition and crystal structure can be obtained by replacing Ca²⁺ by Sr²⁺ by Ba²⁺; or Ti⁴⁺ by Zr⁴⁺ by Sn⁴⁺.³ Goldschmidt found the formation of these AMO₃ type compositions with CaTiO₃-like (*perovskite-like*) structure is dependent on the radius (R_i) of the ions (A²⁺, M⁴⁺, and O²⁻).

$$\alpha = \frac{R_A + R_O}{\sqrt{2} (R_M + R_O)} \quad \text{Eq. (1.1)}$$

In equation 1.1, the factor α later came to be known as the Goldschmidt tolerance factor. The equation comes from the geometric construction of CaTiO₃ (A = Ca, M = Ti) crystal lattice. The lattice contains corner-shared Ti-O octahedra, with Ca²⁺ in the cuboctahedral void (Figure 1.1). Goldschmidt concluded that any combination of A, M, and O that obtains α between 0.8 and 1, would crystallize in the perovskite-like structure. Expectedly, subsequent research found that there exists a large number of ion combinations that satisfy this criterion. Over time, this entire family of compounds came to be known as "perovskites."

Thirty-four years after (1959) Goldschmidt's work on the tolerance factor, C. K. Møller resolved crystal structures of CsPbX₃ (X = Cl, Br, I).⁴ The CsPbX₃ salts were chemically synthesized earlier (1893) by Wells et al.⁵ Using X-ray diffraction, Møller showed that at a particular phase, these compounds resembled the structure of perovskites with Pb-X (X = Cl, Br, I) octahedra and Cs⁺ as the A-site cation; also, they follow the Goldschmidt's rule of tolerance factor (equation 1.1, with R_O substituted by R_X). Møller used the term "*perovskite-like*" to describe these materials. Soon after, in 1978, Weber successfully replaced Cs⁺ with

methylammonium (MA: CH_3NH_3^+) to form $\text{CH}_3\text{NH}_3\text{MX}_3$ ($\text{M} = \text{Pb}, \text{Sn}, \text{X} = \text{I}, \text{Br}$).^{6, 7} Over time, more and more AMX_3 structures and compositions were reported where X is a monovalent halogen anion, M is a bivalent metal cation ($\text{M} = \text{Pb}, \text{Sn}, \text{Ge}$) or a combination of mono and trivalent metal cations ($\text{M} = [\text{Ag}^+/\text{Bi}^{3+}], [\text{Ag}^+/\text{In}^{3+}], [\text{Na}^+/\text{In}^{3+}]$), and A is a monovalent alkali metal or a small organic ammonium cation ($\text{A} = \text{Cs}^+, \text{Rb}^+, \text{MA}^+$, formamidinium (FA^+)).⁸⁻¹⁰ As the compositional space broadened, similar to what happened for its oxide (i.e., $\text{X} = \text{O}$) counterpart, this family of materials lost the "perovskite-like" name and gained the generalized name "perovskites."

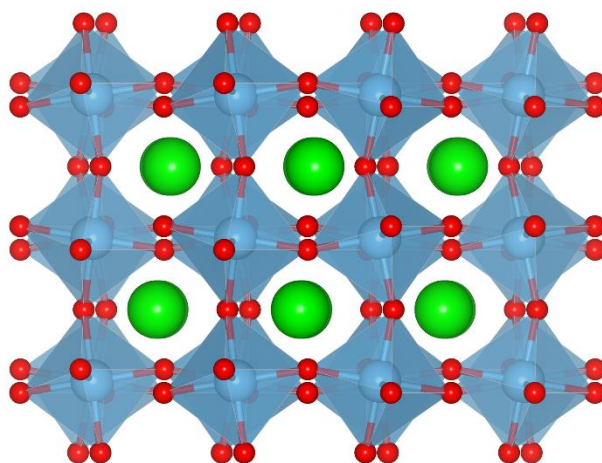


Figure 1.1: Crystal structure of CaTiO_3 ; Ca^{2+} (A-site: green), Ti^{4+} (M-site: blue), and O^{2-} (red).

Apart from the similarity in structure, the perovskites with halogen as anions are remarkably different from their oxide counterparts – in aspects like formation energy, electronic band structure, and optical properties.¹¹ Keeping these differences in mind, more appropriately, these materials are often referred to as "halide perovskites." The differences in their electronic properties make them potential semiconductors for visible-light-driven optoelectronic applications; a field where oxide perovskites did not find many applications because of their large band gap and insulator-like nature.¹²

The halide perovskite family entered the domain of optoelectronic research in 2009 and rose to prominence around 2012 after delivering ~11% photovoltaic efficiency from a solution-

processed device;^{13, 14} Since then, a worldwide effort of the scientific community has resulted in extensive research on this group of materials for optoelectronic applications like photovoltaics, light-emitting diodes (LEDs), lasing, and photodetectors.¹⁵⁻¹⁹ At present, the highest reported photovoltaic efficiency from solution-processed halide perovskite-based solar cell stands above 25%.²⁰ This efficiency is higher than the previously best known photo-absorbing materials like CIGS (copper indium gallium selenide) or CdTe and is comparable to commercial crystalline Si. Notably, devices incorporating all of these high-performing materials have a much higher processing cost than halide perovskites. The success of lead halide perovskites as photovoltaic absorbers also motivated research in the field of LEDs, delivering 22% external quantum efficiency from solution-processed device.^{21, 22} However, large scale optoelectronic applications of the materials will require solving problems like poor stability in ambient conditions, and toxicity of lead.^{23, 24}

1.2 2D layered hybrid perovskites

In all halide perovskite AMX_3 compositions, the six vertices of a single M-X octahedron are shared with six of its neighboring M-X octahedra (see Figure 1.1). If A becomes sufficiently large, this 3D connectivity of octahedra breaks down. At some particular choice of A, a situation arises where the octahedral connectivity exists only in two directions. That is, in one of the directions, two opposite vertices of one octahedron lose connectivity (Figure 1.2). This yields composition like A_2MX_4 , where A is a monovalent organic ammonium cation. There exists a lot of organic cations (as A) that can stabilize structures of this kind. These structures do not fall in the framework developed by Goldschmidt (Equation 1.1). In the sense of the originally coined term "*perovskite*," it can not be called so.

These structures are as if thin 2D layers of halide perovskites are stacked together with organic cations in between. Based on this structural similarity and the presence of both organic and inorganic components in the lattice, these materials are called "*2D layered hybrid*

perovskites.²⁵" The loss of connectivity in one direction and the introduction of the organic/inorganic interface give several new electronic and optical properties.²⁶ The freedom from the Goldschmidt tolerance factor enables a much larger compositional space than that was possible for its predecessor 3D halide perovskites. In addition to all these, the materials are comparatively more resistant towards moisture than 3D halide perovskites because of the presence of large hydrophobic organic cations in the structures.^{27, 28}

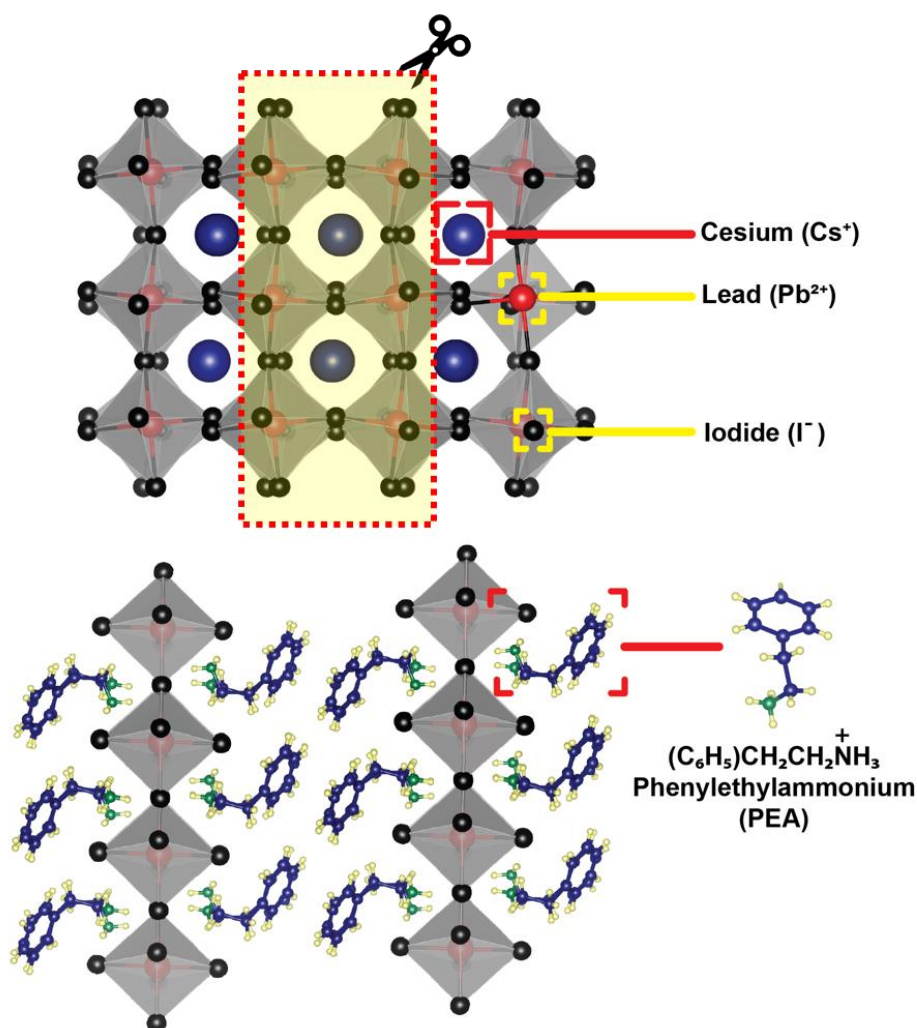


Figure 1.2: Strategy of dimensionality reduction in halide perovskites. The top panel shows the crystal structure of a 3D halide perovskite, CsPbI₃. Replacing Cs⁺ (A-site cation) with larger sized (C₆H₅)CH₂CH₂NH₃⁺ results in the incision of the 3D structure (red dashed line) and formation of (PEA)₂PbI₄ (PEA: phenylethylammonium), a 2D layered hybrid perovskite.

The 2D layered halide perovskite research dates back to the 1980s, long before 3D halide perovskites made their mark as remarkable photo absorber material.^{29, 30} The interest primarily originated because of the observed strong exciton luminescence at room temperature from a

few compositions.³¹ Particularly, researchers like Ishihara and Goto investigated the exciton properties in some 2D layered hybrid perovskites;³²⁻³⁷ Papavassiliou, Mitzi, and Billing reported multiple new compositions and studied their physical properties.^{25, 38-42} In the last decade, the success of 3D halide perovskites for optoelectronic applications has refocused the research interest on these materials.

Modern research in 2D layered hybrid perovskites is devoted broadly in three directions – (a) bringing in new functionality by tuning the composition. Such composition tuning avails novel properties that bear signatures of both the organic A-site cation and the inorganic M-X layer but do not exist independently in either A or M-X materials in their pristine forms – this is only possible in 2D hybrid perovskite structures because of the presence of the A- and M-X interfaces,⁴³⁻⁴⁵ (b) increasing stability of photovoltaic devices by exploiting the hydrophobicity of the A-site organic cations,^{46, 47} and (c) fabrication of high-performing light-emitting devices.⁴⁸⁻⁵¹ The *quantum-well*-like structures of the 2D layered hybrid perovskites make them an obvious choice for light-emitting applications, as we shall see in the later sections.

2D hybrid perovskite research is an emerging field, and several aspects require further attention and understanding. In this thesis, we attempt to focus on the optical properties of these materials. Before proceeding to discuss those optical properties, we will review the basics of three key terms that will come up repeatedly in our discussion – (a) photoluminescence, (b) excitons, and (c) quantum wells.

1.3 A brief review of photoluminescence, excitons, and quantum wells

(a) Photoluminescence

Luminescence is a process in which a non-metallic material radiates electromagnetic radiation from a non-equilibrium state. Such radiation is different from black-body radiation, which involves the material in equilibrium with its surroundings. For the luminescence to occur, the material needs to be supplied with an excess amount of energy by external perturbations. The

excess amount of energy is termed "*excitation energy*." The excitation energy creates the non-equilibrium position ("*excited state*") in the material; the material eventually returns to its equilibrium ("*ground state*"), resulting in the radiation of photons or liberation of heat. If the excitation energy is provided in the form of photons (light), and the emitted energy is also in the form of photons, the process is called photoluminescence.

In the excitation process (Figure 1.3a), photon-matter interaction takes place that perturbs the ground-state electron density in the material. Electrons absorb the excitation energy in the material that elevates them to an energetically higher electronic state. For the case of semiconductors, this process translates to an elevation of the electron from the valence to the conduction band, suppressing the forbidden gap in between them. Such a transition is thus accompanied by the creation of a "hole" in the valence band. The photoluminescence relaxation process then means the recombination of the electron and hole and the generation of light.

Photoluminescence is studied in spectrophotometers. In these measurements, an excitation source is used to provide continuous (Xe-lamp) or pulsed (diode laser) fluence of any particular wavelength of photons. The energy of these photons is typically chosen to be larger than the material's band gap energy. The excitation photons are made incident on the sample, which in turn emits photons corresponding to its energy gaps. The radiated photons' energy and intensity are measured using a photodetector. The energy vs. intensity plot gives information about the position of the excited energy states with respect to the ground state and their transition probabilities.

(b) Exciton

The electron and hole, though separate entities are often found to have their properties correlated. That is, the electron and hole pair acts like a quasiparticle. Such a quasiparticle is termed an "*Exciton*." Figure 1.3b shows such an exciton in a 2D lattice. In the exciton, the electron and hole attract each other with Coulomb force (F). The attractive force determines

the stability of the exciton against external perturbations. The modulus of this attractive force depends on the physical distance (r) between the electron and the hole and the dielectric constant (ϵ) of the medium, along with constant elementary charge (e), as shown in the Coulomb equation.

$$F = -\frac{1}{4\pi\epsilon} \frac{e^2}{r^2} \quad \text{Eq. (1.2)}$$

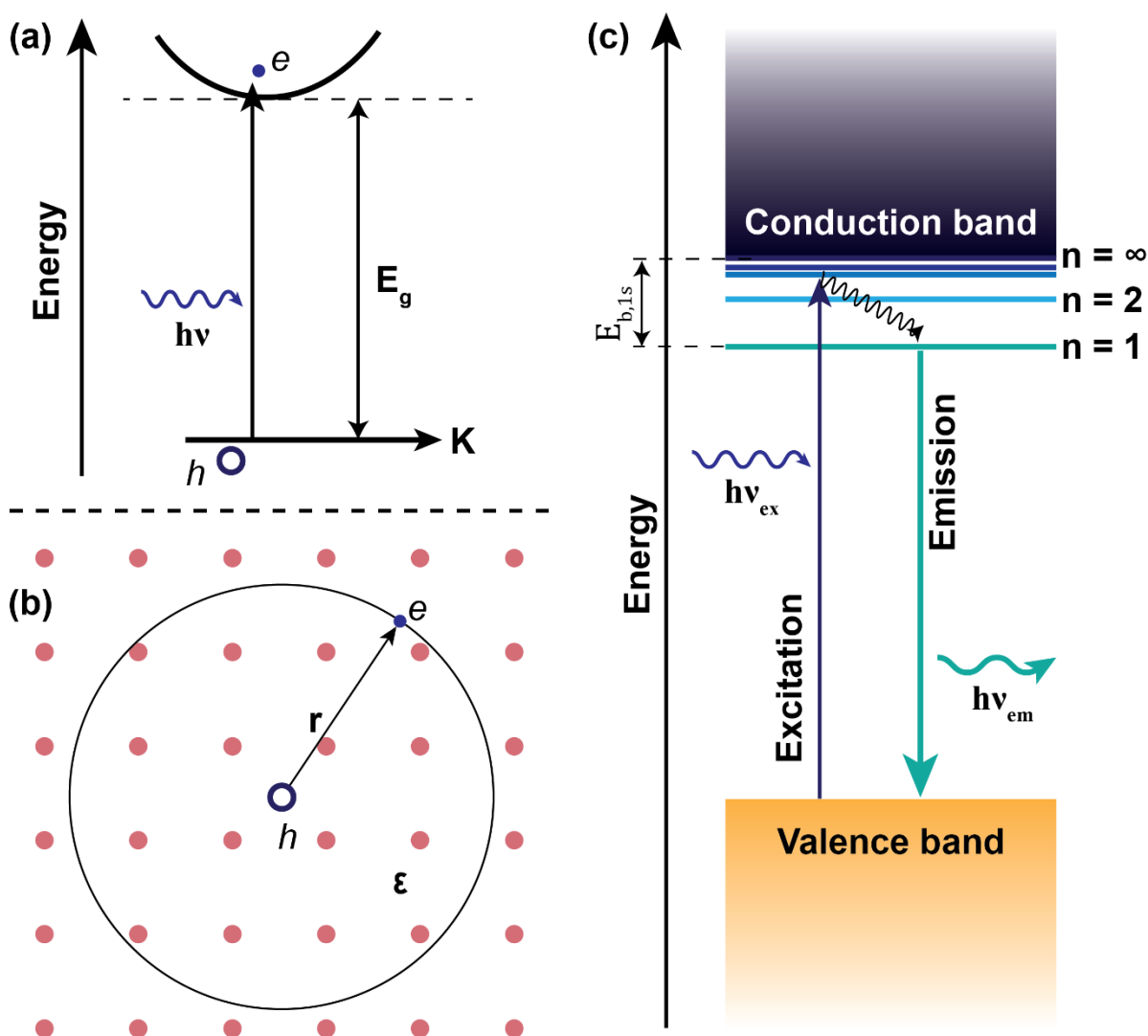


Figure 1.3: (a) Schematic of formation of an exciton by the vertical transition of an electron from the valence to the conduction band (band gap = E_g) by absorption of a photon (Excitation energy = $h\nu$). (b) Schematic of the exciton in a 2D crystal lattice (dielectric constant = ϵ). (c) Definition of exciton binding energy. n ($= 1, 2, 3, \dots$) represents the exciton energy levels, and $E_{b,1s}$ is the binding energy of the 1s exciton. Typically, exciton binding energy refers to the 1s exciton binding energy, $E_{b,1s}$.

In a 3D lattice, the exciton can be thought of as similar to the hydrogen atom, where the attractive force is between the electron and proton. Analogous to the Bohr hydrogen model's orbital states and orbital energy, the exciton model gives the exciton states and exciton binding energies. However, the hole in the exciton is much lighter compared to the proton in the hydrogen atom. Also, the charges of the electron and hole are screened by the dielectric constant of the medium. Both of these factors bring in some considerable changes to the observed properties of the exciton compared to the hydrogen atom. For example, in typical semiconductors, the Bohr radius of an electron in exciton is larger than that in hydrogen. Also, the exciton states' energy is much smaller than the energies of the corresponding electronic states in hydrogen; overall, the exciton is much less stable than the hydrogen atom.⁵² This treatment (also known as the Mott-Wannier exciton model) can explain most optical phenomena involving a semiconductor's exciton.

In this model, the lowest energy state of the exciton is termed as 1s exciton (Figure 1.3c). This 1s exciton binding energy determines the stability of an exciton. The higher the value, the more stable the exciton state is than the conduction band minimum.⁵² The 1s exciton binding energy ($E_{b,1s}$), governed by the F in equation 1.2, is the fundamental parameter that guides exciton's dissociation and recombination probabilities in semiconductors. A material with a high $E_{b,1s}$ is suitable for LED since it will ensure a high radiative recombination rate. On the other hand, a material with low $E_{b,1s}$ is desired for photovoltaic application since photocurrent can conduct only after the photogenerated exciton dissociates into free electron and hole.

(c) Quantum wells

The electron, hole, and exciton in a semiconductor are quantum-mechanical particles. The corresponding wavelengths of the electron and hole and the Bohr radius of the exciton are usually much larger than the lattice constants of the material. This situation allows us to manipulate the particles' behavior by varying the size of the material. For example, in

semiconductors with material dimensions comparable to the Bohr exciton radius, the excitons behave very differently compared to the same material of larger dimensions (*bulk crystal*). One example of the materials of the former kind is "*quantum dots*." Quantum dots utilize the effect of spatial confinement on excitons to change emission color and enhance electron-hole radiative recombination probability; naturally, they are very suitable for light-emitting applications like in quantum-dot light-emitting diode (QLED) display panels.

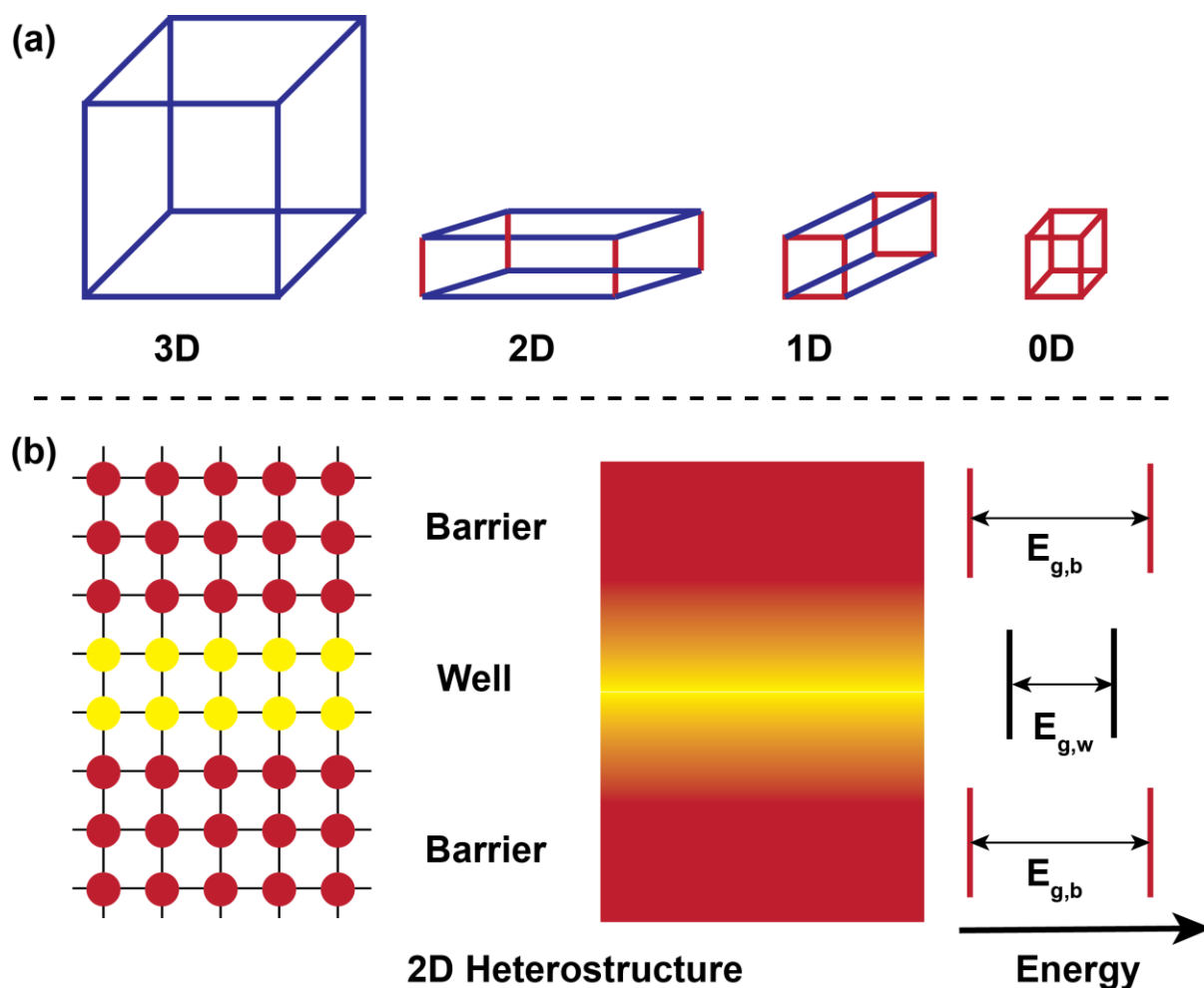


Figure 1.4: (a) Schematic of semiconductor structures of different dimensions. Here, dimension refers to the number of directions where an exciton is expected to move freely (colored blue). (b) Schematic of a quantum well heterostructure. The color gradient marks the interface. Here, the well has a smaller band gap (yellow; $E_{g,w}$) than the barrier (red; $E_{g,b}$). Similar structures where well's band edges fall between the barrier's edges are called "Type-I" heterostructures.

In the last forty years, the advancement of semiconductor synthesis processes and nanotechnology has allowed us to selectively control the size of the semiconductor crystals

down to a few nanometers in length. Such dimensions are where the quantum-confinement effect sets in. Based on the number of dimensions where exciton is *un*-confined, materials can be divided into four families (Figure 1.4a) – zero-dimensional (0D), one-dimensional (1D), two-dimensional (2D), three-dimensional (3D). Previously mentioned quantum dots are 0D material; here, an exciton is confined in all directions. Compared to this, a bulk-crystal is an example of 3D material. In this thesis, our focus is on 2D layered hybrid perovskites. The 2D materials are also called *quantum wells*; because of their apparent similarity with the quantum mechanical particle-in-a-box model with a well-like potential.

Quantum wells usually exist as *heterostructures*. The principal material of interest is embedded in a sandwiched structure with materials of different compositions (Figure 1.4b). The compositions are usually chosen such that the embedded material has a smaller band gap than the embedding matrix. The band edges of the embedding matrix can act as the potential barrier (right panel in Figure 1.4b). Fabrication of such structures is necessary since, for most cases, a semiconductor sheet with a thickness of few angstroms and investigable dimensions can not stand on its own. Apart from the spatial confinement, the interfaces' nature modulates the exciton's behavior in these structures.

A heterostructure where the well-barrier alternative arrangement is repeated multiple times is called a multi-quantum well. Multi-quantum well structures for light-emitting applications have been investigated for the III-V group of semiconductors.⁵³ However, fabrication of these heterostructures involves epitaxial thin-film deposition techniques like molecular beam epitaxy (MBE), metal-organic vapor-phase epitaxy (MOVPE), chemical vapor deposition (CVD). These techniques require high vacuum and, thus, are expensive; but are necessary for obtaining heterostructures with minimal defect concentrations. Solution-based methods, on the other hand, while much cheaper, lack control over thickness of the well/barrier and suffer from resultant material with high defect density. Having precise control over the thickness of the

well/layer is essential for obtaining reproducibility in device performances. Having little to no defects in the lattice is important for obtaining devices with high optoelectronic efficiency.

The 2D layered hybrid perovskites can solve these problems of traditional III-V quantum well heterostructures. This is because the 2D layered hybrid perovskites are self-assembled quantum wells. The layer thicknesses and arrangement are guided by the chosen composition and do not require human intervention. Also, they are necessarily thin sheets of 3D halide perovskites stacked together; so, they are expected to retain many advantages of the 3D halide perovskites like low trap-state densities compared to that in the III-V semiconductor materials, large carrier mobilities, and direct band gap.^{25, 54, 55, 56} Further, they exhibit excellent structural diversity, and the observed properties can be tuned by changing compositions. All these factors make 2D layered hybrid perovskites appealing for optoelectronic research.

1.4 Synthetic methods for 2D layered hybrid perovskites

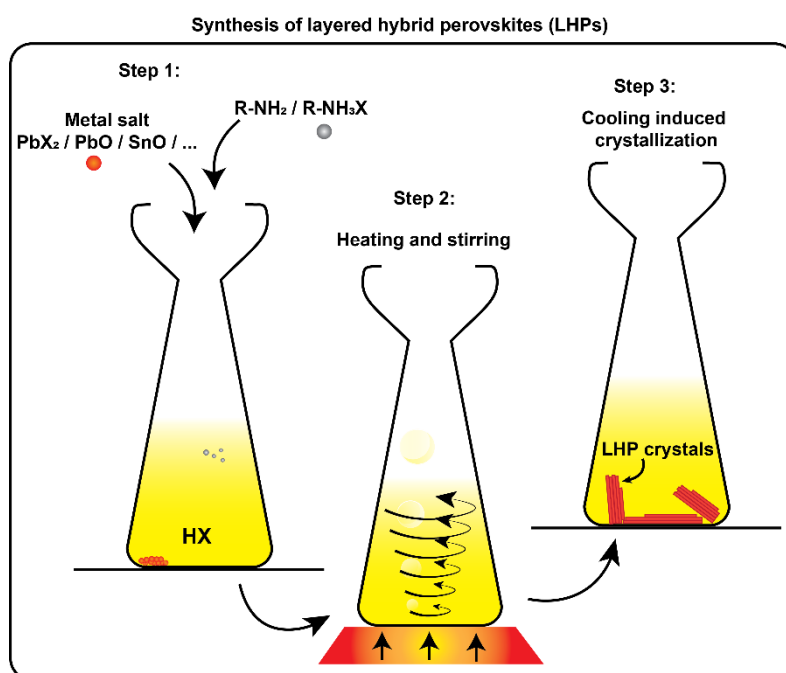


Figure 1.5: Schematic of the acid-precipitation method for preparation of layered hybrid perovskite crystals.

Several synthetic methods have been reported for layered hybrid perovskite crystals. These include solution-phase synthesis methods like acid-precipitation,⁵⁷ crystallization in organic

solvents,⁵⁸ vapor diffusion,⁵⁹ solvothermal synthesis⁶⁰. Also, solid-state synthesis methods like grinding or ball-milling have been reported.⁶¹

Among these, the acid-precipitation method is the most widely used. Figure 1.5 schematically displays the process. In this, aqueous hydrohalic acid (HX; X = Cl, Br, I) is used to dissolve the A-site and M-site precursors. The acid solution has a dual role; it serves as the source of halogen ions and the solvent for the reaction. For the A-site cations, the corresponding amine or its salt is taken. Similarly, for the M-site cation, metal salts such as PbO, SnO, PbX₂ (X = Cl, Br, I), Pb(CH₃COO)₂ are taken. The salts are dissolved in the HX solution by heating and stirring, typically at the boiling condition. The heating and stirring are continued until all the precursors are dissolved, and a clear solution is obtained. This solution is kept undisturbed and cooled down to room temperature. The cooling affords centimeter-sized crystals of the targeted 2D hybrid perovskite composition with the halogen from the HX acid solution. Usually, the molar ratio of A and M in the targeted compositions is maintained by taking an appropriate molar amount of the corresponding precursors. Mixed halide compositions can also be synthesized using this method by mixing HX acids at different molar ratios.

1.5 Challenges

From the perspective of optoelectronic applications, while potentially having two crucial advantages, higher environmental stability compared to 3D halide perovskites and a larger compositional space, 2D layered hybrid perovskites bring in some new challenges. The major challenges are – a) these materials have a larger band gap than the corresponding 3D halide perovskite restricting efficient absorption of the entire visible range of photons, b) the charge transport in one direction is hindered because of the presence of insulating organic cations, and c) the photophysical processes are not adequately understood as they can vary drastically between different compositions.⁶²

The first two mentioned above have been attempted to be solved by intelligent composition design. First, the larger band gap is a direct consequence of their quantum well-like structure, making them less suitable for photovoltaic application. To address this issue, multilayered layered hybrid perovskites have been introduced where more than one octahedral layer are joined together in the stacking direction; effectively, increasing the width of the well and decreasing the spatial confinement.^{46, 63, 64} Devices made of multilayered layered hybrid perovskites outperform devices with 3D halide perovskites in the aspect of environmental stability but are still less efficient for solar energy conversion, possibly owing to the presence of a large number of defect states and higher exciton binding energy. The problem of charge transport has been addressed by making optimum contact at the layer edges and designing compositions with conductive organic cations.^{65, 66}

The third problem mentioned above is a bit broader. In 3D halide perovskites, the composition dependence of exciton properties is easier to map simply because the compositional space is much smaller. In contrast, 2D layered hybrid perovskites offer huge structural diversity. This, while potentially allowing excellent tunability of optical properties by varying composition, also makes it imperative to understand the composition-property relationship by studying as many compositions as possible. Unfortunately, computational methods like DFT based calculations have not found much success in this regard because of the huge unit cell volumes and a large number of atoms in it, along with the presence of organic/inorganic interfaces. This thesis attempts to solve this third problem by exploring the compositional dependence on optical properties. In the following section, we briefly discuss three key phenomena that bring significant changes in the optical properties among different 2D hybrid perovskite compositions.

a) Confinement effects

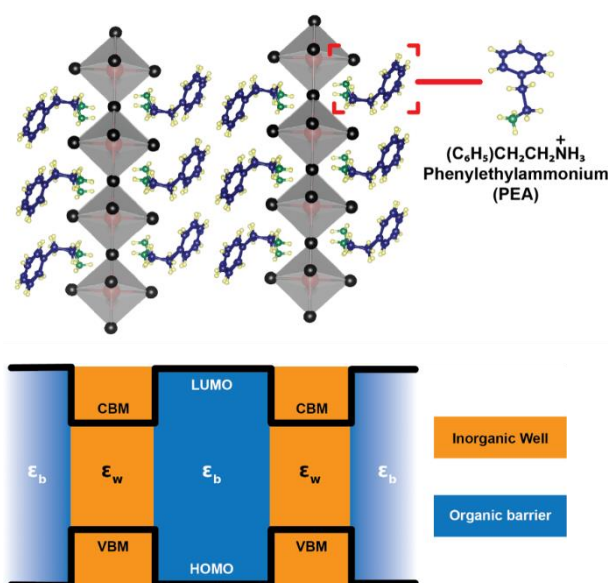


Figure 1.6: Multi quantum well structure of 2D layered hybrid perovskite. In $(\text{PEA})_2\text{PbI}_4$, Pb-I (M-X) octahedra form the well, and the organic PEA cation (A) form the barrier.

Like the Bohr Hydrogen model gives out the 3D Mott-Wannier exciton model, an analogous 2D Schrödinger equation for the electron and hole (also called 2D Wannier model) can be constructed for an exciton confined in a 2D semiconductor medium (See Figure 1.3b). It turns out that the energies of the 2D exciton states resemble the 3D exciton model. For exciton states with $N = 1, 2, 3, \dots$, the energy is expressed by the following equation:

$$E_b^{2D} = \frac{E_b^{3D}}{\left(N - \frac{1}{2}\right)^2} \quad \text{Eq. (1.3)}$$

Here, E_b^{2D} and E_b^{3D} are the binding energy of the N^{th} exciton state of 2D and 3D exciton, respectively. So, for 1s excitons with $N = 1$, $E_b^{2D} = 4E_b^{3D}$, provided both 2D and 3D systems are identical.

The inorganic (M-X) layer in a 2D layered hybrid perovskite like $(\text{PEA})_2\text{PbI}_4$ (PEA: phenylethylammonium) (Figure 1.6) is $\sim 6 \text{ \AA}$ thick. An exciton in this layer will feel strong spatial confinement. Therefore, its $E_{b,1s}$ is expected to increase four times compared to a comparable 3D material like MAPbI_3 . The increased exciton binding energy is also expected to increase the exciton recombination rate in $(\text{PEA})_2\text{PbI}_4$ compared to MAPbI_3 .

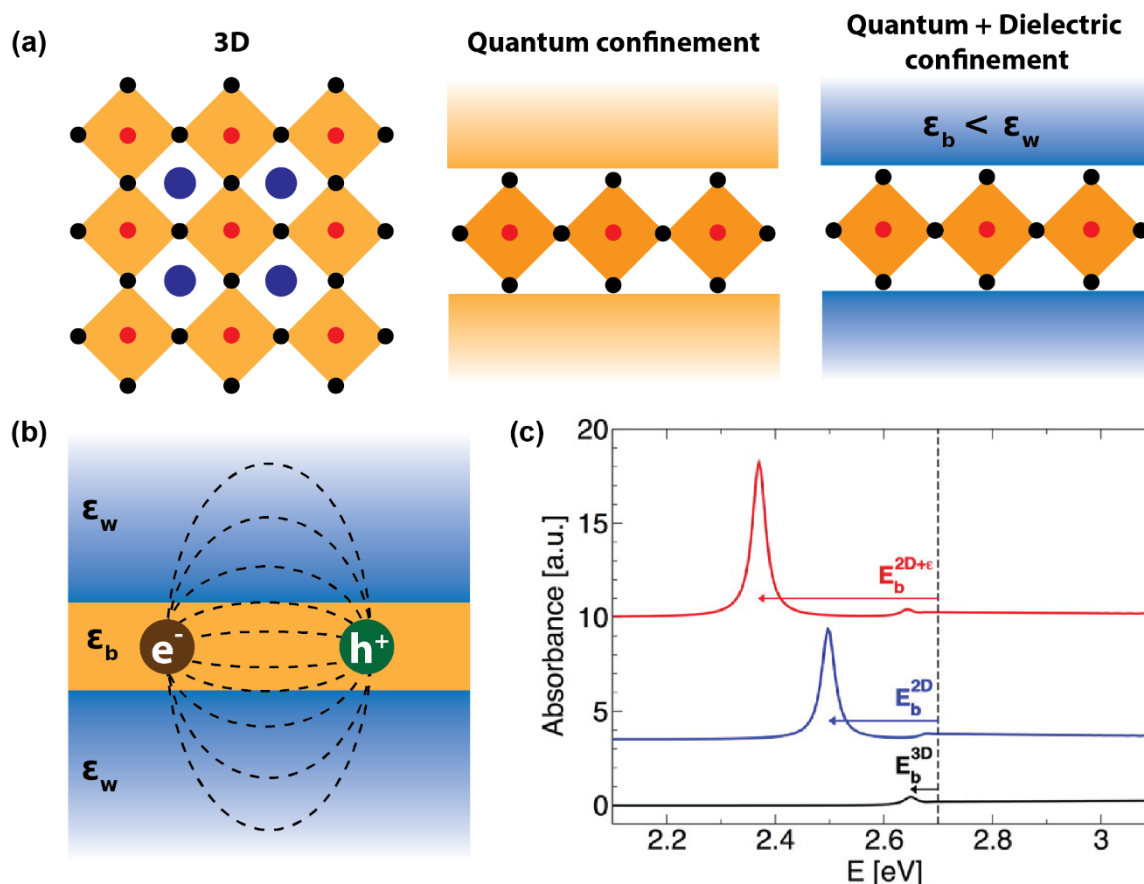


Figure 1.7: Quantum and dielectric confinement effects. (a) Origin of the confinement effects in the halide perovskite lattice. Here, ϵ_w and ϵ_b are the high-frequency dielectric constant of the well and barrier layers, respectively. (b) Schematic of the dielectric confinement in a quantum-well structure. The dashed lines indicate the attractive force acting between the electron and hole. (c) Simulated effect of quantum and dielectric confinement on optical absorption due to 1s exciton. The band gap is set at 2.7 eV, indicated by the vertical dash-line. The black line is the absorbance spectra computed on a hypothetical 3D system having the same high-frequency dielectric constant as that of the well layer (ϵ_w). The small exciton binding energy, E_b^{3D} corresponds to the 3D exciton. Turning on the quantum confinement effect while keeping the dielectric constant homogeneous shifts the resonance peak at lower energy (blue line). Further incorporating the dielectric confinement results in an additional shift and an enhanced exciton resonance (red line). Reprinted from reference with permission from American Chemical Society.⁶⁷

For the case of halide perovskites, when we move from a 3D structure to a 2D layered structure (Figure 1.2), both the dielectric constant ϵ (in equation 1.2) and reduced mass of the exciton (μ) change. So, it is not possible to obtain E_b^{2D} from E_b^{3D} using equation 1.3. If we consider only the "quantum confinement" case in Figure 1.7a, where ϵ is same for 3D systems, 2D well, and 2D barrier, then E_b^{2D} should be close to $4E_b^{3D}$. But in reality, 2D systems like $(\text{PEA})_2\text{PbI}_4$ have 25 times higher 1s exciton binding energy compared to a 3D system like MAPbI_3 .^{68, 69, 70}

To address this issue, on top of the spatial quantum confinement, dielectric confinement was prescribed. Dielectric confinement arises due to the contrast of the dielectric constants between two subsequent layers in a quantum-well structure (right panel of Figure 1.7a). It was theoretically studied by Rytova, Keldysh, and Muljarov, for thin semiconductor films sandwiched between two layers of different dielectric constants.^{71, 72} The idea stems from the fact that the electrical force field of Coulomb attraction between electron and hole in an exciton residing in the well layer, would also penetrate the barrier layer (Figure 1.7b). Therefore, the high-frequency dielectric constant of both the barrier (ϵ_b) and well (ϵ_w) will determine the Coulomb force. If ϵ_b is significantly less than ϵ_w , then the net decrease in charge screening increases the Coulomb force, increasing the exciton binding energy. Such increase in exciton binding energy or exciton confinement because of dielectric contrast in the medium ($\epsilon_b < \epsilon_w$) is termed here as dielectric confinement. The $\left(\frac{\epsilon_w}{\epsilon_b}\right)$ ratio can qualitatively give the extent of dielectric confinement.

Experimentally, the effect of dielectric confinement should be observable in the exciton resonance signals in optical absorption and photoluminescence spectra. While separation of quantum and dielectric confinement effects is not possible by experimental means, computational simulation allows one to visualize the impact of both kinds of confinement on exciton absorption peak (Figure 1.7c). First, the quantum confinement increases the exciton binding energy E_b^{2D} shifting the exciton absorption peak to the lower energy side. Then the addition of dielectric confinement further increases the exciton binding energy $E_b^{2D+\epsilon}$, further blue-shifting the exciton resonance peak.⁶⁷ In both cases, the exciton absorbance intensity increases since incorporating the confinements results in higher oscillator strength of the excitons.

Dielectric confinement is expected to modulate optical properties in all semiconductor heterostructures; for example, III-V semiconductor quantum-well heterostructures like

GaAs/InAs/GaAs.^{73, 74} But in these heterostructures, both the well and barrier are of very similar chemical nature, yielding $\left(\frac{\epsilon_w}{\epsilon_b}\right)$ ratio ~ 1 . So significant effect of dielectric confinement is often not observed. In contrast, in layered 2D hybrid lead halide perovskites, the dielectric mismatch between the inorganic well and the organic barrier layer is significant. For example, in much-studied $(\text{BA})_2\text{PbI}_4$, the $\left(\frac{\epsilon_w}{\epsilon_b}\right)$ ratio is expected to be close to 3. As a result, the enhancement of $E_b^{2D+\epsilon}$ is also expected to be much more significant than what has been observed in the III-V quantum-well heterostructures. Thus, tuning of the $\left(\frac{\epsilon_w}{\epsilon_b}\right)$ ratio by appropriate choice of inorganic and organic layer composition can avail a strategy to tune exciton binding energies of 2D layered hybrid perovskites.

b) Structural distortions

Even when the confinement effects are expected to remain similar, hybrid perovskite compositions show drastic differences in the optical properties.^{75, 76} Such changes in optical properties of layered hybrid perovskites are brought by the distortions in the inorganic layer. Because of the small thickness, the inorganic sub-lattice is very susceptible to deformation by force exerted on them in the form of external perturbation like temperature and pressure.^{77, 78} Also, internal non-covalent interactions originating from the organic cations can act as the force to cause noticeable changes in the inorganic layer's structure.⁷⁹

In order to understand how structural distortions influence the exciton properties in 2D layered hybrid perovskites, we need to look at the electronic band structure of these semiconductors. Figure 1.8a shows the DFT computed electronic bandstructure of $(\text{BA})_2\text{PbI}_4$.⁸⁰ Figure 1.8b shows the electron densities corresponding to the band edge states (VBM and CBM). Notably, the electron densities at the VBM and CBM are localized exclusively in the Pb-I layer. The overlap of the Pb and I orbitals will determine the dispersions (related to carrier effective

masses) and energy of the electronic edge states, determining the optical band gap and exciton emission energies.

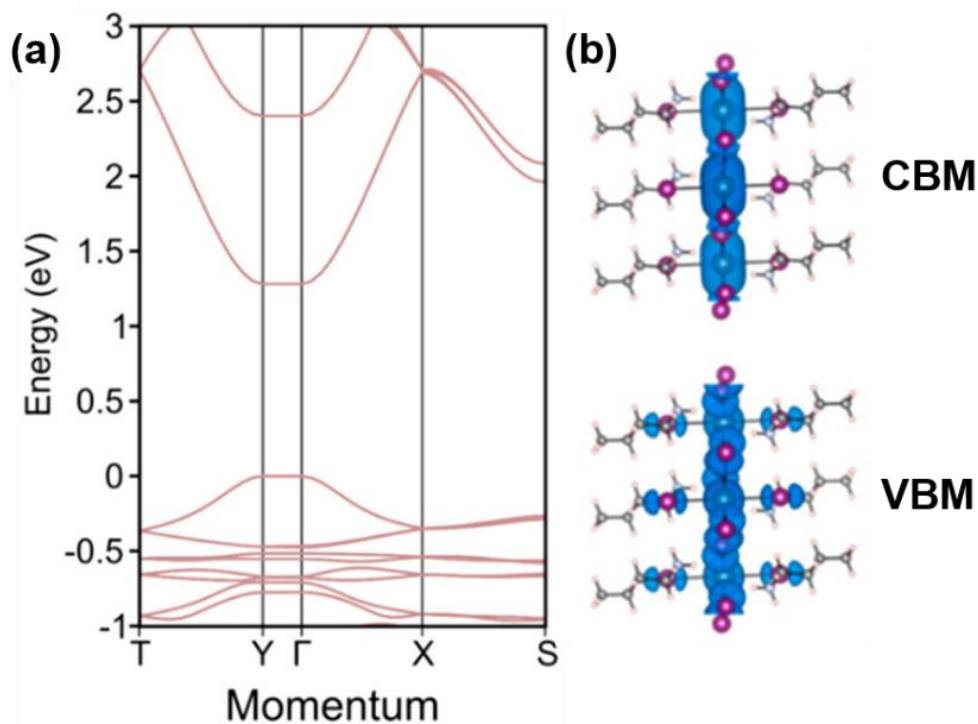


Figure 1.8: DFT computed electronic bandstructure of $(\text{BA})_2\text{PbI}_4$. (b) Corresponding local densities of states at CBM and VBM, showing the localization of electron densities on Pb-I sheets.⁸⁰ Reprinted from reference, with permission from Springer.

The situation remains similar in most 2D hybrid perovskite compositions; the valence and conduction band edges are dominantly defined by the M and X p -orbitals. Due to the directional nature of the p -orbitals, the energies of the edge electronic states are extremely sensitive towards the structural distortions. Distortions, particularly the bending of the metal-halide-metal (M-X-M) bond angle (Figure 1.9a), and the distance of the M-X bond change the extent of overlap of the p -orbitals resulting in different band gaps and exciton emission energies between different hybrid perovskite compositions. A previously reported theoretical study shows that it is possible to bring a band gap change as high as 1 eV by tuning the M-X-M bond angle (Figure 1.9b).⁸¹

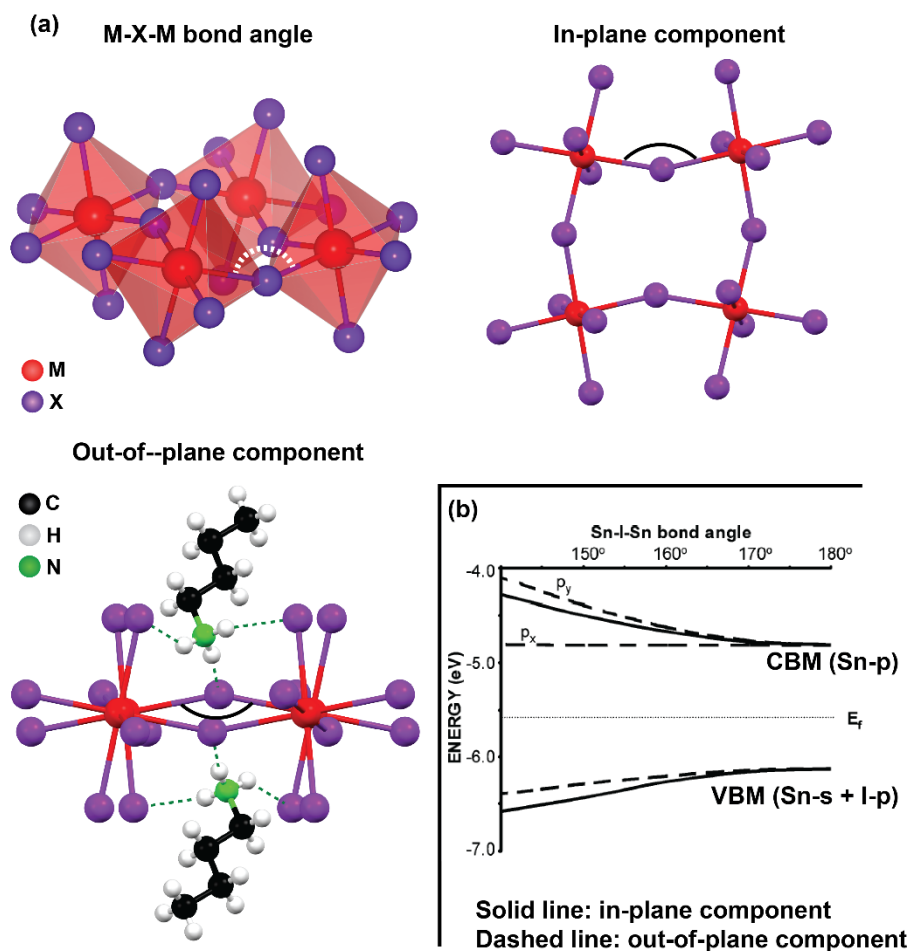


Figure 1.9: (a) metal-halide-metal (M-X-M) bond angle and its components. Non-covalent interactions are shown with green dashed lines. (b) Influence of changing M-X-M bond angle on the band edge energies. Reprinted from reference, with permission from American Chemical Society.⁸¹

c) Exciton trapping

Even while having hundreds of meVs of exciton binding energy, 2D layered hybrid perovskites fail to show high exciton luminescence quantum yield values, unlike their 3D counterparts.⁸² This observation has been attributed to the presence of crystal defects at the interfaces.⁸³ Since the materials are solution-processed at low temperatures, defects like atom vacancy and dangling bonds are expected in all halide perovskite compositions. However, while such defects limit the exciton luminescence quantum yield, they have been hypothesized to play an important role in creating trapped exciton emission in multiple 2D hybrid perovskite compositions.⁸⁴ Unlike traditional semiconductors like CdS, the trapped exciton emission in 2D layered hybrid perovskites is somewhat different. In 2D layered hybrid perovskites, the so-

called "self-trapped exciton (STE)" emission has been common.^{85, 86} The STE emission can potentially be useful for broadband light-emitting applications. In order to understand STE emission, we need to discuss first how defect state emission takes place in traditional semiconductors like CdSe or CuInS₂.⁸⁷⁻⁸⁹

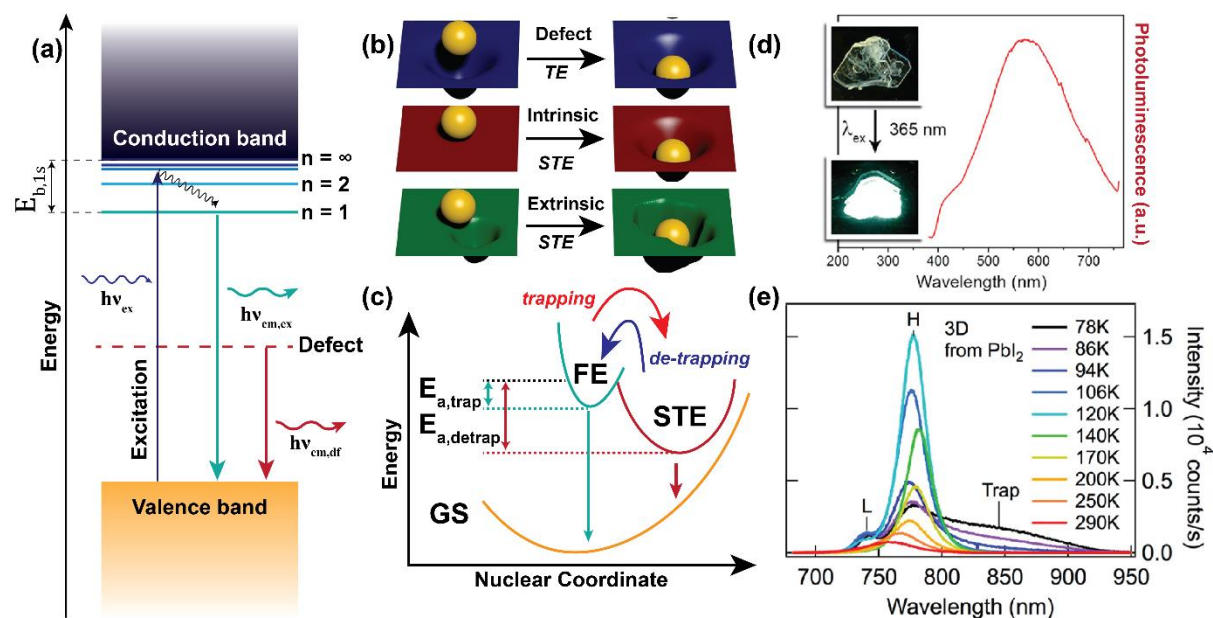


Figure 1.10: Schematic of (a) defect state emission in traditional semiconductors, (b) formation of the self-trapped exciton (STE), (c) mechanism of luminescence from STE. (d) Photoluminescence (PL) spectrum of (EDBE)PbBr₄ (EDBE: 2,2'-(ethylenedioxy)bis(ethylammonium)) powders. Inset shows photographs of one single (EDBE)PbBr₄ crystal. (e) Temperature-dependent PL from MAPbI₃ (MA: methylammonium) thin film. (b), (d), and (e) reprinted with permission from American Chemical Society.^{76, 83}

Crystal defects in semiconductors tend to trap excitons and provide new recombination channels. While for the majority of the cases, such recombination channels are non-radiative and thus, detrimental towards optoelectronic performances, in some cases, the presence of trap states can provide additional stability to a formed exciton and opens up a new radiative recombination pathway (Figure 1.10a). This kind of radiative recombination happens at lower energy than that of the exciton emission. Because of the involvement of vibrational states, trap state emissions are usually broad and have long lifetimes. Incorporating emissive trap states through doping has been an effective strategy for obtaining different emission colors from the same material.^{90, 91}

The top panel in Figure 1.10b schematically shows the process of exciton trapping in the presence of a crystal defect. The primary physical phenomenon that governs exciton trapping is the exciton-lattice coupling. Individual carriers (electron and hole), being charged, attempt to attract or repel ions constituting the lattice. In a perfect crystalline lattice with 3D covalent connectivity, these interactions do not alter the nuclear positions significantly, and exciton-lattice coupling is small. This is since nuclei are always much heavier than the carriers, and the lattice is rigid. In the presence of a defect, the local charge imbalance of the lattice facilitates such interactions, thereby increasing the exciton-lattice coupling; in other words, trapping the exciton. However, in salts like NaCl, or AgCl, the bonds have very little co-valency, and the overall crystal is less rigid; these ionic crystals are examples of so-called "*soft-lattice*." In soft lattices, the exciton-lattice coupling is much stronger, even without the presence of crystal defects.⁵²

Due to the loss of connectivity in one dimension, the 2D hybrid perovskite matrix is inherently soft and flexible. A formed exciton can deform the nuclear positions and electron densities in these systems, forming a transient defect in the excited state (middle panel in Figure 1.10b). In turn, the exciton can get trapped in these defect states, resulting in a very broad and large Stokes shifted (~ 1 eV) emission, often spanning the entire visible spectral region. Such emissions are very desirable for light-emitting applications as they can serve as single-source white light phosphors. These trapped excitons are referred to as STEs, more appropriately, *intrinsic*-STEs. Further, suppose a crystal defect is already present in the lattice in the ground state. In that case, the formation and stabilization of STEs are even more favored near these permanent defects. This type of STEs, formed with the help of a permanent defect, are called *extrinsic*-STEs (bottom panel in Figure 1.10b).

The population of STE is temperature-dependent. Figure 1.10c shows the schematic of exciton trapping in an STE well. A free exciton needs to overcome a small energy barrier $E_{a,trap}$ to cross

over to the STE well. $E_{a,\text{trap}}$ corresponds to the energy required to distort a perfectly crystalline lattice and form the STE well. Naturally, at very low temperatures ($kT < E_{a,\text{trap}}$), STE formation is unlikely. On the other hand, the STE can transfer back to the exciton well at high enough temperatures ($kT > E_{a,\text{detrap}}$). Such temperature dependence uniquely differentiates STE emission from typical trapped exciton emission, where exciton trapping is an almost barrierless process ($E_{a,\text{trap}} \approx 0$ a.u.), but de-trapping is not.

In $A_2\text{PbX}_4$ ($X = \text{Cl}, \text{Br}$) layered hybrid perovskite compositions, at room temperature, STEs afford white-light emission without the need of any external dopants (Figure 1.10d). Such STE emissions can be tuned and made to obtain high photoluminescence quantum yield.^{62, 92} These STEs are believed to be of the extrinsic kind. However, STE's existence, origin, and nature in the 2D hybrid perovskite iodide systems are largely unknown and debated. 3D halide perovskite like MAPbI_3 shows broad trapped exciton emission at lower temperatures (Figure 1.10e), which has been assigned to STE formation at the surface.⁸³ In 2D hybrid perovskite compositions, the overall contribution of interfaces is much higher than that in 3D. Thus, one should expect a more prominent presence of such STE exhibiting broad red emission. However, still most 2D hybrid perovskite $A_2\text{PbI}_4$ compositions do not afford STE emission at room temperature. Also, unlike the bromide and chloride counterparts, the composition dependence of STEs in the iodide 2D hybrid perovskite crystals has not been studied systematically.

1.6 Scope of this thesis

As the compositional space of 2D layered hybrid perovskites is broadening every year, there is a need for a strategy to guide experimental material chemists to find an optimum composition for their choice of application. In this thesis, we attempt to develop that for 2D layered hybrid Pb-halide perovskites.

We identify four potential areas where improvement of understanding or methodology is required –

a) The compositional dependence of confinement effects in the A_2PbX_4 compositions: for light-emitting applications, the compositions are expected to avail a high exciton binding energy so that excitons can have a high probability of radiative recombination. On the other hand, for photovoltaics applications, a small exciton binding energy is required. We hypothesize that this can be achieved by tuning the dielectric confinement by changing A and X.

b) The compositional dependence of emission energy in A_2PbI_4 compositions: The emission energy is related to the band gap as,

$$\text{emission energy} = \text{band gap} - \text{exciton binding energy}$$

If exciton binding energy remains unchanged, emission energy and band gap change in a similar way. Since the non-covalent interactions between the organic and inorganic sub-lattices influence the band gap, it might be possible to tune the emission energies by understanding how different A-site cations non-covalently interact with the Pb-I sub-lattice.

c) Broadband emission in layered hybrid A_2PbI_4 compositions: The broadband emission can enable efficient red emission from these compositions. However, the origin and compositional dependence of broadband emission from these compositions are not appropriately understood. The understanding can potentially help in improving the emission efficiency.

d) Material degradation during spectroscopic analysis: Spectroscopic measurements are essential for the analysis of optical properties. In measurements like temperature-dependent photoluminescence, the experiments typically take a long time. They are sometimes responsible for the samples' degradation due to continuous excitation from a high-intensity laser source. A machine learning-based approach can decrease the overall time of the measurement by interpolating in a sparsely collected dataset.

These four problems described above have been attempted to be tackled in different chapters of this thesis. In the subsequent four chapters, we correlate composition and different exciton

properties in 2D hybrid Pb-halide perovskites using spectroscopic, crystallographic, and computational techniques.

1.7 References

- (1) Breternitz, J.; Schorr, S. What Defines a Perovskite? *Adv. Energy Mater.* **2018**, *8*, 1802366.
- (2) Rose, G. Ueber Einige Neue Mineralien des Urals. *J. Prakt. Chem.* **1840**, *19*, 459-468.
- (3) Goldschmidt, V. M. Die Gesetze der Krystallochemie. *Sci. Nat.* **1926**, *14*, 477-485.
- (4) Møller, C. K. The Structure of Perovskite-Like Caesium Plumbo Trihalides. *København Munksgaard* **1959**.
- (5) Wells, H. L. Über die Cäsium- und Kalium-Bleihalogenide. *Z. anorg. Chem.* **1893**, *3*, 195-210.
- (6) Weber, D. $\text{CH}_3\text{NH}_3\text{PbX}_3$, ein Pb(II)-System mit kubischer Perowskitstruktur / $\text{CH}_3\text{NH}_3\text{PbX}_3$, a Pb(II)-System with Cubic Perovskite Structure. *Z. Naturforsch. B* **1978**, *33*, 1443-1445.
- (7) Weber, D. $\text{CH}_3\text{NH}_3\text{SnBr}_x\text{I}_{3-x}$ ($x = 0-3$), ein Sn(II)-System mit kubischer Perowskitstruktur / $\text{CH}_3\text{NH}_3\text{SnBr}_x\text{I}_{3-x}$ ($x = 0-3$), a Sn(II)-System with Cubic Perovskite Structure. *Z. Naturforsch. B* **1978**, *33*, 862-865.
- (8) Stoumpos, C. C.; Kanatzidis, M. G. Halide Perovskites: Poor Man's High-Performance Semiconductors. *Adv. Mater.* **2016**, *28*, 5778-5793.
- (9) Bartel, C. J.; Clary, J. M.; Sutton, C.; Vigil-Fowler, D.; Goldsmith, B. R.; Holder, A. M.; Musgrave, C. B. Inorganic Halide Double Perovskites with Optoelectronic Properties Modulated by Sublattice Mixing. *J. Am. Chem. Soc.* **2020**, *142*, 5135-5145.
- (10) Chiara, R.; Morana, M.; Malavasi, L. Germanium-based Halide Perovskites: Materials, Properties, and Applications. *ChemPlusChem* **2021**, *6*, 879-888.
- (11) Jena, A. K.; Kulkarni, A.; Miyasaka, T. Halide Perovskite Photovoltaics: Background, Status, and Future Prospects. *Chem. Rev.* **2019**, *119*, 3036-3103.

- (12) Swarnkar, A.; Mir, W. J.; Chakraborty, R.; Jagadeeswararao, M.; Sheikh, T.; Nag, A. Are Chalcogenide Perovskites an Emerging Class of Semiconductors for Optoelectronic Properties and Solar Cell? *Chem. Mater.* **2019**, *31*, 565-575.
- (13) Kojima, A.; Teshima, K.; Shirai, Y.; Miyasaka, T. Organometal Halide Perovskites as Visible-Light Sensitizers for Photovoltaic Cells. *J. Am. Chem. Soc.* **2009**, *131*, 6050-6051.
- (14) Lee, M. M.; Teuscher, J.; Miyasaka, T.; Murakami, T. N.; Snaith, H. J. Efficient Hybrid Solar Cells Based on Meso-Superstructured Organometal Halide Perovskites. *Science* **2012**, *338*, 643-647.
- (15) Xing, G.; Mathews, N.; Lim, S. S.; Yantara, N.; Liu, X.; Sabba, D.; Grätzel, M.; Mhaisalkar, S.; Sum, T. C. Low-Temperature Solution-Processed Wavelength-Tunable Perovskites for Lasing. *Nat. Mater.* **2014**, *13*, 476-480.
- (16) Utzat, H.; Sun, W.; Kaplan, A. E. K.; Krieg, F.; Ginterseder, M.; Spokoyny, B.; Klein, N. D.; Shulenberger, K. E.; Perkinson, C. F.; Kovalenko, M. V.; Bawendi, M. G. Coherent Single-Photon Emission from Colloidal Lead Halide Perovskite Quantum Dots. *Science* **2019**, *363*, 1068-1072.
- (17) Hassan, Y.; Ashton, O. J.; Park, J. H.; Li, G.; Sakai, N.; Wenger, B.; Haghighirad, A.-A.; Noel, N. K.; Song, M. H.; Lee, B. R.; Friend, R. H.; Snaith, H. J. Facile Synthesis of Stable and Highly Luminescent Methylammonium Lead Halide Nanocrystals for Efficient Light Emitting Devices. *J. Am. Chem. Soc.* **2019**, *141*, 1269-1279.
- (18) Wang, K.-H.; Peng, Y.; Ge, J.; Jiang, S.; Zhu, B.-S.; Yao, J.; Yin, Y.-C.; Yang, J.-N.; Zhang, Q.; Yao, H.-B. Efficient and Color-Tunable Quasi-2D CsPbBr_xCl_{3-x} Perovskite Blue Light-Emitting Diodes. *ACS Photonics* **2019**, *6*, 667-676.
- (19) Schlaus, A. P.; Spencer, M. S.; Miyata, K.; Liu, F.; Wang, X.; Datta, I.; Lipson, M.; Pan, A.; Zhu, X. Y. How Lasing Happens in CsPbBr₃ Perovskite Nanowires. *Nat. Commun.* **2019**, *10*, 265.

- (20) Jeong, M.; Choi, I. W.; Go, E. M.; Cho, Y.; Kim, M.; Lee, B.; Jeong, S.; Jo, Y.; Choi, H. W.; Lee, J. et al. Stable Perovskite Solar Cells with Efficiency Exceeding 24.8% and 0.3-V Voltage Loss. *Science* **2020**, *369*, 1615-1620.
- (21) Dong, Y.; Wang, Y.-K.; Yuan, F.; Johnston, A.; Liu, Y.; Ma, D.; Choi, M.-J.; Chen, B.; Chekini, M.; Baek, S.-W. et al. Bipolar-Shell Resurfacing for Blue LEDs Based on Strongly Confined Perovskite Quantum Dots. *Nat. Nanotechnol.* **2020**, *15*, 668-674.
- (22) Ji, K.; Anaya, M.; Abfalterer, A.; Stranks, S. D. Halide Perovskite Light-Emitting Diode Technologies. *Adv. Opt. Mater.* **2021**, *9*, 2002128.
- (23) Xiang, W.; Liu, S.; Tress, W. A Review on the Stability of Inorganic Metal Halide Perovskites: Challenges and Opportunities for Stable Solar Cells. *Energy Environ. Sci.* **2021**, *14*, 2090-2113.
- (24) Dey, A.; Ye, J.; De, A.; Debroye, E.; Ha, S. K.; Bladt, E.; Kshirsagar, A. S.; Wang, Z.; Yin, J.; Wang, Y. et al. State of the Art and Prospects for Halide Perovskite Nanocrystals. *ACS Nano* **2021**, *15*, 10775-10981.
- (25) Mitzi, D. B.; Wang, S.; Feild, C. A.; Chess, C. A.; Guloy, A. M. Conducting Layered Organic-Inorganic Halides Containing <110>-Oriented Perovskite Sheets. *Science* **1995**, *267*, 1473-1476.
- (26) Nag, A. "Plenty of Room" at the Interface of Hybrid Metal Halide Perovskite Single Crystals. *Nano Lett.* **2021**, doi:10.1021/acs.nanolett.1c03247.
- (27) Ian, S.; Ian, C. S.; Eric, T. H.; Diego, S.-I.; Michael, D. M.; Hemamala, I. K. A Layered Hybrid Perovskite Solar Cell Absorber with Enhanced Moisture Stability. *Angew. Chem. Int. Ed.* **2014**, *53*, 11232-11235.
- (28) Cao, D. H.; Stoumpos, C. C.; Farha, O. K.; Hupp, J. T.; Kanatzidis, M. G. 2D Homologous Perovskites as Light-Absorbing Materials for Solar Cell Applications. *J. Am. Chem. Soc.* **2015**, *137*, 7843-7850.

- (29) Mokhlisse, R.; Couzi, M.; Chanh, N. B.; Haget, Y.; Hauw, C.; Meresse, A. Raman Scattering and X-Ray Diffraction Study of Structural Phase Transitions in the Perovskite-Type Layer Compound $(C_3H_7NH_3)_2CdCl_4$. *J. Phys. Chem. Solids* **1985**, *46*, 187-195.
- (30) I., D. Y.; Tamotsu, I.; Yusei, M. In Situ X-Ray Observation on the Intercalation of Weak Interaction Molecules into Perovskite-Type Layered Crystals $(C_9H_{19}NH_3)_2PbI_4$ and $(C_{10}H_{21}NH_3)_2CdCl_4$. *Bull. Chem. Soc. Jpn* **1986**, *59*, 563-567.
- (31) Ishi, J.; Mizuno, M.; Kunugita, H.; Ema, K.; Iwamoto, S.; Hayase, S.; Kondo, T.; Ito, R. Third-Order Optical Nonlinearity due to Excitons and Biexcitons in a Self-Organized Quantum-Well Material $(C_6H_{13}NH_3)_2PbI_4$. *J. Nonlinear Opt. Phys. Mater.* **1998**, *7*, 153-159.
- (32) Ishihara, T.; Takahashi, J.; Goto, T. Exciton State in Two-Dimensional Perovskite Semiconductor $(C_{10}H_{21}NH_3)_2PbI_4$. *Solid State Commun.* **1989**, *69*, 933-936.
- (33) Ishihara, T.; Takahashi, J.; Goto, T. Optical Properties due to Electronic Transitions in Two-Dimensional Semiconductors $(C_nH_{2n+1}NH_3)_2PbI_4$. *Phys. Rev. B* **1990**, *42*, 11099-11107.
- (34) Hong, X.; Ishihara, T.; Nurmikko, A. V. Dielectric Confinement Effect on Excitons in PbI_4 -Based Layered Semiconductors. *Phys. Rev. B* **1992**, *45*, 6961-6964.
- (35) Ishihara, T. Optical Properties of PbI -Based Perovskite Structures. *J. Lumin.* **1994**, *60-61*, 269-274.
- (36) Muljarov, E. A.; Tikhodeev, S. G.; Gippius, N. A.; Ishihara, T. Excitons in Self-Organized Semiconductor/Insulator Superlattices: PbI -Based Perovskite Compounds. *Phys. Rev. B Condens. Matter* **1995**, *51*, 14370-14378.
- (37) Goto, T.; Makino, H.; Yao, T.; Chia, C. H.; Makino, T.; Segawa, Y.; Mousdis, G. A.; Papavassiliou, G. C. Localization of Triplet Excitons and Biexcitons in the Two-Dimensional Semiconductor $(CH_3C_6H_4CH_2NH_3)_2PbBr_4$. *Phys. Rev. B* **2006**, *73*, 115206.

- (38) Koutselas, I. B.; Ducasse, L.; Papavassiliou, G. C. Electronic Properties of Three- and Low-Dimensional Semiconducting Materials with Pb Halide and Sn Halide Units. *J. Condens. Matter Phys.* **1996**, *8*, 1217-1227.
- (39) Mitzi, D. B. Synthesis, Crystal Structure, and Optical and Thermal Properties of $(C_4H_9NH_3)_2MI_4$ ($M = Ge, Sn, Pb$). *Chem. Mater.* **1996**, *8*, 791-800.
- (40) Mitzi, D. B.; Liang, K., Preparation and Properties of $(C_4H_9NH_3)_2EuI_4$: A Luminescent Organic–Inorganic Perovskite with a Divalent Rare-Earth Metal Halide Framework. *Chem. Mater.* **1997**, *9*, 2990-2995.
- (41) Mitzi, D. B. Organic–Inorganic Perovskites Containing Trivalent Metal Halide Layers: The Templating Influence of the Organic Cation Layer. *Inorg. Chem.* **2000**, *39*, 6107-6113.
- (42) Makino, H.; Goto, T.; Yao, T.; Mousdis, G. A.; Papavassiliou, G. C. Induced Absorption and Spontaneous Emission due to Biexciton in Two-Dimensional Semiconductor $(CH_3C_6H_4CH_2NH_3)_2PbBr_4$ Single Crystal. *J. Lumin.* **2005**, *112*, 54-57.
- (43) Long, G.; Sabatini, R.; Saidaminov, M. I.; Lakhwani, G.; Rasmita, A.; Liu, X.; Sargent, E. H.; Gao, W. Chiral-Perovskite Optoelectronics. *Nat. Rev. Mater.* **2020**, *5*, 423-439.
- (44) Guo, W.; Liu, X.; Han, S.; Liu, Y.; Xu, Z.; Hong, M.; Luo, J.; Sun, Z. Room-Temperature Ferroelectric Material Composed of a Two-Dimensional Metal Halide Double Perovskite for X-ray Detection. *Angew. Chem. Int. Ed.* **2020**, *59*, 13879-13884.
- (45) Kim, Y.-H.; Zhai, Y.; Lu, H.; Pan, X.; Xiao, C.; Gaubing, E. A.; Harvey, S. P.; Berry, J. J.; Vardeny, Z. V.; Luther, J. M.; Beard, M. C. Chiral-Induced Spin Selectivity Enables a Room-Temperature Spin Light-Emitting Diode. *Science* **2021**, *371*, 1129-1133.
- (46) Tsai, H.; Nie, W.; Blancon, J.-C.; Stoumpos, C. C.; Asadpour, R.; Harutyunyan, B.; Neukirch, A. J.; Verduzco, R.; Crochet, J. J.; Tretiak, S. et al. High-Efficiency Two-Dimensional Ruddlesden–Popper Perovskite Solar Cells. *Nature* **2016**, *536*, 312-316.

- (47) Ke, W.; Mao, L.; Stoumpos, C. C.; Hoffman, J.; Spanopoulos, I.; Mohite, A. D.; Kanatzidis, M. G. Compositional and Solvent Engineering in Dion–Jacobson 2D Perovskites Boosts Solar Cell Efficiency and Stability. *Adv. Energy Mater.* **2019**, *9*, 1803384.
- (48) Yuan, M.; Quan, L. N.; Comin, R.; Walters, G.; Sabatini, R.; Voznyy, O.; Hoogland, S.; Zhao, Y.; Beauregard, E. M.; Kanjanaboos, P.; Lu, Z.; Kim, D. H.; Sargent, E. H. Perovskite Energy Funnels for Efficient Light-Emitting Diodes. *Nat. Nanotechnol.* **2016**, *11*, 872-877.
- (49) Wang, N.; Cheng, L.; Ge, R.; Zhang, S.; Miao, Y.; Zou, W.; Yi, C.; Sun, Y.; Cao, Y.; Yang, R. et al. Perovskite Light-Emitting Diodes Based on Solution-Processed Self-Organized Multiple Quantum Wells. *Nat. Photonics* **2016**, *10*, 699-704.
- (50) Liu, Y.; Yu, Z.; Chen, S.; Park, J. H.; Jung, E. D.; Lee, S.; Kang, K.; Ko, S.-J.; Lim, J.; Song, M. H. et al. Boosting the Efficiency of Quasi-2D Perovskites Light-Emitting Diodes by Using Encapsulation Growth Method. *Nano Energy* **2021**, *80*, 105511.
- (51) Ren, M.; Cao, S.; Zhao, J.; Zou, B.; Zeng, R. Advances and Challenges in Two-Dimensional Organic–Inorganic Hybrid Perovskites Toward High-Performance Light-Emitting Diodes. *Micro Nano Lett.* **2021**, *13*, 163.
- (52) Pelant, I.; Valenta, J. *Luminescence Spectroscopy of Semiconductors*, Oxford University Press Inc., **2012**; Chapter 7: Luminescence of excitons.
- (53) Dupuis, R. D.; Dapkus, P. D.; Chin, R.; Holonyak, N.; Kirchoefer, S. W. Continuous 300 °K Laser Operation of Single-quantum-well $\text{Al}_x\text{Ga}_{1-x}\text{As}$ -GaAs Heterostructure Diodes Grown by Metal-Organic Chemical Vapor Deposition. *Appl. Phys. Lett.* **1979**, *34*, 265-267.
- (54) Ambrosio, F.; Wiktor, J.; De Angelis, F.; Pasquarello, A. Origin of Low Electron–Hole Recombination Rate in Metal Halide Perovskites. *Energy Environ. Sci.* **2018**, *11*, 101-105.

- (55) Cao, X.; Zhi, L.; Jia, Y.; Li, Y.; Zhao, K.; Cui, X.; Ci, L.; Zhuang, D.; Wei, J. A Review of the Role of Solvents in Formation of High-Quality Solution-Processed Perovskite Films. *ACS Appl. Mater. Inter.* **2019**, *11*, 7639-7654.
- (56) Herz, L. M. Charge-Carrier Mobilities in Metal Halide Perovskites: Fundamental Mechanisms and Limits. *ACS Energy Lett.* **2017**, *2*, 1539-1548.
- (57) Stoumpos, C. C.; Cao, D. H.; Clark, D. J.; Young, J.; Rondinelli, J. M.; Jang, J. I.; Hupp, J. T.; Kanatzidis, M. G. Ruddlesden–Popper Hybrid Lead Iodide Perovskite 2D Homologous Semiconductors. *Chem. Mater.* **2016**, *28*, 2852-2867.
- (58) Liu, Y.; Zhang, Y.; Yang, Z.; Ye, H.; Feng, J.; Xu, Z.; Zhang, X.; Munir, R.; Liu, J.; Zuo, P. et al. Multi-Inch Single-Crystalline Perovskite Membrane for High-Detectivity Flexible Photosensors. *Nat. Commun.* **2018**, *9*, 5302.
- (59) Shi, D.; Adinolfi, V.; Comin, R.; Yuan, M.; Alarousu, E.; Buin, A.; Chen, Y.; Hoogland, S.; Rothenberger, A.; Katsiev, K. et al. Low Trap-State Density and Long Carrier Diffusion in Organolead Trihalide Perovskite Single Crystals. *Science* **2015**, *347*, 519-522.
- (60) Zhang, T.; Yang, M.; Benson, E. E.; Li, Z.; van de Lagemaat, J.; Luther, J. M.; Yan, Y.; Zhu, K.; Zhao, Y. A Facile Solvothermal Growth of Single Crystal Mixed Halide Perovskite $\text{CH}_3\text{NH}_3\text{Pb}(\text{Br}_{1-x}\text{Cl}_x)_3$. *Chem. Commun.* **2015**, *51*, 7820-7823.
- (61) Li, X.; Hoffman, J.; Ke, W.; Chen, M.; Tsai, H.; Nie, W.; Mohite, A. D.; Kepenekian, M.; Katan, C.; Even, J.; Wasielewski, M. R.; Stoumpos, C. C.; Kanatzidis, M. G. Two-Dimensional Halide Perovskites Incorporating Straight Chain Symmetric Diammonium Ions, $(\text{NH}_3\text{C}_m\text{H}_{2m}\text{NH}_3)(\text{CH}_3\text{NH}_3)_{n-1}\text{Pb}_n\text{I}_{3n+1}$ ($m = 4-9$; $n = 1-4$). *J. Am. Chem. Soc.* **2018**, *140*, 12226-12238.
- (62) Smith, M. D.; Connor, B. A.; Karunadasa, H. I. Tuning the Luminescence of Layered Halide Perovskites. *Chem. Rev.* **2019**, *119*, 3104-3139.

- (63) Blancon, J.-C.; Tsai, H.; Nie, W.; Stoumpos, C. C.; Pedesseau, L.; Katan, C.; Kepenekian, M.; Soe, C. M. M.; Appavoo, K.; Sfeir, M. Y. et al. Extremely Efficient Internal Exciton Dissociation Through Edge States in Layered 2D Perovskites. *Science* **2017**, *355*, 1288-1292.
- (64) Fu, W.; Wang, J.; Zuo, L.; Gao, K.; Liu, F.; Ginger, D. S.; Jen, A. K. Y. Two-Dimensional Perovskite Solar Cells with 14.1% Power Conversion Efficiency and 0.68% External Radiative Efficiency. *ACS Energy Lett.* **2018**, *3*, 2086-2093.
- (65) Zhang, X.; Wu, G.; Fu, W.; Qin, M.; Yang, W.; Yan, J.; Zhang, Z.; Lu, X.; Chen, H. Orientation Regulation of Phenylethylammonium Cation Based 2D Perovskite Solar Cell with Efficiency Higher than 11%. *Adv. Energy Mater.* **2018**, *8*, 1702498.
- (66) Gao, Y.; Shi, E.; Deng, S.; Shiring, S. B.; Snaider, J. M.; Liang, C.; Yuan, B.; Song, R.; Janke, S. M.; Liebman-Peláez, A. et al. Molecular Engineering of Organic–Inorganic Hybrid Perovskites Quantum Wells. *Nat. Chem.* **2019**, *11*, 1151-1157.
- (67) Pedesseau, L.; Saponi, D.; Traore, B.; Robles, R.; Fang, H.-H.; Loi, M. A.; Tsai, H.; Nie, W.; Blancon, J.-C.; Neukirch, A. et al. Advances and Promises of Layered Halide Hybrid Perovskite Semiconductors. *ACS Nano* **2016**, *10*, 9776-9786.
- (68) Miyata, A.; Mitioglu, A.; Plochocka, P.; Portugall, O.; Wang, J. T.-W.; Stranks, S. D.; Snaith, H. J.; Nicholas, R. J. Direct Measurement of The Exciton Binding Energy and Effective Masses for Charge Carriers in Organic–Inorganic Tri-Halide Perovskites. *Nat. Phys.* **2015**, *11*, 582.
- (69) Chakraborty, R.; Nag, A. Correlation of Dielectric Confinement and Excitonic Binding Energy in 2D Layered Hybrid Perovskites Using Temperature Dependent Photoluminescence. *J. Phys. Chem. C* **2020**, *124*, 16177-16185.

- (70) Ishihara, T.; Hong, X.; Ding, J.; Nurmikko, A. V. Dielectric Confinement Effect for Exciton and Biexciton States in PbI₄-based Two-Dimensional Semiconductor Structures. *Surf. Sci.* **1992**, *267*, 323-326.
- (71) L.V., K. Coulomb Interaction in Thin Semiconductor and Semimetal Films. *IJETP Lett.* **1979**, *29*, 658.
- (72) Muljarov, E. A.; Tikhodeev, S. G.; Gippius, N. A.; Ishihara, T. Excitons in Self-Organized Semiconductor/Insulator Superlattices: PbI-Based Perovskite Compounds. *Phys. Rev. B* **1995**, *51*, 14370-14378.
- (73) Kumagai, M.; Takagahara, T. Excitonic and Nonlinear-Optical Properties of Dielectric Quantum-Well Structures. *Phys. Rev. B* **1989**, *40*, 12359-12381.
- (74) Kulik, L. V.; Kulakovskii, V. D.; Bayer, M.; Forchel, A.; Gippius, N. A.; Tikhodeev, S. G. Dielectric Enhancement of Excitons in Near-Surface Quantum Wells. *Phys. Rev. B* **1996**, *54*, R2335-R2338.
- (75) Sheikh, T.; Shinde, A.; Mahamuni, S.; Nag, A. Possible Dual Bandgap in (C₄H₉NH₃)₂PbI₄ 2D Layered Perovskite: Single-Crystal and Exfoliated Few-Layer. *ACS Energy Lett.* **2018**, *3*, 2940-2946.
- (76) Smith, M. D.; Karunadasa, H. I. White-Light Emission from Layered Halide Perovskites. *Acc. Chem. Res.* **2018**, *51*, 619-627.
- (77) Tu, Q.; Spanopoulos, I.; Hao, S.; Wolverton, C.; Kanatzidis, M. G.; Shekhawat, G. S.; Dravid, V. P. Probing Strain-Induced Band Gap Modulation in 2D Hybrid Organic–Inorganic Perovskites. *ACS Energy Lett.* **2019**, *4*, 796-802.
- (78) Wang, Y.; Guo, S.; Luo, H.; Zhou, C.; Lin, H.; Ma, X.; Hu, Q.; Du, M.-h.; Ma, B.; Yang, W.; Lü, X. Reaching 90% Photoluminescence Quantum Yield in One-Dimensional Metal Halide C₄N₂H₁₄PbBr₄ by Pressure-Suppressed Nonradiative Loss. *J. Am. Chem. Soc.* **2020**, *142*, 16001-16006.

(79) Li, X.; Hoffman, J. M.; Kanatzidis, M. G. The 2D Halide Perovskite Rulebook: How the Spacer Influences Everything from the Structure to Optoelectronic Device Efficiency. *Chem. Rev.* **2021**, *121*, 2230-2291.

(80) Blancon, J. C.; Stier, A. V.; Tsai, H.; Nie, W.; Stoumpos, C. C.; Traoré, B.; Pedesseau, L.; Kepenekian, M.; Katsutani, F.; Noe, G. T. et al. Scaling Law for Excitons in 2D Perovskite Quantum Wells. *Nat. Commun.* **2018**, *9*, 2254.

(81) Knutson, J. L.; Martin, J. D.; Mitzi, D. B. Tuning the Band Gap in Hybrid Tin Iodide Perovskite Semiconductors Using Structural Templating. *Inorg. Chem.* **2005**, *44*, 4699-4705.

(82) Li, W.; Ma, J.; Cheng, X.; Li, D. Giant Enhancement of Photoluminescence Quantum Yield in 2D Perovskite Thin Microplates by Graphene Encapsulation. *Nano Res.* **2020**, *14*, 1980-1984.

(83) Wu, X.; Trinh, M. T.; Niesner, D.; Zhu, H.; Norman, Z.; Owen, J. S.; Yaffe, O.; Kudisch, B. J.; Zhu, X. Y. Trap States in Lead Iodide Perovskites. *J. Am. Chem. Soc.* **2015**, *137*, 2089-2096.

(84) Li, S.; Luo, J.; Liu, J.; Tang, J. Self-Trapped Excitons in All-Inorganic Halide Perovskites: Fundamentals, Status, and Potential Applications. *J. Phys. Chem. Lett.* **2019**, *10*, 1999-2007.

(85) Dohner, E. R.; Jaffe, A.; Bradshaw, L. R.; Karunadasa, H. I. Intrinsic White-Light Emission from Layered Hybrid Perovskites. *J. Am. Chem. Soc.* **2014**, *136*, 13154-13157.

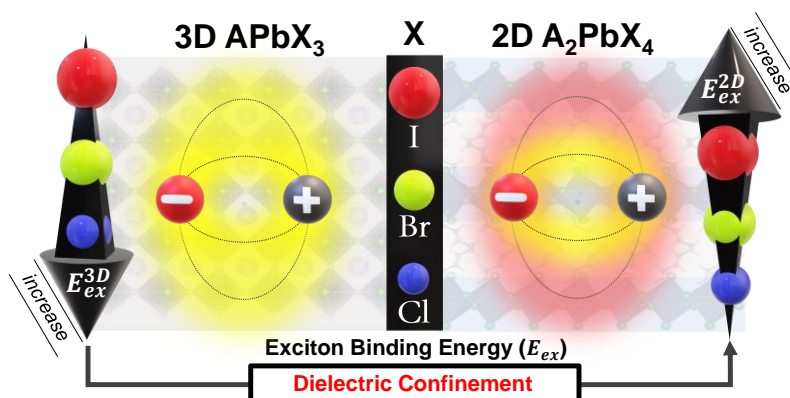
(86) Thomaz, J. E.; Lindquist, K. P.; Karunadasa, H. I.; Fayer, M. D. Single Ensemble Non-Exponential Photoluminescent Population Decays from a Broadband White-Light-Emitting Perovskite. *J. Am. Chem. Soc.* **2020**, *142*, 16622-16631.

(87) Fang, X.; Roushan, M.; Zhang, R.; Peng, J.; Zeng, H.; Li, J. Tuning and Enhancing White Light Emission of II–VI Based Inorganic–Organic Hybrid Semiconductors as Single-Phased Phosphors. *Chem. Mater.* **2012**, *24*, 1710-1717.

- (88) Kraatz, I. T.; Booth, M.; Whitaker, B. J.; Nix, M. G. D.; Critchley, K. Sub-Bandgap Emission and Intraband Defect-Related Excited-State Dynamics in Colloidal CuInS₂/ZnS Quantum Dots Revealed by Femtosecond Pump–Dump–Probe Spectroscopy. *J. Phys. Chem. C* **2014**, *118*, 24102-24109.
- (89) Fuhr, A. S.; Yun, H. J.; Makarov, N. S.; Li, H.; McDaniel, H.; Klimov, V. I. Light Emission Mechanisms in CuInS₂ Quantum Dots Evaluated by Spectral Electrochemistry. *ACS Photonics* **2017**, *4*, 2425-2435.
- (90) Nag, A.; Sarma, D. D. White Light from Mn²⁺-Doped CdS Nanocrystals: A New Approach. *J. Phys. Chem. C* **2007**, *111*, 13641-13644.
- (91) Mir, W. J.; Jagadeeswararao, M.; Das, S.; Nag, A. Colloidal Mn-Doped Cesium Lead Halide Perovskite Nanoplatelets. *ACS Energy Lett.* **2017**, *2*, 537-543.
- (92) Ziming, C.; Zhenchao, L.; Zhen, C.; Ruoxi, X.; Guangruixing, Z.; Linghao, C.; Shi-Jian, S.; Junbiao, P.; Hin-Lap, Y.; Yong, C. Utilization of Trapped Optical Modes for White Perovskite Light Emitting Diodes with Efficiency over 12%. *Joule* **2021**, *5*, 456-466.

CHAPTER 2

Correlation of Dielectric Confinement and Exciton Binding Energy in 2D Hybrid Lead Halide Perovskites



The work presented in this chapter has led to the following publication:

Chakraborty, R.; Nag, A. Correlation of Dielectric Confinement and Excitonic Binding Energy in 2D Layered Hybrid Perovskites Using Temperature Dependent Photoluminescence. *J. Phys. Chem. C* **2020**, *124*, 16177–16185. Copyright permission has been taken from ACS publication for full paper.

Abstract

In 2D layered hybrid perovskite like $(\text{PEA})_2\text{PbX}_4$ (PEA = phenyl ethyl ammonium, X = Cl, Br, I), the dielectric contrast between inorganic well layer (ϵ_w) and organic barrier (ϵ_b) influences the excitonic binding energy (E_{ex}^{2D}). Here, we vary ϵ_w/ϵ_b by varying both the halide anion and the organic cation, and then correlate the influence of the dielectric contrast on E_{ex}^{2D} . We estimate E_{ex}^{2D} by employing temperature (5.4 – 300 K) dependent PL, and find that the change in E_{ex}^{2D} can be qualitatively monitored simply by measuring the PL lifetime at room temperature. E_{ex}^{2D} increases, and therefore, PL lifetime decreases by varying halide ions from Cl to Br to I for $(\text{PEA})_2\text{PbX}_4$. Notably, this trend is opposite to the case of 3D Pb-halide perovskites, where the excitonic binding energy decreases for X = Cl to Br to I. The opposite trend for 2D perovskites is explained by dielectric confinement, where we find $E_{ex}^{2D} \propto (\epsilon_w/\epsilon_b)^m$, with m as an unknown positive number and $\epsilon_w > \epsilon_b$. The dielectric confinement drastically diminishes with increasing ϵ_b . $(\text{EA})_2\text{PbI}_4$ (EA = ethanolanmonium) with $\epsilon_b = 37.7$ shows $E_{ex}^{2D} = 65$ meV, as opposed to $(\text{PEA})_2\text{PbI}_4$ with $\epsilon_b = 3.3$ and $E_{ex}^{2D} = 453$ meV. This correlation of ϵ_w/ϵ_b with E_{ex}^{2D} is critical for optoelectronic applications of 2D layered perovskites.

2.1 Introduction

3D Pb-halide perovskites have generic formula $APbX_3$ where $A^+ = Cs^+$, $CH_3NH_3^+$ (MA^+) or $HC(NH_2)_2^+$ and $X^- = Cl^-$, Br^- or I^- . In the last decade, these perovskites have shown a rather unique combination of excellent optoelectronic properties and easy solution processed material design.¹⁻¹⁴ When the A-site cations in 3D perovskites are replaced with larger ions like $CH_3CH_2CH_2CH_2NH_3^+$ (BA^+), then the semiconducting Pb-X layers get separated from each other by the insulating and hydrophobic organic layers.¹⁵⁻¹⁹ Therefore, charge carriers get confined into atomically thin Pb-X layers, making the layered structure of $(BA)_2PbI_4$ electronically two dimensional (2D), irrespective of the crystal size.²⁰⁻²¹ These 2D layered perovskites too exhibit interesting optical and optoelectronic properties, perhaps with a better moisture stability compared to their 3D Pb-halide perovskites.²²⁻²⁵

The excitonic binding energy is a critical parameter for devices employing photophysical properties of a semiconductor. For the case of 2D perovskites, the excitonic binding energy is often ~10 times higher than that in 3D perovskites. This enhanced excitonic binding energy in 2D perovskites arises from both spatial confinement of charge carriers and dielectric contrast between the organic and inorganic layers.^{16, 26} However, predicting the implications of both of these effects on optical properties of 2D hybrid perovskites are non-trivial, because 3D and 2D perovskites cannot have the same chemical composition. 3D perovskites have a homogenous dielectric constant determining the excitonic binding energy E_{ex}^{3D} . In contrast, $(BA)_2PbI_4$ is composed of inorganic well (w) and organic barrier (b) layers with contrasting high frequency dielectric constants ϵ_w and ϵ_b (see Figure 2.1) respectively. Even if the photogenerated electron and hole remain in the inorganic layers, the lines of attractive forces (Coulomb attraction) between them travel through both the layers. Therefore, ϵ_w and ϵ_b simultaneously influence the excitonic binding energy and carrier dynamics, tailoring the optical properties.^{20,}

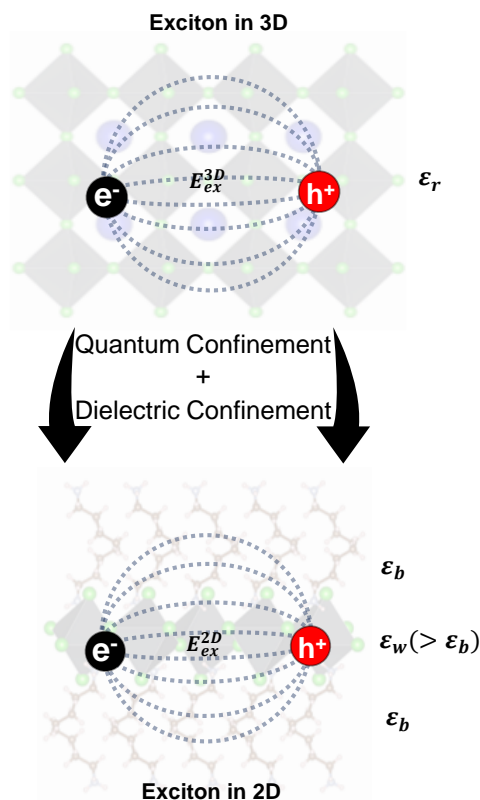


Figure 2.1: The top image shows an exciton in a 3D Pb-halide perovskite like CsPbX_3 or MAPbX_3 (MA: methylammonium) experiencing a homogeneous high frequency dielectric constant (ϵ_r). The bottom image is the case for a 2D hybrid perovskite like $(\text{BA})_2\text{PbX}_4$ with different high frequency dielectric constants for inorganic well (ϵ_w) and organic barrier (ϵ_b). The dotted lines indicate the lines of Coulomb attraction forces between the electron (e^-) and hole (h^+) forming the exciton. This figure is a schematic representation.

To estimate the excitonic binding energy of an ideal 2D semiconductor (E_{ex}^{2D}) well with potential energy barrier, where $\epsilon_w \neq \epsilon_b$, the following equation (equation 2.1) is often used.

$$E_{ex}^{2D} = 4E_{ex}^{3D} (\eta)^2 \quad \eta = \frac{\epsilon_w}{\epsilon_b} \quad \text{Eq. (2.1)}$$

Equation 2.1 was predicted by Keldysh in his pioneering work on excitons in infinitesimally thin semiconductor layer surrounded by dielectric environment.²⁸ In $(\text{BA})_2\text{PbI}_4$, composition of the 2D semiconductor is $(\text{PbI}_4)^{2-}$, which does not exist in the bulk 3D form. So, neither E_{ex}^{3D} nor ϵ_w is known. Also, the barrier, BA^+ does not exist as a pure ion so ϵ_b is also experimentally unknown. Therefore, estimation of E_{ex}^{2D} of 2D layered hybrid perovskites using equation 2.1 is challenging. Computational attempts are now being made considering $(\text{BA})_2\text{PbI}_4$ as a

composite system of charge neutral pseudo-inorganic compound in place of $(\text{PbI}_4)^{2-}$ and pseudo-organic $\text{CH}_3\text{CH}_2\text{CH}_2\text{CH}_3$ (in place of BA^+) components.²⁹

The experimental correlation of ϵ_w and ϵ_b with E_{ex}^{2D} in layered hybrid perovskites of various compositions still remains unclear. In this study, we prepared different compositions of A_2PbX_4 [A = PEA, EA, hexadecyl ammonium (HDA) or octylammonium (OCT); and X = Cl, Br or I], systematically varying both ϵ_w and ϵ_b . Then correlated this change in dielectric constants with E_{ex}^{2D} . PL lifetime and temperature dependent PL provide qualitative and quantitative comparison of E_{ex}^{2D} respectively. Our experimental results establish that $E_{ex}^{2D} \propto (\epsilon_w/\epsilon_b)^m$ with an unknown positive value for m.

2.2 Experimental Section

2.2.1. Chemicals. Lead bromide (PbBr_2 , 99.999%), lead iodide (PbI_2 , 99.999%), lead chloride (PbCl_2 , 98%), caesium carbonate (Cs_2CO_3 , 99.9%), oleic acid (90%), 1-octadecene (90%), oleylamine (70%), trioctylphosphine (TOP, 90%), methyl acetate (99.5%), hydrogen chloride (HCl, 37 wt% in water), hydrogen iodide (HI, 57 wt% in water), hydrogen bromide (HBr, 43 wt% in water), phenylethylamine (>99%), dimethyl sulfoxide (DMSO, >99%), acetonitrile (anhydrous, 99.8%), hexane (anhydrous, >95%), hexadecylamine (98%), and octylamine (99%) are purchased from Merck and ethanolamine (99%) was purchased from Loba Chemie. All chemicals were used without further purification.

2.2.2 Preparation of caesium oleate (Cs-oleate) precursor solution. Cs-oleate stock solution is prepared following reference.³⁰ For a typical synthesis, 0.4 g Cs_2CO_3 is added to 15 mL 1-octadecene in a three-neck round-bottomed flask and the mixture is degassed at 120 °C for 1 hour. N_2 gas is then purged into the flask, followed by an addition of 1.25 mL dried oleic acid. The mixture is heated at 150 °C till complete dissolution of Cs_2CO_3 . The hot solution of Cs-oleate is then cooled down to room temperature and preserved under inert atmosphere. This

Cs-oleate solution is later used for the synthesis of colloidal CsPbX₃ (X = Cl, Br, I) nanocrystals.

2.2.3 Synthesis of colloidal CsPbX₃ (X = Cl, Br, I) nanocrystals. CsPbX₃ nanocrystals are synthesized following a previously reported method,³⁰ after minor modifications. 0.22 mmol PbX₂, 5 mL 1-octadecene, 0.5 mL oleic acid, and 0.5 mL oleylamine are mixed in a three-neck round-bottomed flask. The mixture is degassed at 120 °C for 1 hour. The temperature of the reaction mixture is further increased to 140 °C under N₂ flow. 0.4 mL preheated Cs-oleate solution (0.164 M in 1-octadecene) is injected to it and the reaction is quenched to room temperature using an ice-bath. ~20 mL methyl acetate is added to precipitate out the synthesized nanocrystals. The mixture is then centrifuged at 7800 rpm for 10 minutes in an Eppendorf Centrifuge 5430 instrument. The obtained precipitate is redispersed in 2 mL dry hexane. 8 mL methyl acetate is further added to it, followed by centrifugation at 7800 rpm for 10 minutes. The precipitate is then redispersed in 2 mL dry hexane and used for later studies.

2.2.4 Preparing 2D layered halide perovskite films. Films of A₂PbX₄ [A = PEA, EA, HDA or OCT; and X = Cl, Br or I] are prepared by modifying a method³¹ reported for the synthesis of (PEA)₂PbBr₄. For a given composition such as (PEA)₂PbX₄, 5 mL dimethyl sulfoxide, 5 mL acetonitrile, 0.5 mmol phenylethylamine and 0.2 mL HX (X = Cl, Br, or I) are mixed in a glass vial by sonicating for 5 minutes. To this, 0.25 mmol PbX₂ (X = Cl, Br, I) is added, and the mixture is again sonicated for 5 minutes. The solution obtained after this process is termed here as the precursor solution.

The substrate used for film fabrication for the room temperature optical studies is soda lime glass, and for the low temperature measurements quartz substrates are used. The substrates are thoroughly cleaned with detergent. Then they are dipped in distilled water and are subjected to sonication for 2 hours. The substrates are then dried inside a hot-air oven. Further, they are wiped with an acetone-soaked tissue paper. 50 μL precursor solution is dropped on the substrate

and is spun at 1200 rpm for 30 sec. The films are then heated at 70 °C on a hotplate for 2 minutes. These films are the used for further experiments.

2.2.5 Characterization and optical properties. Powder X-ray diffraction (PXRD) data are collected using a Bruker D8 Advance diffractometer in Bragg–Brentano geometry and operating with Cu K α radiation. Drop-casted films of CsPbX₃ nanocrystals on a glass slide, and as prepared films of A₂PbX₄ (A = PEA, OCT, HDA) are used for PXRD measurements. Field effect scanning electron microscopy (FESEM) measurements are done on Zeiss Ultra Plus SEM instrument. Transmission electron microscopy (TEM) studies are carried out using a JEOL JEM 2100 F field emission transmission electron microscope operating at 200 kV. Apex equipment’s NXG-M1 spin coater system is used for the preparation of 2D halide perovskite films.

UV-visible absorption spectra are recorded in transmission mode using Cary 300 UV-Vis spectrometer. Steady state PL spectra are recorded using Edinburg Instrument’s FLS 980 spectrofluorometer. PL decay dynamics are measured in two separate instruments of different time resolutions. PL decay for (PEA)₂PbI₄ is measured using a time-correlated single-photon counting (TCSPC) setup of Horiba Yvon with an MCP-PMT detector of Hamamatsu, Japan. These samples are excited with a 375 nm pulsed laser source (Horiba Jobin Yvon IBH NanoLED-375L) having pulse width < 100 ps. PL decay for all other samples were measured using Edinburgh Instrument’s FLS-980 spectrometer, with a pulsed LED laser of 340 nm. The measured decay profiles are fitted using a bi-exponential decay function of the form $I_t = I_{t=0} + A_1 \times \exp(-t/\tau_1) + A_2 \times \exp(-t/\tau_2)$. For CsPbCl₃ nanocrystals, a tri-exponential decay function [$I_t = I_{t=0} + A_1 \times \exp(-t/\tau_1) + A_2 \times \exp(-t/\tau_2) + A_3 \times \exp(-t/\tau_3)$] is used. In these equations, I_t and $I_{t=0}$ are PL intensities at any variable time = t, and time = 0 s, respectively. A_i are amplitudes corresponding lifetime components τ_i (i = 1, 2, 3). The average lifetime (τ_{av}) is

calculated using the equation: $\frac{\sum A_i \tau_i^2}{\sum A_i \tau_i}$. Colloidal dispersion of CsPbX₃ nanocrystals and films of A₂PbX₄ (A = PEA, EA, HDA, OCT) are used for all optical measurements.

Low temperature PL measurements are performed in the FLS980 instrument. A 340 nm pulsed LED is used as an excitation source for the (PEA)₂PbBr₄ and (PEA)₂PbCl₂Br₂ and a 405 nm pulsed laser is used for exciting (PEA)₂PbI₄ and (EA)₂PbI₄. The substrates are mounted on a gold-plated sample holder attached to a Lakeshore instruments' closed cycle He-cryostat which is used to achieve the lower temperatures.

2.3 Results and Discussion

PL lifetime of both organic-inorganic hybrid and all-inorganic 3D perovskites with generic formula APbX₃ (A = MA or Cs) has been shown to increase with decreasing electronegativity of halide ions from Cl to I. The trend remains same irrespective of the crystals being micrometer- or nanometer-sized.³²⁻³³ For example, we prepared CsPbX₃ nanocrystals, to show the influence of halide ion on their PL lifetime. Then the PL lifetime trend of CsPbX₃ nanocrystals will be compared with that of 2D layered hybrid perovskite, to highlight the effect of dielectric confinement on excitonic binding energy.

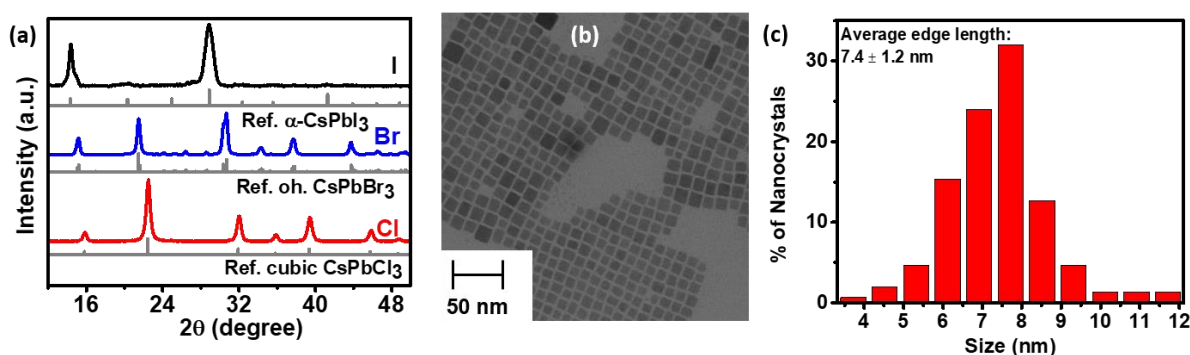


Figure 2.2: Structural properties of colloidal CsPbX₃ nanocrystals. (a) Powder X-ray diffraction (PXRD) patterns of CsPbX₃ (X = Cl, Br, I) nanocrystals with corresponding reference standards; (b) Transmission electron microscopy (TEM) image and (c) corresponding size distribution histogram of CsPbBr₃ nanocrystals.

PXRD data in Figure 2.2a confirm the formation of CsPbCl₃ nanocrystals in the cubic phase, CsPbBr₃ nanocrystals in the orthorhombic phase, CsPbI₃ nanocrystals in the black phase (α or γ).³⁴ The representative TEM image and the corresponding size distribution profile for CsPbBr₃ nanocrystals are shown in Figure 2.2b, and Figure 2.2c, respectively. Cube shaped morphology of CsPbBr₃ with edge-length 7.4 ± 1.2 nm is formed. Other halide compositions also show similar nanocubes.

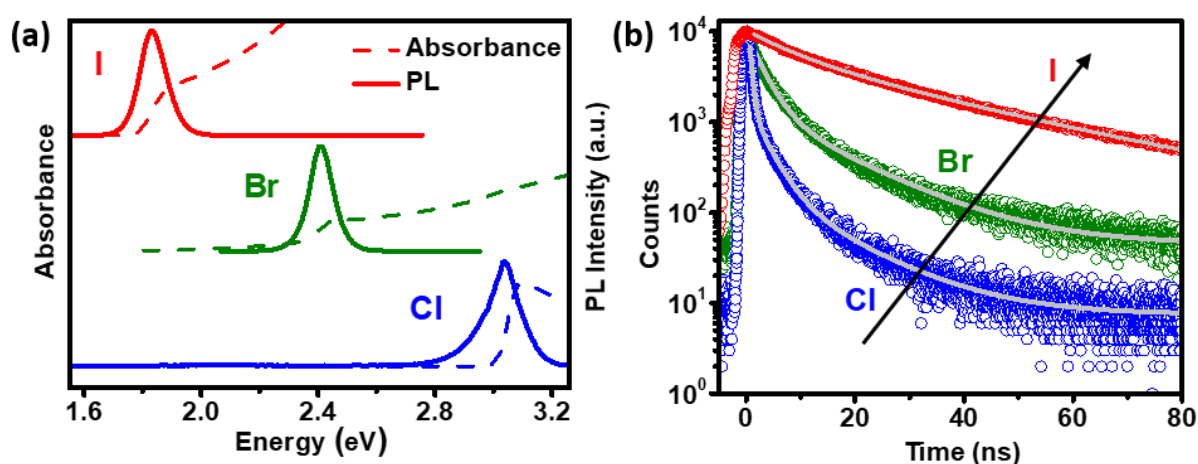


Figure 2.3: Optical properties of colloidal CsPbX₃ nanocrystals (a) UV–visible absorption and PL spectra of CsPbX₃ nanocrystals dispersed in hexane. UV–visible absorption, and PL data are vertically shifted for clear presentation; (b) PL decay dynamics measured at the corresponding emission peaks in (a). Symbols are experimental PL decay data, whereas overlapping solid lines are exponential decay fits.

The UV-visible absorption and PL spectra in Figure 2.3a show band-edge excitonic absorption and emission for CsPbX₃ nanocrystals. The exciton peak red shifts on substituting Cl by Br by I. This decrease in the band gap is caused by an increase in energy of VBM with decreasing electronegativity of the halide ion.³⁵⁻³⁶ The PL decay dynamics in Figure 2.3b are fitted with a bi-exponential function, except for CsPbCl₃ nanocrystals, which required a small contribution from a third exponent. The best fit parameters are given in Table 2.1. Expectedly, average lifetime, τ_{av} decreases with increasing electronegativity of the halide ion.

Table 2.1: The best fit parameters of the excitonic PL decay profiles of CsPbX₃ nanocrystals shown in Figure 2.3b.

Composition	A ₁ (%)	τ ₁ (ns)	A ₂ (%)	τ ₂ (ns)	A ₃ (%)	τ ₃ (ns)	τ _{av} (ns)
CsPbCl ₃	94.3	0.47	5	3.1	0.7	12.3	2.6
CsPbBr ₃	72	2	28	9	--	--	6.5
CsPbI ₃	56	30	44	8	--	--	26

This trend in τ_{av} arises because excitonic binding energy (E_{ex}^{3D}) increases with increasing electronegativity of the halide ions. The change in E_{ex}^{3D} is caused by the change in the high frequency dielectric constant, ϵ_r .³⁷ Since the excitonic binding energy is a manifestation of the Coulomb force acting between the photoexcited electron and hole, the nature of interaction can be expressed by the Coulomb equation of force shown in equation 2.2.

$$F = -\frac{1}{4\pi\epsilon} \frac{e^2}{r^2} \quad \text{Eq. (2.2)}$$

Here, F is the attractive force between two opposing (electron and hole) charges of equal magnitude e, situated at a distance r, in a medium of dielectric constant ϵ (where $\epsilon = \epsilon_0\epsilon_r$, and ϵ_0 is the permittivity of the free space). ϵ_r increases with decreasing electronegativity of the halide ion in the lead-halide network, and thereby the lattice can screen charges better.³⁷⁻³⁸ The decrease in E_{ex}^{3D} causes reduced overlap between the electron and hole wavefunctions, increasing the excitonic PL lifetime, τ_{av} .

Next, we discuss the 2D layered perovskite systems. We have chosen the series (PEA)₂PbX₄ (X = Cl, Br, I) because of its higher PL quantum yield compared to other analogues with different A-site cations.³⁹ The PXRD patterns of (PEA)₂PbX₄ films (Figure 2.4a) show the characteristic equidistance peaks, originating from the (00l) planes.⁴⁰ (00l) peaks correspond to the interlayer distance between the inorganic layers. This interlayer distance is mainly governed by the orientation of A-site cation PEA⁺. So, we do not observe a drastic change in (00l) peak positions with a change in halide ion composition. However, different halide ions

lead to different Pb-X-Pb angles, influencing the orientation of PEA⁺ ions, and therefore, fine-tuning the (00l) peak positions. Representative FESEM image (Figure 2.4b) shows the expected multi-layered morphology of the films. Our samples are closer to the bulk crystal limit than exfoliated ultrathin films. So, influence of the substrate dielectric environment on optical properties of samples are not expected in our measurements.⁴¹⁻⁴²

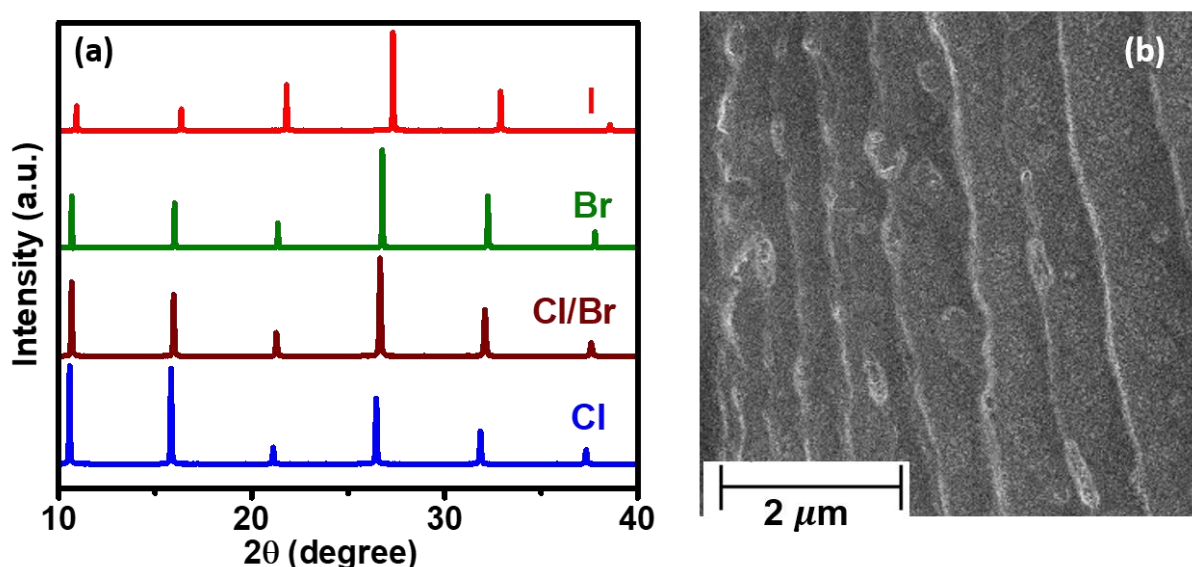


Figure 2.4: Structural properties of colloidal CsPbX₃ nanocrystals (a) PXRD patterns of (PEA)₂PbX₄ films showing (00l) peaks; (b) Field emission scanning electron microscope (FESEM) image of (PEA)₂PbI₄ film.

UV-visible absorption spectra (Figure 2.5a) of films show sharp excitonic peaks for all the (PEA)₂PbX₄ compositions. Similar to CsPbX₃ nanocrystals, the excitonic peaks of (PEA)₂PbX₄ shift to lower wavelengths with increasing electronegativity of the halide ions. It is noteworthy that for a given halide ion, the excitonic peak for 2D layered perovskites is much blue-shifted and sharper compared to the corresponding CsPbX₃ nanocrystals. This blue-shifted and sharper excitonic features are attributed to both strong quantum confinement and dielectric confinement effects in 2D layered perovskites.⁴³ PL spectra (Figure 2.5a) for all the samples show corresponding excitonic emissions. However, for (PEA)₂PbCl₄, the intensity of excitonic PL decreases significantly. Instead, the spectrum is dominated by a broad emission with peak

centred at ~ 2.1 eV. Similar PL spectra for $(\text{PEA})_2\text{PbCl}_4$ have been observed previously and the broad emission has been assigned to self-trapped excitons (STE).^{20, 44-45}

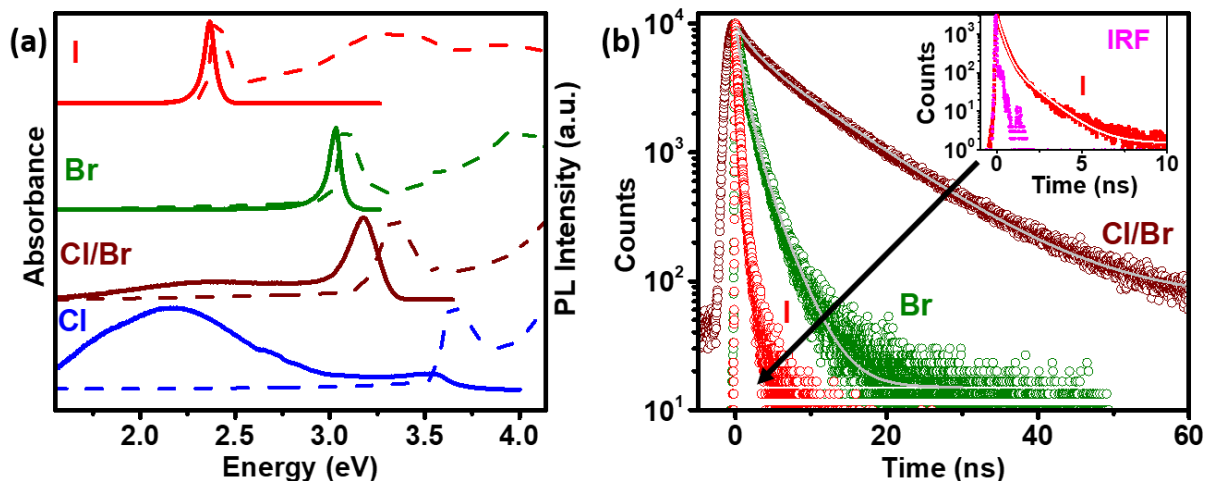


Figure 2.5: Optical properties of $(\text{PEA})_2\text{PbX}_4$ films. (a) UV–visible absorption and PL spectra. UV–visible absorption, and PL data are vertically shifted for clear presentation; (b) PL decay dynamics measured at the corresponding emission peaks for spectra shown in (a). Inset shows lifetime decay for $(\text{PEA})_2\text{PbI}_4$ recorded using an instrument with higher time resolution. IRF represents instrument response function. Symbols in (b) are experimental PL decay data, whereas overlapping solid lines are exponential decay fits.

PL decay dynamics for excitonic emission of $(\text{PEA})_2\text{PbX}_4$ for $X = \text{I}, \text{Br}$ and mixed halide Cl/Br , are shown in Figure 2.5b. We could not reliably record the decay of excitonic PL of $(\text{PEA})_2\text{PbCl}_4$, because of its weak intensity. So we have chosen $(\text{PEA})_2\text{Pb}(\text{Cl/Br})_4$ with $\text{Cl:Br} \sim 1:1$, for our study. For $(\text{PEA})_2\text{PbI}_4$, the decay profile overlaps with the instrument response function (IRF). So, we recorded the PL decay of $(\text{PEA})_2\text{PbI}_4$ using a different instrument with a better time resolution. The higher resolution IRF and PL decay profile of $(\text{PEA})_2\text{PbI}_4$ are shown in the inset of Figure 2.5b. All the PL decay profiles are fitted with bi-exponential decay and the best fit parameters are shown in Table 2.2.

Importantly, the excitonic PL decay of $(\text{PEA})_2\text{PbX}_4$ becomes faster (decrease in average lifetime) as the electronegativity of halides decreases from (Cl/Br) to Br to I . This trend is in stark contrast with that of 3D perovskites, where PL decay becomes slower with decreasing electronegativity of halides. The opposite direction of arrows in Figure 2.3b and 2.5b highlights

these opposite trends. This reverse trend in 2D perovskites can be understood by the dielectric confinement effect, which is represented by $\eta [= (\epsilon_w/\epsilon_b)]$ in equation 2.1. When we changed the halide composition of $(\text{PEA})_2\text{PbX}_4$ from (Cl/Br) to Br to I, ϵ_w systematically increases maintaining a constant value for ϵ_b . In other words, E_{ex}^{2D} increases as a square function of ϵ_w , if we consider equation 2.1 is valid for this 2D perovskite system. Our experimental results suggest that equation 2.1 is qualitatively valid for 2D perovskites. So qualitatively, for 2D hybrid perovskites, we can write $E_{ex}^{2D} \propto (\epsilon_w/\epsilon_b)^m$, where m is a non-zero positive number, probably closer to 2.

Table 2.2: The best fit parameters of the excitonic PL decay profiles of $(\text{PEA})_2\text{PbX}_4$ films as shown in Figure 2.5b.

Composition	A ₁ (%)	τ_1 (ns)	A ₂ (%)	τ_2 (ns)	τ_{av} (ns)
$(\text{PEA})_2\text{Pb}(\text{Cl},\text{Br})_4$	67	10.5	33	2.3	9.7
$(\text{PEA})_2\text{PbBr}_4$	76	1.04	24	2.8	1.8
$(\text{PEA})_2\text{PbI}_4$	91	0.27	9	1.2	0.55

To obtain a quantitative estimate of E_{ex}^{2D} , we measured PL at different temperatures in the range 5.4 K – 300 K. The increasing temperature can provide the activation energy to cause dissociation of the excitons which competes with radiative excitonic recombination.⁴⁶ Thus, by observing the change in the emission intensity with temperature, one can calculate the activation energy of the exciton dissociation, which is nothing but the excitonic binding energy.⁴⁷

PL spectra of $(\text{PEA})_2\text{PbI}_4$ at five representative temperatures are shown in Figure 2.6a. At 5.4 K, two sharp emission peaks separated by ~ 30 meV is observed. The linewidths of both of these peaks increase with increasing temperature and finally appear as one broad asymmetric emission above 100 K. The asymmetry is visible even at the room temperature, suggesting the existence of two emission centres at all temperatures. Figure 2.6b shows PL decay measured

at two peaks 2.37 eV and 2.30 eV at 50 K. The fitting parameters are summarised in Table 2.3. The PL decays are nearly mono-exponential with average lifetime 0.9 and 1.9 ns for 2.37 and 2.30 eV peak, respectively. These fast PL lifetimes suggest that both the peaks are arising from excitonic transitions, and not from defect states which often has lifetime in the order of 100 ns or above.⁴⁸⁻⁴⁹ Earlier report on single crystalline A_2PbI_4 ($A = \text{alkylammonium}$) also reported similar spectral features and were assigned to different kinds of excitons.⁵⁰ The origin of such different kinds of excitons requires further investigation. For our present study, it is important to note that there exist two different types of excitonic emissions for $(\text{PEA})_2\text{PbI}_4$.

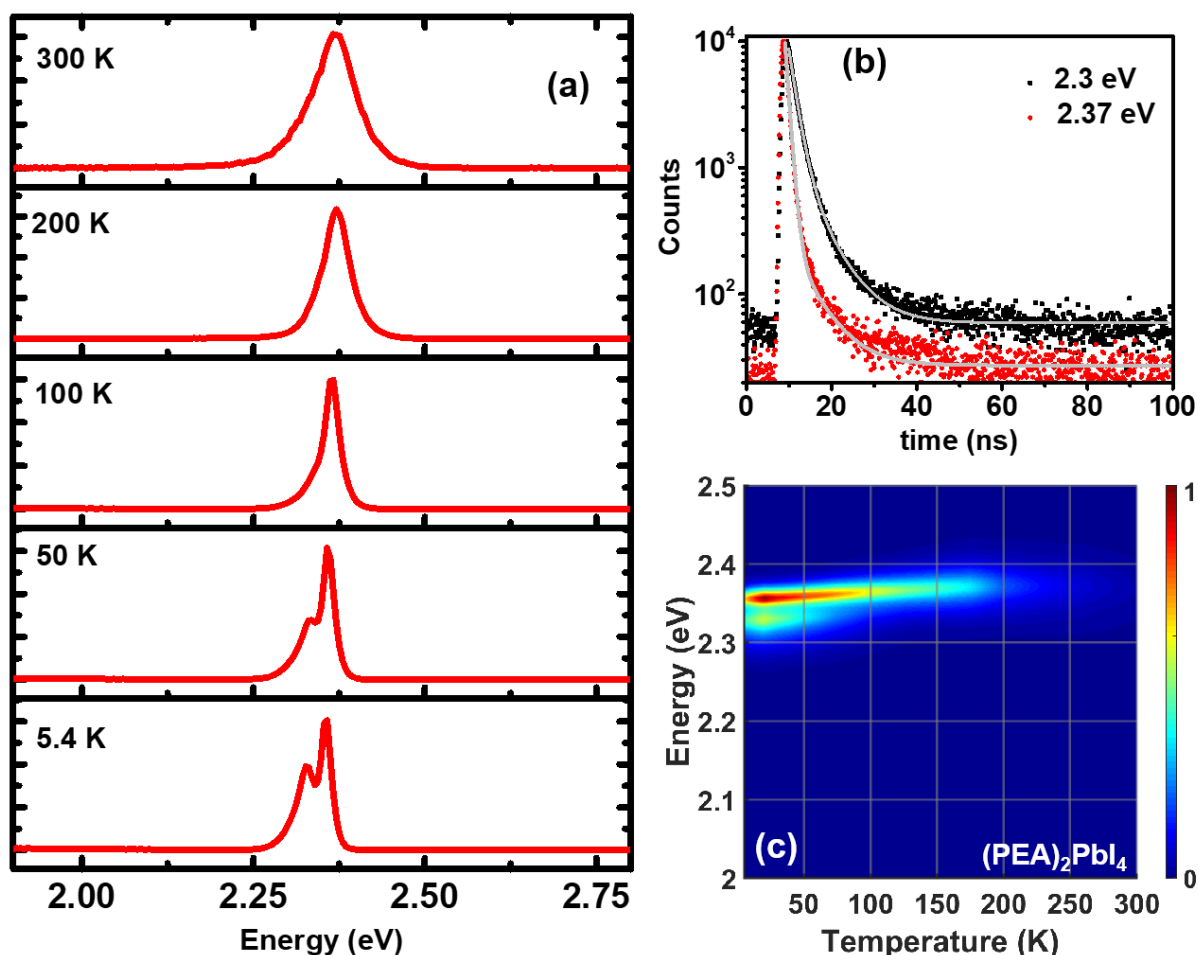


Figure 2.6: Temperature dependent PL of $(\text{PEA})_2\text{PbI}_4$. (a) PL spectra at five representative temperatures showing asymmetric peak. (b) PL decay dynamics measured at 2.30 and 2.37 eV emission peaks at 50 K. The scattered dots are experimental data and the solid lines are bi-exponential decay fit. (c) Pseudocolor map of temperature dependent PL spectra. The vertical colored bar indicates normalized PL intensity scale.

Figure 2.6c shows pseudocolor maps of temperature dependent PL spectra of $(\text{PEA})_2\text{PbI}_4$. The map includes the PL spectra shown in Figure 2.6a, and can resolve two emission peaks at lower temperatures. The PL intensity reflected by the color scale suggests an increase in intensity with decreasing temperature. Also, the most intense PL peak appears to slightly blue-shift with increasing temperatures. The integrated PL intensity and peak positions are plotted in Figure 2.7. The change in the peak energy is very small (~ 20 meV) for the entire temperature range, and more importantly, we do not observe any sudden drastic change in peak energy at any given temperature. These results suggest no major structure phase transition occurs in $(\text{PEA})_2\text{PbI}_4$ at lower temperature, similar to prior report⁵¹.

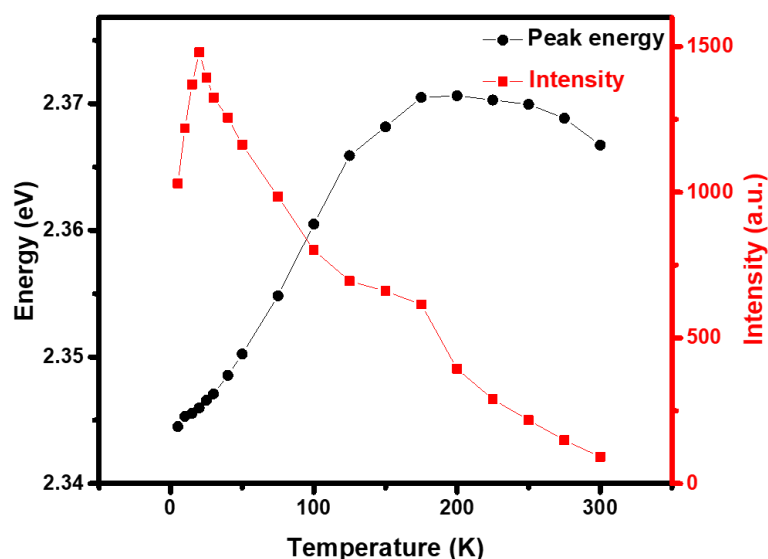


Figure 2.7: Variation of PL peak position and integrated PL intensity with measurement temperature for $(\text{PEA})_2\text{PbI}_4$ film. The corresponding temperature dependent PL spectra is shown in Figure 2.6c.

Pseudocolor maps of temperature dependent PL spectra for $(\text{PEA})_2\text{PbBr}_4$ and $(\text{PEA})_2\text{PbCl}_2\text{Br}_2$ are shown in Figure 2.8a and 2.8b respectively. Corresponding plots of peak energy and integrated intensity are given in Figure 2.8c and 2.8d. Both of these compositions also show asymmetric PL linewidth for the band edge excitonic emission at all temperatures. These results again suggest more than one emission centres contributing to the band edge emission. For $(\text{PEA})_2\text{PbBr}_4$ and $(\text{PEA})_2\text{PbCl}_2\text{Br}_2$, at lower temperatures, an additional broad and weak

emission is observed at lower energies (Figure 2.8a and 2.8b). This broad emission is attributed to STE, and its intensity increases with decreasing temperature.⁵²⁻⁵³ Compared to the band-edge excitonic emission, the STE emission intensity is much smaller at all temperatures. Furthermore, STE emission is spectrally separated from band-edge excitonic emission. So, we do not expect any noticeable interference of STE emission in the calculation (shown below) of binding energies of band-edge excitons from our experimental data.⁴⁴

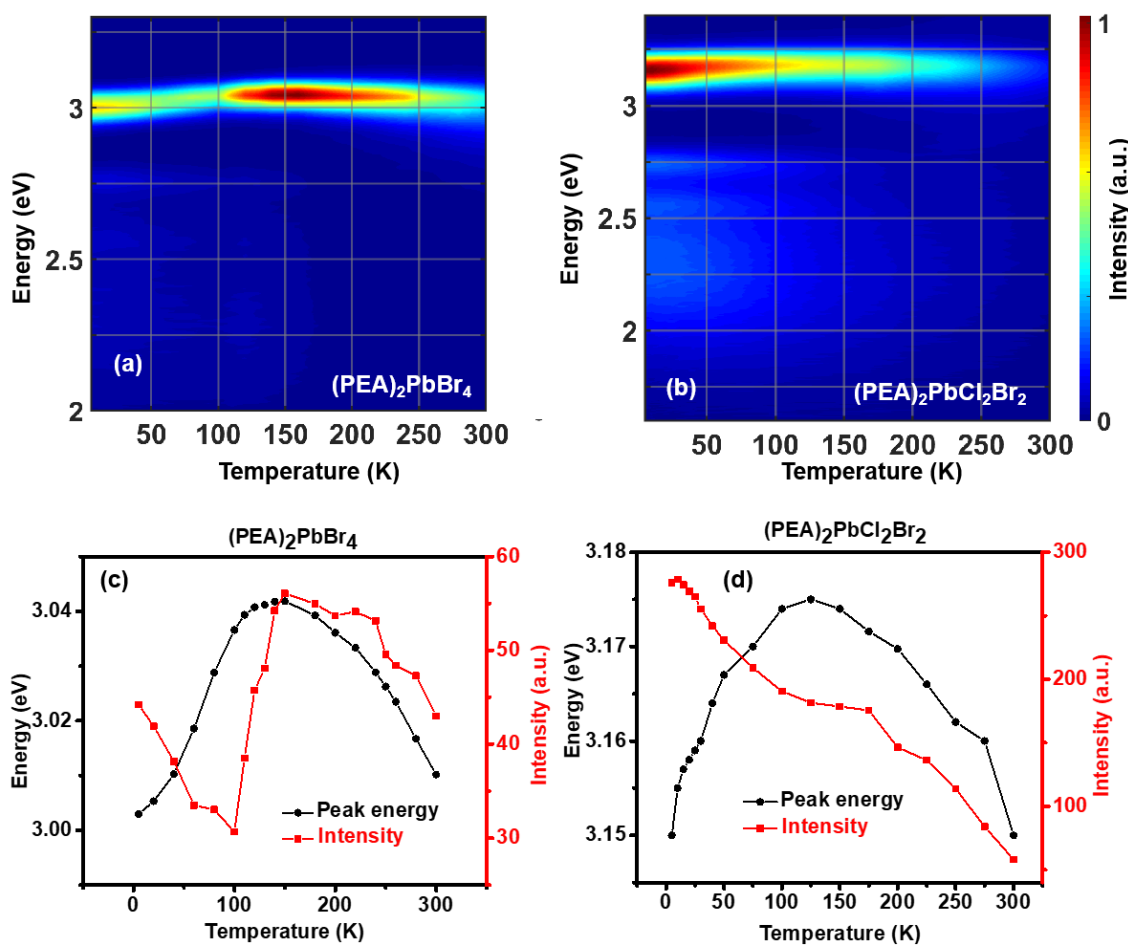


Figure 2.8: Pseudocolor map of temperature dependent PL spectra of (a) $(\text{PEA})_2\text{PbBr}_4$, and (b) $(\text{PEA})_2\text{PbCl}_2\text{Br}_2$ films. The corresponding variation of PL peak position and integrated PL intensity with measurement temperature for (c) $(\text{PEA})_2\text{PbBr}_4$, and (d) $(\text{PEA})_2\text{PbCl}_2\text{Br}_2$.

The temperature (T) dependence of integrated PL intensity, $I(T)$ can be explained by equation 2.3, where E_{ex} is the excitonic binding energy, k_B is the Boltzmann constant, PL intensity at 0 K be I_0 , and B is the pre-exponential factor.

$$I(T) = \frac{I_0}{1 + B e^{-E_{ex}/k_B T}} \quad \text{Eq. (2.3)}$$

In our case, Figure 2.6 and Figure 2.8 show two emission centres for the band edge excitonic emission. So, we use a bi-exponential model following prior report.⁵⁴ The equation 2.3 gets modified into equation 2.4 with two excitonic binding energies E_a and E_b , and two pre-exponential factor A and C .

$$I(T) = \frac{I_0}{1 + A e^{-E_a/k_B T} + C e^{-E_b/k_B T}} \quad \text{Eq. (2.4)}$$

By inverting both sides, equation 2.4 is rearranged to equation 2.5, where $A' = 1/I_0$, $B' = A/I_0$, and $C' = C/I_0$.

$$\frac{1}{I(T)} = A' + B' e^{-E_a/k_B T} + C' e^{-E_b/k_B T} \quad \text{Eq. (2.5)}$$

This bi-exponential decay equation 2.5 is used to fit the experimental $1/I(T)$ vs $1/T$ plots in Figure 2.9.

The equation 2.5 explains decrease in PL intensity with increasing temperature. But for $(\text{PEA})_2\text{PbI}_4$, Figure 2.7 shows that $I(T)$ initially increases with increasing temperature from 5.4 K to 20 K. This could be due to thermal activation of trapped carriers, as observed previously.⁵⁴ Above 20 K, $I(T)$ decreases monotonically with increasing temperature, similar to what is expected from equation 2.5. For $(\text{PEA})_2\text{PbBr}_4$, the $I(T)$ decreases monotonically with increasing temperature only above 150 (Figure 2.8). Thus, different samples have different temperature range where $I(T)$ decreases with increasing temperatures. Therefore, the experimental data of different temperature ranges for different samples are fitted with equation 2.5 in Figure 2.9. The difference in the temperature region for a monotonic decrease in $I(T)$ might be because of the difference in nature of defects trapping the carrier and/or possibility of structural transitions for different samples.

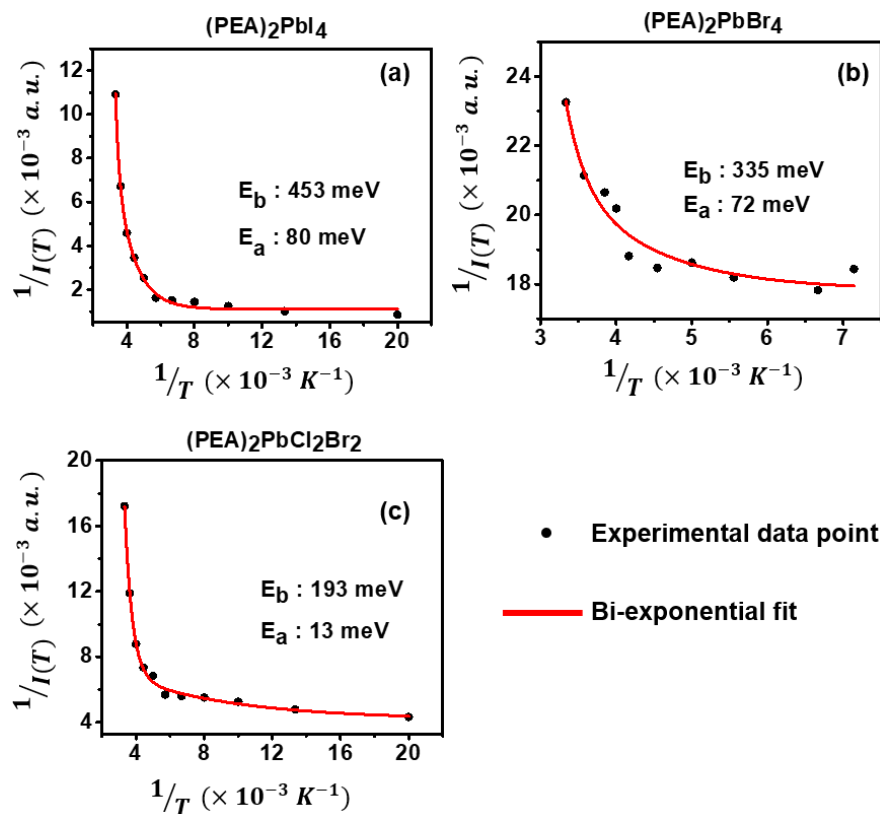


Figure 2.9: Estimation of excitonic binding energy. Experimentally obtained inverse of integrated PL intensity [$1/I(T)$] vs. inverse of temperature ($1/T$) plots fitted using bi-exponential decay equation 2.5, for (a) $(\text{PEA})_2\text{PbI}_4$, (b) $(\text{PEA})_2\text{PbBr}_4$, and (c) $(\text{PEA})_2\text{PbCl}_2\text{Br}_2$.

The best fit parameters of $1/I(T)$ vs $1/T$ plots in Figure 2.9 are shown in Table 2.3. We obtain $E_b = 453$ meV with 99.9% contribution and $E_a = 80$ meV with only 0.1% contribution for $(\text{PEA})_2\text{PbI}_4$. We attribute the higher excitonic binding energy $E_b = 453$ meV to the most intense peak at higher energy and $E_a = 80$ meV to the lower energy peak/tail, since its relative intensity decreases rapidly with increasing temperature. The E_b value in our case falls in between the measured values on ultrathin flakes (490 meV) by Yaffe et al and single crystals (370 meV) by Ishihara et al.^{42, 55} Similar to $(\text{PEA})_2\text{PbI}_4$, excitonic binding energies of $(\text{PEA})_2\text{PbBr}_4$ and $(\text{PEA})_2\text{PbBr}_2\text{Cl}_2$ also obtained by the bi-exponential model, as shown in Figure 2.9b and 2.9c respectively, along with Table 2.3.

Temperature dependent PL data in Figure 2.9 show that the excitonic binding energies of 2D $(\text{PEA})_2\text{PbX}_4$ increases with decreasing electronegativity of halide from Cl to Br to I. Independently, PL lifetime data (Figure 2.5b) also show the same increase in excitonic binding

energy of 2D perovskites with halide composition changing from Cl to Br to I. Schematics shown in Figure 2.10 summarize the trends. E_{ex}^{2D} and E_{ex}^{3D} show opposite trends with halide ion composition. The opposite trends can be explained by the effect of dielectric confinement of 2D hybrid perovskites, as indicated by qualitative equations in Figure 2.10. Consequently, the halide ion compositions influence excitonic absorption, emission and dissociation processes very differently for 2D layered perovskites compared to 3D perovskites.

Table 2.3: The best fit parameters obtained after fitting of temperature dependent integrated PL intensities data shown in Figure 2.9 with a bi-exponential decay equation 2.5.

Sample	B (%)	E_a (meV)	C (%)	E_b (meV)
(PEA)2Pb(Cl/Br)4	0.1	13	99.9	153
(PEA)2PbBr4	0.1	72	99.9	335
(PEA)2PbI4	0.1	80	99.9	453

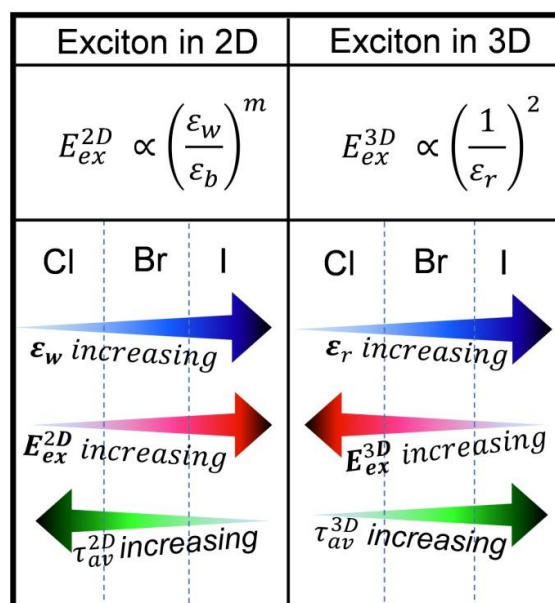


Figure 2.10: Schematics showing the effect of high frequency dielectric constants on excitonic binding energies and average PL lifetimes of 2D and 3D halide perovskites. E_{ex}^{2D} and E_{ex}^{3D} are the excitonic binding energies of the 2D and 3D perovskites, respectively. ϵ_w , and ϵ_b are the high frequency dielectric constant of the inorganic well layer, and the organic barrier layer respectively, in 2D perovskite. ϵ_r is the high frequency dielectric constant of the 3D perovskite. τ_{av}^{2D} , and τ_{av}^{3D} are the average excitonic lifetime of 2D and 3D perovskites, respectively.

Apart from substituting the halide ions to change the ϵ_w , altering the barrier cation also changes the dielectric screening on excitons by changing ϵ_b . To investigate the role of ϵ_b , we have varied the A-site cation. As can be seen in Figure 2.11a, (EA)₂PbI₄ has similar layered structure as that of (PEA)₂PbI₄. However, the highly polarising nature of the O-H bond in EA, induces a significantly higher $\epsilon_b = 37.7$ for (EA)₂PbI₄, compared to $\epsilon_b = 3.3$ of (PEA)₂PbI₄. Thus, one expects an enhanced screening of the charge carriers, and therefore, reduced excitonic binding energy of (EA)₂PbI₄ compared to (PEA)₂PbI₄. Figure 2.11b shows the temperature dependent PL pseudo colormap of (EA)₂PbI₄. Unlike (PEA)₂PbI₄, (EA)₂PbI₄ does not show measurable PL at room temperature. Interestingly, PL peak (~2.26 eV) emerges below 150 K. The PL correspond the band edge exciton, and its intensity increases with decreasing temperature.⁵⁶ Representative PL spectra at different temperatures are shown in Figure 2.11c. PL spectra of (EA)₂PbI₄ are also asymmetric in nature similar to (PEA)₂PbI₄. So, we used bi-exponential decay equation 2.5 to fit experimental $1/I(T)$ vs $1/T$ plot of (EA)₂PbI₄ in Figure 2.11d. The best fit parameters show $E_a = 14$ meV with 1% contribution, and $E_b = 65$ meV with 99% contribution. Interestingly, E_a matches with the previous estimate in ref⁵⁶ where a single emission centre was considered to obtain the binding energy. However, we find ~99% contribution to the fitted curve comes from $E_b = 65$ meV, suggesting that the majority of emissive excitons have a higher binding energy than the previous estimate. This significantly lower $E_b = 65$ meV for (EA)₂PbI₄ compared to $E_b = 453$ meV of (PEA)₂PbI₄, again shows the role of dielectric confinement ($E_{ex}^{2D} \propto (\epsilon_w/\epsilon_b)^m$), where E_{ex}^{2D} (E_b) decreases drastically with higher ϵ_b (37.7) of (EA)₂PbI₄.

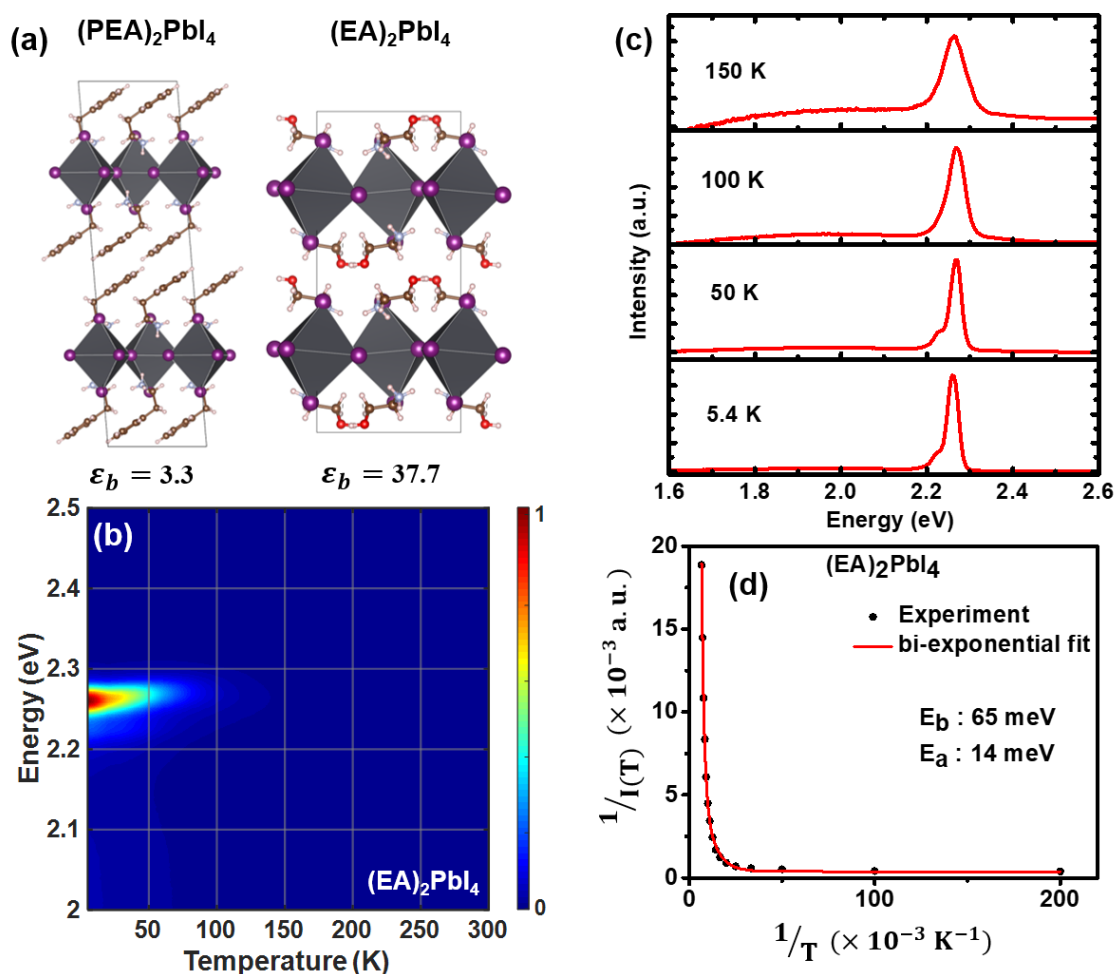


Figure 2.11: Effect of barrier dielectric constant (ϵ_b) on excitonic binding energy. (a) Schematic diagram of both $(\text{PEA})_2\text{PbI}_4$ and $(\text{EA})_2\text{PbI}_4$ showing similar 2D layered structure, but with more than ten-fold different ϵ_b . (b) Pseudo color map of temperature dependent PL data of $(\text{EA})_2\text{PbI}_4$ film. (c) Representative PL spectra at four different temperature recorded from $(\text{EA})_2\text{PbI}_4$ film. (d) Experimentally obtained inverse of integrated PL intensity ($1/I(T)$) vs inverse of temperature ($1/T$) plots of $(\text{EA})_2\text{PbI}_4$ fitted using equation 2.5.

To check how the barrier width influence both quantum and dielectric confinement effects, and therefore E_{ex}^{2D} , we now compare data of $(\text{OCT})_2\text{PbI}_4$ and $(\text{HDA})_2\text{PbI}_4$. Both ϵ_w and ϵ_b remain nearly constant for both samples, but the only difference is the barrier width. PXRD patterns in 2.12a-b allow us to calculate the interlayer spacing for (001) planes using Bragg's equation. The interlayer distances obtained for both samples are schematically presented in Figure 2.12c-d. UV-visible absorption and PL spectra of both $(\text{OCT})_2\text{PbI}_4$ and $(\text{HDA})_2\text{PbI}_4$ are compared in Figure 2.12e. A blue-shift in excitonic absorption and emission is observed for $(\text{HDA})_2\text{PbI}_4$ compared to both $(\text{PEA})_2\text{PbI}_4$ (Figure 2.5) and $(\text{OCT})_2\text{PbI}_4$. This blue-shift results from

structural distortion in the inorganic layer owing to a phase transition that happens above room temperature, and should not be confused with the effect of increased confinement.^{26, 57} Similar phase transition and blue-shift happen to other 2D perovskites systems as well, but at lower temperatures.⁴⁸ PL decays (Figure 2.12f) of both (OCT)₂PbI₄ and (HDA)₂PbI₄ are similar suggesting that difference in barrier width within our experimental range does not really impact the E_{ex}^{2D} . Both these samples show similar PL lifetimes and E_{ex}^{2D} because ϵ_w and ϵ_b in both samples remain nearly constant.

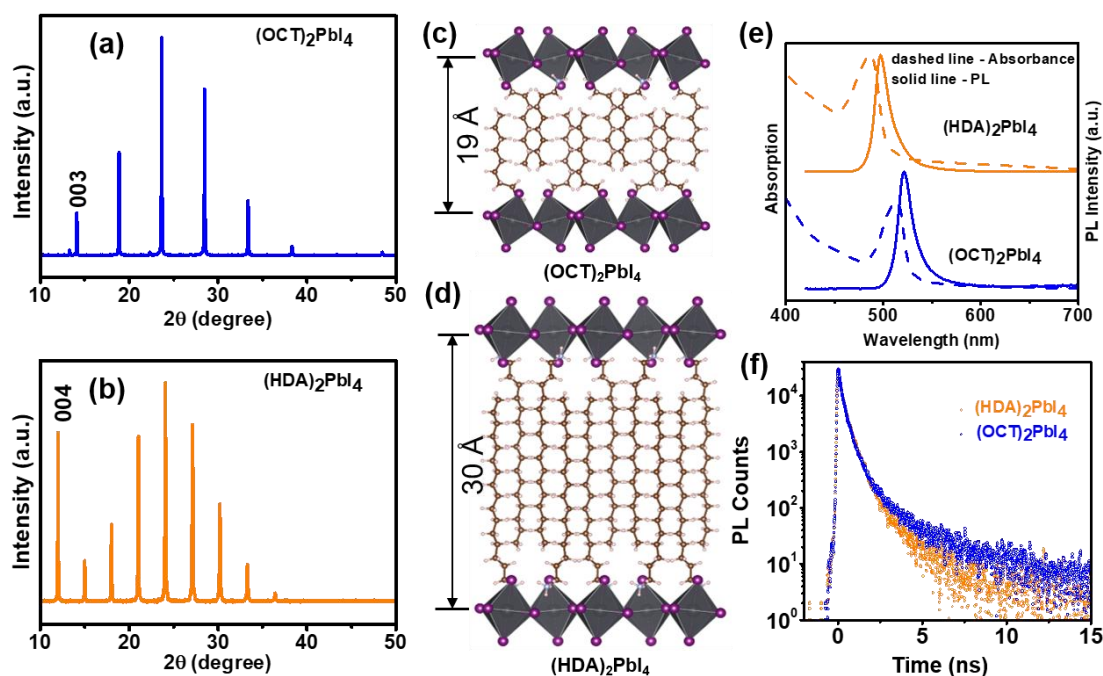


Figure 2.12: Effect of barrier width on excitonic PL lifetime. PXRD patterns of (a) (OCT)₂PbI₄ and (b) (HDA)₂PbI₄ [OCT: octylammonium, HDA: hexadecylammonium]. The patterns are assigned following ref.58-59; Schematic representation of crystal structures of (c) (OCT)₂PbI₄ and (d) (HDA)₂PbI₄ showing interlayer distance obtained from powder XRD patterns shown in (a-b). (e) Comparison of UV-visible absorption and PL spectra of (OCT)₂PbI₄ and (HDA)₂PbI₄. (f) Comparison of PL decay dynamics measured at the corresponding emission peaks shown in Figure (e). OCT: octylammonium and HDA: hexadecyl ammonium.

2.4 Conclusions

We have experimentally elucidated the effect of dielectric screening on excitonic binding energy (E_{ex}^{2D}) of A₂PbX₄. Dielectric constant of barrier (ϵ_b) and well (ϵ_w) are systematically varied by A-site composition (A = PEA, EA, HDA or OCT) and by X-site composition (X = I,

Br or Cl) respectively. To estimate excitonic binding energy, we fitted the variation of PL intensity with temperature (5.4 to 300 K) using a bi-exponential decay (equation 2.5). The predominant component contributing to the PL have excitonic binding energies of 193 meV for (PEA)₂PbCl₂Br₂, 335 meV for (PEA)₂PbBr₄ and 453 meV for (PEA)₂PbI₄. The increase in excitonic binding energy is reflected in the decrease in excitonic PL lifetime, by varying the X-site from Cl to Br to I. This trend of E_{ex}^{2D} is opposite of that 3D perovskites, where E_{ex}^{3D} decreases (PL lifetime increases) for CsPbX₃ nanocrystals moving from Cl to Br to I. Our experimental data show $E_{ex}^{2D} \propto (\epsilon_w/\epsilon_b)^m$ with unknown positive value of m, which is often termed as dielectric confinement with $\epsilon_w > \epsilon_b$. To verify the correlation further, we compare (PEA)₂PbI₄ with (EA)₂PbI₄. (EA)₂PbI₄ with significantly higher ϵ_b , where $\epsilon_w < \epsilon_b$, the effect of dielectric confinement diminishes showing a significantly smaller exciting binding energy of ~65 meV, as compared to 453 meV for (PEA)₂PbI₄. Furthermore, we find that (OCT)₂PbI₄ and (HDA)₂PbI₄ with similar ϵ_w and ϵ_b but with different inter-layer spacings, exhibit similar E_{ex}^{2D} . The correlation between dielectric confinement and E_{ex}^{2D} is important for light absorption, emission, exciton dissociation and charge transport. Therefore, our findings will be beneficial for designing 2D layered halide perovskites with desired optical and optoelectronic applications.

2.5 References

- (1) Kojima, A.; Teshima, K.; Shirai, Y.; Miyasaka, T. Organometal Halide Perovskites as Visible-Light Sensitizers for Photovoltaic Cells. *J. Am. Chem. Soc.* **2009**, *131*, 6050-6051.
- (2) Lee, M. M.; Teuscher, J.; Miyasaka, T.; Murakami, T. N.; Snaith, H. J. Efficient Hybrid Solar Cells Based on Meso-Superstructured Organometal Halide Perovskites. *Science* **2012**, *338*, 643-647.

- (3) Etgar, L.; Gao, P.; Xue, Z.; Peng, Q.; Chandiran, A. K.; Liu, B.; Nazeeruddin, M. K.; Grätzel, M. Mesoscopic $\text{CH}_3\text{NH}_3\text{PbI}_3/\text{TiO}_2$ Heterojunction Solar Cells. *J. Am. Chem. Soc.* **2012**, *134*, 17396-17399.
- (4) Sim, K. M.; Swarnkar, A.; Nag, A.; Chung, D. S. Phase Stabilized α - CsPbI_3 Perovskite Nanocrystals for Photodiode Applications. *Laser Photonics Rev.* **2018**, *12*, 1700209.
- (5) Akkerman, Q. A.; Rainò, G.; Kovalenko, M. V.; Manna, L. Genesis, Challenges and Opportunities for Colloidal Lead Halide Perovskite Nanocrystals. *Nat. Mater.* **2018**, *17*, 394-405.
- (6) Haque, A.; Ravi, V. K.; Shanker, G. S.; Sarkar, I.; Nag, A.; Santra, P. K. Internal Heterostructure of Anion-Exchanged Cesium Lead Halide Nanocubes. *J. Phys. Chem. C* **2018**, *122*, 13399-13406.
- (7) Hazarika, A.; Zhao, Q.; Gauding, E. A.; Christians, J. A.; Dou, B.; Marshall, A. R.; Moot, T.; Berry, J. J.; Johnson, J. C.; Luther, J. M. Perovskite Quantum Dot Photovoltaic Materials Beyond the Reach of Thin Films: Full-Range Tuning of A-Site Cation Composition. *ACS Nano* **2018**, *12*, 10327-10337.
- (8) Kumawat, N. K.; Swarnkar, A.; Nag, A.; Kabra, D. Ligand Engineering to Improve the Luminance Efficiency of CsPbBr_3 Nanocrystal Based Light-Emitting Diodes. *J. Phys. Chem. C* **2018**, *122*, 13767-13773.
- (9) Dutta, A.; Behera, R. K.; Pal, P.; Baitalik, S.; Pradhan, N. Near-Unity Photoluminescence Quantum Efficiency for All CsPbX_3 (X=Cl, Br, and I) Perovskite Nanocrystals: A Generic Synthesis Approach. *Angew. Chem. Int. Ed.* **2019**, *58*, 5552-5556.
- (10) Chen, J.; Dong, C.; Idriss, H.; Mohammed, O. F.; Bakr, O. M. Metal Halide Perovskites for Solar-to-Chemical Fuel Conversion. *Adv. Energy Mater.* **2019**, 1902433.
- (11) Seth, S.; Ahmed, T.; De, A.; Samanta, A. Tackling the Defects, Stability, and Photoluminescence of CsPbX_3 Perovskite Nanocrystals. *ACS Energy Lett.* **2019**, *4*, 1610-1618.

- (12) Rastogi, P.; Chu, A.; Gréboval, C.; Qu, J.; Noubé, U. N.; Chee, S.; Goyal, M.; Khalili, A.; Xu, X. Z.; Cruguel, H. et al. Pushing Absorption of Perovskite Nanocrystals into the Infrared. *Nano Lett.* **2020**, *20*, 3999-4006.
- (13) Zhong, J.-X.; Wu, W.-Q.; Liao, J.-F.; Feng, W.; Jiang, Y.; Wang, L.; Kuang, D.-B. The Rise of Textured Perovskite Morphology: Revolutionizing the Pathway toward High-Performance Optoelectronic Devices. *Adv. Energy Mater.* **2020**, *10*, 1902256.
- (14) Ravi, V. K.; Saikia, S.; Yadav, S.; Nawale, V.; Nag, A. CsPbBr₃/ZnS Core/Shell Type Nanocrystals for Enhancing Luminescence Lifetime and Water Stability. *ACS Energy Lett.* **2020**, *5*, 1794-1796.
- (15) Mitzi, D. B.; Wang, S.; Feild, C. A.; Chess, C. A.; Guloy, A. M. Conducting Layered Organic-Inorganic Halides Containing <110>-Oriented Perovskite Sheets. *Science* **1995**, *267*, 1473-1476.
- (16) Stoumpos, C. C.; Cao, D. H.; Clark, D. J.; Young, J.; Rondinelli, J. M.; Jang, J. I.; Hupp, J. T.; Kanatzidis, M. G. Ruddlesden–Popper Hybrid Lead Iodide Perovskite 2D Homologous Semiconductors. *Chem. Mater.* **2016**, *28*, 2852-2867.
- (17) Sheikh, T.; Nag, A. Mn Doping in Centimeter-Sized Layered 2D Butylammonium Lead Bromide (BA₂PbBr₄) Single Crystals and Their Optical Properties. *J. Phys. Chem. C* **2019**, *123*, 9420-9427.
- (18) Zhou, L.; Liao, J.-F.; Huang, Z.-G.; Wei, J.-H.; Wang, X.-D.; Chen, H.-Y.; Kuang, D.-B. Intrinsic Self-Trapped Emission in 0D Lead-Free (C₄H₁₄N₂)₂In₂Br₁₀ Single Crystal. *Angew. Chem. Int. Ed.* **2019**, *58*, 15435-15440.
- (19) Cho, J.; DuBose, J. T.; Kamat, P. V. Charge Carrier Recombination Dynamics of Two-Dimensional Lead Halide Perovskites. *J. Phys. Chem. Lett.* **2020**, *11*, 2570-2576.
- (20) Katan, C.; Mercier, N.; Even, J. Quantum and Dielectric Confinement Effects in Lower-Dimensional Hybrid Perovskite Semiconductors. *Chem. Rev.* **2019**, *119*, 3140-3192.

- (21) Sheikh, T.; Nawale, V.; Pathoor, N.; Phadnis, C.; Chowdhury, A.; Nag, A. Molecular Intercalation and Electronic Two Dimensionality in Layered Hybrid Perovskites. *Angew. Chem. Int. Ed.* **2020**, *59*, 11653-11659.
- (22) Smith, I. C.; Hoke, E. T.; Solis-Ibarra, D.; McGehee, M. D.; Karunadasa, H. I. A Layered Hybrid Perovskite Solar-Cell Absorber with Enhanced Moisture Stability. *Angew. Chem. Int. Ed.* **2014**, *53*, 11232-11235.
- (23) Blancon, J.-C.; Tsai, H.; Nie, W.; Stoumpos, C. C.; Pedesseau, L.; Katan, C.; Kepenekian, M.; Soe, C. M. M.; Appavoo, K.; Sfeir, M. Y. et al. Extremely Efficient Internal Exciton Dissociation through Edge States in Layered 2D Perovskites. *Science* **2017**, *355*, 1288-1292.
- (24) Hu, J.; Oswald, I. W. H.; Hu, H.; Stuard, S. J.; Nahid, M. M.; Yan, L.; Chen, Z.; Ade, H.; Neilson, J. R.; You, W. Aryl-Perfluoroaryl Interaction in Two-Dimensional Organic–Inorganic Hybrid Perovskites Boosts Stability and Photovoltaic Efficiency. *ACS Materials Lett.* **2019**, *1*, 171-176.
- (25) Wei, Y.; Chu, H.; Tian, Y.; Chen, B.; Wu, K.; Wang, J.; Yang, X.; Cai, B.; Zhang, Y.; Zhao, J. Reverse-Graded 2D Ruddlesden–Popper Perovskites for Efficient Air-Stable Solar Cells. *Adv. Energy Mater.* **2019**, *9*, 1900612.
- (26) Blancon, J. C.; Stier, A. V.; Tsai, H.; Nie, W.; Stoumpos, C. C.; Traoré, B.; Pedesseau, L.; Kepenekian, M.; Katsutani, F.; Noe, G. T. et al. Scaling Law for Excitons in 2D Perovskite Quantum Wells. *Nat. Commun.* **2018**, *9*, 2254.
- (27) Yin, J.; Maity, P.; Naphade, R.; Cheng, B.; He, J. H.; Bakr, O. M.; Bredas, J. L.; Mohammed, O. F. Tuning Hot Carrier Cooling Dynamics by Dielectric Confinement in Two-Dimensional Hybrid Perovskite Crystals. *ACS Nano* **2019**, *13*, 12621-12629.
- (28) L.V., K. Coulomb Interaction in Thin Semiconductor and Semimetal Films. *IJETP Lett.* **1979**, 658.

- (29) Traore, B.; Pedesseau, L.; Assam, L.; Che, X.; Blancon, J-C.; Tsai, H.; Nie, W.; Stoumpos, C. C.; Kanatzidis, M. G.; Tretiak, S. et al. Composite Nature of Layered Hybrid Perovskites: Assessment on Quantum and Dielectric Confinements and Band Alignment. *ACS Nano* **2018**, *12*, 3321-3332.
- (30) Protesescu, L.; Yakunin, S.; Bodnarchuk, M. I.; Krieg, F.; Caputo, R.; Hendon, C. H.; Yang, R. X.; Walsh, A.; Kovalenko, M. V. Nanocrystals of Cesium Lead Halide Perovskites (CsPbX₃, X = Cl, Br, and I): Novel Optoelectronic Materials Showing Bright Emission with Wide Color Gamut. *Nano Lett.* **2015**, *15*, 3692-3696.
- (31) Yao, D.; Zhang, C.; Zhang, S.; Yang, Y.; Du, A.; Waclawik, E.; Yu, X.; Wilson, G. J.; Wang, H. 2D–3D Mixed Organic–Inorganic Perovskite Layers for Solar Cells with Enhanced Efficiency and Stability Induced by N-Propylammonium Iodide Additives. *ACS Appl. Mater. Interfaces* **2019**, *11*, 29753-29764.
- (32) Shi, D.; Adinolfi, V.; Comin, R.; Yuan, M.; Alarousu, E.; Buin, A.; Chen, Y.; Hoogland, S.; Rothenberger, A.; Katsiev, K. et al. Low Trap-State Density and Long Carrier Diffusion in Organolead Trihalide Perovskite Single Crystals. *Science* **2015**, *347*, 519-522
- (33) Tong, Y.; Bladt, E.; Aygüler, M. F.; Manzi, A.; Milowska, K. Z.; Hintermayr, V. A.; Docampo, P.; Bals, S.; Urban, A. S.; Polavarapu, L. et al. Highly Luminescent Cesium Lead Halide Perovskite Nanocrystals with Tunable Composition and Thickness by Ultrasonication. *Angew. Chem. Int. Ed.* **2016**, *55*, 13887-13892.
- (34) Mir, W. J.; Swarnkar, A.; Nag, A. Postsynthesis Mn-Doping in CsPbI₃ Nanocrystals to Stabilize the Black Perovskite Phase. *Nanoscale* **2019**, *11*, 4278-4286.
- (35) Ravi, V. K.; Markad, G. B.; Nag, A. Band Edge Energies and Excitonic Transition Probabilities of Colloidal CsPbX₃ (X = Cl, Br, I) Perovskite Nanocrystals. *ACS Energy Lett.* **2016**, *1*, 665-671.

- (36) Liashenko, T. G.; Cherotchenko, E. D.; Pushkarev, A. P.; Pakštas, V.; Naujokaitis, A.; Khubezhov, S. A.; Polozkov, R. G.; Agapev, K. B.; Zakhidov, A. A.; Shelykh, I. A. et al. Electronic Structure of CsPbBr_{3-x}Cl_x Perovskites: Synthesis, Experimental Characterization, and DFT Simulations. *Phys. Chem. Chem. Phys.* **2019**, *21*, 18930-18938.
- (37) Galkowski, K.; Mitioglu, A.; Miyata, A.; Plochocka, P.; Portugall, O.; Eperon, G. E.; Wang, J. T-W.; Stergiopoulos, T.; Stranks, S. D.; Snaith, H. J. et al. Determination of the Exciton Binding Energy and Effective Masses for Methylammonium and Formamidinium Lead Tri-Halide Perovskite Semiconductors. *Energy Environ. Sci.* **2016**, *9*, 962-970.
- (38) Harrison, W. A.; Klepeis, J. E. Dielectric Screening in Semiconductors. *Phys. Rev. B* **1988**, *37*, 864-873.
- (39) Kawano, N.; Koshimizu, M.; Sun, Y.; Yahaba, N.; Fujimoto, Y.; Yanagida, T.; Asai, K. Effects of Organic Moieties on Luminescence Properties of Organic-Inorganic Layered Perovskite-Type Compounds. *J. Phys. Chem. C* **2014**, *118*, 9101-9106.
- (40) Ma, D.; Fu, Y.; Dang, L.; Zhai, J.; Guzei, I. A.; Jin, S. Single-Crystal Microplates of Two-Dimensional Organic-Inorganic Lead Halide Layered Perovskites for Optoelectronics. *Nano Res.* **2017**, *10*, 2117-2129.
- (41) Cho, Y.; Berkelbach, T. C. Optical Properties of Layered Hybrid Organic-Inorganic Halide Perovskites: A Tight-Binding GW-BSE Study. *J. Phys. Chem. Lett.* **2019**, *10*, 6189-6196.
- (42) Yaffe, O.; Chernikov, A.; Norman, Z. M.; Zhong, Y.; Velauthapillai, A.; van der Zande, A.; Owen, J. S.; Heinz, T. F. Excitons in Ultrathin Organic-Inorganic Perovskite Crystals. *Phys. Rev. B* **2015**, *92*, 045414.
- (43) Pedesseau, L.; Saponi, D.; Traore, B.; Robles, R.; Fang, H-H.; Loi, M. A.; Tsai, H.; Nie, W.; Blancon, J-C.; Neukirch, A.; Tretiak, S.; Mohite, A. D.; Katan, C.; Even, J.; Kepenekian,

M. Advances and Promises of Layered Halide Hybrid Perovskite Semiconductors. *ACS Nano* **2016**, *10*, 9776-9786.

(44) Thirumal, K.; Chong, W. K.; Xie, W.; Ganguly, R.; Muduli, S. K.; Sherburne, M.; Asta, M.; Mhaisalkar, S.; Sum, T. C.; Soo, H. S. et al. Morphology-Independent Stable White-Light Emission from Self-Assembled Two-Dimensional Perovskites Driven by Strong Exciton–Phonon Coupling to the Organic Framework. *Chem. Mater.* **2017**, *29*, 3947-3953.

(45) Zhou, G.; Li, M.; Zhao, J.; Molokeev, M. S.; Xia, Z. Single-Component White-Light Emission in 2D Hybrid Perovskites with Hybridized Halogen Atoms. *Adv. Opt. Mater.* **2019**, *7*, 1901335.

(46) Chon, B.; Bang, J.; Park, J.; Jeong, C.; Choi, J. H.; Lee, J.-B.; Joo, T.; Kim, S. Unique Temperature Dependence and Blinking Behavior of CdTe/CdSe (Core/Shell) Type-II Quantum Dots. *J. Phys. Chem. C* **2011**, *115*, 436-442.

(47) Lee, S. M.; Moon, C. J.; Lim, H.; Lee, Y.; Choi, M. Y.; Bang, J. Temperature-Dependent Photoluminescence of Cesium Lead Halide Perovskite Quantum Dots: Splitting of the Photoluminescence Peaks of CsPbBr₃ and CsPb(Br/I)₃ Quantum Dots at Low Temperature. *J. Phys. Chem. C* **2017**, *121*, 26054-26062.

(48) Sheikh, T.; Shinde, A.; Mahamuni, S.; Nag, A. Possible Dual Bandgap in (C₄H₉NH₃)₂PbI₄ 2D Layered Perovskite: Single-Crystal and Exfoliated Few-Layer. *ACS Energy Lett.* **2018**, *3*, 2940-2946.

(49) Berends, A. C.; Rabouw, F. T.; Spoor, F. C. M.; Bladt, E.; Grozema, F. C.; Houtepen, A. J.; Siebbeles, L. D. A.; de Mello Donegá, C. Radiative and Nonradiative Recombination in CuInS₂ Nanocrystals and CuInS₂-Based Core/Shell Nanocrystals. *J. Phys. Chem. Lett.* **2016**, *7*, 3503-3509.

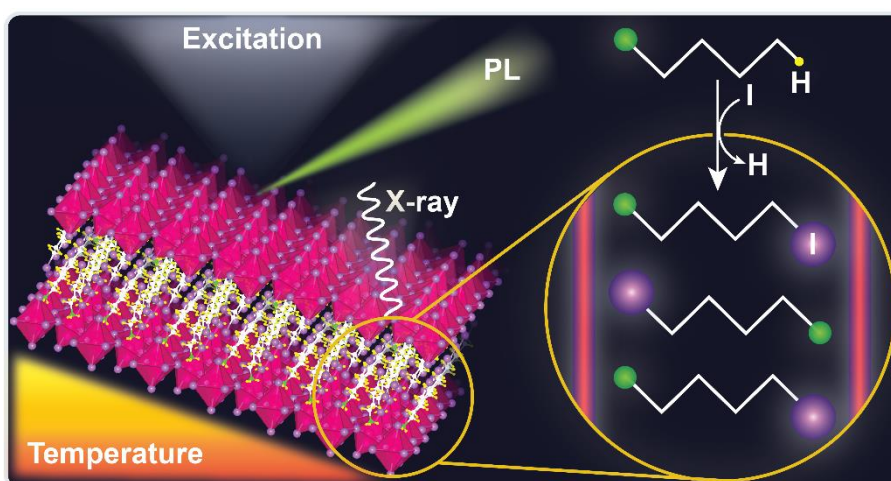
- (50) Shi, E.; Deng, S.; Yuan, B.; Gao, Y.; Akriti,; Yuan, L.; Davis, C. S.; Zemlyanov, D.; Yu, Y. ; Huang, L. et al. Extrinsic and Dynamic Edge States of Two-Dimensional Lead Halide Perovskites. *ACS Nano* **2019**, *13*, 1635-1644.
- (51) Ishihara, T.; Hong, X.; Ding, J.; Nurmikko, A. V. Dielectric Confinement Effect for Exciton and Biexciton States in PbI₄-Based Two-Dimensional Semiconductor Structures. *Surf. Sci.* **1992**, *267*, 323-326.
- (52) Wu, X.; Trinh, M. T.; Niesner, D.; Zhu, H.; Norman, Z.; Owen, J. S.; Yaffe, O.; Kudisch, B. J.; Zhu, X. Y. Trap States in Lead Iodide Perovskites. *J. Am. Chem. Soc.* **2015**, *137*, 2089-2096.
- (53) Smith, M. D.; Connor, B. A.; Karunadasa, H. I. Tuning the Luminescence of Layered Halide Perovskites. *Chem. Rev.* **2019**, *119*, 3104-3139.
- (54) Woo, H. C.; Choi, J. W.; Shin, J.; Chin, S.-H.; Ann, M. H.; Lee, C.-L. Temperature-Dependent Photoluminescence of CH₃NH₃PbBr₃ Perovskite Quantum Dots and Bulk Counterparts. *J. Phys. Chem. Lett.* **2018**, *9*, 4066-4074.
- (55) Ishihara, T.; Takahashi, J.; Goto, T. Exciton State in Two-Dimensional Perovskite Semiconductor (C₁₀H₂₁NH₃)₂PbI₄. *Solid State Commun.* **1989**, *69*, 933-936.
- (56) Cheng, B.; Li, T-Y.; Maity, P.; Wei, P-C.; Nordlund, D.; Ho, K-T.; Lien, D-H.; Lin, C-H.; Liang, R-Z.; Miao, X. et al. Extremely Reduced Dielectric Confinement in Two-Dimensional Hybrid Perovskites with Large Polar Organics. *Commun. Phys.* **2018**, *1*, 80.
- (57) Filip, M. R.; Eperon, G. E.; Snaith, H. J.; Giustino, F. Steric Engineering of Metal-Halide Perovskites with Tunable Optical Band Gaps. *Nat. Commun.* **2014**, *5*, 5757.
- (58) Billing, D. G.; Lemmerer, A. Synthesis, Characterization and Phase Transitions of the Inorganic–Organic Layered Perovskite-Type Hybrids [(C_nH_{2n+1}NH₃)₂PbI₄] (n = 12, 14, 16 and 18). *New J. Chem.* **2008**, *32*, 1736-1746.

- (59) Lemmerer, A.; Billing, D. G. Synthesis, Characterization and Phase Transitions of the Inorganic–Organic Layered Perovskite-Type Hybrids $[(C_nH_{2n+1}NH_3)_2PbI_4]$, $n = 7, 8, 9$ and 10 . *Dalton Trans.* **2012**, *41*, 1146-1157.

CHAPTER 3

Non-covalent Iodine-Iodine Interactions and Exciton Emission in $(\text{I}-(\text{CH}_2)_n\text{-NH}_3)_2\text{PbI}_4$

($n = 2-6$)



The work presented in this chapter has led to the following publication:

Chakraborty, R.; Sheikh, T.; Nag, A. Iodine-Iodine Interactions Suppressing Phase Transitions of 2D Layered Hybrid $(\text{I}-(\text{CH}_2)_n\text{-NH}_3)_2\text{PbI}_4$ ($n = 2-6$) Perovskites. *Chem. Mater.* **2022**, *34*, 288-296. Copyright permission has been taken from ACS publication for full paper.

Abstract

2D layered hybrid perovskites like $(\text{H}-(\text{CH}_2)_6\text{-NH}_3)_2\text{PbI}_4$ have hydrogen bonding interactions between organic and inorganic sub-lattices, influencing structure and properties. When a halogenated organic cation is used forming layered perovskites like $(\text{I}-(\text{CH}_2)_6\text{-NH}_3)_2\text{PbI}_4$, a new non-covalent interaction between iodine-tail of organic cation and iodine of Pb-I inorganic sub-lattice is introduced. How does the new iodine-iodine interaction, in conjunction with hydrogen bonds, modulate the crystal structure and optical properties of layered hybrid perovskites? Here we address this question providing new insights and functionality. We prepared single crystals of $(\text{I}-(\text{CH}_2)_n\text{-NH}_3)_2\text{PbI}_4$ ($n = 2-6$) and measured single-crystal X-ray diffraction and photoluminescence at different temperatures. All the samples ($n = 2-6$) do not show temperature-dependent phase transition in the range of 10 K to 296 K (~room temperature), in contrast to samples containing non-halogenated organic cations. Then we introduce a structural parameter (r) indicating symmetry of hydrogen bonding ($-\text{NH}_3$ group) with respect to inorganic sub-lattice. Lower values of r indicate more symmetry in hydrogen bonding, leading to a higher Pb-I-Pb bond angle and lower band gap for $n = 5-6$. Higher r increases asymmetry in hydrogen bonding, decreasing band gap for $n = 2-4$.

3.1 Introduction

2D layered hybrid lead halide perovskites A_2PbI_4 typically have non-halogenated A-site cations like $\text{H}-(\text{CH}_2)_6\text{-NH}_3^+$. Recently, halogenated A-site cations like $\text{I}-(\text{CH}_2)_6\text{-NH}_3^+$ have been introduced.^{1, 2} Substitution of the terminal hydrogen with I in the A-site cation introduces a new non-covalent halogen-halogen interaction between the I of A-site molecule and I of inorganic Pb-I layer.^{3, 4} The $-\text{NH}_3$ head group of A-site cation interacts with one Pb-I layer through hydrogen bonding, and the $-\text{I}$ tail of the same A-site cation interacts with another Pb-I layer through iodine-iodine interactions (Figure 3.1). How do these two non-covalent interactions influence the crystal structure and band gap of 2D layered hybrid perovskites? Here we address this question by making single crystals of $(\text{I}-(\text{CH}_2)_n\text{-NH}_3)_2\text{PbI}_4$ ($n = 2-6$) and exploring their structure and optical properties over a wide temperature range of 10 K to 300 K.

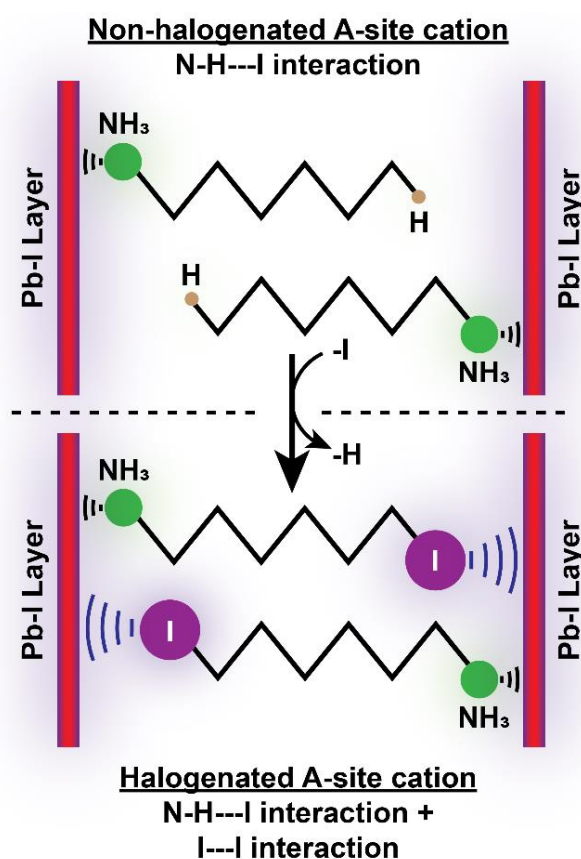


Figure 3.1. Schematic showing the introduction of iodine-iodine interaction between inorganic (Pb-I) layer and organic (halogenated A-site cation) layer.

The overall structure of A_2PbI_4 can be thought of as a composite of alternating 2D inorganic negatively-charged Pb-I layers and positively-charged organic A- layers, yielding a multi-quantum well structure.⁵⁻⁹ Though the electronic and optical properties mainly originate from the orbital interactions in the Pb-I layers, the choice of the A-site cation has a direct influence on the excitons through dielectric confinement.¹⁰⁻¹² A-site cation also plays a crucial role in controlling the optical properties of the layered perovskites by imparting structural distortions in the inorganic layer through non-covalent interactions.^{13, 14} Thus, It becomes possible to control optical properties by modifying the non-covalent interactions through A-site cation engineering.^{15, 16-17}

In this regard, halogenated organic ammonium cations like $\text{I}-(\text{CH}_2)_6\text{-NH}_3^+$ open up new opportunity to tailor the structure and optical property. For example, C-I bond helps to intercalate molecules like I_2 in the organic sub-lattice, resulting in large tunability of the exciton binding energy.^{2,11} Also, halogenated A-site cations have been reported to improve the moisture-stability of halide perovskites.¹⁸ A more generic material design strategy is to utilize iodine-iodine interaction between A-site cation and Pb-I inorganic layer (Figure 3.1) to control structural parameters, and therefore, control electronic and optical properties.

Our single-crystal X-ray diffraction (SCXRD) and PL data show that all the five samples of $(\text{I}-(\text{CH}_2)_n\text{-NH}_3)_2\text{PbI}_4$ ($n=2-6$) do not show any structural phase transition across the temperature range of 10 K to 300 K. Such absence of phase transition is surprising compared to prior reports of typical 2D layered hybrid perovskites with non-halogenated monovalent A-site cations. The absence of temperature-dependent phase transition, or in other words, the increased structural stability of $(\text{I}-(\text{CH}_2)_n\text{-NH}_3)_2\text{PbI}_4$ ($n = 2-6$), has been attributed to this new iodine-iodine interaction. Then we define new structural parameters that indicate the location of $-\text{NH}_3$ groups with respect to the surrounding inorganic sub-lattice. These structural parameters help to

explain the nature of hydrogen bonding interactions that control the Pb-I-Pb bond angle and band gap of $(\text{I}-(\text{CH}_2)_n\text{-NH}_3)_2\text{PbI}_4$ ($n = 2-6$).

3.2 Experimental Section

3.2.1 Chemicals. Hydroiodic acid (Sigma Aldrich, HI, 57% w/w in water), lead oxide (Sigma Aldrich, PbO, 99.9%), ethanolamine (Sigma Aldrich, HO-(CH₂)₂-NH₃, >99%), 3-amino-1-propanol (Sigma Aldrich, HO-(CH₂)₃-NH₃, >99%), 4-amino-1-butanol (Sigma Aldrich, HO-(CH₂)₄-NH₃, 98%), 5-amino-1-pentanol (Sigma Aldrich, HO-(CH₂)₅-NH₃, >92%), 6-amino-1-hexanol (Sigma Aldrich, HO-(CH₂)₆-NH₃, 97%), hypophosphorus acid (Avra chemicals, H₃PO₂, 50% w/w in water).

3.2.2 Synthesis of $(\text{I}-(\text{CH}_2)_n\text{-NH}_3)_2\text{PbI}_4$ ($n = 2-6$) single crystals. The single crystals are synthesized using a modified acid-precipitation method.¹⁹ At room temperature (296 K), in a 100 ml glass beaker, 5 mmol PbO is dissolved in a solution of 40 mL HI (57% w/w in water) and 5 mL H₃PO₂ (50% w/w in water), by sonicating in an ultrasonic bath sonicator for 10 minutes. Dissolution of the PbO powder forms a bright yellow solution. The solution is cooled to ~278 K using an ice-water bath. In this solution, 10 mmol of the corresponding alcohol amine (H₂N-(CH₂)_n-OH; $n = 2-6$) is added dropwise. The solution is stirred using a magnetic stirrer and heated for 30 minutes in an oil-bath maintained at 383 K. At the experimental conditions, the -OH group of the alcohol amine becomes labile and gets converted to $\text{I}-(\text{CH}_2)_n\text{-NH}_3^+$.¹ After 30 minutes, the heating and stirring are stopped, and the clear transparent solution is kept undisturbed. The A₂PbI₄ single crystals form in the solution overnight (~12 hours). The crystals are collected using suction filtration and are dried under nitrogen flow.

3.2.3 Structural characterization. SCXRD data are collected in Bruker Apex Duo diffractometer using Mo K α radiation ($\lambda = 0.71 \text{ \AA}$). The single crystals are mounted on the glass-tip sample holder and are kept under a constant flow of nitrogen throughout the experiment. The integrations of the collected data and numerical absorption corrections are

done using APEX3 software. The structures are solved by the direct method and refined by full-matrix least-squares on F^2 using the SHELXTL software package. All atoms are refined anisotropically without any constraints.

3.2.4 Optical properties. Optical diffused reflectance spectra are collected at room temperature using an integrating sphere in Shimadzu UV3600 plus UV-vis-NIR spectrophotometer. For these measurements, BaSO_4 powder is used as a reference of 100% reflectance. The diffused reflectance signal is converted to absorbance using the Kubelka-Munk function.²⁰ Steady-state PL and PL excitation (PLE) spectra are recorded using the FLS 980 spectrophotometer (Edinburgh Instruments). A 405 nm (3.06 eV) picosecond pulsed diode laser is used as the excitation source for recording the PL, and a Xe-lamp is used for recording PLE spectra. For low-temperature PL measurements, a closed-cycle He-cryostat from Advanced Research Systems is used. The single-crystalline samples are placed in between two sapphire plates (PELCO; 0001 plane cut and double-side polished) that are further placed in a gold-plated sample holder with indium wire as the thermal contact. The sample holder is then mounted on the copper cold-finger, and indium foils are used for optimum thermal contact. The sample holder is placed such that the incident beam on the sample and the detected light emission from the sample makes 45° angle on the upper sapphire plate.

3.3 Results and Discussion

3.3.1 Iodine-Iodine interaction suppressing temperature-dependent phase transitions of $(\text{I}-(\text{CH}_2)_4\text{-NH}_3)_2\text{PbI}_4$. Layered hybrid perovskites containing non-halogenated monovalent A-site cations typically show structural phase transitions at lower temperatures.^{21, 22} Since halogenated A-site cations like $\text{I}-(\text{CH}_2)_4\text{-NH}_3^+$ can introduce new non-covalent interactions, we explore the effect of temperature on the crystal structure of layered hybrid perovskites like $(\text{I}-(\text{CH}_2)_4\text{-NH}_3)_2\text{PbI}_4$. We have measured the SCXRD data of $(\text{I}-(\text{CH}_2)_4\text{-NH}_3)_2\text{PbI}_4$ at 100 K and 296 K (near room temperature). Figure 3.2a shows the crystal structure at 296 K. The refined

structural parameters are shown in Table 3.2. Layered perovskite structure with space group $\text{P2}_1/\text{c}$ is obtained 296 K. A small part of the crystal structure is enlarged in Figure 3.2b (left panel). The interesting point is to observe the iodine-iodine interactions, indicated by the yellow dashed lines. The distance between the two iodine atoms is 3.96 Å, which is shorter than the sum of Van der Waals radius (4.3 Å) for iodine, and thus approaches the limit of non-covalent halogen-bonding.^{23, 24}

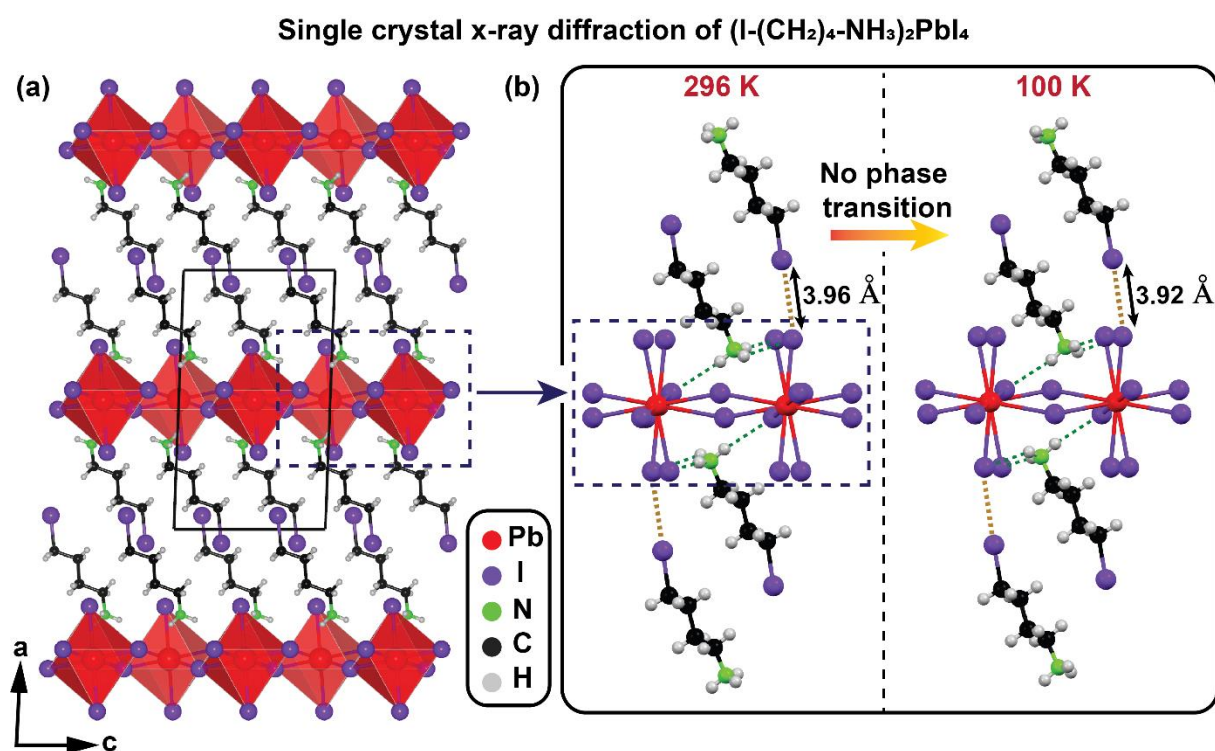


Figure 3.2. Crystal structure of $(\text{I}-(\text{CH}_2)_4\text{-NH}_3)_2\text{PbI}_4$. (a) Structure obtained from single-crystal x-ray diffraction (SCXRD) at 296 K (near room temperature). The solid black box indicates the unit cell boundary. (b) Magnified view of a small part of the crystal shown in Figure 3.2a at 296 K and its comparison with the structure at 100 K. Non-covalent hydrogen bonding and iodine-iodine interactions between $\text{I}-(\text{CH}_2)_4\text{-NH}_3^+$ cations and inorganic Pb-I anionic layers are shown by green and yellow dashed lines, respectively.

The right panel in the Figure 3.2b shows the crystal structure at 100 K. The crystal structure at both temperatures, 100 K and 296 K, remains unchanged. It is noteworthy that $(\text{I}-(\text{CH}_2)_4\text{-NH}_3)_2\text{PbI}_4$ does not show a structural phase transition in the temperature range of 100 K to 296 K. This observation is in sharp contrast to $(\text{H}-(\text{CH}_2)_4\text{-NH}_3)_2\text{PbI}_4$ (with non-halogenated A-site cation), that show two different structures above and below 250 K (Figure 3.3).^{22, 25} The

suppression of temperature-dependent phase transition $(I-(CH_2)_4-NH_3)_2PbI_4$ might be originating from the iodine-iodine interaction that restricts the movement of the organic cations in space.

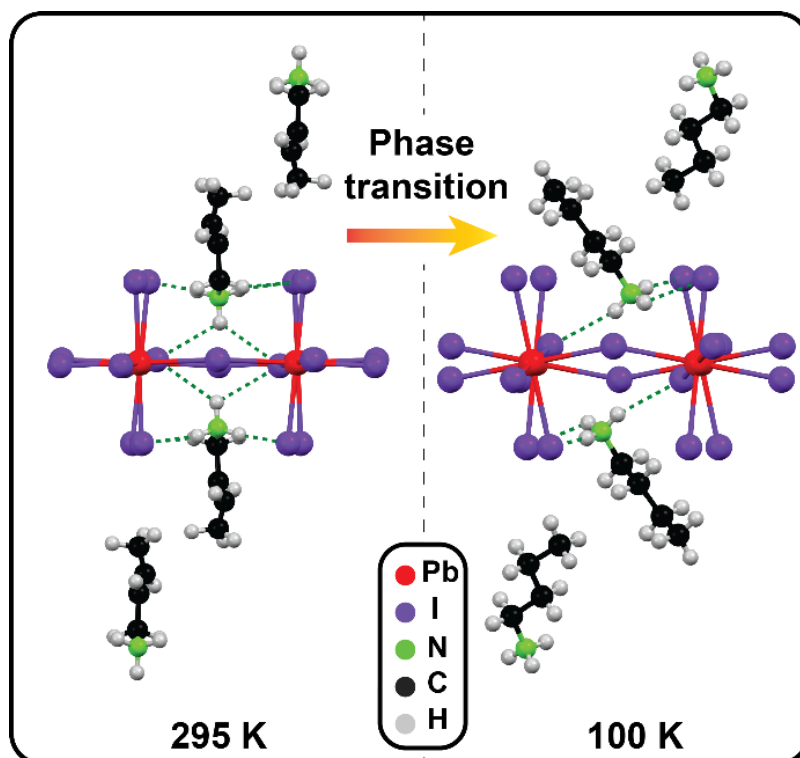


Figure 3.3: The non-covalent interactions (green dashed lines) at different temperatures in crystalline butylammonium lead iodide, $(H-(CH_2)_4-NH_3)_2PbI_4$. The figure is obtained based on SCXRD data reported in prior references: for 100 K data ref²², and for 295 K data ref²⁵.

Temperature-dependent structural phase transition typically changes the band gap of layered perovskites with non-halogenated monovalent A-site cations. For example, $(H-(CH_2)_4-NH_3)_2PbI_4$ shows a sudden change in excitonic emission peak (\sim band gap) position from 2.38 eV at 250 K to 2.53 eV at 225 K.²² This sudden change of 150 meV in peak position is attributed to the structural phase transition. In contrast, $(I-(CH_2)_4-NH_3)_2PbI_4$ does not exhibit temperature-dependent phase transition. Therefore, one would not expect such a transition in band gap as well.

Figure 3.4a shows the absorption and PL spectra recorded from single crystals of $(I-(CH_2)_4-NH_3)_2PbI_4$ at room temperature. The absorption spectrum shows two absorption edges.

Similarly, two emission peaks corresponding to both absorption edges are observed at 2.36 and 2.49 eV in the PL spectra. Prior literature reported that the single crystals of similar 2D layered hybrid lead halide perovskites with non-halogenated A-site cation show such two emission and absorption features, and both the features had been assigned to excitonic states.^{22, 26-28} The higher energy excitonic emission was attributed to isolated Pb-I layers (quantum well), and the lower energy excitonic emission was dominated by possible interactions between Pb-I layers at the layer-edges.^{28, 29}

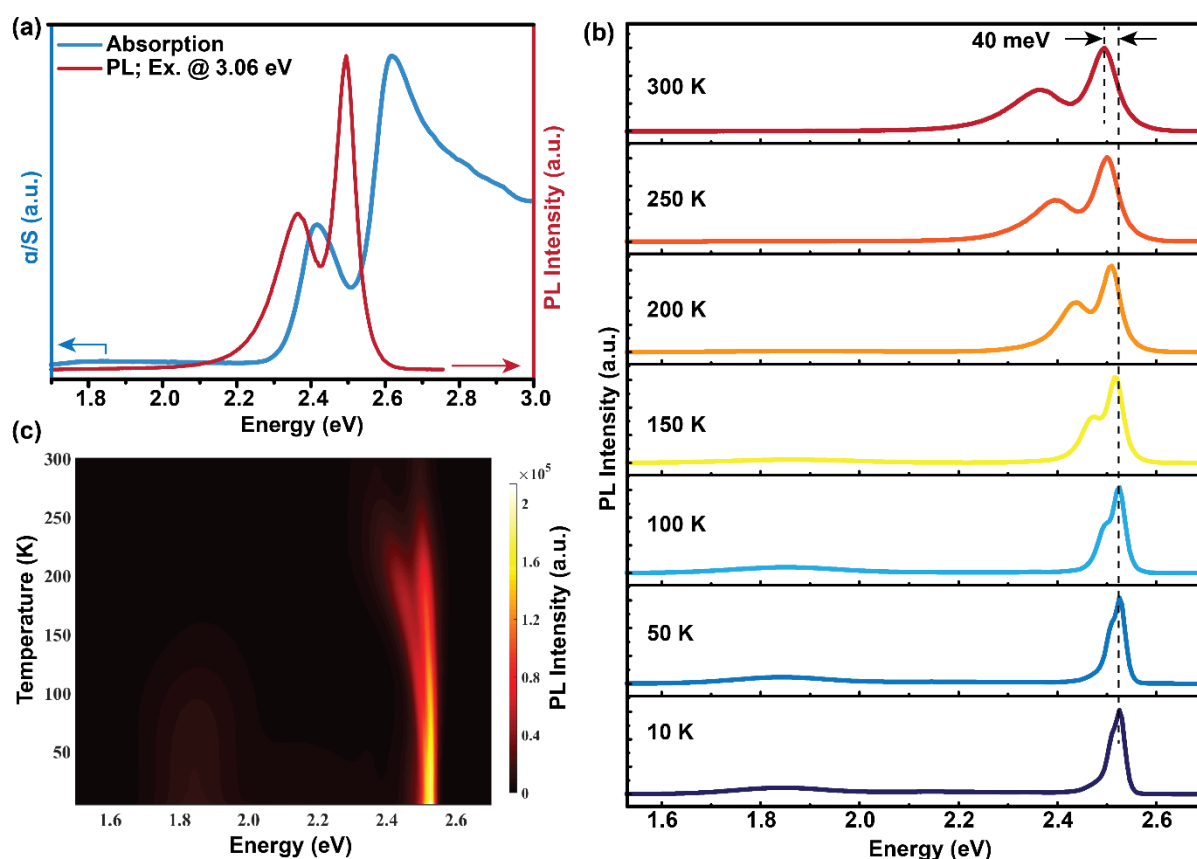


Figure 3.4. Optical properties of $(\text{I}-(\text{CH}_2)_4\text{-NH}_3)_2\text{PbI}_4$ single crystal. (a) Optical absorption and PL spectra recorded at room temperature. The absorption spectrum is obtained by Kubelka-Munk transformation of the diffused reflectance spectrum, $\alpha/S = (1 - R)^2/2R$. Here, R is the reflectance, α is the absorption coefficient, and S is the scattering coefficient. (b) PL spectra recorded at a few representative temperatures in the 10-300 K range. (c) Pseudo colormap of temperature-dependent PL.

Figure 3.4b shows the evolution of the PL spectrum on lowering the temperature. The higher energy excitonic emission peak systematically blue-shifts by about 40 meV by decreasing the temperature from 300 K to 10 K. Previously reported 2D layered perovskites show both red-

and blue-shifts of the emission peak with decreasing temperature, depending on the composition.^{11, 30} Such shifts are associated with the change in Pb-I-Pb bond angles.^{13, 31} For example, in Figure 3.4b, the blue-shift is because of the decrease in Pb-I-Pb bond angle (Figure 3.5) with decreasing temperature. The decrease in the angle typically increases the band gap, explaining the blue-shift of the excitonic emission peak at lower temperatures.²²

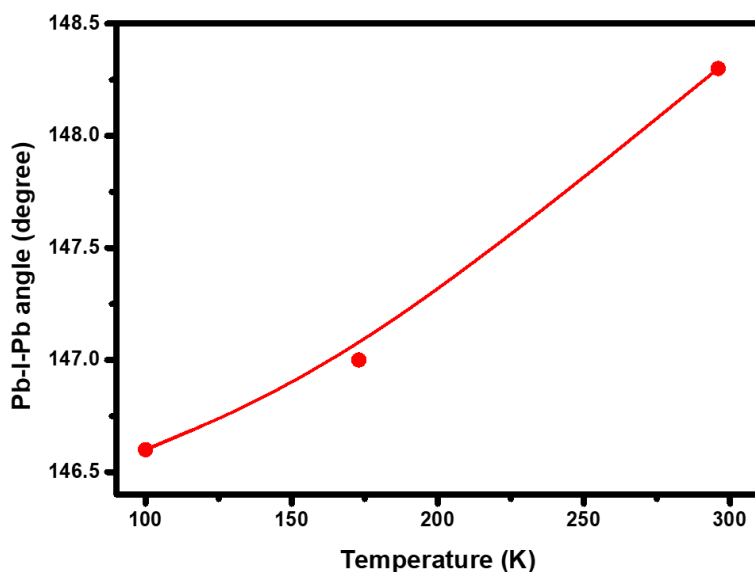


Figure 3.5: Change in the measured Pb-I-Pb bond angle with temperature in crystalline $(I-(CH_2)_4-NH_3)_2PbI_4$; the angles are obtained from SCXRD. Angle at 173 K is obtained from SCXRD data reported in ref¹.

Interestingly, we do not observe an abrupt shift in the position of high-energy PL peak at any specific temperature region. The pseudo colormap of the temperature-dependent PL spectra in Figure 3.4c also shows the absence of abrupt change in excitonic emission peak energy or intensity at any specific temperature. These temperature-dependent PL data suggest that the sample does not undergo a structural phase transition in the entire temperature range 300 K to 10 K and corroborate the findings of SCXRD data (Figure 3.2b).

Expectedly, the intensity of overall PL emission increases steadily with decreasing temperatures, at least till 200 K, because of the suppression of non-radiative recombination channels at lower temperatures. Also, the width of the excitonic emission peak decreases due to reduced exciton-phonon coupling. At temperatures lower than 200 K, along with the

excitonic emissions, a weak broad emission is observed at lower energy, with a peak at 1.9 eV. PLE spectra (Figure 3.6) recorded at this emission feature suggest that the excitation is through band-edge excitons. Similar broad emission, with a large Stokes shift compared to the absorption edges, has been a common feature in prior reports of layered hybrid lead halide perovskites and has been previously assigned to self-trapped exciton (STE) emissions.^{32,33}

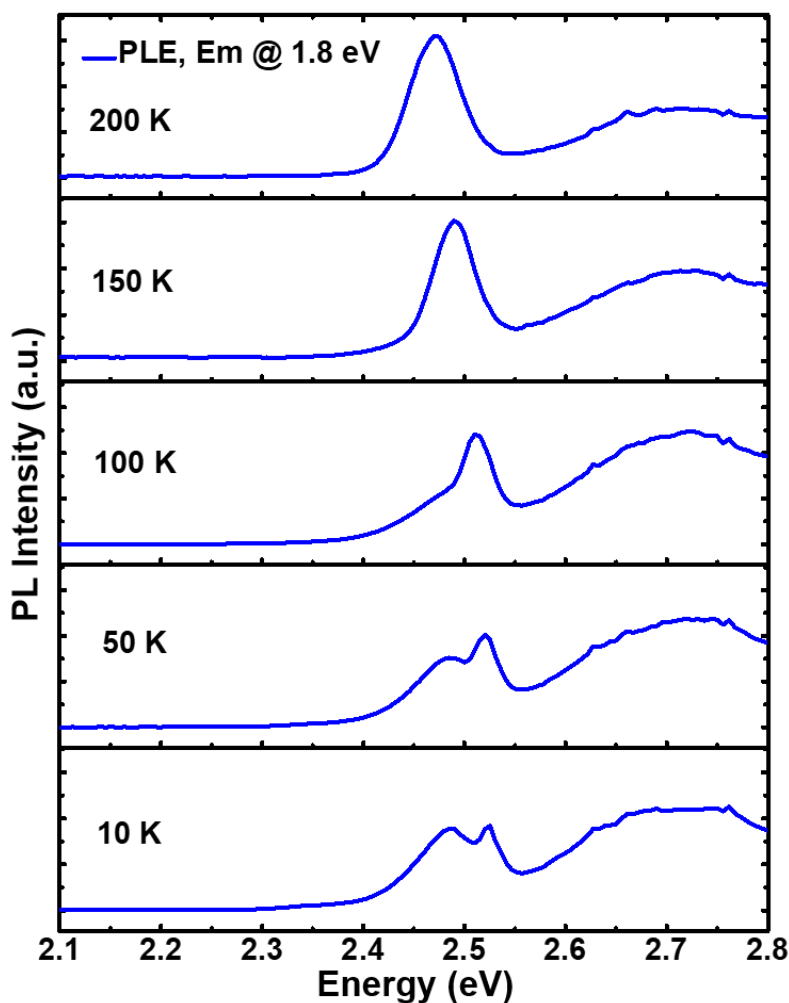


Figure 3.6: Photoluminescence excitation (PLE) spectra of $(\text{I}-(\text{CH}_2)_4\text{-NH}_3)_2\text{PbI}_4$ single crystals recorded at different temperatures.

3.3.2 The generic $(\text{I}-(\text{CH}_2)_n\text{-NH}_3)_2\text{PbI}_4$ series with $n = 2-6$. After exploring the specific sample $(\text{I}-(\text{CH}_2)_4\text{-NH}_3)_2\text{PbI}_4$ ($n = 4$), now we discuss the generic sample series $(\text{I}-(\text{CH}_2)_n\text{-NH}_3)_2\text{PbI}_4$ with $n = 2-6$. The structural parameters obtained from SCXRD are shown in Table 3.2 to 3.6. All the samples ($n = 2-6$) show a 2D layered hybrid perovskite structure. The layered

perovskite structure has not been reported for $(\text{H}-(\text{CH}_2)_2\text{-NH}_3)_2\text{PbI}_4$, $n = 2$ with non-halogenated organic cation. So, the stabilization of $(\text{I}-(\text{CH}_2)_2\text{-NH}_3)_2\text{PbI}_4$ in the layered perovskite structure with monoclinic $\text{P}2_1/\text{c}$ space group is probably facilitated due to the overall longer length of the organic cation by replacing H with I and the introduction of the iodine-iodine interaction.³

Based on how alternating inorganic layers stack, 2D LHPs are divided in two groups – Ruddlesden-Popper phase, and Dion-Jacobsen phase.^{19, 34, 35} Figure 3.7a schematically shows the difference. For $(\text{I}-(\text{CH}_2)_n\text{-NH}_3)_2\text{PbI}_4$ with $n = 2-5$ ($\text{P}2_1/\text{c}$ space group), the composition is similar to a Ruddlesden-Popper phase with monovalent organic cation, but the structure is like Dion-Jacobsen phase where Pb-I layers eclipse each other (Figure 3.7b). Typical Dion-Jacobsen phase has bivalent A-site cation having $-\text{NH}_3$ groups at both ends, that interact with adjacent Pb-I layers, enforcing the Pb-I layers to eclipse each other.³⁶ In $(\text{I}-(\text{CH}_2)_n\text{-NH}_3)_2\text{PbI}_4$ ($n = 2-5$), though the A-site cations are monovalent with only one $-\text{NH}_3$ group, the iodine-iodine interaction at the cation's tail is the reason why they still crystallize in the Dion-Jacobsen like structure. However, the sample with $n = 6$ crystallizes in an orthorhombic Pbca space group having Ruddlesden-Popper like structure. This does not mean that the iodine-iodine interactions are absent in $n = 6$. As we observe, the I-I distance for $n = 6$ at 100 K is 3.81 Å, still shorter than the sum of Van der Waals radius (4.3 Å) for iodine. We attribute this transition from Dion-Jacobsen like ($n = 2-5$) to Ruddlesden-Popper like ($n = 6$) structure to the increased freedom of the carbon backbone and increased alkyl-alkyl interactions on increasing the carbon number from $n = 2-5$ to $n = 6$.¹⁸

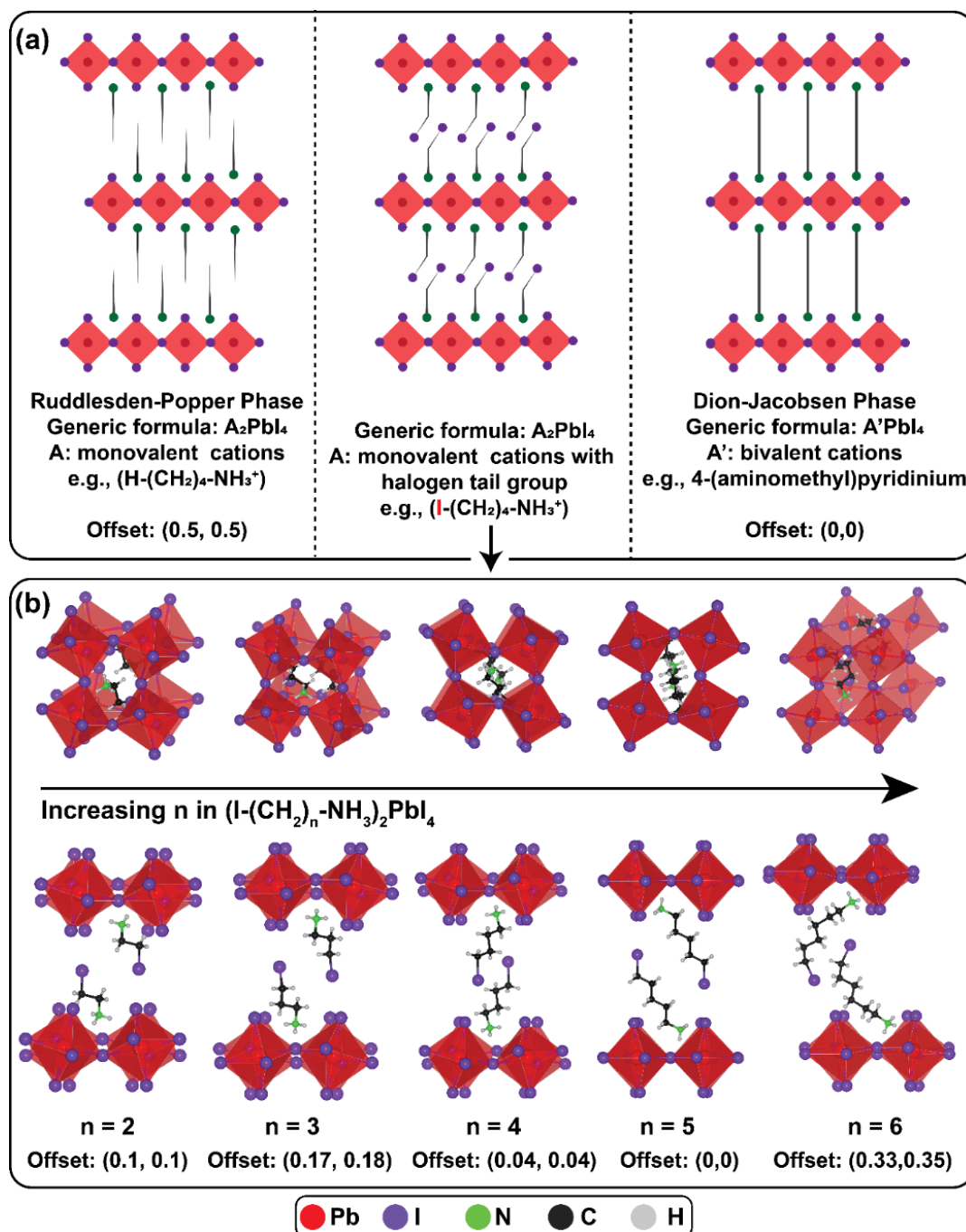


Figure 3.7: (a) Schematic of different phases in monolayered halide perovskite compositions. The offset values indicate the translation required for alternate Pb-I layers to eclipse each other in the fraction of in-plane unit cell constants. Left panel shows the layer stacking in the Ruddlesden-Popper phase, where a monovalent ammonium cation is used, and the alternate Pb-I layers are shifted by half unit cell constants in both Pb-I-Pb linkage directions. Right panel shows the stacking in Dion-Jacobsen phase; here, a bivalent ammonium cation is used and the Pb-I layers are perfectly on top of each other. The middle panel shows the layered perovskite structure with monovalent cations with a halogen tail group. The schematic shows that the compositions are Ruddlesden-Popper like, but the stacking is Dion-Jacobsen like. (b) Layer stacking in $(I-(CH_2)_n-NH_3)_2PbI_4$ ($n = 2-6$) layered perovskite crystal structures at 100 K, obtained from SCXRD. The top panel shows the view of two subsequent layers from top, and the bottom panel shows the same layers from side. Based on the offset values, $n = 2-5$ can be regarded as Dion-Jacobsen like, and $n = 6$ can be regarded as Ruddlesden-Popper like.¹⁸

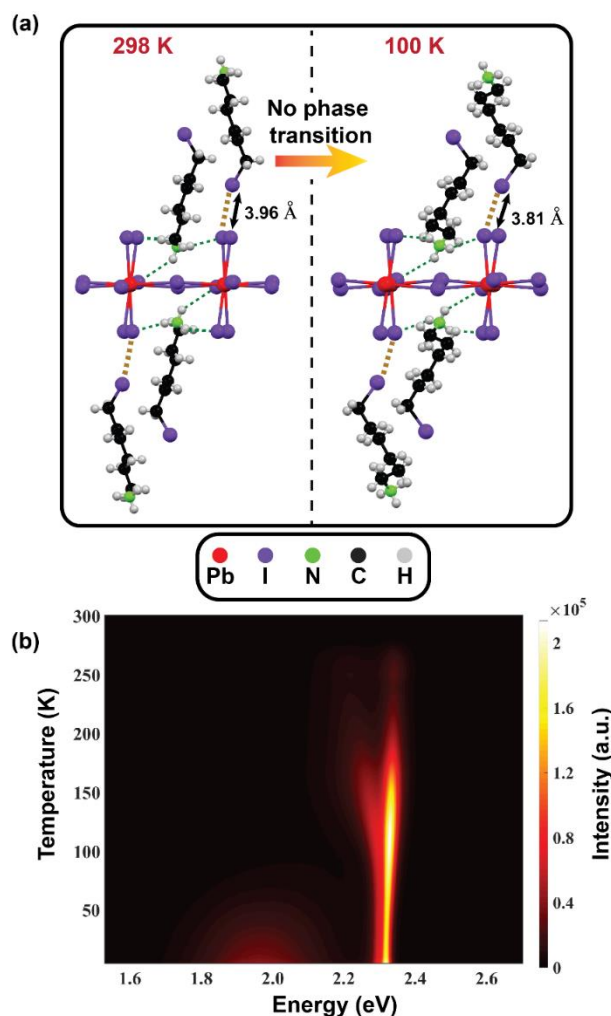


Figure 3.8: (a) Non-covalent interactions in $(\text{I}-(\text{CH}_2)_6\text{-NH}_3)_2\text{PbI}_4$ at room temperature (298 K) and 100 K; hydrogen bonding and iodine-iodine interactions between $\text{I}-(\text{CH}_2)_6\text{-NH}_3^+$ cations and inorganic Pb-I layers are shown by green and yellow dashed lines. The structure at room temperature (298 K) taken from SCXRD data reported in ref². Refinement parameters of our SCXRD data recorded at 100 K is given in Table 3.6. (b) Pseudocolormap of temperature-dependent PL.

Interestingly, all the samples ($n = 2-6$) show the absence of temperature-dependent structural phase transition, similar to the $n = 4$ sample, discussed above. For example, Figure 3.8 shows the situation for $n = 6$ sample. This absence of temperature-dependent phase transition is because of iodine-iodine interaction between organic A-site cation and Pb-I layers (Figure 3.2b), providing additional structural stability over the wide temperature range of 10 K to 296 K. This absence is in contrast to the layered hybrid Pb halide perovskites with non-halogenated monovalent A-site cation. This enhanced structural stability might also increase the moisture

resistance of the samples similar to prior reports suggesting halogen-halogen, cation- π or other such interactions improving water stability of hybrid metal halide perovskites.^{18, 37, 38}

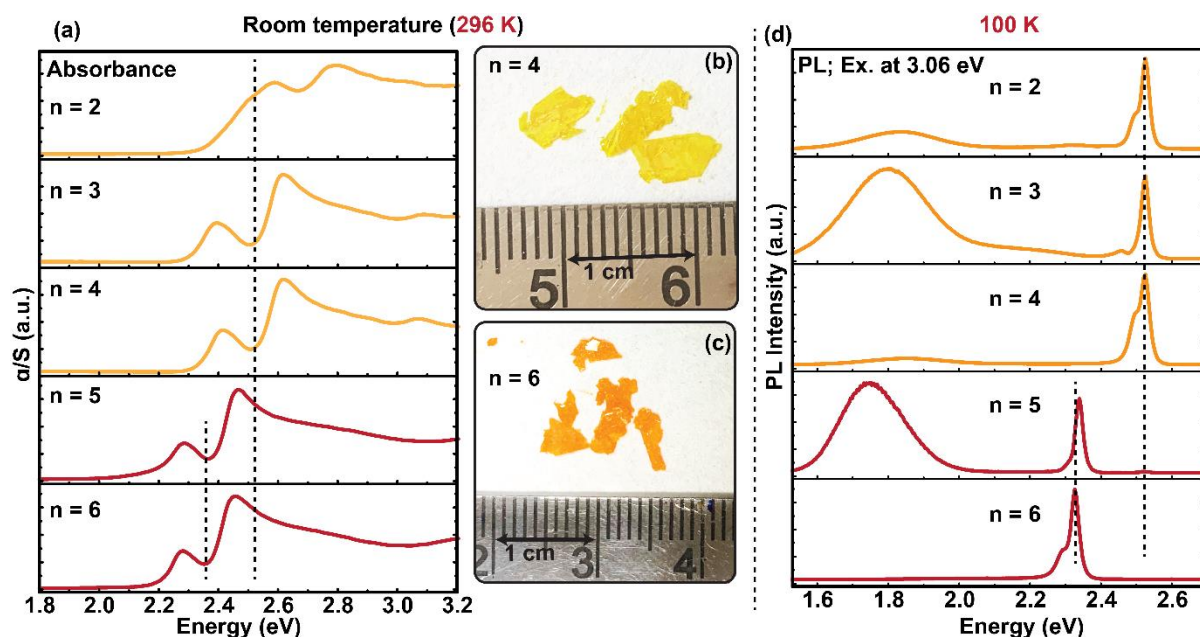


Figure 3.9. Optical properties of $(I-(CH_2)_n-NH_3)_2PbI_4$ ($n = 2-6$) single crystals. (a) Optical absorption spectra obtained from recorded diffused reflectance data at room temperature. α and S denote absorption coefficient and scattering coefficient, respectively. Digital photographs of single crystals with (b) $n = 4$, and (c) $n = 6$. (d) PL spectra recorded at 100 K.

Figure 3.9a shows the optical absorption spectra of $(I-(CH_2)_n-NH_3)_2PbI_4$ ($n = 2-6$) recorded at room temperature. All samples show two absorption edges, similar to the $n = 4$ sample, discussed in Figure 3.4a. However, the edge positions vary between samples. Both lower energy and higher energy edges follow the same trend with the variation of n . For $n = 2$, the two edges are sufficiently broad and merged together, making their distinction difficult. Increasing n from 3 to 4, the positions of edges remain unchanged. However, on a further increase of carbon number from $n = 4$ to 5, there is a drastic red-shift of the absorption edges. The positions of edges for $n = 5$ and 6 are similar. Based on the energies of absorption edges, we can divide the samples into two groups: $n = 3-4$ having a lower band gap, and $n = 5-6$ with a higher band gap. The optical properties of the $n = 2$ sample resemble the former group. Consequently, the colors of the samples for the two groups are somewhat different. For example, Figures 3.9b and 3.9c show bright yellow and orange color of single crystals of

samples with $n = 4$ and 6 , respectively. The difference of the absorption edges (color) is also reflected in the PL spectra recorded at room temperature and 10 K, of samples with $n = 4$ and 6 , as shown in Figure 3.10.

Figure 3.9d shows the PL spectra of $(\text{I}-(\text{CH}_2)_n\text{-NH}_3)_2\text{PbI}_4$ ($n = 2-6$) single crystals, recorded at 100 K. The higher energy excitonic emission, attributed to isolated Pb-I quantum well layers, dominates the PL at lower temperatures (refer to prior discussion of Figure 3.4). The PL spectra for samples with $n = 2-4$ show higher energy emission peak at 2.53 eV, while for $n = 5-6$, the emission peak shifts to 2.34 ($n = 5$) and 2.33 ($n = 6$) eV. This sudden red-shift observed in the PL at 100 K at the bordering values from $n = 4$ to 5 is in agreement with the room-temperature optical absorption (Figure 3.9a) and PL, as well as PL at 10 K (Figure 3.10) measurements.

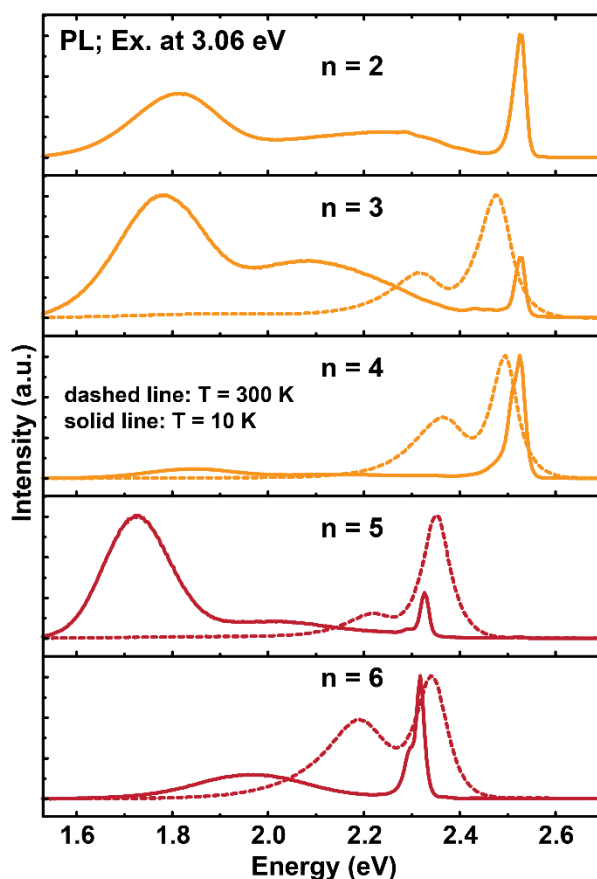


Figure 3.10: PL spectra recorded from single crystalline $(\text{I}-(\text{CH}_2)_n\text{-NH}_3)_2\text{PbI}_4$ samples at room temperature (300 K) and 10 K.

3.3.3 Pb-I-Pb bond angle influences PL peak position (band gap) of $(I-(CH_2)_n-NH_3)_2PbI_4$ ($n = 2-6$).

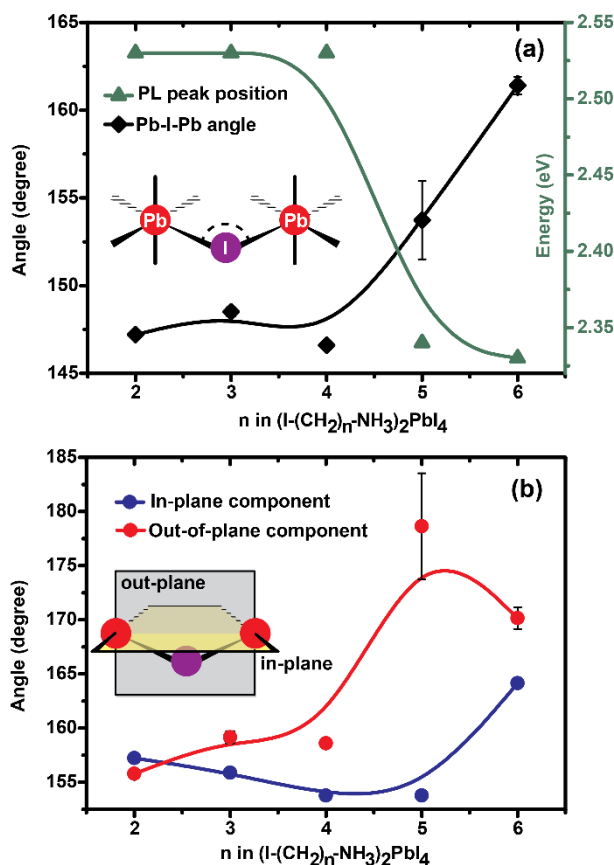


Figure 3.11. Correlation of high-energy PL peak position (excitonic band gap) and structural properties of $(I-(CH_2)_n-NH_3)_2PbI_4$ ($n = 2-6$), measured at 100 K. (a) Comparison of high-energy PL peak position (obtained from Figure 4d) and Pb-I-Pb bond angle obtained from SCXRD data. Inset shows the schematic representation of the Pb-I-Pb bond angle that also determines the extent of tilting between the corner shared Pb-I octahedra. (b) Decomposition of Pb-I-Pb bond angle to in-plane and out-of-plane components. Inset shows the perpendicular planes on which the Pb-I-Pb bond angle is projected to get in-plane and out-of-plane components. For the Pb-I-Pb angle (also called “tilt-angle”) and its components, the error propagation is calculated as per the methodology given by Smith et al.⁴⁰

Samples with $n = 2-4$ show similar peak energies and are very different compared to samples with $n = 5-6$ (Figure 4). Why so? To answer this question, we analyzed the Pb-I-Pb bond angles (inset of Figure 3.11a) obtained from our SCXRD data. Figure 3.11a correlates the Pb-I-Pb bond angle with high-energy PL peak position, both measured at 100 K, for $(I-(CH_2)_n-NH_3)_2PbI_4$ ($n = 2-6$). Bond angles and PL peak positions (reflecting excitonic band gap) remain similar for $n = 2-4$. But for $n = 5$ and 6 , the bond angle increases and thereby decreasing the PL peak energy. The observation agrees with the expectation that an increase in the Pb-I-Pb

bond angle (up to the 180° for an ideal cubic perovskite structure) increases the overlap of Pb and I orbitals, decreasing the band gap.^{13, 39}

Furthermore, the Pb-I-Pb bond angle can be decomposed into two components based on its projection on perpendicular planes, shown in the inset of Figure 3.11b. The decomposition of Pb-I-Pb bond angle to in-plane and out-of-plane components provides more insights owing to the directional nature of Pb and I *p*-orbitals.¹³ Figure 3.11b shows that at 100 K, the in-plane component of the Pb-I-Pb bond angle remains the same for both $n = 4$ (153.8°) and $n = 5$ (153.8°), but there is a drastic change in the out-of-plane component from 158.6° ($n = 4$) to 178.6° ($n = 5$). Thus, the increase in the out-of-plane component seems to be the primary reason for the experimentally observed increase in Pb-I-Pb bond angle and the corresponding decrease in excitonic band gap (Figure 3.11a) by changing n from 4 to 5.

3.3.4 Structural parameters controlling hydrogen bonding and Pb-I-Pb bond angle. While iodine-iodine interactions are important for structural stability, the other non-covalent interaction, namely hydrogen bonds (see Figure 3.2b) between the A-site ammonium ion and I of the Pb-I inorganic layer, is expected to play a more important role in determining the Pb-I-Pb bond angles. The hydrogen bonds are influenced by the position of the $-\text{NH}_3$ group with respect to the Pb-I inorganic sub-lattice. Here, we define the position of the $-\text{NH}_3$ group by introducing a few structural parameters that can be obtained from the experimental SCXRD data. Figure 6a shows the unit cell of Pb-I inorganic sub-lattice of $(\text{I}-(\text{CH}_2)_6\text{-NH}_3)_2\text{PbI}_4$ at 100 K. The intersecting (100), (001), and (010) planes that pass through the Pb atoms are shown in different colors. Using the perpendicular distances of the nitrogen atom of the $-\text{NH}_3$ group from this set of planes, it is possible to indicate the position of the ammonium group. Figure 3.12b shows the distance (labeled as d_0) of the nitrogen atom from the (001) Pb-plane (yellow dashed line). Figure 3.12c shows the intersecting (100) and (010) Pb-planes, indicating their perpendicular distances d_1 and d_2 from the nitrogen atoms, respectively. To generalize it for all

the samples of $(\text{I}(\text{CH}_2)_n\text{-NH}_3)_2\text{PbI}_4$ with $n = 2-6$, we define d_1 in a way that it always corresponds to the longer distance from either of the (010) and (100) planes, and d_2 corresponds to the shorter distance, and the ratio, $r (= \frac{d_1}{d_2}) \geq 1$. The value of $r = 1$ ($d_1 = d_2$) indicates that the $-\text{NH}_3$ group is symmetrically located between the (100) and (010) Pb-planes (see Figure 3.12c).

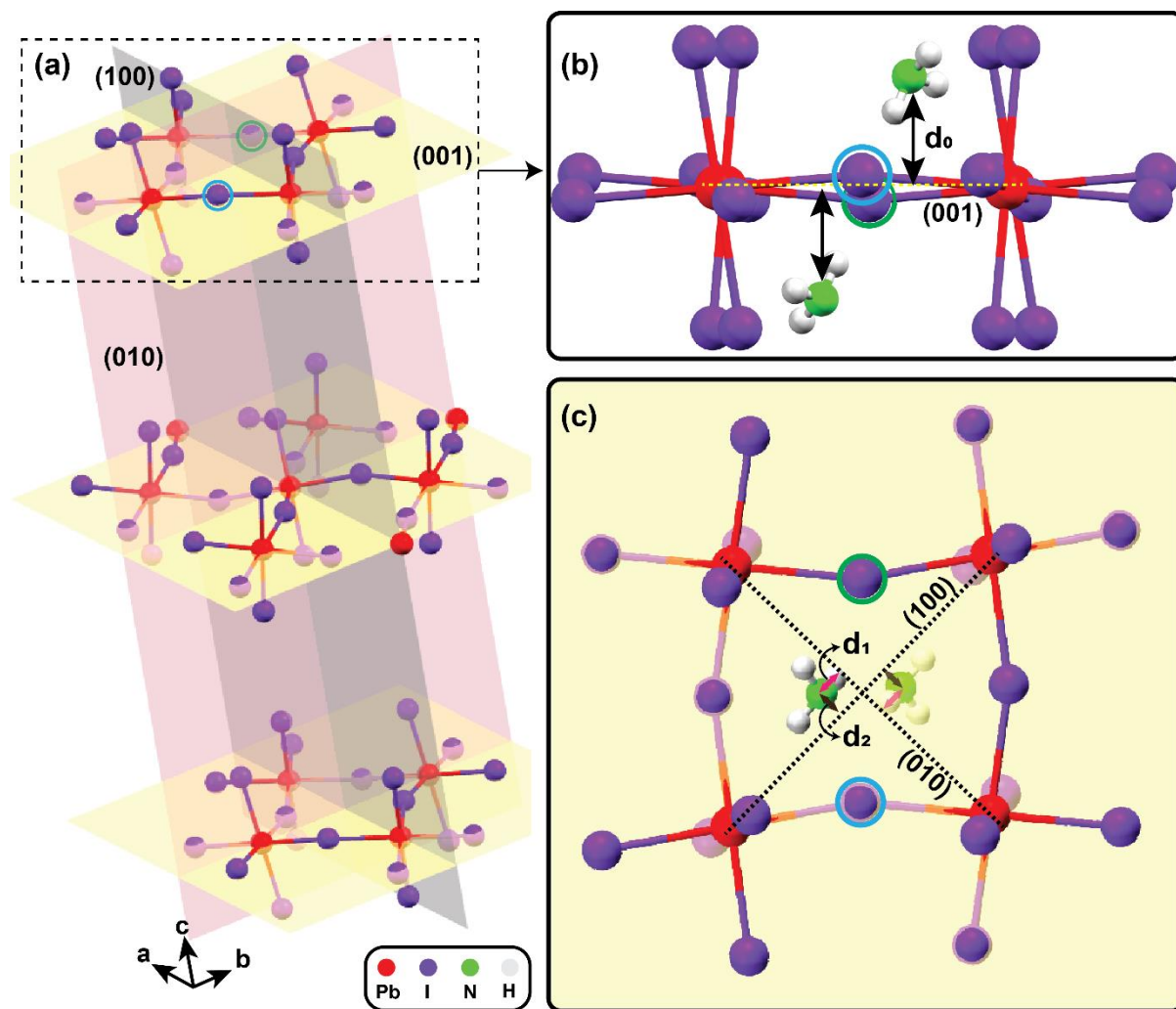


Figure 3.12. Defining structural parameters to indicate the position of $-\text{NH}_3$ group of $(\text{I}(\text{CH}_2)_6\text{-NH}_3)_2\text{PbI}_4$ using SCXRD data at 100 K. (a) Yellow-shaded (001), grey-shaded (100), and pink-shaded (010) planes are shown. The organic cations are removed for clarity. Position of the $-\text{NH}_3$ groups with respect to (b) the (001) plane (yellow dashed line), and (c) (100) and (010) planes (black dashed lines). The green and blue rings around two iodine atoms are placed just to track the same iodine atoms when the structure is visualized from different directions across Figure (a-c).

Can these structural parameters (tabulated in Table 3.1) correlate the nature of hydrogen bonding with Pb-I-Pb bond angles? Except for the $n = 6$ composition, all other samples have a similar value of d_0 (~ 2.6 Å). So, the difference in Pb-I-Pb bond angle and, therefore, different

band gaps, between $n = 4$ and $n = 5$ samples, is not contributed by d_0 . Instead, we correlate r with Pb-I-Pb bond angle (Figure 3.13).

Table 3.1: Structural parameters d_0 , d_1 , d_2 and r as defined in Figure 6a and relevant discussion in the manuscript. The structural parameters are obtained from SCXRD data, and define the position of $-\text{NH}_3$ group with respect Pb-I inorganic layer. The structural parameters have been correlated with Pb-I-Pb bond angle in $(\text{I}-(\text{CH}_2)_n\text{-NH}_3)_2\text{PbI}_4$ at 100 K.

n in $\text{I}-(\text{CH}_2)_n\text{-}$ NH_3	Distance of nitrogen from planes (\AA)			$r (= \frac{d_1}{d_2})$	Pb-I-Pb angle (degree)		
	d_0	d_1	d_2		Measured bond angle	In-plane	Out-of- plane
2	2.58	0.97	0.21	4.58	147.2 ± 0.1	157.2 ± 0.1	155.8 ± 0.2
3	2.62	0.88	0.45	1.93	148.5 ± 0.2	155.9 ± 0.2	159.2 ± 0.5
4	2.63	0.67	0.11	6.35	146.6 ± 0.1	153.8 ± 0.1	158.6 ± 0.2
5	2.6	0.66	0.61	1.07	153.7 ± 2.2	153.8 ± 0.1	178.6 ± 4.9
6	2.47	0.7	0.68	1.03	161.4 ± 0.5	164.2 ± 0.3	170.2 ± 1.0

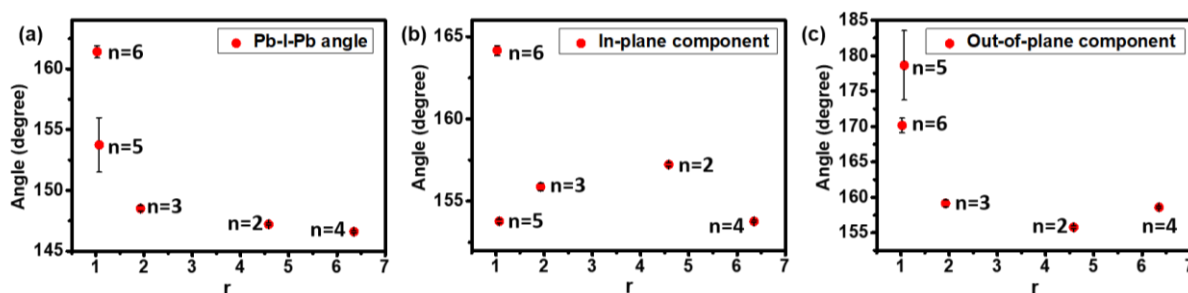


Figure 3.13: Variation of (a) the Pb-I-Pb angle, (b) in-plane component, and (c) out-of-plane component with structural parameter $r = d_1/d_2$. The values of these parameters are also tabulated in Table 3.1.

With increasing r , the angle decreases. Figure 3.14a-b shows the case of $n = 5$ sample, with a low value of $r = 1.1$. As r approaches 1, the $-\text{NH}_3$ group is equidistant from both (100) and (010) Pb-planes (black dashed lines in Figure 3.14a). This enforces the third hydrogen to be equidistant from two bridging iodine atoms, making their interactions symmetric as well, as shown by the blue dashed lines in Figure 3.14b. At this symmetric placement of the $-\text{NH}_3$ groups, both top, and bottom of plane $-\text{NH}_3$ groups impart forces on the bridging I equally,

increasing the in-plane component of Pb-I-Pb bond angle but causes negligible distortion of the out-of-plane component.

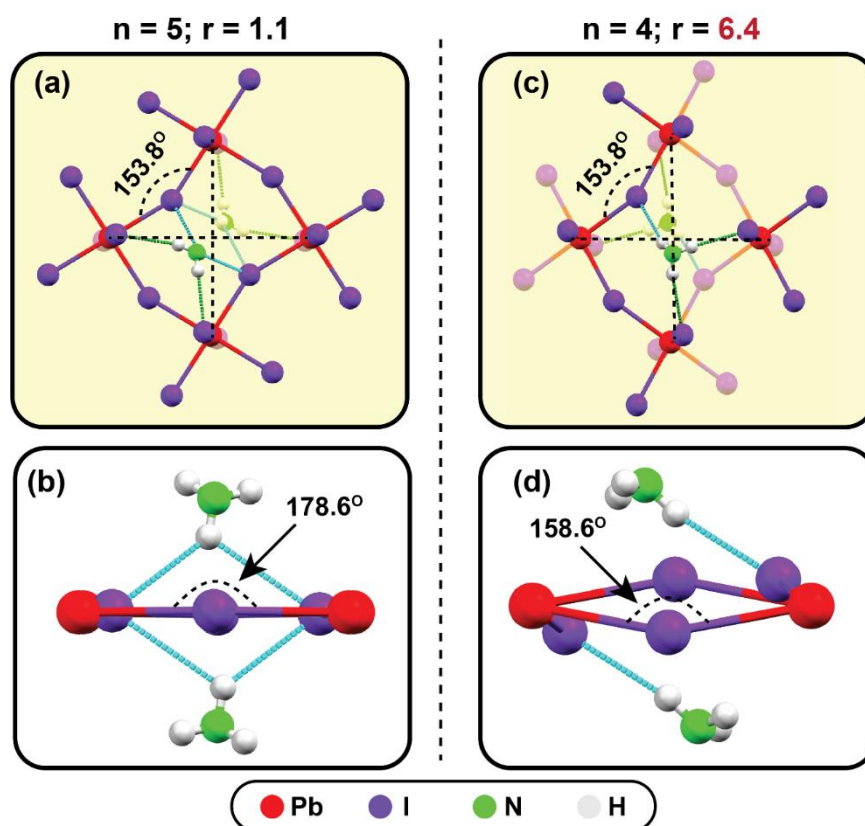


Figure 3.14. N-H...I interactions in $(\text{I}-(\text{CH}_2)_n\text{-NH}_3)_2\text{PbI}_4$ ($n = 4, 5$) crystals at 100 K; (a-b) for $n = 5$, and (c-d) for $n = 4$. Except for NH_3 , the rest of the organic cation has been removed for clarity. (a, c) show the in-plane components, and (b, d) show the out-of-plane component of the Pb-I-Pb bond angle.

On the other hand, the $n = 4$ sample shows a high value of $r = 6.4$ (Figure 3.14 c-d). The placement of the $-\text{NH}_3$ group becomes asymmetric with increasing r . In Figure 3.14c-d, the magnitude of the attractive force from a single asymmetrically placed NH_3 group is almost equal to that in Figure 3.14a-b with two symmetrically placed $-\text{NH}_3$ groups. This is evident by the same in-plane component for $n = 4$ and 5. However, since the $-\text{NH}_3$ group is asymmetric for $n = 4$, the iodines do not experience the same magnitude of attraction from the top and bottom of the Pb-I plane. Thus, in this case, both in-plane and out-of-plane components decrease, causing a large overall deviation of the Pb-I-Pb angle, thereby increasing the band gap. Overall, samples with $n = 2-4$ show higher values of $r (>2)$, introducing asymmetry in

hydrogen bonding interactions, which in turn decreases the Pb-I-Pb bond angle, increasing the band gap. For samples with $n = 5-6$, r values approach 1 exhibiting more symmetric hydrogen bonding and higher Pb-I-Pb bond angles, with reduced band gap.

3.4 Conclusions

We have explored the influence of the iodine-iodine interactions and hydrogen bond on the structure and optical properties in 2D layered hybrid $(\text{I}-(\text{CH}_2)_n\text{-NH}_3)_2\text{PbI}_4$ ($n = 2-6$) perovskites. For that, we synthesized the single crystals and measured SCXRD and PL over a wide temperature range. Interestingly, all the samples ($n = 2-6$) do not undergo a structural phase transition in the wide temperature window of 10-300 K due to the additional iodine-iodine interaction. This observation is unusual since the layered perovskites with non-halogenated monovalent A-site cations typically undergo structural phase transitions in such temperature window. However, similar to $(\text{H}-(\text{CH}_2)_n\text{-NH}_3)_2\text{PbI}_4$, $(\text{I}-(\text{CH}_2)_n\text{-NH}_3)_2\text{PbI}_4$ also show interesting excitonic absorption and emission properties. Therefore, the enhanced structural rigidity of $(\text{I}-(\text{CH}_2)_n\text{-NH}_3)_2\text{PbI}_4$ might be useful for optical and optoelectronic applications where low-temperature stability is critical. On the other hand, the change in the orientation of the organic cation on increasing carbon number (n) in the $\text{I}-(\text{CH}_2)_n\text{-NH}_3^+$ backbone causes a change in the optical band gap. This band gap change is mainly attributed to the change in the position of the $-\text{NH}_3$ group, defined by our structural parameter r . Lower values of r (≈ 1) yield more symmetric hydrogen bonding interactions and lower band gap. Overall, we envisage that the halogen bonding interactions, like iodine-iodine interactions in $(\text{I}-(\text{CH}_2)_n\text{-NH}_3)_2\text{PbI}_4$, is a useful strategy to enhance structural stability of metal halide perovskite materials and devices, without compromising their optical and optoelectronic properties.

Table 3.2: Crystallographic data for (I-(CH₂)_n-NH₃)₂PbI₄ with n = 4.

Chemical formula	C ₈ H ₂₂ I ₂ N ₂ Pb		C ₈ H ₂₂ I ₂ N ₂ Pb	
Formula weight	1114.86 g/mol		1114.86 g/mol	
Temperature	100(2) K		296(2) K	
Wavelength	0.71073 Å		0.71073 Å	
Crystal system	monoclinic		monoclinic	
Space group	P 1 21/c 1		P 1 21/c 1	
Unit cell dimensions	a = 15.3387(6) Å	α = 90°	a = 15.439(6) Å	α = 90°
	b = 8.1956(3) Å	β = 91.7900(10)°	b = 8.398(4) Å	β = 92.170(12)°
	c = 9.0425(3) Å	γ = 90°	c = 9.018(3) Å	γ = 90°
Volume	1136.18(7) Å ³		1168.4(8) Å ³	
Z	2		2	
Density (calculated)	3.259 g/cm ³		3.169 g/cm ³	
Absorption coefficient	15.565 mm ⁻¹		15.136 mm ⁻¹	
F(000)	968		968	
Theta range for data collection	2.66 to 24.71°		2.64 to 32.10°	
Index ranges	-18 ≤ h ≤ 18, -9 ≤ k ≤ 9, -10 ≤ l ≤ 10		-22 ≤ h ≤ 22, -12 ≤ k ≤ 12, -13 ≤ l ≤ 8	
Reflections collected	19632		21762	
Independent reflections	1944 [R(int) = 0.0303]		3735 [R(int) = 0.0416]	
Coverage of independent reflections	99.90%		91.30%	
Absorption correction	Multi-Scan		Multi-Scan	
Structure solution technique	direct methods		direct methods	
Structure solution program	SHELXT 2014/5 (Sheldrick, 2014)		SHELXT 2014/5 (Sheldrick, 2014)	
Refinement method	Full-matrix least-squares on F ²		Full-matrix least-squares on F ²	
Refinement program	SHELXL-2017/1 (Sheldrick, 2017)		SHELXL-2018/3 (Sheldrick, 2018)	
Function minimized	Σ w(F _o ² - F _c ²) ²		Σ w(F _o ² - F _c ²) ²	
Data / restraints / parameters	1944 / 0 / 82		3735 / 0 / 82	
Goodness-of-fit on F ²	0.826		0.801	
Δ/σ _{max}	0.002		0.005	
Final R indices	1911 data; I > 2σ(I)	R1 = 0.0135, wR2 = 0.0334	3256 data; I > 2σ(I)	R1 = 0.0365, wR2 = 0.0885
	all data	R1 = 0.0141, wR2 = 0.0337	all data	R1 = 0.0436, wR2 = 0.0930
Weighting scheme	w=1/[σ ² (F _o ²)+(0.0100P) ² +0.6000P] where P=(F _o ² +2F _c ²)/3		w=1/[σ ² (F _o ²)+(0.0400P) ² +1.0840P] where P=(F _o ² +2F _c ²)/3	
Largest diff. peak and hole	0.083 and -0.112 eÅ ⁻³		0.346 and -0.438 eÅ ⁻³	
R.M.S. deviation from mean	0.027 eÅ ⁻³		0.076 eÅ ⁻³	

Table 3.3: Crystallographic data for (I-(CH₂)_n-NH₃)₂PbI₄ with n = 2.

Chemical formula	C ₄ H ₁₄ I ₆ N ₂ Pb	
Formula weight	1058.76 g/mol	
Temperature	100(2) K	
Wavelength	0.71073 Å	
Crystal system	monoclinic	
Space group	P 1 21/c 1	
Unit cell dimensions	a = 12.5133(8) Å	α = 90°
	b = 8.7825(5) Å	β = 98.028(2)°
	c = 8.6180(5) Å	γ = 90°
Volume	937.82(10) Å ³	
Z	2	
Density (calculated)	3.749 g/cm ³	
Absorption coefficient	18.847 mm ⁻¹	
F(000)	904	
Theta range for data collection	2.84 to 28.34°	
Index ranges	-16 ≤ h ≤ 16, -11 ≤ k ≤ 11, -11 ≤ l ≤ 9	
Reflections collected	15544	
Independent reflections	2335 [R(int) = 0.0470]	
Coverage of independent reflections	99.50%	
Absorption correction	Multi-Scan	
Structure solution technique	direct methods	
Structure solution program	SHELXT 2014/5 (Sheldrick, 2014)	
Refinement method	Full-matrix least-squares on F ²	
Refinement program	SHELXL-2018/3 (Sheldrick, 2018)	
Function minimized	Σ w(F _o ² - F _c ²) ²	
Data / restraints / parameters	2335 / 0 / 64	
Goodness-of-fit on F ²	0.763	
Δ/σ _{max}	0.062	
Final R indices	2264 data; I > 2σ(I)	R1 = 0.0287, wR2 = 0.0934
	all data	R1 = 0.0298, wR2 = 0.0953
Weighting scheme	w = 1/[σ ² (F _o ²) + (0.1000P) ² + 3.6000P] where P = (F _o ² + 2F _c ²)/3	
Largest diff. peak and hole	0.999 and -1.705 eÅ ⁻³	
R.M.S. deviation from mean	0.271 eÅ ⁻³	

Table 3.4: Crystallographic data for (I-(CH₂)_n-NH₃)₂PbI₄ with n = 3.

Chemical formula	C ₆ H ₁₈ I ₆ N ₂ Pb		C ₆ H ₁₈ I ₆ N ₂ Pb	
Formula weight	1086.81 g/mol		1086.81 g/mol	
Temperature	100(2) K		296(2) K	
Wavelength	0.71073 Å		0.71073 Å	
Crystal system	monoclinic		monoclinic	
Space group	P 1 21/c 1		P 1 21/c 1	
Unit cell dimensions	a = 13.991(4) Å	α = 90°	a = 14.276(5) Å	α = 90°
	b = 9.024(2) Å	β = 99.255(7)°	b = 8.892(3) Å	β = 99.766(17)°
	c = 8.463(2) Å	γ = 90°	c = 8.563(3) Å	γ = 90°
Volume	1054.6(5) Å ³		1071.3(7) Å ³	
Z	2		2	
Density (calculated)	3.422 g/cm ³		3.369 g/cm ³	
Absorption coefficient	16.764 mm ⁻¹		16.504 mm ⁻¹	
F(000)	936		936	
Theta range for data collection	4.18 to 26.36°		2.71 to 26.49°	
Index ranges	-17<=h<=17, -11<=k<=11, -10<=l<=10		-17<=h<=17, -9<=k<=11, -10<=l<=10	
Reflections collected	12328		16986	
Independent reflections	2154 [R(int) = 0.0784]		2192 [R(int) = 0.0784]	
Coverage of independent reflections	99.60%		98.80%	
Absorption correction	Multi-Scan		Multi-Scan	
Structure solution technique	direct methods		direct methods	
Structure solution program	SHELXT 2014/5 (Sheldrick, 2014)		SHELXT 2014/5 (Sheldrick, 2014)	
Refinement method	Full-matrix least-squares on F ²		Full-matrix least-squares on F ²	
Refinement program	SHELXL-2018/3 (Sheldrick, 2018)		SHELXL-2018/3 (Sheldrick, 2018)	
Function minimized	Σ w(F _o ² - F _c ²) ²		Σ w(F _o ² - F _c ²) ²	
Data / restraints / parameters	2154 / 0 / 73		2192 / 0 / 71	
Goodness-of-fit on F ²	0.717		1.240	
Δ/σ _{max}	0.007		0.000	
Final R indices	2071 data; I>2σ(I)	R1 = 0.0421, wR2 = 0.0979	1975 data; I>2σ(I)	R1 = 0.0401, wR2 = 0.1376
	all data	R1 = 0.0436, wR2 = 0.0990	all data	R1 = 0.0454, wR2 = 0.1464
Weighting scheme	w=1/[σ ² (F _o ²)+(0.0100P) ² +5.5000P] where P=(F _o ² +2F _c ²)/3		w=1/[σ ² (F _o ²)+(0.0100P) ²] where P=(F _o ² +2F _c ²)/3	
Largest diff. peak and hole	0.335 and -0.419 eÅ ⁻³		1.460 and -2.028 eÅ ⁻³	
R.M.S. deviation from mean	0.079 eÅ ⁻³		0.283 eÅ ⁻³	

Table 3.5: Crystallographic data for (I-(CH₂)_n-NH₃)₂PbI₄ with n = 5.

Chemical formula	C ₁₀ H ₂₆ I ₆ N ₂ Pb	
Formula weight	1142.92 g/mol	
Temperature	100(2) K	
Wavelength	0.71073 Å	
Crystal system	monoclinic	
Space group	P 1 21/c 1	
Unit cell dimensions	a = 16.230(3) Å	α = 90°
	b = 8.8550(15) Å	β = 90.211(4)°
	c = 8.5953(14) Å	γ = 90°
Volume	1235.3(4) Å ³	
Z	2	
Density (calculated)	3.073 g/cm ³	
Absorption coefficient	14.321 mm ⁻¹	
F(000)	1000	
Theta range for data collection	2.30 to 28.17°	
Index ranges	-21 ≤ h ≤ 21, -11 ≤ k ≤ 10, -11 ≤ l ≤ 11	
Reflections collected	17069	
Independent reflections	3015 [R(int) = 0.0869]	
Coverage of independent reflections	99.30%	
Absorption correction	Multi-Scan	
Structure solution technique	direct methods	
Structure solution program	SHELXT 2014/5 (Sheldrick, 2014)	
Refinement method	Full-matrix least-squares on F ²	
Refinement program	SHELXL-2018/3 (Sheldrick, 2018)	
Function minimized	Σ w(F _o ² - F _c ²) ²	
Data / restraints / parameters	3015 / 0 / 83	
Goodness-of-fit on F ²	0.813	
Δ/σ _{max}	0.014	
Final R indices	2720 data; I > 2σ(I)	R1 = 0.0410, wR2 = 0.0979
	all data	R1 = 0.0498, wR2 = 0.1046
Weighting scheme	w = 1/[σ ² (F _o ²) + 0.1000P] where P = (F _o ² + 2F _c ²)/3	
Largest diff. peak and hole	0.087 and -0.068 eÅ ⁻³	
R.M.S. deviation from mean	0.012 eÅ ⁻³	

Table 3.6: Crystallographic data for (I-(CH₂)_n-NH₃)₂PbI₄ with n = 6.

Chemical formula	C ₁₂ H ₃₀ I ₆ N ₂ Pb	
Formula weight	1170.97 g/mol	
Temperature	100(2) K	
Wavelength	0.71073 Å	
Crystal system	orthorhombic	
Space group	P b c a	
Unit cell dimensions	a = 9.2624(13) Å	α = 90°
	b = 8.8305(12) Å	β = 90°
	c = 31.368(5) Å	γ = 90°
Volume	2565.6(7) Å ³	
Z	4	
Density (calculated)	3.031 g/cm ³	
Absorption coefficient	13.794 mm ⁻¹	
F(000)	2064	
Theta range for data collection	2.55 to 24.71°	
Index ranges	-10 ≤ h ≤ 10, -9 ≤ k ≤ 10, -36 ≤ l ≤ 36	
Reflections collected	11318	
Independent reflections	2171 [R(int) = 0.1148]	
Coverage of independent reflections	97.40%	
Absorption correction	Multi-Scan	
Structure solution technique	direct methods	
Structure solution program	SHELXT 2014/5 (Sheldrick, 2014)	
Refinement method	Full-matrix least-squares on F ²	
Refinement program	SHELXL-2018/3 (Sheldrick, 2018)	
Function minimized	Σ w(Fo ² - Fc ²) ²	
Data / restraints / parameters	2171 / 0 / 100	
Goodness-of-fit on F ²	0.970	
Δ/σ _{max}	0.009	
Final R indices	1966 data; I > 2σ(I)	R1 = 0.0564, wR2 = 0.1458
	all data	R1 = 0.0607, wR2 = 0.1512
Weighting scheme	w = 1/[σ ² (Fo ²) + (0.1000P) ²] where P = (Fo ² + 2Fc ²)/3	
Largest diff. peak and hole	0.433 and -0.372 e ⁻ Å ⁻³	
R.M.S. deviation from mean	0.079 e ⁻ Å ⁻³	

3.5 References

- (1) Lemmerer, A.; Billing, D. G. Effect of Heteroatoms in the Inorganic–organic Layered Perovskite-type Hybrids $[(ZC_nH_{2n}NH_3)_2PbI_4]$, $n = 2, 3, 4, 5, 6$; $Z = OH, Br$ and I ; and $[(H_3NC_2H_4S_2C_2H_4NH_3)PbI_4]$. *CrystEngComm* **2010**, *12*, 1290-1301.
- (2) Smith, M. D.; Pedesseau, L.; Kepenekian, M.; Smith, I. C.; Katan, C.; Even, J.; Karunadasa, H. I. Decreasing the Electronic Confinement in Layered Perovskites through Intercalation. *Chem. Sci.* **2017**, *8*, 1960-1968.
- (3) Sourisseau, S.; Louvain, N.; Bi, W.; Mercier, N.; Rondeau, D.; Boucher, F.; Buzaré, J.-Y.; Legein, C. Reduced Band Gap Hybrid Perovskites Resulting from Combined Hydrogen and Halogen Bonding at the Organic-Inorganic Interface. *Chem. Mater.* **2007**, *19*, 600-607.
- (4) Robertson, C. C.; Wright, J. S.; Carrington, E. J.; Perutz, R. N.; Hunter, C. A.; Brammer, L. Hydrogen Bonding vs. Halogen Bonding: the Solvent Decides. *Chem. Sci.* **2017**, *8*, 5392-5398.
- (5) Muljarov, E. A.; Tikhodeev, S. G.; Gippius, N. A.; Ishihara, T. Excitons in Self-organized Semiconductor/Insulator Superlattices: PbI-based Perovskite Compounds. *Phys. Rev. B Condens. Matter* **1995**, *51*, 14370-14378.
- (6) Katan, C.; Mercier, N.; Even, J. Quantum and Dielectric Confinement Effects in Lower-Dimensional Hybrid Perovskite Semiconductors. *Chem. Rev.* **2019**, *119*, 3140-3192.
- (7) Dey, A.; Ye, J.; De, A.; Debroye, E.; Ha, S. K.; Bladt, E.; Kshirsagar, A. S.; Wang, Z.; Yin, J.; Wang, Y., et al. State of the Art and Prospects for Halide Perovskite Nanocrystals. *ACS Nano* **2021**, *15*, 10775-10981.
- (8) Kennard, R. M.; Dahlman, C. J.; Chung, J.; Cotts, B. L.; Mikhailovsky, A. A.; Mao, L.; DeCrescent, R. A.; Stone, K. H.; Venkatesan, N. R.; Mohtashami, Y., et al. Growth-Controlled Broad Emission in Phase-Pure Two-Dimensional Hybrid Perovskite Films. *Chem. Mater.* **2021**, *33*, 7290-7300.

- (9) Kim, Y.-H.; Zhai, Y.; Lu, H.; Pan, X.; Xiao, C.; Gauding, E. A.; Harvey, S. P.; Berry, J. J.; Vardeny, Z. V.; Luther, J. M., et al. Chiral-induced Spin Selectivity Enables a Room-temperature Spin Light-emitting Diode. *Science* **2021**, *371*, 1129-1133.
- (10) Ishihara, T.; Takahashi, J.; Goto, T. Exciton State in Two-dimensional Perovskite Semiconductor $(\text{C}_{10}\text{H}_{21}\text{NH}_3)_2\text{PbI}_4$. *Solid State Commun.* **1989**, *69*, 933-936.
- (11) Chakraborty, R.; Nag, A. Correlation of Dielectric Confinement and Excitonic Binding Energy in 2D Layered Hybrid Perovskites Using Temperature Dependent Photoluminescence. *J. Phys. Chem. C* **2020**, *124*, 16177-16185.
- (12) Passarelli, J. V.; Mauck, C. M.; Winslow, S. W.; Perkinson, C. F.; Bard, J. C.; Sai, H.; Williams, K. W.; Narayanan, A.; Fairfield, D. J.; Hendricks, M. P., et al. Tunable Exciton Binding Energy in 2D Hybrid Layered Perovskites through Donor-acceptor Interactions within the Organic Layer. *Nat. Chem.* **2020**, *12*, 672-682.
- (13) Knutson, J. L.; Martin, J. D.; Mitzi, D. B. Tuning the Band Gap in Hybrid Tin Iodide Perovskite Semiconductors Using Structural Templating. *Inorg. Chem.* **2005**, *44*, 4699-4705.
- (14) Smith, M. D.; Connor, B. A.; Karunadasa, H. I. Tuning the Luminescence of Layered Halide Perovskites. *Chem. Rev.* **2019**, *119*, 3104-3139.
- (15) Zhang, C.; Kuang, D.-B.; Wu, W.-Q. A Review of Diverse Halide Perovskite Morphologies for Efficient Optoelectronic Applications. *Small Methods* **2020**, *4*, 1900662.
- (16) Li, X.; Hoffman, J. M.; Kanatzidis, M. G. The 2D Halide Perovskite Rulebook: How the Spacer Influences Everything from the Structure to Optoelectronic Device Efficiency. *Chem. Rev.* **2021**, *121*, 2230–2291.
- (17) Chakraborty, R.; Nag, A. Dielectric Confinement for Designing Compositions and Optoelectronic Properties of 2D Layered Hybrid Perovskites. *Phys. Chem. Chem. Phys.* **2021**, *23*, 82-93.

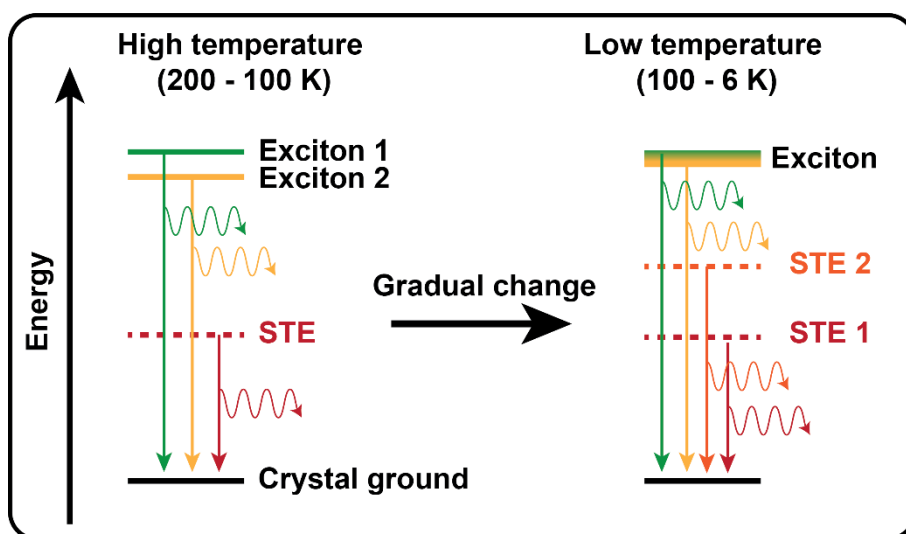
- (18) Tremblay, M.-H.; Bacsá, J.; Zhao, B.; Pulvirenti, F.; Barlow, S.; Marder, S. R. Structures of $(4-Y-C_6H_4CH_2NH_3)_2PbI_4$ {Y = H, F, Cl, Br, I}: Tuning of Hybrid Organic Inorganic Perovskite Structures from Ruddlesden–Popper to Dion–Jacobson Limits. *Chem. Mater.* **2019**, *31*, 6145-6153.
- (19) Stoumpos, C. C.; Cao, D. H.; Clark, D. J.; Young, J.; Rondinelli, J. M.; Jang, J. I.; Hupp, J. T.; Kanatzidis, M. G. Ruddlesden–Popper Hybrid Lead Iodide Perovskite 2D Homologous Semiconductors. *Chem. Mater.* **2016**, *28*, 2852-2867.
- (20) Eickhoff, T.; Grosse, P.; Theiss, W. Diffuse Reflectance Spectroscopy of Powders. *Vib. Spectrosc.* **1990**, *1*, 229-233.
- (21) Billing, D. G.; Lemmerer, A. Synthesis, Characterization and Phase Transitions in the Inorganic-organic Layered Perovskite-type Hybrids $[(C_nH_{2n+1}NH_3)_2PbI_4]$, $n = 4, 5$ and 6 . *Acta Cryst. B* **2007**, *63*, 735-747.
- (22) Sheikh, T.; Shinde, A.; Mahamuni, S.; Nag, A. Possible Dual Bandgap in $(C_4H_9NH_3)_2PbI_4$ 2D Layered Perovskite: Single-Crystal and Exfoliated Few-Layer. *ACS Energy Lett.* **2018**, *3*, 2940-2946.
- (23) Cavallo, G.; Metrangolo, P.; Milani, R.; Pilati, T.; Priimagi, A.; Resnati, G.; Terraneo, G. The Halogen Bond. *Chem. Rev.* **2016**, *116*, 2478-2601.
- (24) He, Y.; Zhang, J.; Lei, L.; Kong, W. Self-Assembly of Iodine in Superfluid Helium Droplets: Halogen Bonds and Nanocrystals. *Angew. Chem. Int. Ed.* **2017**, *56*, 3541-3545.
- (25) Mitzi, D. B. Synthesis, Crystal Structure, and Optical and Thermal Properties of $(C_4H_9NH_3)_2MI_4$ (M = Ge, Sn, Pb). *Chem. Mater.* **1996**, *8*, 791-800.
- (26) Nawale, V. V.; Sheikh, T.; Nag, A. Dual Excitonic Emission in Hybrid 2D Layered Tin Iodide Perovskites. *J. Phys. Chem. C* **2020**, *124*, 21129-21136.

- (27) DeCrescent, R. A.; Du, X.; Kennard, R. M.; Venkatesan, N. R.; Dahlman, C. J.; Chabinyo, M. L.; Schuller, J. A. Even-Parity Self-Trapped Excitons Lead to Magnetic Dipole Radiation in Two-Dimensional Lead Halide Perovskites. *ACS Nano* **2020**, *14*, 8958-8968.
- (28) Sheikh, T.; Nawale, V.; Pathoor, N.; Phadnis, C.; Chowdhury, A.; Nag, A. Molecular Intercalation and Electronic Two Dimensionality in Layered Hybrid Perovskites. *Angew. Chem. Int. Ed.* **2020**, *59*, 11653-11659.
- (29) Wang, K.; Wu, C.; Jiang, Y.; Yang, D.; Wang, K.; Priya, S. Distinct conducting layer edge states in two-dimensional (2D) halide perovskite. *Sci. Adv.* **2019**, *5* : eaau3241.
- (30) Yin, J.; Naphade, R.; Maity, P.; Gutiérrez-Arzaluz, L.; Almalawi, D.; Roqan, I. S.; Brédas, J.-L.; Bakr, O. M.; Mohammed, O. F. Manipulation of Hot Carrier Cooling Dynamics in Two-dimensional Dion–Jacobson Hybrid Perovskites via Rashba Band Splitting. *Nat. Commun.* **2021**, *12*, 3995.
- (31) Kamminga, M. E.; de Wijs, G. A.; Havenith, R. W. A.; Blake, G. R.; Palstra, T. T. M. The Role of Connectivity on Electronic Properties of Lead Iodide Perovskite-Derived Compounds. *Inorg. Chem.* **2017**, *56*, 8408-8414.
- (32) Dohner, E. R.; Jaffe, A.; Bradshaw, L. R.; Karunadasa, H. I. Intrinsic White-Light Emission from Layered Hybrid Perovskites. *J. Am. Chem. Soc.* **2014**, *136*, 13154-13157.
- (33) Paritmongkol, W.; Powers, E. R.; Dahod, N. S.; Tisdale, W. A. Two Origins of Broadband Emission in Multilayered 2D Lead Iodide Perovskites. *J. Phys. Chem. Lett.* **2020**, *11*, 8565-8572.
- (34) Li, X.; Ke, W.; Traoré, B.; Guo, P.; Hadar, I.; Kepenekian, M.; Even, J.; Katan, C.; Stoumpos, C. C.; Schaller, R. D.; Kanatzidis, M. G. Two-Dimensional Dion–Jacobson Hybrid Lead Iodide Perovskites with Aromatic Diammonium Cations. *J. Am. Chem. Soc.* **2019**, *141*, 12880-12890.

- (35) Acharyya, P.; Ghosh, T.; Pal, K.; Kundu, K.; Singh Rana, K.; Pandey, J.; Soni, A.; Waghmare, U. V.; Biswas, K. Intrinsically Ultralow Thermal Conductivity in Ruddlesden–Popper 2D Perovskite $\text{Cs}_2\text{PbI}_2\text{Cl}_2$: Localized Anharmonic Vibrations and Dynamic Octahedral Distortions. *J. Am. Chem. Soc.* **2020**, *142*, 15595-15603.
- (36) Mao, L.; Ke, W.; Pedesseau, L.; Wu, Y.; Katan, C.; Even, J.; Wasielewski, M. R.; Stoumpos, C. C.; Kanatzidis, M. G. Hybrid Dion–Jacobson 2D Lead Iodide Perovskites. *J. Am. Chem. Soc.* **2018**, *140*, 3775-3783.
- (37) Kim, J.; Cho, S.; Dinic, F.; Choi, J.; Choi, C.; Jeong, S. M.; Lee, J.-S.; Voznyy, O.; Ko, M. J.; Kim, Y. Hydrophobic Stabilizer-anchored Fully Inorganic Perovskite Quantum Dots Enhance Moisture Resistance and Photovoltaic Performance. *Nano Energy* **2020**, *75*, 104985.
- (38) Sheikh, T.; Maqbool, S.; Mandal, P.; Nag, A. Introducing Intermolecular Cation- π Interactions for Water-Stable Low Dimensional Hybrid Lead Halide Perovskites. *Angew. Chem. Int. Ed.* **2021**, *60*, 18265-18271.
- (39) Du, K.-z.; Tu, Q.; Zhang, X.; Han, Q.; Liu, J.; Zauscher, S.; Mitzi, D. B. Two-Dimensional Lead(II) Halide-Based Hybrid Perovskites Templated by Acene Alkylamines: Crystal Structures, Optical Properties, and Piezoelectricity. *Inorg. Chem.* **2017**, *56*, 9291-9302.
- (40) Smith, M. D.; Jaffe, A.; Dohner, E. R.; Lindenberg, A. M.; Karunadasa, H. I. Structural Origins of Broadband Emission from Layered Pb–Br Hybrid Perovskites. *Chem. Sci.* **2017**, *8*, 4497-4504.

CHAPTER 4

Two Self-Trapped Excitonic Emission in 2D Hybrid Lead Iodide Perovskite Single Crystals



Abstract

The radiative recombination of self-trapped excitons (STEs) and the consequent ultra-broad emission in 2D layered hybrid halide perovskites is interesting, but poorly understood phenomena. Among these, the luminescence behaviour of STEs in the iodide-based compositions remains little explored. Here, we use single crystalline samples of two different phases of 2D hybrid lead iodide perovskite – namely, Ruddlesden-Popper, and Dion-Jacobsen phases – to investigate the sensitization mechanism of the STE emission. Using temperature-dependent photoluminescence spectroscopy, in both samples, we find the presence of not one, but two distinctly different broad emissive states at lower temperatures, presumably arising from two different STEs. The excitation mechanisms and PL lifetimes of the two states suggest that they possibly originate at very different crystal environments.

4.1 Introduction

Layered hybrid perovskites like A_2PbX_4 ($X = Cl, Br$; $A =$ organic ammonium cation) show interesting optical properties including broadband emission. The appearance of ultra-broad emission spanning the entire visible spectrum with negligible self-absorption, makes them potential candidates for application as white light phosphor converted light emitting diodes.¹⁻³ However, the broad emission for compositions with $X = I$ is less explored, possibly because in most compositions the emission appears at temperatures below the room temperature.⁴ In this chapter, using temperature-dependent luminescence spectroscopy, we elucidate the nature and excitation mechanism of broadband emission in layered hybrid perovskite single crystals with $X = I$, and different A-site cations.

The A_nPbI_4 ($n = 1$ or 2) hybrid perovskite structure is similar as that of A_2PbX_4 with $X = Cl$ and Br . The structure consists layers of connected corner-shared $Pb-I$ octahedra with A-site cations in between. They show 2D electronic structure with electron and holes confined in the atomically thin $Pb-I$ layers. Consequently, a high exciton binding energy with promising light-emission applications are observed.⁵⁻⁷ Though the optical properties originate from the orbital interactions in the $Pb-I$ layers, the choice of the A-site cation has a direct influence on the excitons through dielectric confinement.⁸⁻¹¹ Importantly, A-site cation plays a crucial role in determining the distortions of the layered perovskites, and therefore, indirectly controlling optical properties. In particular, the distortion of the octahedra connecting $Pb-X-Pb$ bond angle within an inorganic layer has been linked with the emergence of the broad emission in chloride and bromide compositions.¹²⁻¹⁵

The broad emissions have been hypothesized to be arising from radiative recombination of self-trapped excitons (STEs) along with possible participation of permanent crystal defects (*extrinsic*-STEs).¹⁶⁻²⁰ Self-trapped states are transient states that form due to strong exciton-lattice coupling at the excited state.²¹⁻²⁴ These can be thought of transient crystal distortions induced by the excitons. Further, presence of a permanent crystal defect or lattice distortions

make the formation and stabilization of such STE states much more favourable. When an exciton is trapped in such a state, the excited state energy is red-shifted compared to the free exciton state. Recombination of such trapped excitons generate a very broad emission spectrum due to the participation of the lattice vibronic levels at the excited state.

Single crystals of hybrid layered lead iodide perovskites have not been explored much in the context of STE emission. It has been observed in prior literature that single-crystals have significantly different excitonic emission than films of A_2PbI_4 compositions.²⁵ In particular, single crystals show unique position-dependent PL emission where the edges of the crystals emit and absorb photons at lower energies than the interior of the crystal, seemingly having two different excitonic states.²⁶ The difference in co-ordination environment at the edge and interior of the crystal, is also expected to give rise to different degree of distortions of the Pb-I layer. An obvious question arises: do the two excitonic emissions give rise to different STE states as well?

To answer this question, we study the temperature-dependent luminescence behaviour of monolayered lead iodide perovskite single crystals. Two different families of these materials exist – namely, Ruddlesden-Popper (RP), and Dion-Jacobsen (DJ).^{15,27-29} The crystal structures of RP and DJ differ in the orientation of the alternate Pb-I layers. We chose hexylammonium ($CH_3-(CH_2)_5-NH_3^+$) and 4-(aminomethyl)pipyridinium (4-AMP²⁺) as A-site cations to form RP composition, $((CH_3-(CH_2)_5-NH_3)_2PbI_4$ and DJ composition, $(4-AMP)PbI_4$, respectively. Single crystals for both materials are prepared and their phase purity is analysed by X-ray diffraction measurements. Both steady state and excited state PL have been measured in the temperature range 6 – 300 K. Other than the excitonic emissions, two broad STE peaks are observed at low temperatures for both samples. The PL excitation and decay measurements are used to probe the excitation and recombination mechanisms that suggests the STE peaks possibly originate at different crystal environments.

4.2 Experimental Section

4.2.1 Chemicals. Hydroiodic acid (Sigma Aldrich, HI, 57% w/w in water), lead oxide (Sigma Aldrich, PbO, >99%), hexylamine (Sigma Aldrich, CH₃-(CH₂)₅-NH₂, 99%), 4-(aminomethyl)pyridine (Sigma Aldrich, 99%), hypophosphorus acid (Avra chemicals, H₃PO₂, 50% w/w in water).

4.2.2 Synthesis of (CH₃-(CH₂)₅-NH₃)₂PbI₄ and (4-AMP)PbI₄ single crystals. Crystals of (CH₃-(CH₂)₅-NH₃)₂PbI₄ and (4-AMP)PbI₄ are prepared by acid-precipitation method. Typically, 5 mmol of PbO is dissolved in 30 ml of HI by sonication for 10 minutes at room temperature. Complete dissolution of PbO affords a clear transparent solution. In it 2.5 ml of H₃PO₂ is added. Presence of H₃PO₂ is necessary to inhibit the oxidation of I⁻ to I₃⁻.¹⁵ The solution is then cooled to ~5 °C using an ice-bath. At this temperature, 10 mmol of hexylamine, or 5 mmol of 4-(aminomethyl)pyridine is added dropwise. Addition of the amines makes the solution turbid orange, possibly due to the formation of microcrystalline layered perovskite compositions. The solutions are then taken out of the ice-bath and placed in a silicone oil-bath. The solution is stirred and heated at 95 °C until the solution turns transparent again. Heating and stirring are then stopped, and the solutions are kept undisturbed for 12 hours. By this time, the solution temperature decreases and comes down to room temperature. The cooling affords large millimetre-sized crystals of the layered perovskite compositions. The crystals are isolated from the acid solutions using filtration and dried under nitrogen.

4.2.3 Characterization. PXRD data are collected at room temperature using a Bruker D8 Advance diffractometer in Bragg–Brentano geometry and operating with Cu K α ($\lambda = 1.54 \text{ \AA}$) radiation. Steady-state PL and PL excitation (PLE) spectra are recorded using the FLS 980 spectrophotometer (Edinburgh Instruments). A 405 nm (3.06 eV) picosecond pulsed diode laser is used as the excitation source for recording the PL, and a Xe-lamp is used for recording PL excitation (PLE) spectra. For low-temperature PL measurements, a closed-cycle He-cryostat [Advanced Research Systems; ARS] is used. The single-crystalline samples are placed

in between two sapphire plates [PELCO; 0001 plane cut and double-side polished] that are further placed in a gold-plated sample holder with indium wire as the thermal contact. The sample holder is then mounted on the copper cold-finger and indium foils are used for optimum thermal contact. The sample holder is placed such that the incident beam on the sample and the detected light emission from the sample makes 45° angle on the upper sapphire plate. The time-correlated single photon counting (TCSPC) measurements are done using the 405 nm (3.06 eV) picosecond laser excitation. The radiative lifetimes are fitted with either biexponential or mono-exponential decay functions of the form $I_t = I_{t=0} + \sum_i A_i \times \exp(-t/\tau_i)$. I_t and $I_{t=0}$ are PL intensities at any variable time = t , and time = 0 s, respectively. A_i are amplitudes corresponding lifetime components τ_i ($i = 1$ for mono-exponential, 2 for bi-exponential). The average lifetime (τ_{av}) is calculated using the equation: $\frac{\sum A_i \tau_i^2}{\sum A_i \tau_i}$.

4.3 Results and Discussion

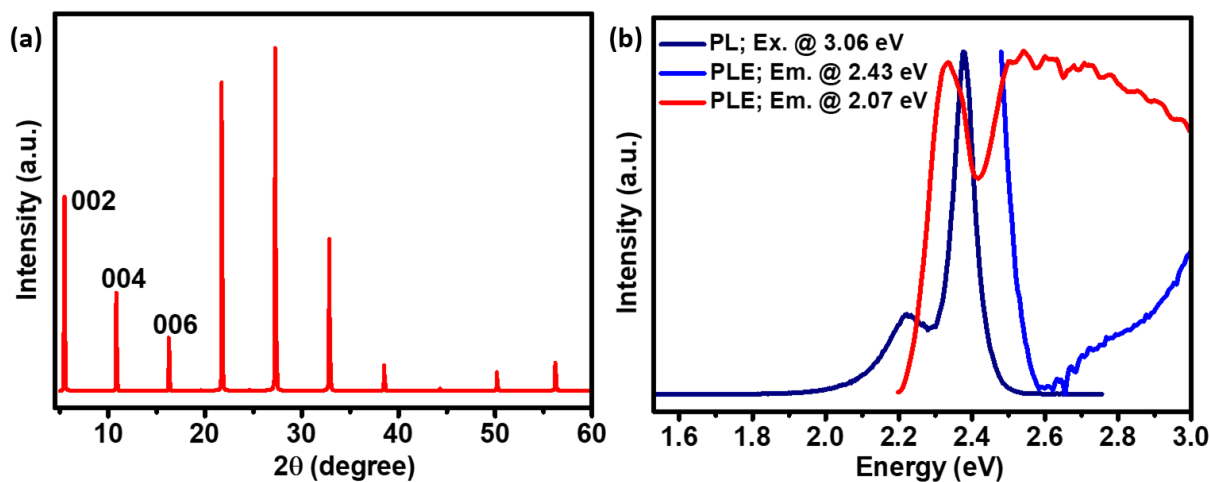


Figure 4.1: (a) PXRD pattern of $(\text{CH}_3-(\text{CH}_2)_5\text{-NH}_3)_2\text{PbI}_4$ single crystals. (b) PL and PL excitation (PLE) recorded from a single crystal of $(\text{CH}_3-(\text{CH}_2)_5\text{-NH}_3)_2\text{PbI}_4$ at room temperature.

Synthesized single crystals were used for all structural and optical analysis. Figure 4.1a shows the PXRD pattern recorded at room temperature from single crystals of $(\text{CH}_3-(\text{CH}_2)_5\text{-NH}_3)_2\text{PbI}_4$. Reported structure from single-crystal X-ray diffraction experiment suggests, in this crystal, the Pb-I layers stack along the c-axis of the unit cell.³⁰ The characteristic (00l)

peaks in the PXRD pattern suggests an interlayer distance of 16.4 Å between the inorganic Pb-I layers, matching with the reported structure. Figure 4.1b shows the PL and PLE recorded from one single crystal at room temperature. The PL spectrum shows two emissions at 2.22 and 2.38 eV. It has previously been shown in prior literature that single crystals of similar layered hybrid lead halide perovskites show such two emission features, and both features have been assigned to excitonic states.^{26, 31, 32} Among these, the higher energy peak (2.38 eV) arises at the interior the Pb-I layers, while the lower energy peak (2.22 eV) arises at the layer edges possibly due to inter-layer interactions.²⁶ Importantly, the lower energy emission is not a consequence of point defects in the crystal.²⁵ PLE recorded at 2.43 eV shows a step-like feature at ~2.7 eV possibly arising at the band edges. The assignment of the band edge in our PLE spectrum agrees with that observed in electroabsorption experiments in prior report.³³ In contrast, the PLE recorded at a lower energy position (2.07 eV) shows a step-like feature at 2.5 eV. The considerable difference in the PLE suggests very different excitation mechanism of the two excitonic emissions. Notably, we do not observe any red-shifted broad emission from these crystals at room temperature.³⁴

Figure 4.2a shows the pseudocolormap of temperature-dependent emission from single-crystalline $(\text{CH}_3-(\text{CH}_2)_5\text{-NH}_3)_2\text{PbI}_4$. The excitonic emission ~2.3 eV is visible at all temperatures in the range 300 – 6 K. Figure 4.2b shows the integrated intensity measured for the excitonic emissions at a few representative temperature points. On decreasing temperature, the intensity steadily increases till 200 K. The increase is due to the reduction of non-radiative recombination at lower temperatures. Figure 4.2c shows the higher energy excitonic peak position at different temperatures. The peak slightly red-shifts with decreasing temperature. This red-shift is due to an increase in the Pb-I-Pb bond angle with decreasing temperature, and subsequent stabilization of the CBM.³⁵ There is no drastic changes in the peak position, suggesting that the sample does not undergo any structural phase transition in the investigated

temperature range. This observation corroborates well with previously reported SCXRD-derived structures at different temperatures.³⁰

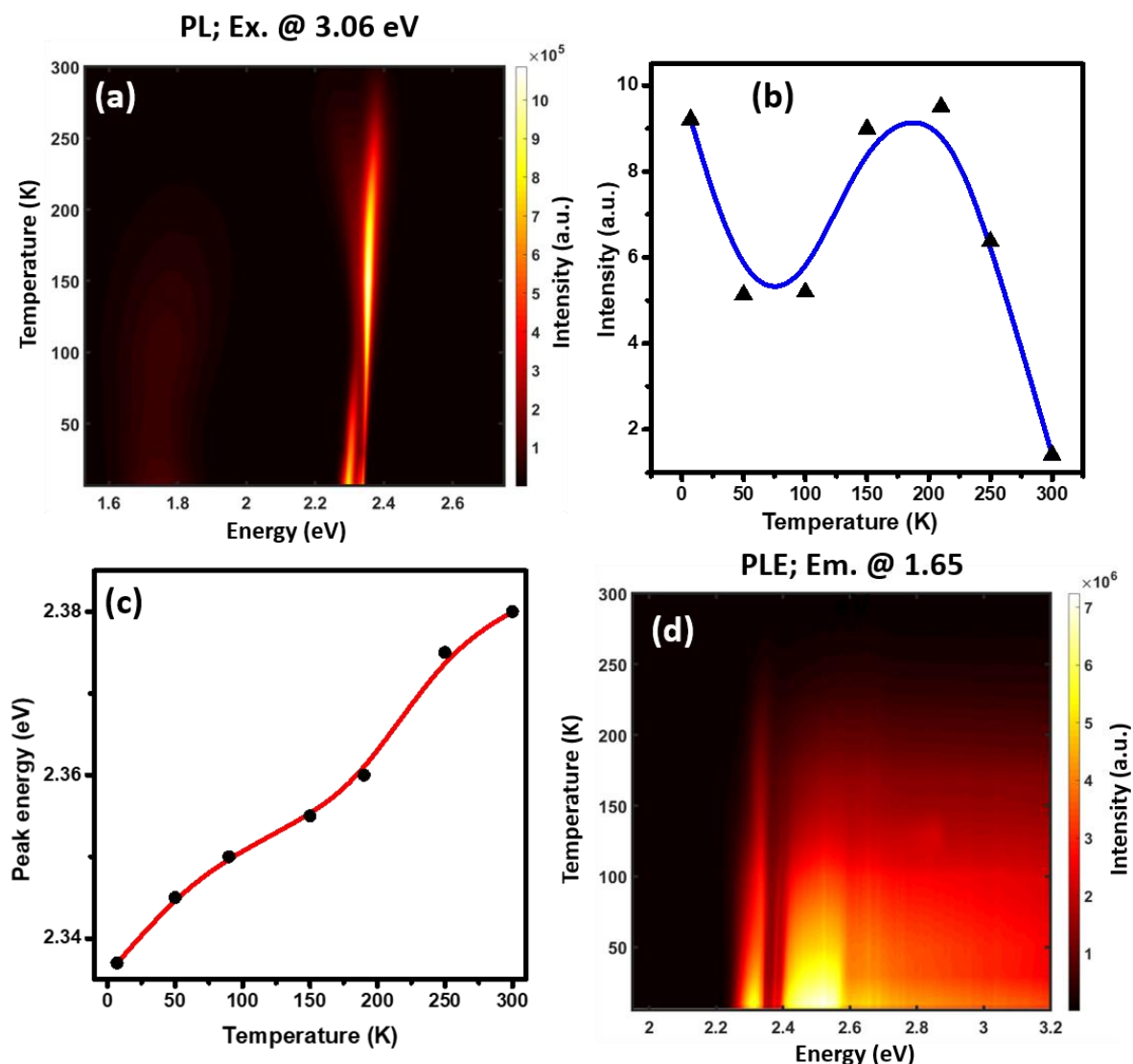


Figure 4.2: Temperature-dependent luminescence properties of $(\text{CH}_3-(\text{CH}_2)_5-\text{NH}_3)_2\text{PbI}_4$ single crystals. (a) Pseudocolormap of PL. (b) Integrated intensity of the excitonic emission. (c) The higher energy excitonic peak position at different temperatures. (d) PLE for emission at 1.65 eV.

The pseudocolormap shows an appearance of a weakly-intense red-shifted broad emission around 200 K with a peak ~ 1.8 eV and full-width-at-half-maxima (fwhm) ~ 200 meV. Similar broad emissions have been a common feature in multiple hybrid layered lead chloride and bromide compositions, and are assigned to the radiative recombination of STEs.^{12, 36} The PLE recorded at this broad emission feature (Figure 4.2d) at different temperatures show strong absorption near 2.3 eV that red-shifts with lowering of temperature, matching with the

behaviour of the excitonic emission in Figure 4.2a. Importantly, we observe negligible absorption at lower energies. Thus, the free exciton resonance is the principal excitation mechanism for the broad emission. The broad emission is probably originating from a trapped excitonic state, present deep inside the band gap. The trapped excitonic state is sensitized by the free excitonic state through an energy-transfer mechanism.

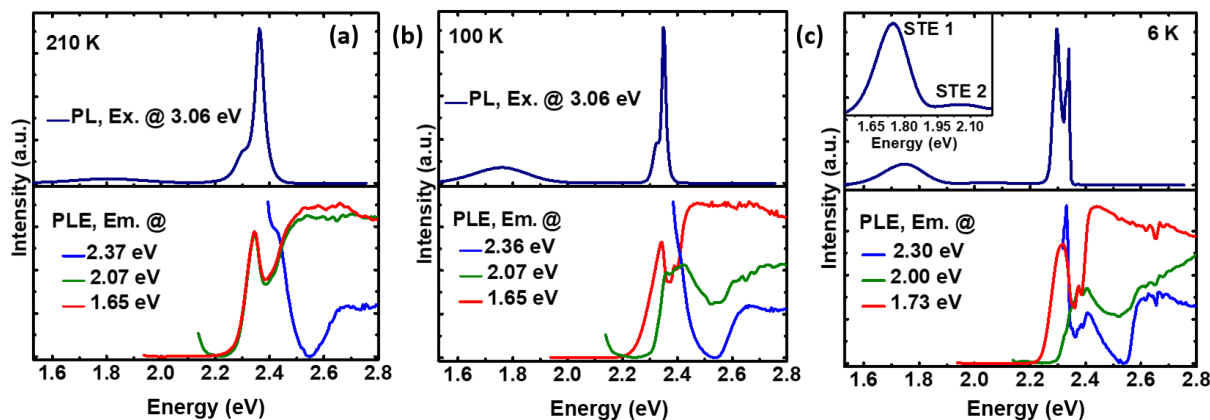


Figure 4.3: Comparison of PL (upper panel), and PLE (lower panel) at different energies, at (a) 210 K, (b) 100 K, and (c) 6 K. Inset for 6 K emission shows two broad emission features.

To correlate the excitation and emission behaviour at different temperatures, we compare their PL and PLE spectra. Figure 4.3 shows the temperature-dependent changes in emission and excitation behaviour at three characteristic temperatures. At 210 K (Figure 4.3a), the PLE recorded at different energies of the STE emission (2.07 and 1.65 eV) are similar and show a single peak at 2.34 eV and a step-like feature at ~ 2.5 eV. The PLE is similar to that observed for the lower energy excitonic emission at room temperature (in Figure 4.1b). The excitation mechanism of the STE emission undergoes substantial changes at further lowering of temperatures. At 100 K (Figure 4.3b), PLE recorded at higher energy side of the STE emission (2.07 eV) is different from the same recorded at the lower energy side (1.65 eV). The higher energy PLE edge is blue-shifted from the lower energy one by ~ 100 meV. An appearance of a step-like feature ~ 2.6 eV is also evident for the higher energy PLE, and it energetically resembles the step-like feature recorded for the higher energy excitonic emission at 2.36 eV. The difference in PLE at different positions of the STE emission becomes most apparent at 6

K (Figure 4.3c). The emission spectrum recorded at 6 K shows presence two broad emission feature; the higher energy one peaks at 2.07 eV (STE 2), while the lower energy one is at 1.75 eV (STE 1). The appearance of STE 2 suggests the possibility of the presence of a second type of exciton trap state in this material.

The large fwhm of both the STE peaks suggest either strong exciton-phonon coupling or presence of multiple trapping states in the sample. To confirm the behaviour of the STE states, we recorded PLE and measured PL lifetime at different energies of both the STE peaks at 6 K. While PLE tracks difference in excitation mechanism, PL lifetime gives information about emission mechanism.

Figure 4.4a shows the PLE recorded at multiple different energies of STE 1. All PLE spectra are similar. The PLE recorded at STE 2 at different energies (Figure 4.4b) are also similar among themselves. Figure 4.4c shows the PL decay recorded at different energies, and Figure 4.4d shows the average PL lifetime extracted from the decay data. Table 4.1 summarizes the obtained fitting parameters. The radiative lifetimes of both STE 1 and STE 2 are microseconds long. In contrast, the excitonic PL lifetime is much shorter (<1 ns). The long lifetime of the broad emissions is expected for trapped excitonic recombination where lattice distortions provide additional stabilization to the excitons, delaying their recombination. However, the lifetime recorded at different energies of STE 1 and STE 2 are similar among themselves, but significantly different from each other (Figure 4.4d). Overall, both of these experiments point to the same fact that the STE 1 and STE 2 emissions are significantly different from each other and possibly originate at different environments of the crystals.

Table 4.1: The best fit parameters of the PL decay profile of $(\text{CH}_3-(\text{CH}_2)_5\text{-NH}_3)_2\text{PbI}_4$ single crystals at 6 K as shown in Figure 4.4c.

Energy (eV)	A ₁ (%)	τ_1 (μ s)	A ₂ (%)	τ_2 (μ s)	τ_{av} (μ s)
1.65	100	3.9	--	--	3.9
1.75	100	3.8	--	--	3.8
1.81	100	3.7	--	--	3.7
2.07	95.4	0.11	4.6	2.1	1.06
2.16	96.4	0.11	3.6	2.3	1.07
2.34	100	<0.0001	--	--	<0.0001

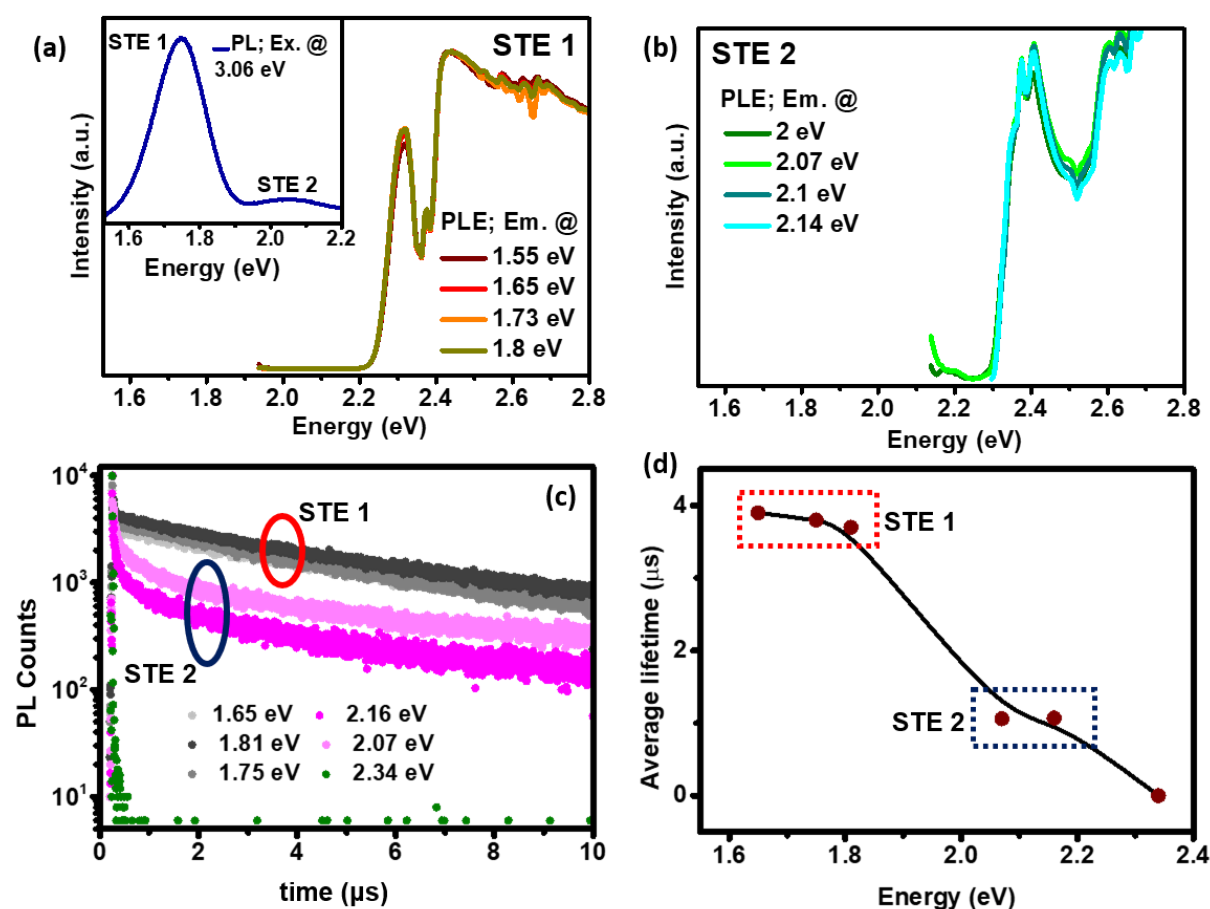


Figure 4.4: Luminescence properties of $(\text{CH}_3-(\text{CH}_2)_5-\text{NH}_3)_2\text{PbI}_4$ single crystals at 6 K. PLE recorded at different energies of (a) STE1, and (b) STE2. Inset in Figure 4.4a shows the STE emissions, same as the inset of Figure 4.3c. (c) PL decay dynamics measured at different energies of the PL spectrum (Figure 4.3c). (d) Average lifetime calculated from the PL decay shown in Figure 4.4c. The fitting parameters are tabulated in Table 4.1.

This observation of two different types of STE emissions in the single-crystalline samples is not unique to $(\text{CH}_3-(\text{CH}_2)_5-\text{NH}_3)_2\text{PbI}_4$. We made similar observation in multiple different

layered hybrid lead iodide compositions. Figure 4.5 shows representative case for DJ perovskite (4-AMP)PbI₄. In this crystal, the inorganic Pb-I layers are stacked along the a-axis of the crystal.²⁷ Figure 4.5a shows the PXRD pattern of (4-AMP)PbI₄. The presence of the (*h*00) peaks obtains an interlayer spacing between the inorganic layers of 10.5 Å, shorter than that observed for previously discussed sample, (H₃C-(CH₂)₅-NH₃)₂PbI₄. The reduction of interlayer distance in (4-AMP)PbI₄ is due to the presence of (4-AMP²⁺) cation, which is a small bivalent diammonium cation.

Figure 4.5b shows the PL spectrum of single-crystalline (4-AMP)PbI₄ recorded at 6 K. Two excitonic emission peaks are visible at 2.38 and 2.34 eV. Similarly, two broad STE peaks dominate the lower energy region, with peaks at ~2.0 (STE 2) and 1.66 (STE 1) eV. Compared to (H₃C-(CH₂)₅-NH₃)₂PbI₄ (Figure 4.3c), in this sample, the relative intensity of the STE emissions is higher than that of the excitonic emissions. This might be a consequence of lower extent of quantum confinement on the free excitons and consequent lower exciton binding energy in (4-AMP)PbI₄, because of the decreased interlayer spacing of the Pb-I layers.^{27, 37}

Figure 4.5c shows the PLE spectra recorded at different energies of the STE band. Noticeably, PLE spectra at STE 1 shows two peaks at 2.37 and 2.33 eV, matching with the two excitonic emission peaks in Figure 4.5b. The PLE recorded at STE 2 shows only one absorption feature at 2.37 eV corresponding to the higher energy excitonic emission. This suggests that STE 1 is sensitized by two exciton states, while STE 2 is selectively sensitized by the higher energy exciton state only. This observation matches with that for (H₃C-(CH₂)₅-NH₃)₂PbI₄ (Figure 4.4a-b).

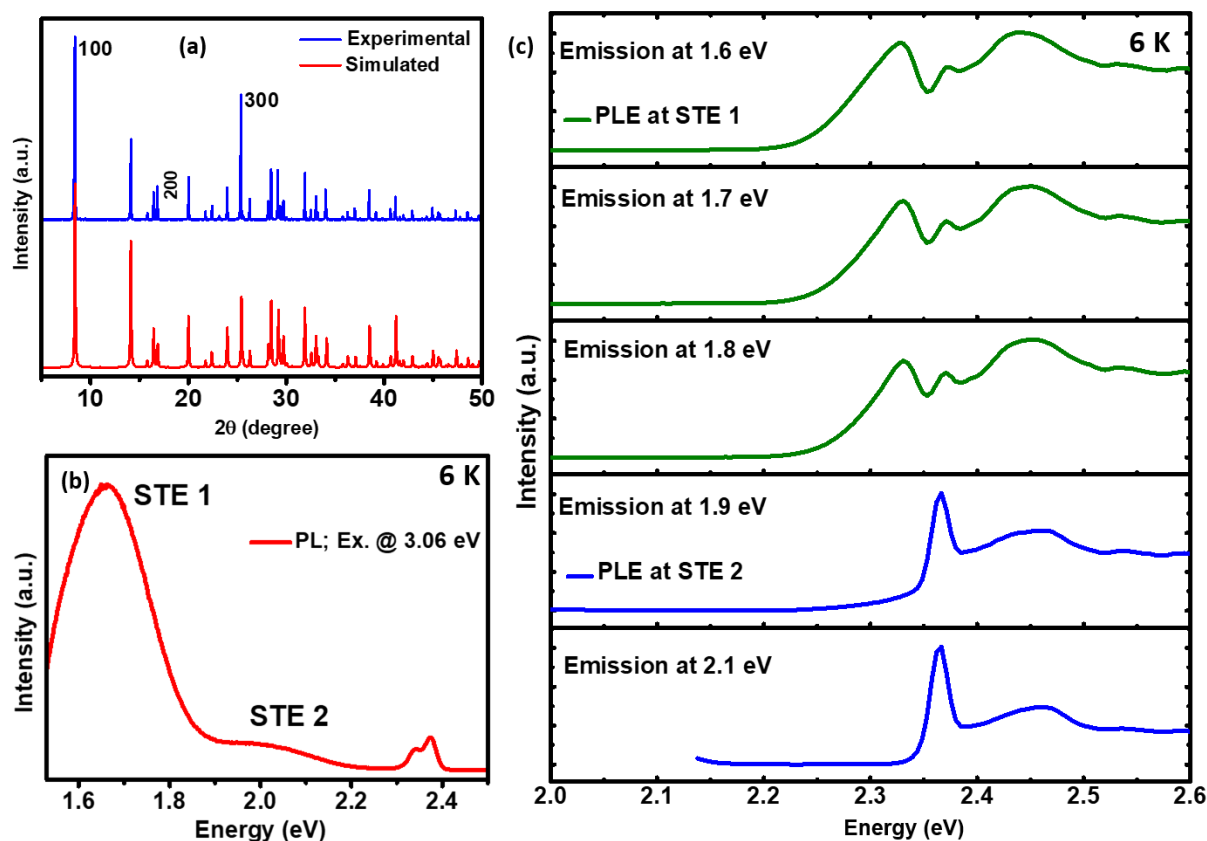


Figure 4.5: (a) PXRD pattern of synthesized (4-AMP)PbI₄ (4-AMP: 4-aminomethylpiperidinium) at room temperature. (b) PL from single-crystals of (4-AMP)PbI₄ at 6 K. (c) PLE measured at a few representative energies of STE emissions at 6 K.

4.4 Conclusions

To conclude, we showed that the broad Stokes-shifted emission in 2D layered iodide perovskite single crystals consists of two kinds of STE emissive states at lower temperatures. PL excitation and decay measurements suggested that the excitation and emission behaviour of these STE states are very different and they probably originate at two very different environments in the crystal. The observation remains same irrespective of crystal structure and organic ammonium cation used in layered hybrid lead iodide compositions. In (4-AMP)PbI₄ for example, while the higher energy STE is sensitized by higher energy excitons at 2.38 eV, the lower energy STE has an additional sensitizing contribution from the lower energy excitonic state at 2.34 eV. At higher temperatures, the interior of the crystal and the layer edge has been found to give rise to different excitonic emissions. Similar difference might be instrumental in forming the two STE states in these materials.

4.5 References

- (1) Dohner, E. R.; Jaffe, A.; Bradshaw, L. R.; Karunadasa, H. I. Intrinsic White-Light Emission from Layered Hybrid Perovskites. *J. Am. Chem. Soc.* **2014**, *136*, 13154-13157.
- (2) Thirumal, K.; Chong, W. K.; Xie, W.; Ganguly, R.; Muduli, S. K.; Sherburne, M.; Asta, M.; Mhaisalkar, S.; Sum, T. C.; Soo, H. S.; Mathews, N. Morphology-Independent Stable White-Light Emission from Self-Assembled Two-Dimensional Perovskites Driven by Strong Exciton–Phonon Coupling to the Organic Framework. *Chem. Mater.* **2017**, *29*, 3947-3953.
- (3) Zhou, G.; Li, M.; Zhao, J.; Molokeev, M. S.; Xia, Z. Single-Component White-Light Emission in 2D Hybrid Perovskites with Hybridized Halogen Atoms. *Adv. Opt. Mater.* **2019**, *7*, 1901335.
- (4) Wu, X.; Trinh, M. T.; Niesner, D.; Zhu, H.; Norman, Z.; Owen, J. S.; Yaffe, O.; Kudisch, B. J.; Zhu, X. Y. Trap States in Lead Iodide Perovskites. *J. Am. Chem. Soc.* **2015**, *137*, 2089-2096.
- (5) Muljarov, E. A.; Tikhodeev, S. G.; Gippius, N. A.; Ishihara, T. Excitons in Self-Organized Semiconductor/Insulator Superlattices: PbI-based Perovskite Compounds. *Phys. Rev. B Condens. Matter* **1995**, *51*, 14370-14378.
- (6) Zahra, H.; Hichri, A.; Jaziri, S. Comparative Study of the Exciton Binding Energies of Thin and Ultrathin Organic-Inorganic Perovskites due to Dielectric Mismatch Effects. *J. Appl. Phys.* **2017**, *122*, 015701.
- (7) Passarelli, J. V.; Mauck, C. M.; Winslow, S. W.; Perkinson, C. F.; Bard, J. C.; Sai, H.; Williams, K. W.; Narayanan, A.; Fairfield, D. J.; Hendricks, M. P. et al. Tunable Exciton Binding Energy in 2D Hybrid Layered Perovskites through Donor-Acceptor Interactions within the Organic Layer. *Nat. Chem.* **2020**, *12*, 672-682.
- (8) Kawano, N.; Koshimizu, M.; Sun, Y.; Yahaba, N.; Fujimoto, Y.; Yanagida, T.; Asai, K. Effects of Organic Moieties on Luminescence Properties of Organic–Inorganic Layered Perovskite-Type Compounds. *J. Phys. Chem. C* **2014**, *118*, 9101-9106.

- (9) Tan, S.; Zhou, N.; Chen, Y.; Li, L.; Liu, G.; Liu, P.; Zhu, C.; Lu, J.; Sun, W.; Chen, Q.; Zhou, H. Effect of High Dipole Moment Cation on Layered 2D Organic–Inorganic Halide Perovskite Solar Cells. *Adv. Energy Mater.* **2019**, *9*, 1803024.
- (10) Fu, Y.; Jiang, X.; Li, X.; Traore, B.; Spanopoulos, I.; Katan, C.; Even, J.; Kanatzidis, M. G.; Harel, E. Cation Engineering in Two-Dimensional Ruddlesden–Popper Lead Iodide Perovskites with Mixed Large A-Site Cations in the Cages. *J. Am. Chem. Soc.* **2020**, *142*, 4008–4021.
- (11) Gélvez-Rueda, M. C.; Van Gompel, W. T. M.; Herckens, R.; Lutsen, L.; Vanderzande, D.; Grozema, F. C. Inducing Charge Separation in Solid-State Two-Dimensional Hybrid Perovskites through the Incorporation of Organic Charge-Transfer Complexes. *J. Phys. Chem. Lett.* **2020**, *11*, 824–830.
- (12) Cortecchia, D.; Neutzner, S.; Srimath Kandada, A. R.; Mosconi, E.; Meggiolaro, D.; De Angelis, F.; Soci, C.; Petrozza, A. Broadband Emission in Two-Dimensional Hybrid Perovskites: The Role of Structural Deformation. *J. Am. Chem. Soc.* **2017**, *139*, 39–42.
- (13) Mao, L.; Wu, Y.; Stoumpos, C. C.; Traore, B.; Katan, C.; Even, J.; Wasielewski, M. R.; Kanatzidis, M. G. Tunable White-Light Emission in Single-Cation-Templated Three-Layered 2D Perovskites $(\text{CH}_3\text{CH}_2\text{NH}_3)_4\text{Pb}_3\text{Br}_{10-x}\text{Cl}_x$. *J. Am. Chem. Soc.* **2017**, *139*, 11956–11963.
- (14) Smith, M. D.; Connor, B. A.; Karunadasa, H. I. Tuning the Luminescence of Layered Halide Perovskites. *Chem. Rev.* **2019**, *119*, 3104–3139.
- (15) Li, X.; Hoffman, J. M.; Kanatzidis, M. G. The 2D Halide Perovskite Rulebook: How the Spacer Influences Everything from the Structure to Optoelectronic Device Efficiency. *Chem. Rev.* **2021**, *121*, 2230–2291.
- (16) Booker, E. P.; Thomas, T. H.; Quarti, C.; Stanton, M. R.; Dashwood, C. D.; Gillett, A. J.; Richter, J. M.; Pearson, A. J.; Davis, N. J. L. K.; Siringhaus, H. et al. Formation of Long-

Lived Color Centers for Broadband Visible Light Emission in Low-Dimensional Layered Perovskites. *J. Am. Chem. Soc.* **2017**, *139*, 18632-18639.

(17) Cortecchia, D.; Yin, J.; Petrozza, A.; Soci, C. White Light Emission in Low-Dimensional Perovskites. *J. Mater. Chem. C* **2019**, *7*, 4956-4969.

(18) Yu, J.; Kong, J.; Hao, W.; Guo, X.; He, H.; Leow, W. R.; Liu, Z.; Cai, P.; Qian, G.; Li, S. et al. Broadband Extrinsic Self-Trapped Exciton Emission in Sn-Doped 2D Lead-Halide Perovskites. *Adv. Mater.* **2019**, *31*, 1806385.

(19) Kahmann, S.; Tekelenburg, E. K.; Duim, H.; Kamminga, M. E.; Loi, M. A. Extrinsic Nature of the Broad Photoluminescence in Lead Iodide-based Ruddlesden–Popper Perovskites. *Nat. Commun.* **2020**, *11*, 2344.

(20) Paritmongkol, W.; Powers, E. R.; Dahod, N. S.; Tisdale, W. A. Two Origins of Broadband Emission in Multilayered 2D Lead Iodide Perovskites. *J. Phys. Chem. Lett.* **2020**, *11*, 8565-8572.

(21) Hu, T.; Smith, M. D.; Dohner, E. R.; Sher, M.-J.; Wu, X.; Trinh, M. T.; Fisher, A.; Corbett, J.; Zhu, X. Y.; Karunadasa, H. I.; Lindenberg, A. M. Mechanism for Broadband White-Light Emission from Two-Dimensional (110) Hybrid Perovskites. *J. Phys. Chem. Lett.* **2016**, *7*, 2258-2263.

(22) Cortecchia, D.; Yin, J.; Bruno, A.; Lo, S.-Z. A.; Gurzadyan, G. G.; Mhaisalkar, S.; Brédas, J.-L.; Soci, C. Polaron Self-Localization in White-Light Emitting Hybrid Perovskites. *J. Mater. Chem. C* **2017**, *5*, 2771-2780.

(23) Yin, J.; Li, H.; Cortecchia, D.; Soci, C.; Brédas, J.-L. Excitonic and Polaronic Properties of 2D Hybrid Organic–Inorganic Perovskites. *ACS Energy Lett.* **2017**, *2*, 417-423.

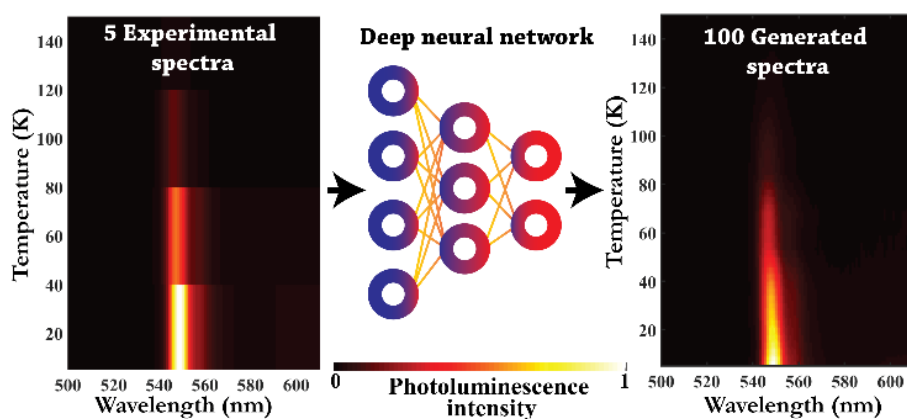
(24) Wang, X.; Meng, W.; Liao, W.; Wang, J.; Xiong, R.-G.; Yan, Y. Atomistic Mechanism of Broadband Emission in Metal Halide Perovskites. *J. Phys. Chem. Lett.* **2019**, *10*, 501-506.

- (25) Sheikh, T.; Shinde, A.; Mahamuni, S.; Nag, A. Possible Dual Bandgap in $(\text{C}_4\text{H}_9\text{NH}_3)_2\text{PbI}_4$ 2D Layered Perovskite: Single-Crystal and Exfoliated Few-Layer. *ACS Energy Lett.* **2018**, *3*, 2940-2946.
- (26) Sheikh, T.; Nawale, V.; Pathoor, N.; Phadnis, C.; Chowdhury, A.; Nag, A. Molecular Intercalation and Electronic Two Dimensionality in Layered Hybrid Perovskites. *Angew. Chem. Int. Ed.* **2020**, *59*, 11653-11659.
- (27) Stoumpos, C. C.; Cao, D. H.; Clark, D. J.; Young, J.; Rondinelli, J. M.; Jang, J. I.; Hupp, J. T.; Kanatzidis, M. G. Ruddlesden–Popper Hybrid Lead Iodide Perovskite 2D Homologous Semiconductors. *Chem. Mater.* **2016**, *28*, 2852-2867.
- (28) Mao, L.; Ke, W.; Pedesseau, L.; Wu, Y.; Katan, C.; Even, J.; Wasielewski, M. R.; Stoumpos, C. C.; Kanatzidis, M. G. Hybrid Dion–Jacobson 2D Lead Iodide Perovskites. *J. Am. Chem. Soc.* **2018**, *140*, 3775-3783.
- (29) Tremblay, M.-H.; Bacsá, J.; Zhao, B.; Pulvirenti, F.; Barlow, S.; Marder, S. R. Structures of $(4\text{-Y-C}_6\text{H}_4\text{CH}_2\text{NH}_3)_2\text{PbI}_4$ {Y = H, F, Cl, Br, I}: Tuning of Hybrid Organic Inorganic Perovskite Structures from Ruddlesden–Popper to Dion–Jacobson Limits. *Chem. Mater.* **2019**, *31*, 6145-6153.
- (30) Billing, D. G.; Lemmerer, A. Synthesis, Characterization and Phase Transitions in the Inorganic–Organic Layered Perovskite-Type Hybrids $[(\text{C}_n\text{H}_{2n+1}\text{NH}_3)_2\text{PbI}_4]$, n = 4, 5 and 6. *Acta Cryst. B* **2007**, *63*, (5), 735-747.
- (31) Nawale, V. V.; Sheikh, T.; Nag, A. Dual Excitonic Emission in Hybrid 2D Layered Tin Iodide Perovskites. *J. Phys. Chem. C* **2020**, *124*, 21129-21136.
- (32) DeCrescent, R. A.; Du, X.; Kennard, R. M.; Venkatesan, N. R.; Dahlman, C. J.; Chabynyc, M. L.; Schuller, J. A. Even-Parity Self-Trapped Excitons Lead to Magnetic Dipole Radiation in Two-Dimensional Lead Halide Perovskites. *ACS Nano* **2020**, *14*, 8958-8968.

- (33) Tanaka, K.; Sano, F.; Takahashi, T.; Kondo, T.; Ito, R.; Ema, K. Two-Dimensional Wannier Excitons in a Layered-Perovskite-Type Crystal $(\text{C}_6\text{H}_{13}\text{NH}_3)_2\text{PbI}_4$. *Solid State Commun.* **2002**, *122*, 249-252.
- (34) Zhang, Q.; Ji, Y.; Chen, Z.; Vella, D.; Wang, X.; Xu, Q.-H.; Li, Y.; Eda, G. Controlled Aqueous Synthesis of 2D Hybrid Perovskites with Bright Room-Temperature Long-Lived Luminescence. *J. Phys. Chem. Lett.* **2019**, *10*, 2869-2873.
- (35) Knutson, J. L.; Martin, J. D.; Mitzi, D. B. Tuning the Band Gap in Hybrid Tin Iodide Perovskite Semiconductors Using Structural Templating. *Inorg. Chem.* **2005**, *44*, 4699-4705.
- (36) Li, S.; Luo, J.; Liu, J.; Tang, J. Self-Trapped Excitons in All-Inorganic Halide Perovskites: Fundamentals, Status, and Potential Applications. *J. Phys. Chem. Lett.* **2019**, *10*, 1999-2007.
- (37) Chakraborty, R.; Sheikh, T.; Ghosh, P.; Nag, A. Neural Networks for Analysis of Optical Properties in 2D Layered Hybrid Lead Halide Perovskites. *J. Phys. Chem. C* **2021**, *125*, 5251-5259.

CHAPTER 5

Neural Networks for Analysis of Optical Properties in 2D Layered Hybrid Lead Halide Perovskites



The work presented in this chapter has led to the following publication:

Chakraborty, R.; Sheikh, T.; Ghosh, P.; Nag, A. Neural Networks for Analysis of Optical Properties in 2D Layered Hybrid Lead Halide Perovskites. *J. Phys. Chem. C* **2021**, *125*, 5251-5259. Copyright permission has been taken from the ACS publication for full paper.

Abstract

Chemical compositions of layered hybrid perovskites can be varied easily, and thereby, intrinsic properties like exciton binding energy and band gap can be varied over a wide range. We have prepared $(\text{PEA})_2\text{PbI}_4$, $(\text{EA})_2\text{PbI}_4$ and $(\text{CHA})_2\text{Pb}(\text{Br}_{1-x}\text{I}_x)_4$ exhibiting distinctly different optical properties. To estimate exciton binding energy, PL spectra are recorded at various temperatures in the range of 300 to 5.6 K. However, the measurements take a long time. To reduce time and cost of experiments, and also avoid possibility of sample degradation during the measurement, we have employed here a machine learning method, namely, deep neural network (DNN). It generates hundreds of PL spectra at different temperatures, using only a few (5-7) experimental spectra. The DNN spectra are then used to estimate exciton binding energies, and other optical parameters. This demonstrated method reduces the data collection time from about 13 hours to 3 hours. Furthermore, DNN is used to generate optical absorption spectra of $(\text{CHA})_2\text{Pb}(\text{Br}_{1-x}\text{I}_x)_4$ for a large number of compositions “x”, using experimental optical absorption spectra of only a few compositions as inputs. We envisage that the demonstrated method will be helpful for the search of materials with desired optoelectronic properties in the vast compositional space of halide perovskites.

5.1 Introduction

2D layered hybrid perovskites like $(\text{PEA})_2\text{PbI}_4$ (PEA = phenylethylammonium) have emerged as an interesting class of semiconductors for optical and optoelectronic applications.¹⁻¹² The nanoscale interactions between the inorganic well and organic barrier layers provide chiroptical properties and dielectric confinement of excitons.¹³⁻¹⁸ Importantly, the crystal structure of 2D layered hybrid perovskites does not require to satisfy the Goldsmith tolerance factor.¹⁹ Consequently, there are enormous possibilities of changing the compositions of inorganic and organic layers, and thereby, controlling their optical properties.^{14, 20} To achieve the optimized composition, a large amount of data needs to be generated and analysed. Can machine learning-based methods help us with a quicker and better analysis of optical properties? Here we reveal how machine learning can provide insights about optical emission and absorption processes of A_2PbX_4 2D layered hybrid perovskites, with varying compositions of organic A-site cations and halide X-site anions.

Exciton binding energy is an important parameter to design optical and optoelectronic applications. A large exciton binding energy causes an exciton to radiatively recombine at room temperature, and are desired for applications like light emitting diodes and display technologies.^{21,22} In contrast, smaller exciton binding energy is sought after when high-degree of exciton dissociation is required – e.g., in solar cells or photodetectors.²³ Controlled external perturbation in the form of temperature is a useful way of exploring exciton photophysics.^{24,25} The increasing temperature of the lattice causes the atomic sites to vibrate more, and consequently, the vibration can couple with an exciton present in the lattice. This coupling controls PL linewidth and intensity. It becomes thus possible to quantify the exciton binding energy from temperature-dependent PL spectra.

To extract a reliable value of exciton binding energy, PL spectra at large numbers of temperatures (typically in the range of 300 to 5 K) are required. But increasing the number of data points increases the time of experiment. For example, our cryostat requires about four

hours to obtain sufficient vacuum and then ~2 hours to cool down to ~5 K. Then while heating the sample, temperature is stabilized at a given temperature and PL spectra are recorded. For each temperature, the process takes about 25 minutes. Therefore, if we collect PL spectra at thirty different temperatures, then the whole process takes up about 13 hours for one sample. In addition to the increase in time and cost of such experiments, the prolonged exposure of the hybrid perovskite samples to high-vacuum and constant photo-excitation can sometime lead to changes in the sample influencing their PL properties – which would result in an error in the determination of exciton binding energy.^{26,27}

To reduce the experimental time along with improvement in data analysis, we have employed a machine learning technique, namely, DNN. DNNs are a special class of the neural network models with multiple “hidden layers”. DNNs found applications in multiple science and technology related fields including spectroscopy.²⁸⁻³⁰ One of the most used applications of DNN is image recognition where the model learns to categorize object based on their common features. Temperature-dependent PL spectra can be thought of a combination of multiple features which evolve as functions of temperature. Thus, it becomes possible to train a DNN model which learns to isolate the distinct features of the spectrum and how those features change with temperature. However, utilizing DNNs in the above-mentioned way would require previously recorded experimental spectra for making any prediction. Thus, DNNs are different from first-principle based calculations as the DNN model does not take in any information regarding the electronic interactions in the system to generate predictions.

We used a few (5-7) experimental PL spectra to generate hundreds of DNN PL spectra in the temperature range of 300 to 5 K. The samples used are (PEA)₂PbI₄, (EA)₂PbI₄ and (CHA)₂Pb(Br_{1-x}I_x)₄. Using the DNN spectra, exciton binding energies for different compositions are estimated. Exciton binding energy varies non-linearly with composition “x” of (CHA)₂Pb(Br_{1-x}I_x)₄, and DNN analysis help us to predict the composition for a desired

exciton binding energy. Finally, we extend DNN to predict optical absorption spectra of $(\text{CHA})_2\text{Pb}(\text{Br}_{1-x}\text{I}_x)_4$, for different “x”. It is important to note that the entire exercise can be performed on a web browser without the need of any expensive computational facility.

5.2 Experimental Section

5.2.1 Chemicals. Hydrogen iodide (HI, 57 wt% in water), hydrogen bromide (HBr, 43 wt% in water), phenylethylamine (>99%), cyclohexylamine (>99%), lead oxide (PbO, >99%), ethanolamine (99%), dimethyl sulfoxide (DMSO, >99%), acetonitrile (anhydrous, 99.8%) are purchased from Merck. All chemicals are used without further purification.

5.2.2 Preparation of $(\text{PEA})_2\text{PbI}_4$ and $(\text{CHA})_2\text{Pb}(\text{Br}_{1-x}\text{I}_x)_4$ single crystals. Single crystals are prepared by cooling induced crystallization method similar to prior reports.³¹ 0.25 mmol PbO is taken in a beaker and 50 mL of HX (X = Br, I) is added to it. For synthesizing single crystals with different “x” of $(\text{CHA})_2\text{Pb}(\text{Br}_{1-x}\text{I}_x)_4$, the HX was taken in the following molar ratios of HI:HBr- 0.02 for x = 0.18, 0.04 for x = 0.42, 0.06 for x=0.47, 0.15 for x = 0.6, 0.24 for x = 0.67, 0.63 for x = 0.73, and 0.95 for x = 0.88. The mixture is then sonicated till all the PbO powder dissolves completely. The solution is then cooled using an ice-water bath, and in it 0.6 mmol phenylethylamine or cyclohexylamine is added. These amines in the presence of HX turn into the corresponding ammonium ions in-situ. This addition makes the solution turn turbid, possibly because of the formation of powder-like A_2PbX_4 . The solution is then heated in an oil bath at 110 °C till it becomes clear. The heating is then stopped and the solution is kept undisturbed for one day. As the solution cools down naturally, plate-like single crystals of A_2PbI_4 start appearing at the bottom of the beaker.

5.2.3 Thin film of $(\text{EA})_2\text{PbI}_4$. The thin films of $(\text{EA})_2\text{PbI}_4$ are prepared on quartz glass substrates following the method that was previously reported.^{32,33} Concisely, 5 mL dimethyl sulfoxide, 5 mL acetonitrile, 0.5 mmol ethylamine and 0.2 mL HI are mixed in a glass vial by sonicating for 5 minutes. To this, 0.25 mmol PbI_2 is added, and the mixture is again sonicated

for 5 minutes. 50 μL of this precursor solution is dropped on the substrate and is spun at 1200 rpm for 30 sec. Subsequently, the film is heated at 70 $^{\circ}\text{C}$ on a hotplate for 2 minutes.

5.2.4 Characterization and optical properties. PXRD patterns are collected using a Bruker D8 Advance diffractometer in Bragg–Brentano geometry and operating with Cu $K\alpha$ radiation. The energy dispersive X-ray spectroscopy (EDS) compositional analysis are done on Zeiss Ultra Plus SEM instrument. Apex equipment’s NXG-M1 spin coater system is used for the preparation of $(\text{EA})_2\text{PbI}_4$ films.

UV-visible absorption spectra are recorded in diffused reflectance mode using Shimadzu UV3600 plus UV-Vis spectrometer. In this method, the diffused reflectance data are collected and are converted to absorption using Kubelka-Munk transformation [$\alpha/S = (1 - R)^2/2R$], where α is the absorption coefficient, S is the scattering coefficient, and R is the diffused reflectance.³⁴ Temperature-dependent PL spectra are recorded using Edinburg Instrument’s FLS 980 spectrofluorometer using a xenon lamp as the radiation source. 405 nm photons are used as the excitation source for all samples. The samples are mounted on a gold-plated sample holder having quartz windows and are attached to an Advanced Research System’s closed cycle He-cryostat and Lakeshore instruments’ temperature controller which is used to achieve the lower temperatures.

5.2.5 Neural network models. The neural network models are created using Keras with Tensorflow backend.³⁵ Tensorflow is an open-source end-to-end package for machine-learning applications. We use a multi-layered DNN for prediction of PL and absorption spectra. For both of these models, we use Adam optimization algorithm for performing the stochastic gradient descent based on the error calculated by mean squared error.³⁶ The DNN for generating the temperature-dependent PL spectra and composition dependent absorption spectra is modelled using two symmetric units. Each unit can further be decomposed into three

hidden layers which consist 1024, 2, and 1024 nodes in sequence. Since our training dataset is small, we use a dropout layer at the end of each unit to avoid overfitting.

For fitting exciton binding energy against composition shown in Figure 5a, we use two-layer shallow neural network (sNN). The sNN model for fitting the exciton binding energy uses two layers of 64 and 128 nodes in sequence.

5.3 Results and Discussion

(PEA)₂PbI₄ is one of the most studied layered lead iodide perovskite compositions because it offers rich exciton properties and better stability compared to others.^{37,38} Figure 5.1a shows the PXRD data for (PEA)₂PbI₄ single crystals. The sharp equidistant peaks originate from the (00l) planes. The interlayer spacing of 15.7 Å calculated from these peaks confirm the formation of crystalline (PEA)₂PbI₄. Figure 5.1b shows the UV-visible absorption spectrum. The absorption spectrum shows an exciton feature at 523 nm, corresponding to the 1s exciton resonance. These characterization results match with previous reports of (PEA)₂PbI₄.³⁹

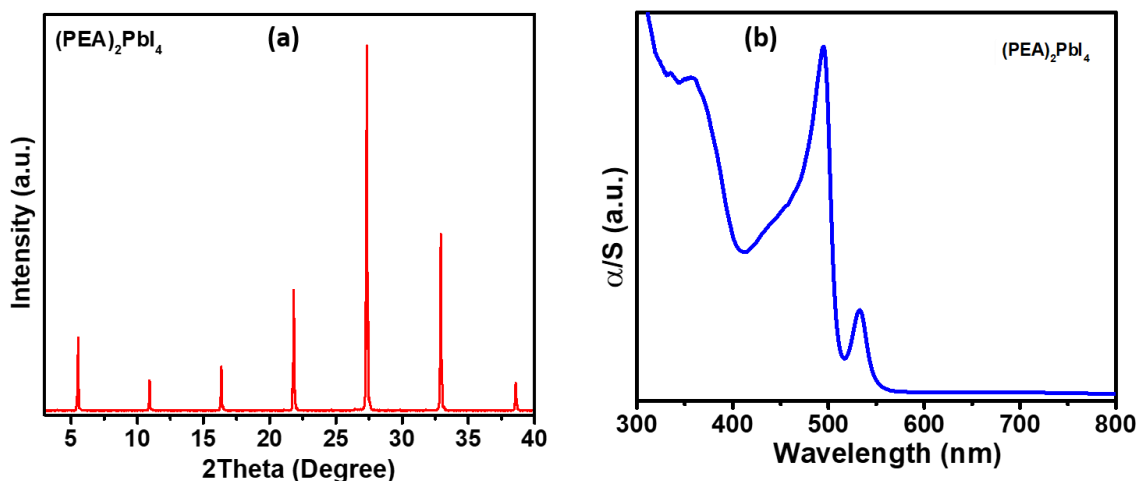


Figure 5.1: Characterization of (PEA)₂PbI₄ single crystals. (a) PXRD (b) UV-visible absorption spectrum. α is the absorption coefficient and S is the scattering coefficient. The experimental data are measured in the diffused reflectance mode and then converted to absorption data.

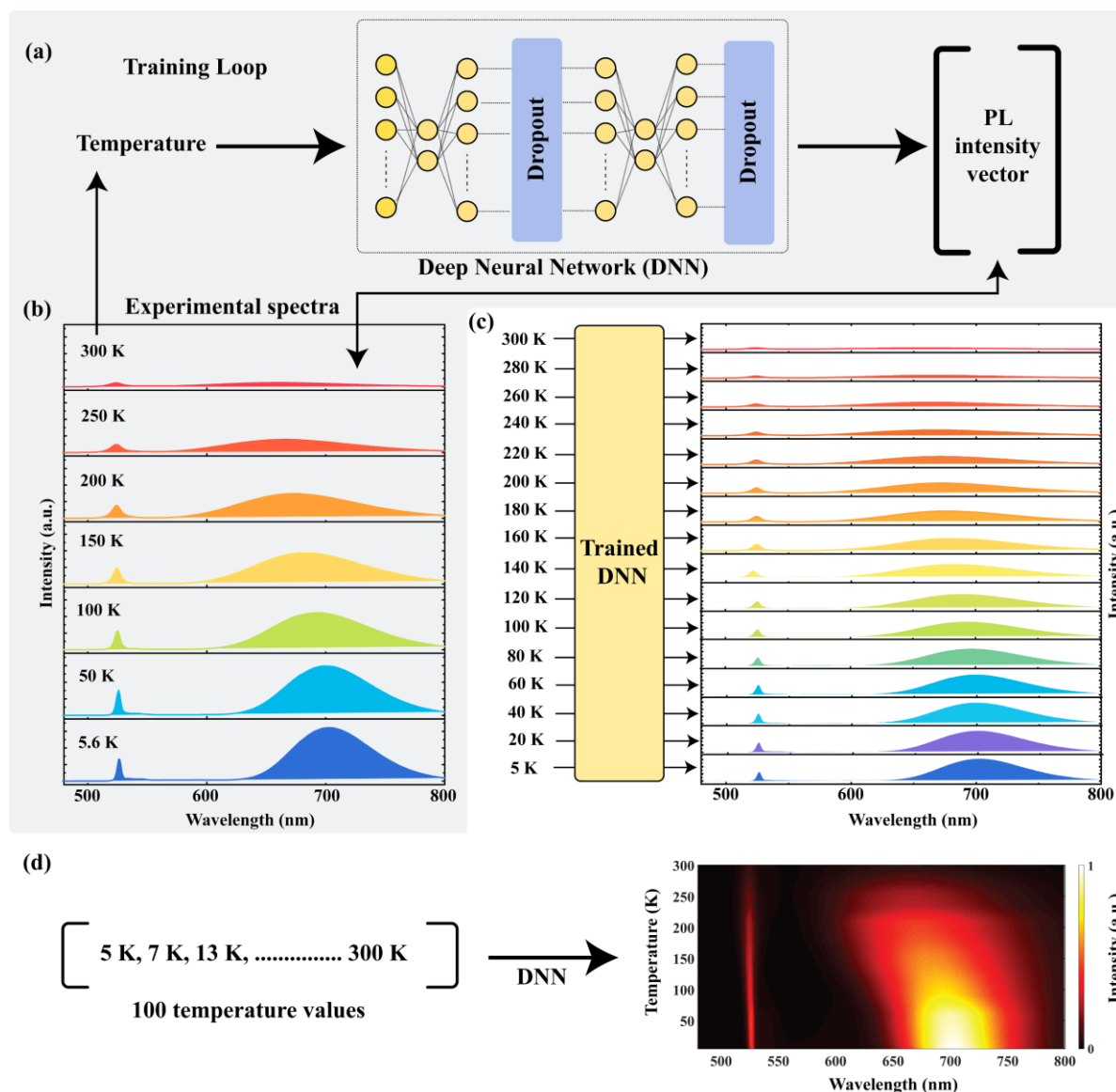


Figure 5.2: Generation of temperature-dependent PL spectra using deep neural network (DNN). (a) Schematic of the DNN architecture showing the hidden layers that contain two units of 1024, 2, and 1024 nodes in sequence. (b) Experimental PL spectra of (PEA)₂PbI₄ single crystals at different temperatures, used for training the DNN model shown in Figure 1a. The double headed arrow indicates the error minimization task. (c) DNN predicted PL spectra at a few representative temperature points. (d) Pseudocolormap of temperature-dependent PL intensity obtained from DNN spectra at 100 different temperatures.

PL recorded from crystalline samples of (PEA)₂PbI₄ are used for training the DNN model and the subsequent validation. Figure 5.2a shows the schematic of the DNN architecture that is used for predicting the temperature-dependent PL spectra. For the training loop, experimentally measured PL spectra at seven different temperatures (Figure 5.2b) are used. The DNN model takes in the temperature values and the corresponding experimental PL spectrum as inputs. The

training objective is to reduce the error between the DNN output intensity vector and the experimentally observed ones at these seven different temperatures. The model training stops when the model can predict the PL spectrum with >90% accuracy for the seven temperature points. Then the trained model is used to generate PL spectra of the sample at new temperatures for which experimental spectra are not available.

Figure 5.2c shows a few DNN predicted spectra at different temperatures. Expectedly, the DNN spectra (Figure 5.2c) have similar features compared to the experimental input spectra (Figure 5.2b). The PL spectra at all temperatures contain two features - an excitonic emission peak ~526 nm and the longer-wavelength region is dominated by a broad emission feature. The broad emission can be attributed to the self-trapping of excitons (STE).⁴⁰⁻⁴² The DNN model is used on a set of hundred temperature values in the range 5 K to 300 K to generate a smooth pseudocolormap as shown in Figure 5.2d.

To check the validity of our DNN model, we compared the salient features of the DNN predicted PL spectra with that of the experimental ones. For comparison, we measured the experimental spectra of (PEA)₂PbI₄ single crystals at a large number of different temperatures, requiring a prolonged experiment time. (PEA)₂PbI₄ single crystals are stable, surviving the experimental conditions. Then we compare the parameters of these large numbers of experimental spectra, with the DNN spectra obtained using only seven experimental spectra following the method shown in Figure 5.2. In essence, the experimental dataset apart from the seven training spectra acts as the test dataset for this method.

Figure 5.3a compares the experimental and DNN spectra of (PEA)₂PbI₄ single crystals at a few representative temperatures. The experimental and the predicted spectra match very well. The close agreement between the full width at half maxima (FWHM) of the exciton emission in the experimental and the DNN generated datasets is shown in Figure 5.3b. We have also compared the temperature-dependent integrated intensity of exciton emission, $I(T)$, obtained from the

DNN spectra with that of experimental spectra. The inverse of this quantity, $1/I(T)$ is the relevant parameter for obtaining the exciton binding energy. Figure 5.3c shows the agreement of $1/I(T)$ values obtained from both DNN and experiments.

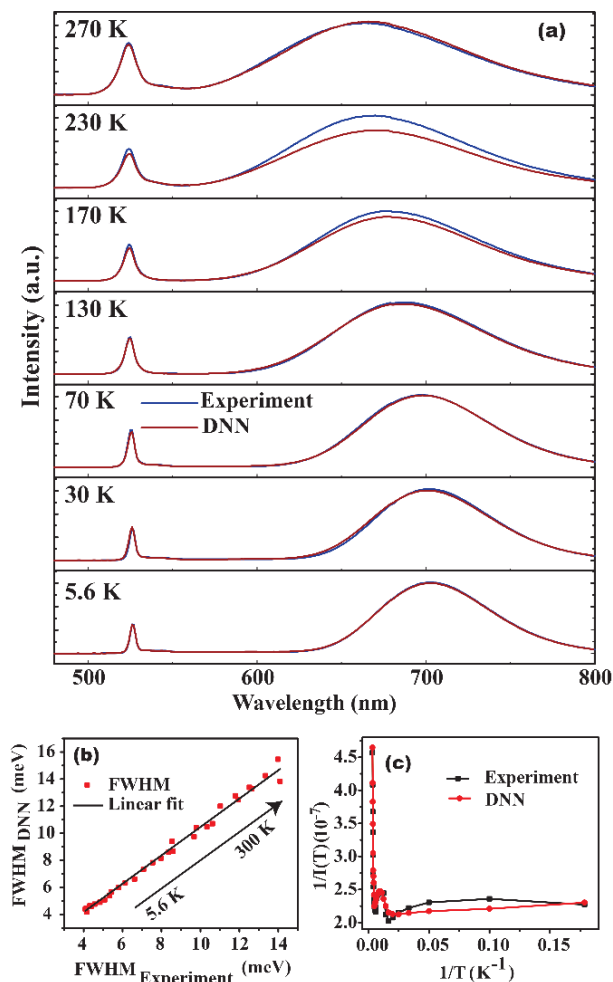


Figure 5.3: Validation of DNN-generated dataset for $(\text{PEA})_2\text{PbI}_4$ single crystals. (a) Experimental spectra overlapped with DNN-generated spectra of $(\text{PEA})_2\text{PbI}_4$ single crystals for a few representative temperatures. (b) Comparison of FWHM of the exciton emission with peak at ~ 526 nm obtained from experimental spectra ($\text{FWHM}_{\text{Experiment}}$) [x-axis] and the DNN spectra (FWHM_{DNN}) [y-axis]. The black arrow indicates the increase in temperature in the range 5.6 K to 300 K. The linear fit has a slope of 1.05 and intercept 0. (c) Comparison between the inverse of integrated intensity ($1/I(T)$) of the exciton emission of the experimental and the DNN-generated spectra at different temperatures (T).

Similar to the FWHM and intensity, the temperature dependence of the exciton emission peak position also shows agreement between the two datasets (Figure 5.4). Comparing all these different spectral properties, it appears that our method for generating temperature-dependent

PL spectra using DNN produces dataset keeping the exciton features same as that of the experimental dataset.

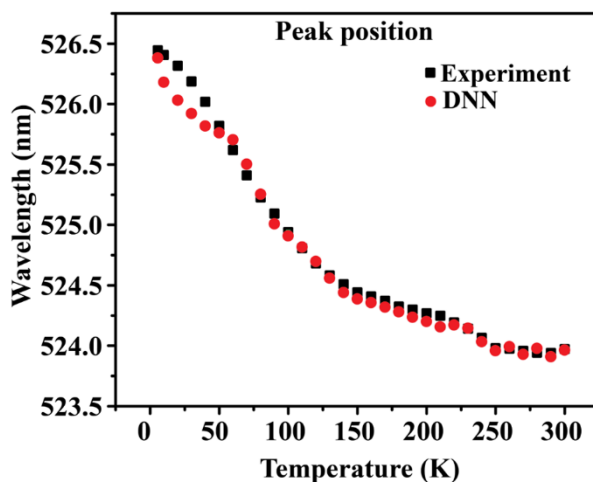


Figure 5.4: Variation of the excitonic emission peak with temperature in experimental and DNN-generated datasets for $(\text{PEA})_2\text{PbI}_4$ single crystals.

After testing the usefulness of DNN for $(\text{PEA})_2\text{PbI}_4$, we employed DNN to obtain exciton binding energy of $(\text{EA})_2\text{PbI}_4$. The PL properties of $(\text{PEA})_2\text{PbI}_4$ and $(\text{EA})_2\text{PbI}_4$ are very different, reflecting intrinsic differences in their exciton photophysics. The high-frequency dielectric constant (ϵ_∞) of PEA is 3.3, whereas, EA has $\epsilon_\infty = 37.7$.⁴³ This difference in ϵ_∞ of A-site cations significantly changes the dielectric confinement of exciton.²⁰ For a given inorganic layer, the exciton binding energy decreases with increasing ϵ_∞ of organic cations. So $(\text{EA})_2\text{PbI}_4$ with high ϵ_∞ exhibit a smaller exciton binding energy. Consequently, radiative PL emission from this sample can only be observed at lower temperatures below 200 K.

Figure 5.5a shows the pseudocolormap of exciton emission obtained using experimental PL spectra of $(\text{EA})_2\text{PbI}_4$ thin film, recorded at five different temperatures. Equation 5.1 describes the temperature dependence of integrated PL intensity, $I(T)$.⁴⁴ Here, E_a is the exciton binding energy, k_B is the Boltzmann constant, PL intensity at 0 K be I_0 , and A is the pre-exponential factor.

$$I(T) = \frac{I_0}{1 + Ae^{-E_a/k_B T}} \quad \text{Eq. (5.1)}$$

By inverting both sides, equation 5.1 is rearranged to equation 5.2, where $A' = 1/I_0$, and $B' = A/I_0$.

$$\frac{1}{I(T)} = A' + B'e^{-E_a/kT} \quad \text{Eq. (5.2)}$$

This exponential decay equation 5.2 is used to fit the inversed intensity vs temperature plots to obtain the exciton binding energy.

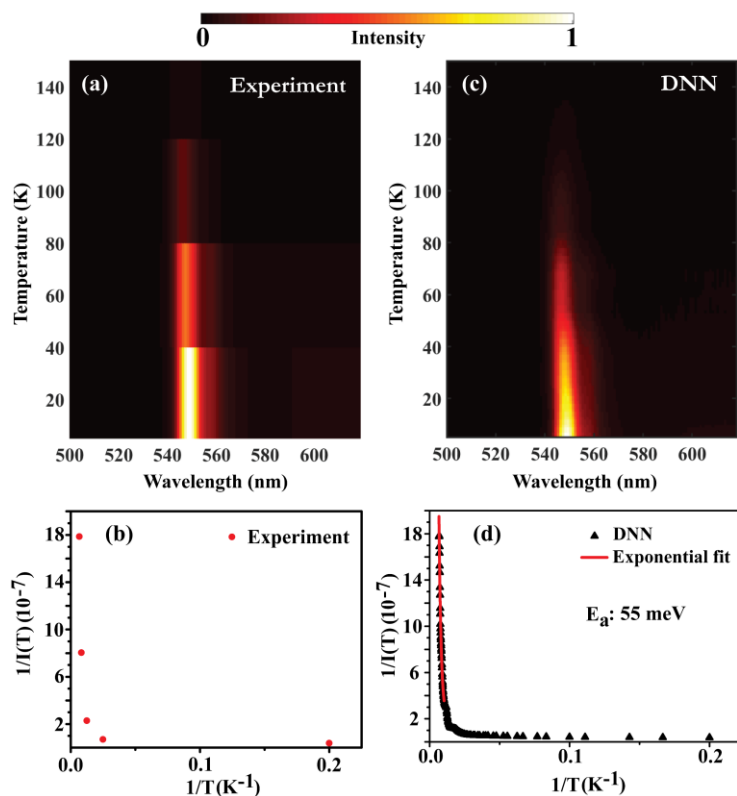


Figure 5.5: Estimation of exciton binding energy from DNN-generated dataset of $(\text{EA})_2\text{PbI}_4$ thin film. (a) Pseudocolormap generated from experimental PL spectra of $(\text{EA})_2\text{PbI}_4$ thin film at five different temperatures. (b) Inverse PL intensity vs. inverse temperature plot obtained from experimental PL spectra. (c) Predicted PL pseudocolormap obtained using DNN. (d) Inverse intensity vs. inverse temperature plot of the DNN-generated data and fitting using equation 5.2 for estimating exciton binding energy (E_a).

Figure 5.5b is the experimental inversed intensity vs. inversed temperature plot. There are not enough data points for a reasonable fitting using equation 5.2. So, we used these five experimental spectra to train the DNN model, and subsequently, obtain a set of hundred DNN generated PL spectra. Figure 5.5c shows the pseudocolormap of DNN generated PL spectra. The smooth change in color gradient in Figure 5.5c is because of the larger number of DNN

PL spectra, compared to sudden color changes seen in Figure 5.5a, which is generated using only five experimental spectra. The $1/I(T)$ vs. $1/T$ profile obtained from DNN spectra are shown in Figure 5.5d. DNN provided lots of data points in Figure 5.5d, which can be fitted using equation 5.2. The fitted curve yields the exciton binding energy of 55 meV. The results are in agreement with prior results suggesting that the DNN generated dataset can be trusted for exciton binding energy calculations.³²

This method of calculating exciton binding energies using DNN PL spectra obtained from a small number of experimental temperature-dependent PL spectra decreases the measurement time down to about three hours for a sample. Thus, DNN is more useful when one needs to carry out a study where multiple sample compositions are required to be analysed. For example, we mapped the variation of the exciton binding energy as a function of halide composition for $(\text{CHA})_2\text{Pb}(\text{Br}_{1-x}\text{I}_x)_4$ series of single crystals. In the framework of dielectric confinement, the exciton binding energy is expected to increase with increasing iodine contribution in the composition.^{20, 32} However, the increment is not expected to be linear with increasing the composition of iodine. There are multiple contributions that impact the electronic properties in these materials. One of the important factors in this regard is the structure of the lattice. It has often been pointed out that structural distortions cause the formation of self-trapped excitons in many compositions of such layered hybrid perovskites.^{45,46} While the effect of such self-trapped excitons on the free exciton emission is not yet completely understood, it is anticipated that such structural distortions will have some effect on the exciton dynamics. Therefore, simplistic theoretical prediction of exciton binding energy for a given composition is challenging. In contrast, a composition-exciton binding energy map can help to extract the exciton binding energies of a given related composition. So, we chose to study a compositional space of $(\text{CHA})_2\text{Pb}(\text{Br}_{1-x}\text{I}_x)_4$ by varying the halide ion compositions. The composition “x” is measured by EDS analysis. Experimental spectra at seven different temperatures are used as

input for training the DNN model, from which exciton binding energy is calculated. The pseudocolormaps obtained from the corresponding seven experimental spectra are shown in Figure 5.6.

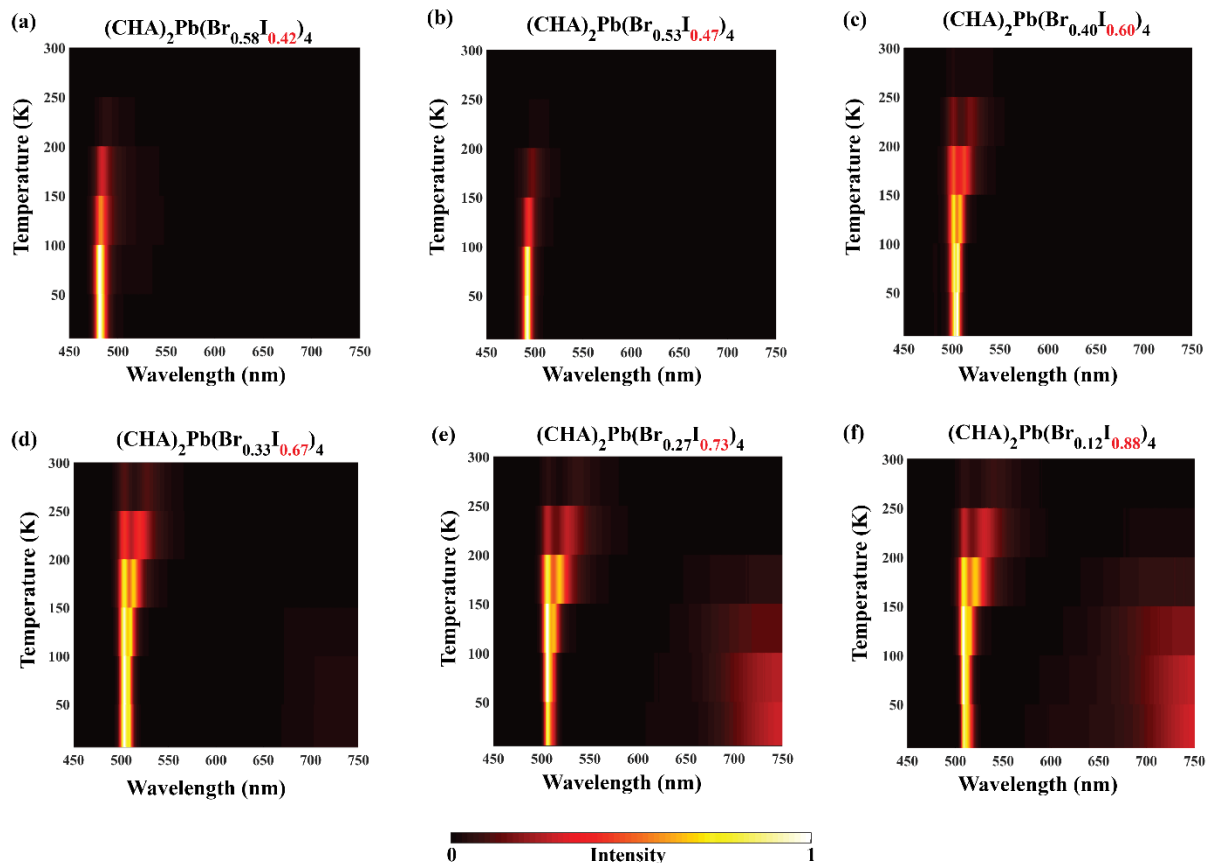


Figure 5.6: (a-f) Pseudocolormaps generated from experimentally measured PL spectra measured at seven different temperatures (5.6, 50, 100, 150, 200, 250, and 300 K) for $(\text{CHA})_2\text{Pb}(\text{Br}_{1-x}\text{I}_x)_4$ single crystals with different compositions “x”.

Figure 5.7a-f show the DNN generated temperature-dependent PL pseudocolormaps and the corresponding $1/I(T)$ vs. $1/T$ plots for the exciton emission of $(\text{CHA})_2\text{Pb}(\text{Br}_{1-x}\text{I}_x)_4$ single crystals with different values of compositions “x”. An increase in iodine concentration increases the PL intensity at higher temperatures. Such temperature dependency suggests higher exciton binding energies with increasing iodine concentration. The DNN predicted $1/I(T)$ vs. $1/T$ plots of exciton emissions are fitted using equation 5.2 in the region where it obtains the best fit. Some of the compositions show two emission features near the expected

exciton emission wavelength at higher temperatures. It is generally believed that the origins of both of these features are excitons, perhaps at different environments.¹⁶

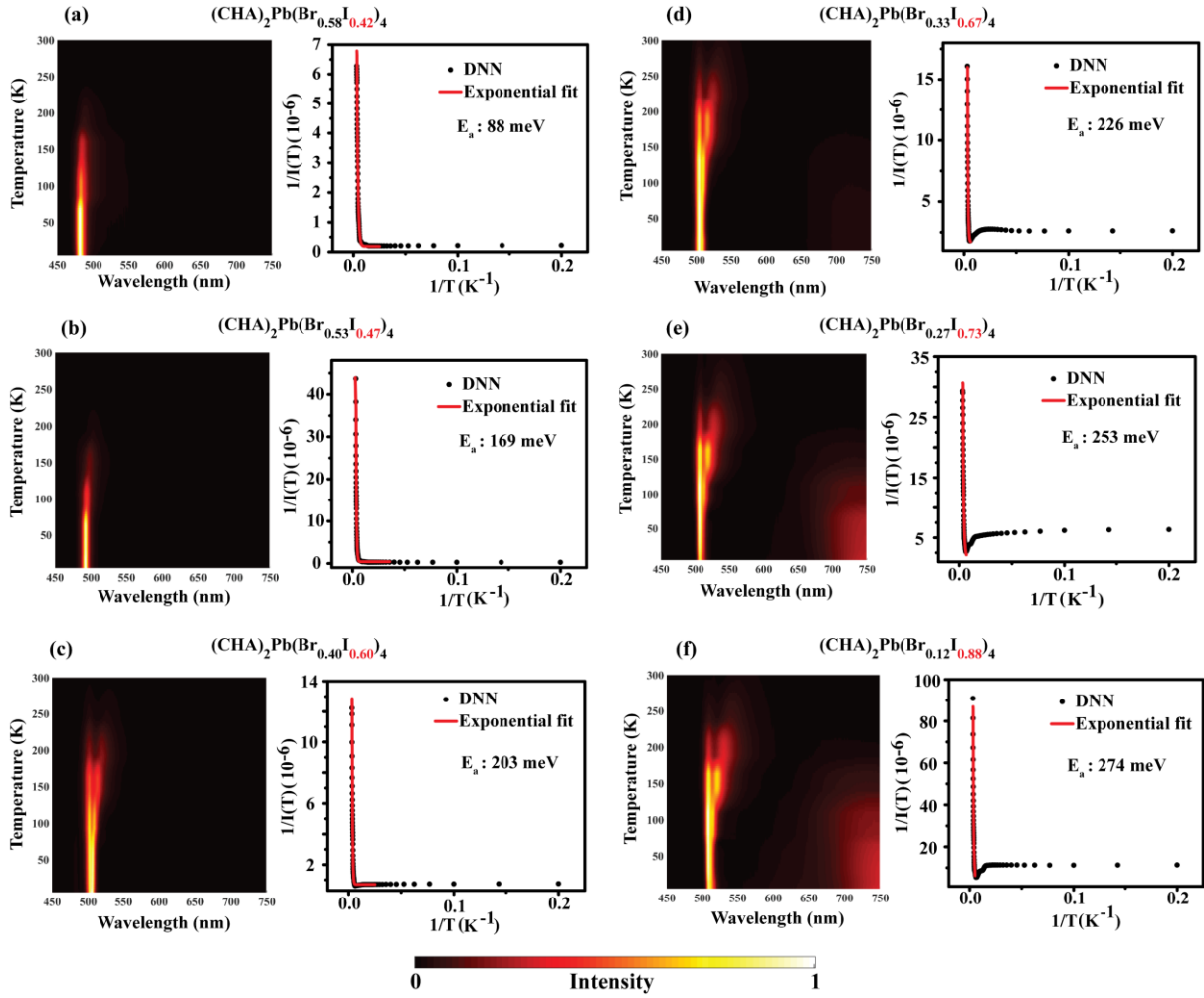


Figure 5.7: Estimation of exciton binding energy for different halide ion compositions of $(\text{CHA})_2\text{Pb}(\text{Br}_{1-x}\text{I}_x)_4$. (a-f) temperature-dependent PL pseudocolormap and corresponding inverse intensity ($1/I(T)$) vs. inverse temperature ($1/T$) plots for the exciton emission. Both kinds of plots are obtained using DNN predicted PL spectra at different temperatures. For each of the sample compositions, experimental PL spectra at seven different temperatures are used to generate DNN data set. The exciton binding energies are obtained by fitting the $1/I(T)$ vs. $1/T$ plots using equation 5.2.

Thus, we use the combined integrated intensity of both features to calculate the exciton binding energy. Note that calculating the exciton binding energy this way gives an averaged-out picture and the calculated values might differ when more sophisticated techniques are used that can probe the difference of exciton binding energies between the two emission centres. The obtained exciton binding energies for different compositions are noted in the corresponding figures. The exciton binding energy systematically increases with increasing iodine

concentration “ x ”. Note that, dielectric confinement of exciton increases with increasing iodine concentration.³² Also, an increase in iodine concentration is expected to increase barrier height between inorganic well and organic barrier, increasing the quantum confinement effect.⁴⁷ Both the enhancement of dielectric and quantum confinement effect, increases the exciton binding energy with a systematic increase in iodine concentration “ x ”.

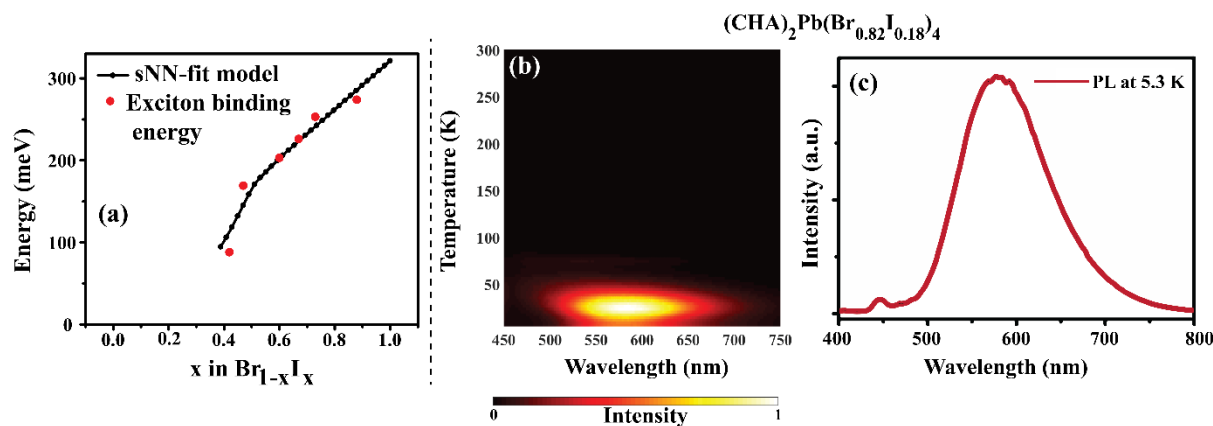


Figure 5.8: Exciton binding energy for different compositions of $(\text{CHA})_2\text{Pb}(\text{Br}_{1-x}\text{I}_x)_4$. (a) Composition dependence of the exciton binding energy (red dots) obtained from DNN generated data of Figure 5.7. The variation of exciton binding energy with composition is fitted (black line-symbol) using a shallow neural-network (sNN) model. The sNN fit helps us to predict the composition “ x ” for a targeted exciton binding energy. For example, for $x = 0.18$ i.e., for the sample $(\text{CHA})_2\text{Pb}(\text{Br}_{0.82}\text{I}_{0.18})_4$, sNN model suggests very small exciton binding energy. (b) The temperature-dependent experimental PL pseudocolormap of $(\text{CHA})_2\text{Pb}(\text{Br}_{0.82}\text{I}_{0.18})_4$ shows absence of significant exciton emission, even at low temperatures, agreeing with the very small exciton binding energy predicted by Figure 5.8a. (c) PL recorded from $(\text{CHA})_2\text{Pb}(\text{Br}_{0.82}\text{I}_{0.18})_4$ crystals at 5.3 K.

The red dots in Figure 5.8a show the exciton binding energy (obtained from Figure 5.7) values of $(\text{CHA})_2\text{Pb}(\text{Br}_{1-x}\text{I}_x)_4$ as a function of the composition “ x ”. The composition dependence is fitted with a sNN model. The fitting obtains <1% error from the measured exciton binding energies of Figure 5.7. The predicted values from this fitted model are plotted as the black line-symbol. The supposed linear behavior predicted by the model at $x < 0.5$ might not be entirely accurate, as the experimental data points used for this fitting range are limited. But the model provides a qualitative trend in this lower iodine composition region. For example, the model suggests very small exciton binding energy at $x < 0.2$. To verify that, we synthesized a composition with $x = 0.18$. Based on the optical band gap of $(\text{CHA})_2\text{Pb}(\text{Br}_{0.82}\text{I}_{0.18})_4$, the exciton

emission is expected at around 460 nm at room temperature. The temperature-dependent experimental PL pseudocolormap in Figure 5.8b does not show significant exciton emission even at 5.3 K. Instead, the PL is dominated by a STE with peak around 578 nm, along with a small feature around 447 nm observed at 5.3 K, probably originating from the exciton resonance (Figure 5.8c). This result agrees with the prediction (Figure 5.8a) of very small exciton binding energy for $x = 0.18$.

Finally, we have used DNN to predict optical absorption spectra of $(\text{CHA})_2\text{Pb}(\text{Br}_{1-x}\text{I}_x)_4$ single crystals, and correlated the optical bandgap with halide compositions. The band edges of halide perovskites are defined by orbitals of metal and halogen. The band gap is expected to decrease with decreasing halide ion's electronegativity in its composition.⁴⁸ The subtle changes in the structural parameters, e.g., bond length and angles, are known to impart significant change in the observed bandgap and thereby, band gap does not vary linearly with composition "x".⁴⁹ We prepared eight single crystal samples of $(\text{CHA})_2\text{Pb}(\text{Br}_{1-x}\text{I}_x)_4$ with varying "x" and measured their absorption spectra (Figure 5.9). These absorption spectra are obtained by Kubelka-Munk transformation of the diffused reflectance spectra.³⁴

The experimental absorption spectra of five of these samples ($x = 0.42, 0.47, 0.67, 0.88, 1.0$) are used to train a DNN model. Similar to the model for obtaining temperature-dependent PL spectrum, the model here is also trained till the accuracy of the predicted absorption spectra is >90% compared to the corresponding experimental absorption spectra of a given composition. We note that more numbers of the experimental samples are required in the low-iodine composition region to map the compositional change more precisely. So, we have limited the DNN training in the composition range $0.4 < x < 1.0$

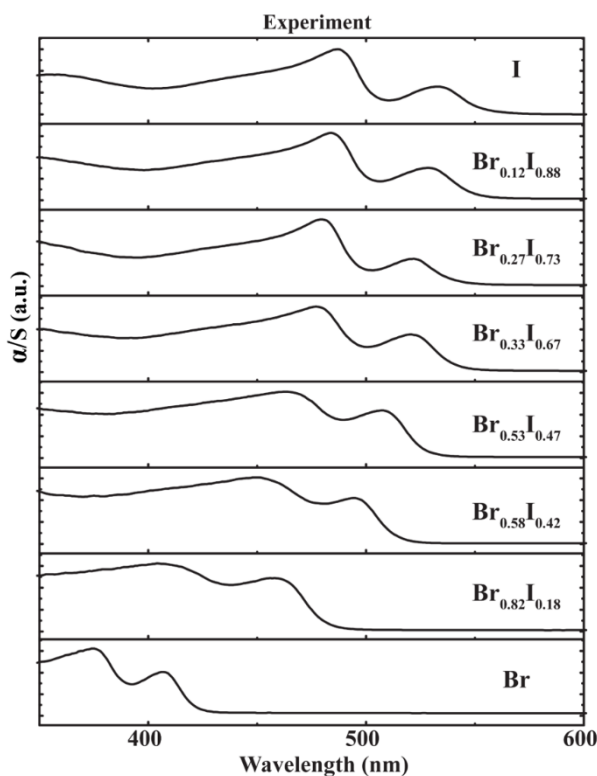


Figure 5.9: UV-visible absorption spectra of $(\text{CHA})_2\text{Pb}(\text{Br}_{1-x}\text{I}_x)_4$ single crystals. The absorption spectra are obtained from the measured diffused reflectance spectra. Here, α is the absorption coefficient and S is the scattering coefficient.

After the completion of the training, DNN can predict the optical absorption spectra for any composition in between $x = 0.4$ and 1. Figure 5.10 shows the DNN predicted absorption spectra for a few representative compositions. For validation, we have compared the DNN spectra with experimental absorption spectra for samples with $x = 0.6$ and 1. Note that the absorption spectra for $x = 0.6$ was not part of the set that is used for training the network while the spectra for $x = 1$ was included in the training. The DNN generated absorption spectra match well with the experimental ones. DNN allows us to generate optical absorption spectra (and estimate band gap) for a large number of compositions, other than the experimentally prepared compositions ($x = 0.42, 0.47, 0.67, 0.88, 1.0$). However, in the present case, we can not map the composition dependent change in absorption co-efficient as our choice of samples are in single crystalline form where surface roughness varies from crystal to crystal, and so does the scattering properties.

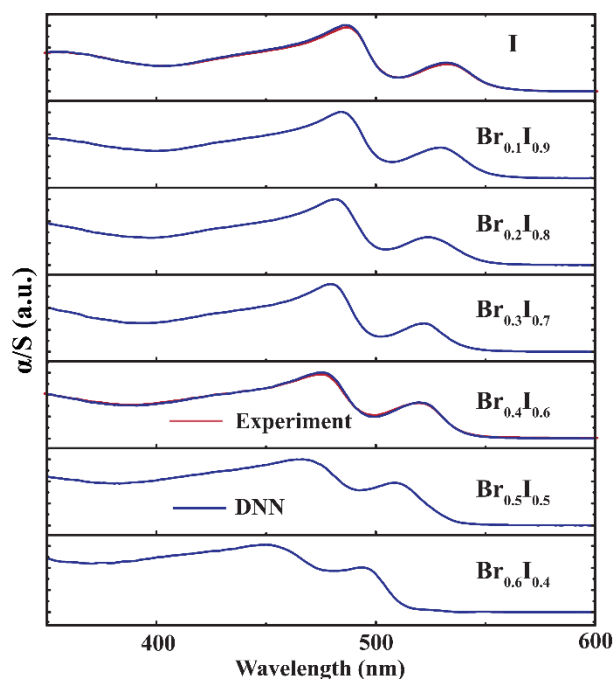


Figure 5.10: Composition dependence of optical absorption spectra of $(\text{CHA})_2\text{Pb}(\text{Br}_{1-x}\text{I}_x)_4$ single crystals. DNN generated absorption spectra of a few representative compositions, and comparison with experimental data for $x = 1$ and 0.6 . The experimental data are measured in the diffused reflectance mode and then converted to absorption data by using Kubelka-Munk transformation, where α is the absorption coefficient and S is the scattering coefficient.

5.4 Conclusions

We have demonstrated that a machine learning method, DNN can successfully generate PL and optical absorption spectra of 2D layered hybrid perovskites at different temperatures and compositions. Experimental PL spectra of $(\text{PEA})_2\text{PbI}_4$ at seven different temperatures are used to train the DNN model, which in turn generates a hundred PL spectra at different temperatures in the range of 5 to 300 K. Such DNN model decreases the experiment time significantly. These DNN generated PL spectra are used for estimating exciton binding energies of $(\text{EA})_2\text{PbI}_4$ and $(\text{CHA})_2\text{Pb}(\text{Br}_{1-x}\text{I}_x)_4$ with varying “ x ”. The exciton binding energy increases from 88 meV for $x = 0.42$ to 274 meV for $x = 0.88$ of $(\text{CHA})_2\text{Pb}(\text{Br}_{1-x}\text{I}_x)_4$. This trend in exciton binding energy is the result of increasing dielectric and quantum confinement of the excitons with increasing iodine content. To further explore the utility of DNN, we have generated the composition dependent optical absorption spectra of $(\text{CHA})_2\text{Pb}(\text{Br}_{1-x}\text{I}_x)_4$ series of samples at any value of $0.4 \leq x \leq 1$. This method of analysing optical properties will be beneficial for sensitive samples

and also for quick exploration of different materials, to search for a desired exciton property. Importantly, the construction and employment of such DNN models are simple and all tools required for the same are freely available. The main caveat of this presented method remains that it does not take into account the structural changes and electronic many-body interactions for generating predictions of optical properties and, is completely dependent on experimental data. This is also the reason why properties which change drastically from sample to sample (e.g., composition dependence of the STE in PL spectrum) can not be reliably predicted. While this approach makes it useful where first-principle based predictions (time-dependent DFT, or GW+BSE) are difficult, it only remains scientifically reliable where a coarse dataset can be experimentally obtained and, the DNN generated dataset can be experimentally validated.

5.5 References

- (1) Kojima, A.; Teshima, K.; Shirai, Y.; Miyasaka, T. Organometal Halide Perovskites as Visible-Light Sensitizers for Photovoltaic Cells. *J. Am. Chem. Soc.* **2009**, *131*, 6050-6051.
- (2) Yangui, A.; Garrot, D.; Lauret, J. S.; Lusson, A.; Bouchez, G.; Deleporte, E.; Pillet, S.; Bendeif, E. E.; Castro, M.; Triki, S.; et al. Optical Investigation of Broadband White-Light Emission in Self-Assembled Organic–Inorganic Perovskite (C₆H₁₁NH₃)₂PbBr₄. *J. Phys. Chem. C* **2015**, *119*, 23638-23647.
- (3) Miyata, A.; Mitioglu, A.; Plochocka, P.; Portugall, O.; Wang, J. T.-W.; Stranks, S. D.; Snaith, H. J.; Nicholas, R. J. Direct Measurement of the Exciton Binding Energy and Effective Masses for Charge Carriers in Organic–Inorganic Tri-Halide Perovskites. *Nat. Phys.* **2015**, *11*, 582-587.
- (4) Guo, Z.; Wu, X.; Zhu, T.; Zhu, X.; Huang, L. Electron-Phonon Scattering in Atomically Thin 2D Perovskites. *ACS Nano* **2016**, *10*, 9992-9998.

- (5) Zhai, Y.; Baniya, S.; Zhang, C.; Li, J.; Haney, P.; Sheng, C.-X.; Ehrenfreund, E.; Vardeny, Z. V. Giant Rashba Splitting in 2D Organic-Inorganic Halide Perovskites Measured by Transient Spectroscopies. *Sci. Adv.* **2017**, *3*, e1700704.
- (6) Mao, L.; Stoumpos, C. C.; Kanatzidis, M. G. Two-Dimensional Hybrid Halide Perovskites: Principles and Promises. *J. Am. Chem. Soc.* **2019**, *141*, 1171-1190.
- (7) Mohanty, A.; Swain, D.; Govinda, S.; Row, T. N. G.; Sarma, D. D. Phase Diagram and Dielectric Properties of $\text{MA}_{1-x}\text{FA}_x\text{PbI}_3$. *ACS Energy Lett.* **2019**, *4*, 2045-2051.
- (8) Zhong, J.-X.; Wu, W.-Q.; Liao, J.-F.; Feng, W.; Jiang, Y.; Wang, L.; Kuang, D.-B. The Rise of Textured Perovskite Morphology: Revolutionizing the Pathway toward High-Performance Optoelectronic Devices. *Adv. Energy Mater.* **2020**, *10*, 1902256.
- (9) Bera, S.; Behera, R. K.; Pradhan, N. α -Halo Ketone for Polyhedral Perovskite Nanocrystals: Evolutions, Shape Conversions, Ligand Chemistry, and Self-Assembly. *J. Am. Chem. Soc.* **2020**, *142*, 20865-20874.
- (10) Rastogi, P.; Chu, A.; Greboval, C.; Qu, J.; Noumbe, U. N.; Chee, S. S.; Goyal, M.; Khalili, A.; Xu, X. Z.; Cruguel, H.; et al. Pushing Absorption of Perovskite Nanocrystals into the Infrared. *Nano Lett.* **2020**, *20*, 3999-4006.
- (11) Chakrabarty, A.; Satija, S.; Gangwar, U.; Sapra, S. Precursor-Mediated Synthesis of Shape-Controlled Colloidal CsPbBr_3 Perovskite Nanocrystals and Their Nanofiber-Directed Self-Assembly. *Chem. Mater.* **2020**, *32*, 721-733.
- (12) Shi, E.; Yuan, B.; Shiring, S. B.; Gao, Y.; Akriti; Guo, Y.; Su, C.; Lai, M.; Yang, P.; Kong, J.; et al. Two-Dimensional Halide Perovskite Lateral Epitaxial Heterostructures. *Nature* **2020**, *580*, 614-620.
- (13) Katan, C.; Mercier, N.; Even, J. Quantum and Dielectric Confinement Effects in Lower-Dimensional Hybrid Perovskite Semiconductors. *Chem. Rev.* **2019**, *119*, 3140-3192.

- (14) Passarelli, J. V.; Mauck, C. M.; Winslow, S. W.; Perkinson, C. F.; Bard, J. C.; Sai, H.; Williams, K. W.; Narayanan, A.; Fairfield, D. J.; Hendricks, M. P.; et al. Tunable Exciton Binding Energy in 2D Hybrid Layered Perovskites through Donor-Acceptor Interactions within the Organic Layer. *Nat. Chem.* **2020**, *12*, 672-682.
- (15) Zhang, H.-Y.; Song, X.-J.; Chen, X.-G.; Zhang, Z.-X.; You, Y.-M.; Tang, Y.-Y.; Xiong, R.-G. Observation of Vortex Domains in a Two-Dimensional Lead Iodide Perovskite Ferroelectric. *J. Am. Chem. Soc.* **2020**, *142*, 4925-4931.
- (16) Sheikh, T.; Nawale, V.; Pathoor, N.; Phadnis, C.; Chowdhury, A.; Nag, A. Molecular Intercalation and Electronic Two Dimensionality in Layered Hybrid Perovskites. *Angew. Chem. Int. Ed.* **2020**, *59*, 11653-11659.
- (17) Nawale, V. V.; Sheikh, T.; Nag, A. Dual Exciton Emission in Hybrid 2D Layered Tin Iodide Perovskites. *J. Phys. Chem. C* **2020**, *124*, 21129–21136.
- (18) Long, G.; Sabatini, R.; Saidaminov, M. I.; Lakhwani, G.; Rasmita, A.; Liu, X.; Sargent, E. H.; Gao, W. Chiral-Perovskite Optoelectronics. *Nat. Rev. Mater.* **2020**, *5*, 423-439.
- (19) Goldschmidt, V. M. Die Gesetze der Krystallochemie. *Naturwissenschaften* **1926**, *14*, 477-485.
- (20) Chakraborty, R.; Nag, A. Dielectric Confinement for Designing Compositions and Optoelectronic Properties of 2D Layered Hybrid Perovskites. *Phys. Chem. Chem. Phys.* **2021**, *23*, 82-93.
- (21) Wang, N.; Cheng, L.; Ge, R.; Zhang, S.; Miao, Y.; Zou, W.; Yi, C.; Sun, Y.; Cao, Y.; Yang, R.; et al. Perovskite Light-Emitting Diodes Based on Solution-Processed Self-Organized Multiple Quantum Wells. *Nat. Photonics* **2016**, *10*, 699-704.
- (22) Sun, B.; Xu, Y.; Chen, Y.; Huang, W. Two-Dimensional Ruddlesden–Popper Layered Perovskite for Light-Emitting Diodes. *APL Mater.* **2020**, *8*, 040901.

- (23) Zhu, X.; Xu, Z.; Zuo, S.; Feng, J.; Wang, Z.; Zhang, X.; Zhao, K.; Zhang, J.; Liu, H.; Priya, S.; et al. Vapor-Fumigation for Record Efficiency Two-Dimensional Perovskite Solar Cells with Superior Stability. *Energy Environ. Sci.* **2018**, *11*, 3349-3357.
- (24) Gong, X.; Voznyy, O.; Jain, A.; Liu, W.; Sabatini, R.; Piontkowski, Z.; Walters, G.; Bappi, G.; Nokhrin, S.; Bushuyev, O.; et al. Electron–Phonon Interaction in Efficient Perovskite Blue Emitters. *Nat. Mater.* **2018**, *17*, 550-556.
- (25) Wang, S.; Ma, J.; Li, W.; Wang, J.; Wang, H.; Shen, H.; Li, J.; Wang, J.; Luo, H.; Li, D. Temperature-Dependent Band Gap in Two-Dimensional Perovskites: Thermal Expansion Interaction and Electron–Phonon Interaction. *J. Phys. Chem. Lett.* **2019**, *10*, 2546-2553.
- (26) Deretzis, I.; Alberti, A.; Pellegrino, G.; Smecca, E.; Giannazzo, F.; Sakai, N.; Miyasaka, T.; Magna, A. L., Atomistic Origins of CH₃NH₃PbI₃ Degradation to PbI₂ in Vacuum. *Appl. Phys. Lett.* **2015**, *106*, 131904.
- (27) Hofstetter, Y. J.; García-Benito, I.; Paulus, F.; Orlandi, S.; Grancini, G.; Vaynzof, Y., Vacuum-Induced Degradation of 2D Perovskites. *Front. Chem.* **2020**, *8*, 66.
- (28) Rupp, M.; Ramakrishnan, R.; von Lilienfeld, O. A. Machine Learning for Quantum Mechanical Properties of Atoms in Molecules. *J. Phys. Chem. Lett.* **2015**, *6*, 3309-3313.
- (29) Gómez-Bombarelli, R.; Aguilera-Iparraguirre, J.; Hirzel, T. D.; Duvenaud, D.; Maclaurin, D.; Blood-Forsythe, M. A.; Chae, H. S.; Einzinger, M.; Ha, D.-G.; Wu, T.; et al. Design of Efficient Molecular Organic Light-Emitting Diodes by A High-Throughput Virtual Screening and Experimental Approach. *Nat. Mater.* **2016**, *15*, 1120-1127.
- (30) Ghosh, K.; Stuke, A.; Todorović, M.; Jørgensen, P. B.; Schmidt, M. N.; Vehtari, A.; Rinke, P. Deep Learning Spectroscopy: Neural Networks for Molecular Excitation Spectra. *Adv. Sci.* **2019**, *6*, 1801367.

- (31) Stoumpos, C. C.; Cao, D. H.; Clark, D. J.; Young, J.; Rondinelli, J. M.; Jang, J. I.; Hupp, J. T.; Kanatzidis, M. G. Ruddlesden–Popper Hybrid Lead Iodide Perovskite 2D Homologous Semiconductors. *Chem. Mater.* **2016**, *28*, 2852-2867.
- (32) Yao, D.; Zhang, C.; Zhang, S.; Yang, Y.; Du, A.; Waclawik, E.; Yu, X.; Wilson, G. J.; Wang, H. 2D–3D Mixed Organic–Inorganic Perovskite Layers for Solar Cells with Enhanced Efficiency and Stability Induced by n-Propylammonium Iodide Additives. *ACS Appl. Mater. Inter.* **2019**, *11*, 29753-29764.
- (33) Chakraborty, R.; Nag, A. Correlation of Dielectric Confinement and Exciton Binding Energy in 2D Layered Hybrid Perovskites Using Temperature-dependent Photoluminescence. *J. Phys. Chem. C* **2020**, *124*, 16177-16185.
- (34) Eickhoff, T.; Grosse, P.; Theiss, W. Diffuse Reflectance Spectroscopy of Powders. *Vib. Spectrosc.* **1990**, *1*, 229-233.
- (35) Tensorflow. <https://github.com/tensorflow/tensorflow.git>. (accessed January 7, 2021).
- (36) Kingma, D. P.; Ba, J. Adam: A Method for Stochastic Optimization. **2017**, arXiv:Computer Science - Machine Learning/1412.6980 [cs.LG]. arXiv.org e-print archive. <https://arxiv.org/abs/1412.6980> (accessed January 7, 2021).
- (37) Leyden, M. R.; Matsushima, T.; Qin, C.; Ruan, S.; Ye, H.; Adachi, C. Amplified Spontaneous Emission in Phenylethylammonium Methylammonium Lead Iodide Quasi-2D Perovskites. *Phys. Chem. Chem. Phys.* **2018**, *20*, 15030-15036.
- (38) Fang, H.-H.; Yang, J.; Adjokatse, S.; Tekelenburg, E.; Kamminga, M. E.; Duim, H.; Ye, J.; Blake, G. R.; Even, J.; Loi, M. A. Band-Edge Exciton Fine Structure and Exciton Recombination Dynamics in Single Crystals of Layered Hybrid Perovskites. *Adv. Funct. Mater.* **2020**, *30*, 1907979.

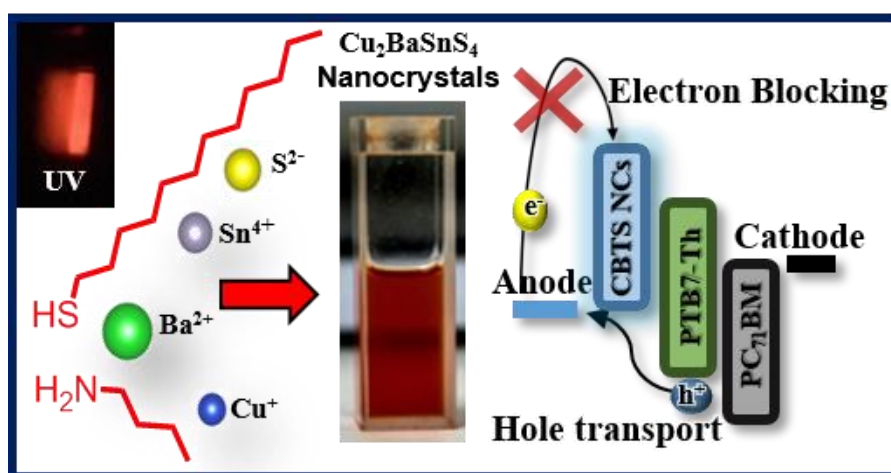
- (39) Ma, D.; Fu, Y.; Dang, L.; Zhai, J.; Guzei, I. A.; Jin, S. Single-Crystal Microplates of Two-Dimensional Organic–Inorganic Lead Halide Layered Perovskites for Optoelectronics. *Nano Res.* **2017**, *10*, 2117-2129.
- (40) Li, S.; Luo, J.; Liu, J.; Tang, J. Self-Trapped Excitons in All-Inorganic Halide Perovskites: Fundamentals, Status, and Potential Applications. *J. Phys. Chem. Lett.* **2019**, *10*, 1999-2007.
- (41) Paritmongkol, W.; Powers, E. R.; Dahod, N. S.; Tisdale, W. A. Two Origins of Broadband Emission in Multilayered 2D Lead Iodide Perovskites. *J. Phys. Chem. Lett.* **2020**, *11*, 8565-8572.
- (42) Zhou, G.; Su, B.; Huang, J.; Zhang, Q.; Xia, Z. Broad-Band Emission in Metal Halide Perovskites: Mechanism, Materials, and Applications. *Mater. Sci. Eng. R Rep.* **2020**, *141*, 100548.
- (43) Yin, J.; Maity, P.; Naphade, R.; Cheng, B.; He, J. H.; Bakr, O. M.; Bredas, J. L.; Mohammed, O. F. Tuning Hot Carrier Cooling Dynamics by Dielectric Confinement in Two-Dimensional Hybrid Perovskite Crystals. *ACS Nano* **2019**, *13*, 12621-12629.
- (44) Savenije, T. J.; Ponseca, C. S.; Kunneman, L.; Abdellah, M.; Zheng, K.; Tian, Y.; Zhu, Q.; Canton, S. E.; Scheblykin, I. G.; Pullerits, T.; et al. Thermally Activated Exciton Dissociation and Recombination Control the Carrier Dynamics in Organometal Halide Perovskite. *J. Phys. Chem. Lett.* **2014**, *5*, 2189-2194.
- (45) Dohner, E. R.; Jaffe, A.; Bradshaw, L. R.; Karunadasa, H. I. Intrinsic White-Light Emission from Layered Hybrid Perovskites. *J. Am. Chem. Soc.* **2014**, *136*, 13154-13157.
- (46) Li, S.; Luo, J.; Liu, J.; Tang, J. Self-Trapped Excitons in All-Inorganic Halide Perovskites: Fundamentals, Status, and Potential Applications. *J. Phys. Chem. Lett.* **2019**, *10*, 1999-2007.

- (47) Traore, B.; Pedesseau, L.; Assam, L.; Che, X.; Blancon, J.-C.; Tsai, H.; Nie, W.; Stoumpos, C. C.; Kanatzidis, M. G.; Tretiak, S. et al. Composite Nature of Layered Hybrid Perovskites: Assessment on Quantum and Dielectric Confinements and Band Alignment. *ACS Nano* **2018**, *12*, 3321-3332.
- (48) Pisanu, A.; Coduri, M.; Morana, M.; Ciftci, Y. O.; Rizzo, A.; Listorti, A.; Gaboardi, M.; Bindi, L.; Quelo, V. I. E.; Milanese, C. et al. Exploring the Role of Halide Mixing in Lead-Free BZA₂SnX₄ Two Dimensional Hybrid Perovskites. *J. Mater. Chem. A* **2020**, *8*, 1875-1886.
- (49) Goyal, A.; McKechnie, S.; Pashov, D.; Tumas, W.; van Schilfgaarde, M.; Stevanović, V. Origin of Pronounced Nonlinear Band Gap Behavior in Lead–Tin Hybrid Perovskite Alloys. *Chem. Mater.* **2018**, *30*, 3920-3928.

Appendix

Appendix A

Colloidal Synthesis, Optical Properties and Hole Transport Layer Applications of $\text{Cu}_2\text{BaSnS}_4$ (CBTS) Nanocrystals



The work presented in this chapter has led to the following publication:

Chakraborty, R.; Sim, K. M.; Shrivastava, M.; Adarsh, K. V.; Chung, D. S.; Nag, A. Colloidal Synthesis, Optical Properties and Hole Transport Layer Applications of $\text{Cu}_2\text{BaSnS}_4$ (CBTS) Nanocrystals. *ACS Appl. Energy Mater.* **2019**, 2, 3049-3055. Copyright permission has been taken from ACS publication for full paper.

Abstract

$\text{Cu}_2\text{BaSnS}_4$ (CBTS) is an emerging earth abundant and environmentally benign semiconductor. But there is no prior report of colloidal CBTS nanocrystals. Here we developed a colloidal synthesis of CBTS nanocrystals by rational design. Photophysical properties of these nanocrystals are elucidated using absorption and photoluminescence spectroscopy. A ligand exchange protocol is implemented to stabilize the nanocrystals in both polar and nonpolar solvents. Finally, thin films of CBTS nanocrystals grown at room temperature is used as hole transport layer (HTL) in organic photodiode yielding a high peak specific detectivity ($>3.2 \times 10^{12}$ Jones) with low noise equivalent power (9.20×10^{-14} W Hz^{0.5}). These results suggest that our colloidal CBTS nanocrystals have potentials for optoelectronic applications.

A.1 Introduction

Earth-abundant, environmentally benign and low-cost solution processed materials are desired for large scale optoelectronic applications. For example, $\text{Cu}_2\text{ZnSn}(\text{S}_x\text{Se}_{1-x})_4$ (CZTSSe) and related compositions have been reported as solution processed earth abundant materials, showing solar cell efficiency of $\sim 13\%$.¹⁻³ Colloidal NCs of CZTSSe also showed interesting optoelectronic properties.⁴⁻⁷ But it has been found that the similarity in ionic radius (r_i), and coordination number (CN), particularly between Cu and Zn gives rise to intrinsic anti-site defects (Cu_{Zn} and Zn_{Cu}) in CZTSSe.⁸ To overcome such cationic disorder, it was suggested that the Zn^{2+} ($r_i = 0.74 \text{ \AA}$, CN = 4) can be replaced with Ba^{2+} ($r_i = 1.56 \text{ \AA}$, CN = 8),⁹ forming $\text{Cu}_2\text{BaSn}(\text{S}_x\text{Se}_{1-x})_4$ (CBTSSe).¹⁰⁻¹²

Both theoretical (high defect formation energy) and experimental studies (narrow band-edge PL, lower band tailing) suggest the minimal presence of deep cation (Cu-Ba and Cu-Sn) antisite defects in CBTSSe.¹⁰⁻¹² Early results show promising optoelectronic applications of CBTSSe with solar cell efficiency of 5.2%,¹² high efficiency ($\sim 12 \text{ mA/cm}^2$ at 0 V/RHE)¹³ of CBTSSe based photoelectrochemical (PEC) reduction of water to H_2 ,¹⁴ and as hole transport layer (HTL)¹⁵ in perovskite solar cell. But one of the material design problems is poor solubility of precursors for solution processed synthesis of CBTSSe. Particularly, solution processibility of Ba precursors is limited, which probably is the main reason for the absence of prior report on colloidal synthesis of CBTS NCs. Two interesting reports emerged recently reporting molecular precursor inks to form solution processed films of CBTS.^{16, 17} In both reports, films of molecular ink were first prepared, which were then annealed at $> 350 \text{ }^\circ\text{C}$ giving rise to CBTS films. But till date, there is no report of forming CBTS composition dispersed in solution phase, unlike the case of colloidal CZTS NCs. Therefore, forming solution-processed films of CBTS at low temperatures ($< 150 \text{ }^\circ\text{C}$), or using high surface area of CBTS NCs for future catalytic applications are not possible. Also, colloidal dispersion of nanocrystals allows us to study their

intrinsic optical absorption and emission properties, in the absence of the effect of substrate and scattering effect. All these aspects motivated us to prepare colloidal CBTS NCs.

Here, we report the first colloidal synthesis of CBTS NCs and studied their optical and hole transport properties. We employed a different strategy for synthesis, where colloidal CBTS NCs (not molecular precursors) are prepared in solution phase. These NCs can be dispersed in a range of both polar and non-polar solvents by appropriate surface engineering. Films of CBTS NCs prepared at room temperature show superior hole transport and electron blocking performances compared to commonly used PEDOT:PSS, in organic photodiode (OPD).

A.2 Experimental Section

A.2.1 Chemicals. Copper (I) Iodide (CuI , 99.999%, Aldrich), tin (IV) bis(acetylacetonate) dichloride ($\text{Sn}(\text{acac})_2\text{Cl}_2$, 98%, Aldrich), barium acetylacetonate hydrate ($\text{Ba}(\text{acac})_2 \cdot x\text{H}_2\text{O}$, Aldrich), thioacetamide ($\geq 99\%$, Sigma-Aldrich), 1-dodecanethiol (DDT, $\geq 98\%$, Aldrich), n-butylamine (BA, 99.5%, Aldrich), oleylamine (70%, Aldrich), chloroform ($\geq 99\%$, Aldrich), toluene (99.8%, Aldrich), chloroform-d(99.8 atom % D, Aldrich), ethanol, formamide ($\geq 98\%$, Fluka), ammonium sulphide solution (40-48 wt. % in H_2O , Sigma-Aldrich), and acetonitrile (anhydrous, 99.8%, Sigma-Aldrich), poly(3,4-ethylenedioxythiophene) doped with poly(styrene sulfonate)(PEDOT:PSS, Clevios), (poly([2,6'-4,8-di(5-ethylhexylthienyl)benzo[1,2-b;3,3-b]dithiophene](3-fluoro-2[(2-ethylhexyl)carbonyl]thieno[3,4-b]thiophenediyl))) (PTB7-Th, 1-Materials), ([6,6]-Phenyl-C71-butyric acid methyl ester)(PC71BM, 1-Materials).

A.2.2 Synthesis of $\text{Cu}_2\text{BaSnS}_4$ (CBTS) nanocrystals (NCs). In a three neck round bottomed (RB) flask, 0.25 mmol $\text{Sn}(\text{acac})_2\text{Cl}_2$, 0.25 mmol $\text{Ba}(\text{acac})_2 \cdot x\text{H}_2\text{O}$, 0.5 mmol CuI , and 1 mmol thioacetamide (TAA) were taken. N_2 was purged into this RB and 1.5 mL DDT along with 3 mL BA were added to it. Subsequent processes were carried out under inert N_2 atmosphere. The mixture was stirred and it was heated up to 65 °C and kept for 7 hours. In a separate RB,

10 mL oleylamine was degassed by application of vacuum and N_2 gas alternatively at $120\text{ }^\circ\text{C}$ for about two hours. This dried oleylamine, after cooling to $\sim 70\text{ }^\circ\text{C}$ was injected to the CBTS reaction mixture and the temperature was raised to $115\text{ }^\circ\text{C}$. This temperature was maintained for 3 hours, after which, the mixture was cooled to $25\text{ }^\circ\text{C}$ by using an ice-bath. Under vigorous stirring, 5 mL toluene was added to it and stirred for five minutes. The mixture was then brought into the room environment. Then the mixture was centrifuged at 6500 rpm for 4 minutes. The precipitate was well dispersed in toluene, followed by addition of ethanol until the solution becomes cloudy. This cloudy solution was centrifuged at 7500 rpm for 4 minutes. The precipitate was then dispersed in 2 mL CHCl_3 and centrifuged at 7000 rpm for 3 minutes to separate larger sized crystals. The supernatant containing colloidal CBTS NCs was used for further analysis.

A.2.3 S^{2-} Ligand Exchange. For the ligand exchange reactions, 200 μL $(\text{NH}_4)_2\text{S}$ was mixed with 5 mL Formamide. This was added slowly into a vial containing 5 mL ($\sim 10\text{ mg/mL}$) CBTS NC dispersion in CHCl_3 . Both solution/dispersion form separate phases, which are clearly visible by the difference in colors. This two-phase system was stirred vigorously for 15 minutes. Following which, the vial was not disturbed for two minutes. After the ligand exchange, the CHCl_3 phase turns colourless and the formamide phase becomes red, because of transfer of CBTS NCs to the formamide phase. The formamide phase was carefully separated out and acetonitrile was added dropwise until the solution becomes cloudy. The solution was then centrifuged at 7500 rpm for 4 minutes. The precipitate was redispersed in 2 mL of Formamide.

A.2.4 Characterization. PXRD measurements were performed using a Bruker D8 Advance X-ray diffractometer with $\text{Cu K}\alpha$ radiation (1.54 \AA). Reference PXRD pattern was taken from Crystal Diffract software. Transmission electron microscopy (TEM) experiments were carried out using JEOL JEM 2200 FS field emission transmission electron microscope at 200 kV. For

TEM measurements, dilute dispersions of colloidal NCs were drop casted on the carbon coated copper grids. Ultraviolet–visible (UV–vis) absorption spectra were taken using a Thermo Scientific (Evolution 300) UV–vis spectrometer. Steady-state PL and PL decay dynamics were carried out on FLS 980 (Edinburgh Instruments). Fourier transform infrared spectroscopy (FTIR) spectra were recorded using a Bruker ALPHA II FTIR , and Proton nuclear magnetic resonance (NMR) was recorded using a Bruker Avance operating at 400 MHz.

A.2.5 Calculation of excitonic Bohr diameter.

$$\text{Excitonic Bohr radius, } a_b = a_0 \varepsilon_r \frac{m_0}{\mu} \quad \text{Eq.(A.1)}$$

where $a_0 = 0.53 \text{ \AA}$

Relative permittivity, $\varepsilon_r = 5.4$ for CBTS

Rest mass of electron, $m_0 = 9.11 \times 10^{-31} \text{ kg}$

Reduced mass of exciton, $\mu = 1 / \left(\frac{1}{m_e} + \frac{1}{m_h} \right)$

For CBTS, effective mass of electron, $m_e = 0.33 m_0$, and of hole, $m_h = 1.31 m_0$.

Putting these values in the equation A.1, we get $a_b = 1.1 \text{ nm}$.

$$\begin{aligned} \text{Then Excitonic Bohr diameter} &= 2 \times a_b \\ &= 2.2 \text{ nm} \end{aligned}$$

Values for ε_r , m_e , and m_h for bulk CBTS are taken from ref¹⁸.

A.2.6 Application of CBTS NCs in organic photodiode (OPD).

OPD related experiments are carried out by K. M. Sim and D. S. Chung at Department of Energy Science & Engineering, Daegu Gyeongbuk Institute of Science & Technology (DGIST), Daegu, Republic of Korea.

A.2.6.1 OPD Fabrication: The patterned ITO (indium tin oxide) glasses were cleaned with detergent, distilled water, acetone, isopropanol by sequential sonication each for 10 min. The PEDOT:PSS (poly(3,4-ethylenedioxythiophene) doped with poly(styrene sulfonate)) layer was

fabricated by using spin-coating at 5000 rpm for 60 s. Then the PEDOT:PSS coated ITO glass was annealed at 150 °C for 10 min. The CBTS NCs layer was fabricated with CBTS NCs dispersion (6 mg/mL) by using spin-coating at 5000 rpm for 60 s. Then the CBTS NCs layer was washed with methanol to remove residual ligand. Then PTB7-Th (poly([2,6'-4,8-di(5-ethylhexylthienyl)benzo[1,2-b;3,3-b]dithiophene](3-fluoro-2[(2-ethylhexyl)carbonyl]thieno[3,4-b]thiophenediyl))) and PC71BM ([6,6]-Phenyl-C71-butyric acid methyl ester) solution of 21 mg/mL in chlorobenzene was spin-coated on the HTL (hole transport layer). LiF and Al were deposited through a shadow mask with a thermal evaporator at the deposition rate of 0.5–1 Å s⁻¹ and the vacuum pressure of ~10⁻⁶ Torr.

A.2.6.2 Film and Device Characterization: Ultraviolet photoelectron spectroscopy (UPS) experiments were performed in an ultrahigh-vacuum chamber (base pressure ≈ 10⁻¹⁰ Torr) with ESCALAB 250Xi of Thermo Scientific. Results were corrected for charging effects using an Au reference sample. The current density–voltage (*J*–*V*) characteristics were measured using a Keithley 2450 under monochromatic illumination from a 150-W Xenon arc lamp assembled with a 1/8-m monochromator. The photocurrent spectra were measured by synchronizing the monochromator with the source meter. The noise measurements were conducted with a SR 830 Lock-In amplifier. For the measurement of the LDR, a monochromator and a 520-nm laser (1.5 × 10⁻¹ W cm⁻²) were used. To measure the 3-dB frequency, the same laser was used with a TDS5052 digital phosphor oscilloscope (Tektronix) with a measured light intensity of 1 μW cm⁻²

A.2.6.3 *J_d*-*V* curve analysis to calculate ideality factor: Equation A.5 can be re-written as

$$\frac{dV}{dJ_d} = \frac{\eta kT}{q(J_d + J_s)} + R_s \quad \text{Eq.(A.2)}$$

In equation A.2, ideality factor was calculated by using slope of the dV/dJ_d^{-1} vs. J_d^{-1} plot.¹⁹⁻²¹

A.2.6.4 Space charge limited current (SCLC) analysis to calculate mobility of both OPDs with CBTS and PEDOT:PSS as a HTL.^{22, 23}

Au/HTLs/Au structure was introduced and the experimentally obtained J - V plots were fitted with Mott-Gurney equation

$$J = \frac{9}{8} \varepsilon_r \varepsilon_0 \frac{E^2}{L} \mu \quad \text{Eq.(A.3)}$$

where E is the electric field, L is the thickness of the active layer, and ε_r and ε_0 is the relative dielectric constant and the permittivity of free space, respectively.

A.2.6.5 Operating Speed and LDR of OPD: In many cases of photodiode applications, photodiodes are required to have high operation speed and ability to detect a wide range of light intensities. In particular, the operating speed of OPDs in an electronic device determines the bandwidth of the signal transmission and signal conversion. Also, the range of measurable light is an essential element for expressing the brightness and color of an image. Operating speed of OPDs is represented by -3 dB cutoff frequency with external pulsed illumination. -3 dB cutoff frequency means that a frequency for which the output signal current of the OPDs is -3 dB of the initial signal current. Because the both of HTLs are so thin that it cannot affect the resistance and transit time within the device, the OPDs with CBTS NCs HTL show -3 dB cutoff frequency of 12.5k dB which is similar to the 12.3k of OPDs with PEDOT:PSS. In the case of conventional imaging application, they are operated with frame rates of around 100 frames/s.²⁴ The value of 12.5k dB of OPDs with CBTS NCs HTL is sufficiently fast for video applications. In order to extract the correct signal from the light, it is important to have a constant responsivity for wide range of light intensities. This is expressed as LDR, which is defined as

$$\text{LDR} = 20 \log\left(\frac{J_{max}}{J_{min}}\right) \quad \text{Eq.(A.4)}$$

where J_{max} and J_{min} are the maximum and minimum value of the measurable current density, respectively. The LDR of OPD with PEDOT:PSS and CBTS NCs are measured under 0.1 V.

In the case of OPD with PEDOT:PSS HTL, the value of LDR is 85 dB due to the high noise current. However, in the case of OPD with CBTS NCs HTL, the noise current was suppressed by the high injection barrier, and high LDR value of 150 dB was shown. The LDR value is comparable to the LDR of recently reported high performance OPDs.^{25, 26}

A.3 Results and Discussion

A.3.1 Synthesis, characterization and surface modifications of colloidal CBTS NCs.

McCarthy et al recently reported a molecular ink as precursor for $\text{Cu}_2\text{BaSnS}_4$ by dissolution of metal sulphides (BaS and Cu_2S) and oxide (SnO) in an ethanedithiol (EDT)-ethylenediamine (EN) 1:4 v/v mixture at 50 °C for 11 days, followed by gentle heating with a heat gun.¹⁶ Such a binary solvent couple of a short chain thiol and EN (termed as “alkahest”) has been used previously to dissolve bulk inorganic materials as precursors for many similar semiconductor materials including CZTSe and $\text{Cu}(\text{In,Ga})\text{Se}_2$.²⁷⁻³⁰ We anticipate two major problems for the synthesis of colloidal NCs: (i) the solvent couple is so aggressive that it will disintegrate any NCs (in case it forms) to molecular species, and (ii) absence of suitable capping ligands that can provide colloidal stability to NCs. To overcome these problems, we need a solvent system that is aggressive enough to dissociate Ba precursor (along with other precursors), but it should be mild enough such that the targeted NCs do not disintegrate. Therefore, more soluble precursors and less aggressive solvent mixture are required. Then in the presence of suitable surface capping ligands, colloidal CBTS NCs can be obtained.

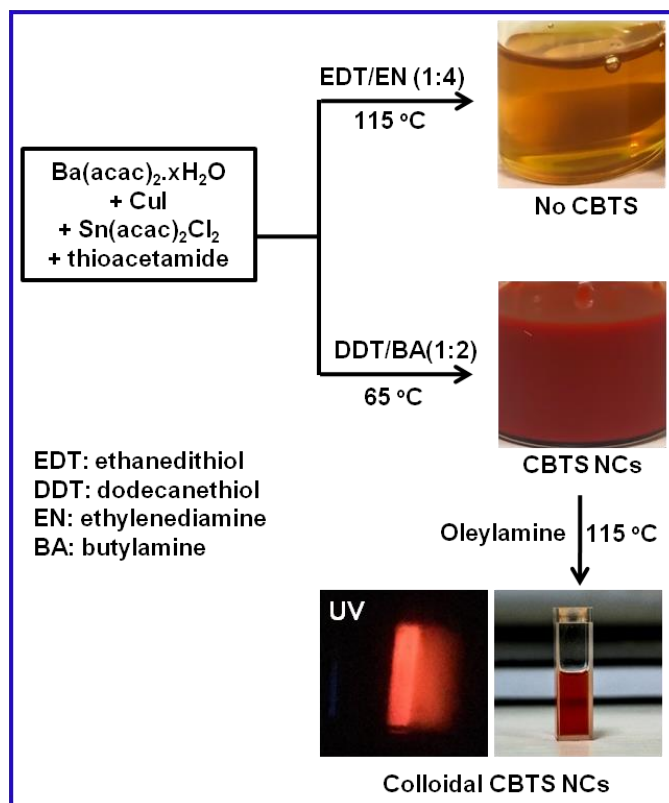


Figure A.1: Synthesis of colloidal CBTS NCs: Schematics representing the synthesis design of organic capped colloidal CBTS NCs.

To achieve more soluble precursors, we used halide and acetylacetonate (acac) salt of metals (see Figure A.1), instead of using metal sulphides and oxides reported by McCarthy et al¹⁶. This step was motivated by the prior report²⁸ suggesting metal halide and acetylacetonate salts have better solubility in alkaline systems. Then we included thioacetamide in the reaction mixture as source for sulphide. Thioacetamide decomposes at lower temperature (~ 100 °C) compared to other molecular sulphide sources.³¹ When we took 0.25 mmol $\text{Ba}(\text{acac})_2 \cdot x\text{H}_2\text{O}$, 0.25 mmol of $\text{Sn}(\text{acac})_2\text{Cl}_2$, 0.5 mmol CuI and 1 mmol thioacetamide in the 1:4 v/v EDT/EN solvent mixture and heated at 115 °C, a clear yellow solution is obtained within 10 hours (Figure 1). This is significantly faster than 11 days required with sulfide and oxide precursors with the same solvent mixture.¹⁶ This result suggests a better solubility of precursors, particularly $\text{Ba}(\text{acac})_2 \cdot x\text{H}_2\text{O}$ over BaS in the solvent mixture. But 1:4 v/v EDT/EN solvent mixture is still very aggressive forming yellow molecular solution, but it did not form colloidal CBTS NCs.

It was suggested earlier that a longer alkyl chain with single functional group is less aggressive alkali solvent.³⁰ So we replaced EDT with DDT, and EN with butylamine (BA) in the solvent mixture. When the reaction is carried out in 1:2 v/v DDT/BA solvent mixture, a turbid red colored dispersion is obtained instead of a clear yellow solution obtained with EDT/EN solvent mixture (Figure 1). The turbidity may occur because of supersaturation of the precursors, but the color difference (yellow to red) suggests formation of a new product.

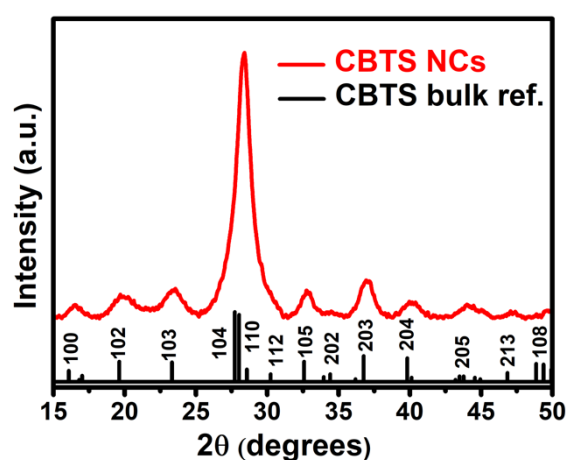


Figure A.2: PXRD data of the turbid product obtained first step of the reaction in 1:2 v/v mixture of DDT/BA. It confirms the formation of CBTS NCs in the expected trigonal phase.

PXRD of the red turbid product in Figure A.2 confirms the formation phase pure CBTS NCs with trigonal phase. We note that, similar CBTS NCs are also prepared using DDT/EN solvent mixture, but we preferred BA over EN because of corrosive hazardous nature of EN and also EN has poor miscibility with DDT. Although CBTS NCs are formed in DDT/BA, the NCs are not colloidal stable and precipitate out. To improve the colloidal stability, we stirred the reaction mixture containing CBTS with dried oleylamine at 115 °C for 3 hours (see Figure A.1). The obtained colloidal CBTS NCs are stable emitting light under UV radiation. Based on these findings, our final reaction is the two-step process discussed in Figure A.1, but carried out in a three neck round bottomed flask maintaining N_2 atmosphere. Figure A.3 shows the change in the appearance of reaction mixture during various stages of the reaction. Subsequently, CBTS NCs are isolated and dispersed in a nonpolar solvent.

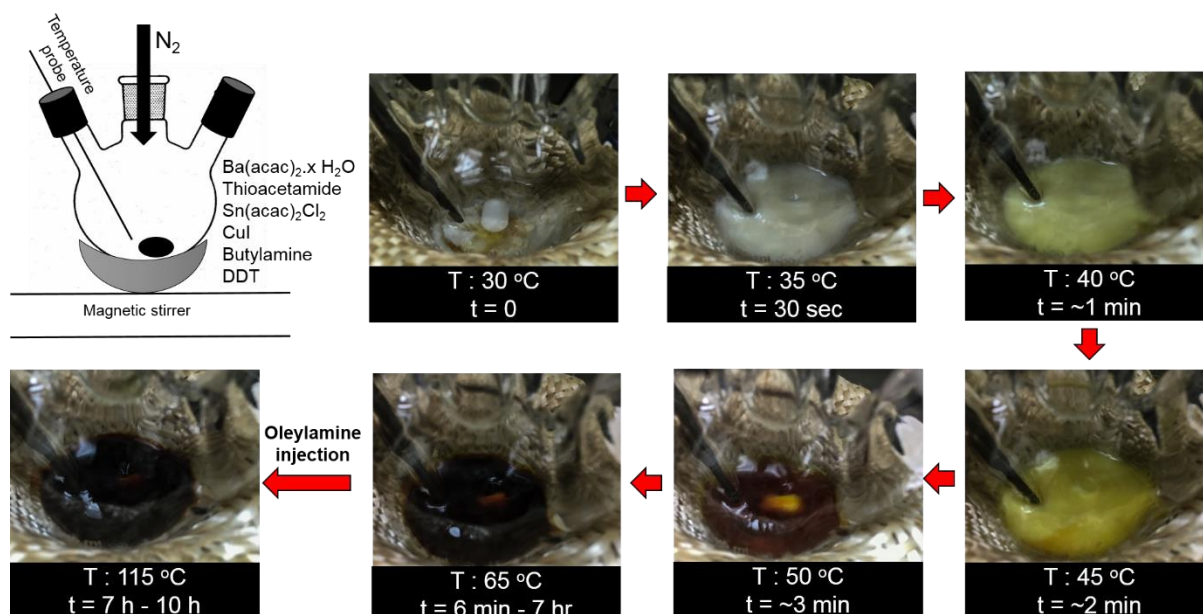


Figure A.3: Photographs showing the different stages of synthesis of colloidal CBTS NCs.

PXRD patterns in Figure A.4a confirm the formation of trigonal phase of CBTS NCs, similar to their bulk counterparts.¹⁴ The broad nature of PXRD peaks suggests the nanometer-sized crystals. Transmission electron microscopy (TEM) image in Figure A.4b and corresponding selected area electron diffraction (SAED) pattern in Figure A.4c confirm the formation of CBTS NCs. Shapes of NCs are somewhat irregular, but Figure A.4d suggest an average size (approximated diameter) of NCs is 12 ± 2.5 nm. High resolution TEM image in Figure A.4e of SI show lattice fringes of 3.2 \AA interplanar distance corresponding to the (110) or (104) planes of trigonal CBTS lattice. Proton nuclear magnetic resonance (NMR) data in Figure A.4f suggest that the surfaces of CBTS NCs are mainly capped with oleylamine along with possible contribution from DDT.

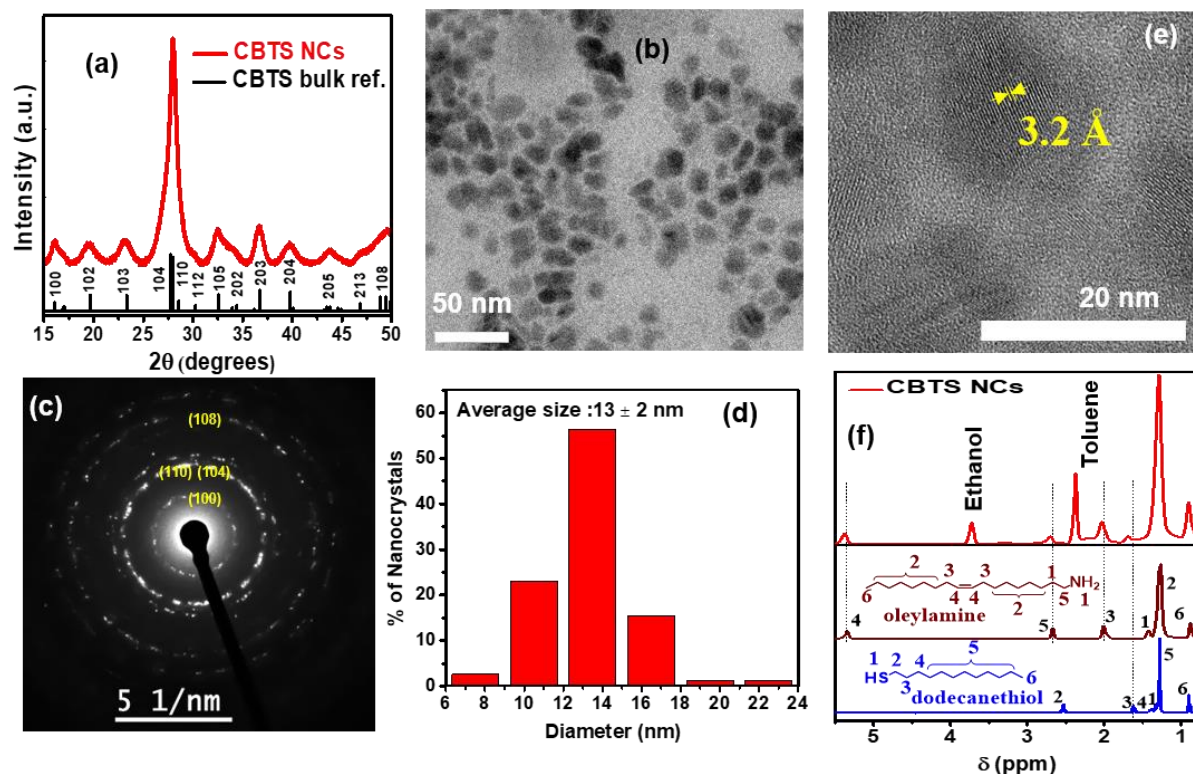


Figure A.4: Structural characterization of CBTS NCs. (a) PXRD pattern, (b) TEM image, (c) Selected area electron diffraction (SAED) pattern (d) Size distribution plot obtained from TEM images (e) HRTEM image showing the 3.2 Å interplanar distance.

UV-visible absorption spectrum of colloidal CBTS NCs in Figure A.5a and corresponding Tauc plot in Figure A.5b suggest a bandgap of 2.1 eV (~590 nm), agreeing with prior reports¹⁴ of bulk CBTS. The absence of a significant effect of quantum confinement in our CBTS NCs is expected since the size of NCs is significantly larger than the calculated Bohr excitonic diameter of 2.2 nm. PL peak at 2.03 eV (Figure A.5a), corresponds to the band edge emission of CBTS NCs. PL decay dynamics in A.5c show ~55% contribution from nonradiative decay channels with lifetime <1 ns, along with radiative decay channels with lifetimes 3.4 and 12.1 ns. Note that the solution phase optical absorption and emission properties of CBTS are free from contribution arising due to substrates and scattering.

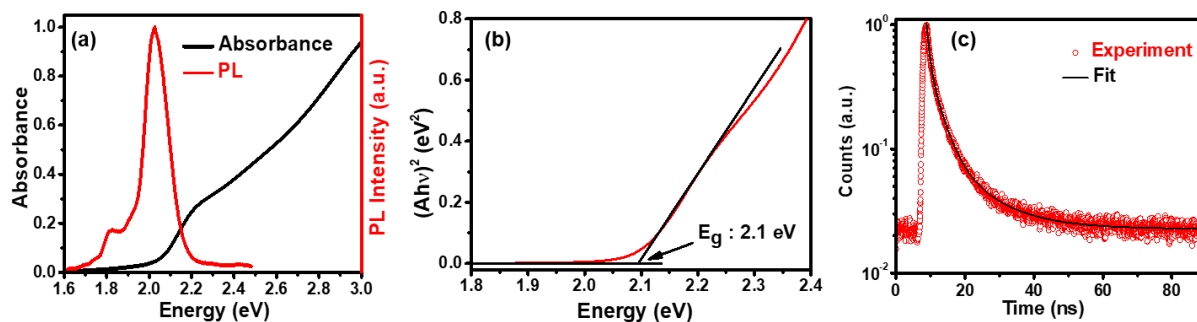


Figure A.5: Optical characterization of CBTS NCs. (a) UV-visible absorption and PL spectra of organic capped CBTS NCs. (b) Tauc plot corresponding to UV-visible absorption spectrum in Figure A.5a. Direct bandgap of CBTS is considered. (c) PL decay dynamics fitted using a tri-exponential decay. The obtained lifetimes are $\tau_1 = 0.8$ ns with contribution $a_1 = 55\%$, $\tau_2 = 3.4$ ns with $a_2 = 38\%$, and $\tau_3 = 12.1$ ns with contribution $a_3 = 7\%$.

These organic capped CBTS NCs form colloidal dispersions in nonpolar media like hexane, chloroform, and toluene. To get rid of the organic ligands, and make colloidal dispersion of CBTS in polar solvents, we carried out S^{2-} ligand exchange following a reported³²⁻³⁴ protocol. Red colored organic capped NCs are dispersed in chloroform and are immiscible polar solvent formamide. But after the ligand exchange reaction with $(\text{NH}_4)_2\text{S}$, the sulfide capped CBTS easily transfers to the formamide phase leaving behind the colorless chloroform phase (Figure A.6a). Fourier transform infrared spectroscopy (FTIR) spectra in Figure A.6b show almost disappearance of the doublet bands at 2852 and 2922 cm^{-1} corresponding to C-H stretching in the original organic ligands, after the S^{2-} ligand exchange reaction. These results confirm the success of ligand exchange reaction. S^{2-} capped NCs can be dispersed in a series of polar solvents like DMF, DMSO, formamide, and water. Figure A.6c-d show that dispersing the CBTS NCs in these polar solvents preserves the Therefore, our colloidal synthesis and surface modification allow colloidal dispersion of CBTS NCs in a wide range of both nonpolar and polar solvents, as shown in Figure A.6e. This diversity of solvents for colloidal CBTS NCs will be useful to fabricate device/film for various applications. But it is to be noted that the S^{2-} capped nanocrystals tend to get agglomerated when stored in the ambient condition probably because of oxidation of S^{2-} ions. Importantly, when the ligand exchange and further processing

are carried out inside an N_2 -filled glove box, the colloidal dispersion of S^{2-} capped CBTS are stable for more than 7 days.

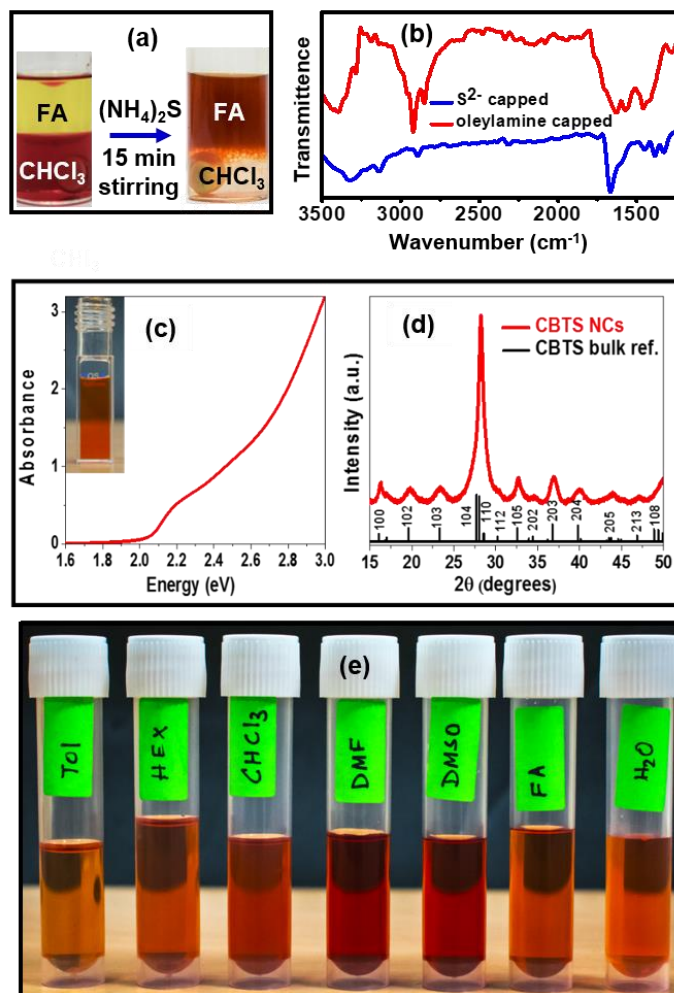


Figure A.6: Surface engineering of CBTS NCs. (a) Photographs showing ligand exchange reaction. Organic ligands from NC surface are replaced by S^{2-} ligands. Consequently, NCs transfer from nonpolar CHCl_3 phase to polar formamide (FA) phase after the S^{2-} ligand exchange. (b) FTIR spectra of CBTS NCs showing the exchange organic ligands with S^{2-} ligands. (c) Optical absorption spectrum of S^{2-} capped CBTS NCs dispersed in water. Inset shows the colloidal dispersion of NCs in water. (d) PXRD pattern of the S^{2-} capped CBTS NCs after precipitating from water dispersion. (e) CBTS NCs in both nonpolar and polar solvents with varying range of static dielectric constant (ϵ). Tol: toluene ($\epsilon = 2.4$), Hex: hexane ($\epsilon = 1.6$), CHCl_3 ($\epsilon = 4.8$), DMF: N,N-dimethylformamide ($\epsilon = 36.7$), DMSO: dimethyl sulfoxide ($\epsilon = 46.7$), FA: formamide ($\epsilon = 111$), H_2O ($\epsilon = 80$).

A.3.2 HTL application of CBTS NCs film in a OPD. After the synthesis and optical properties, we explore these newly developed colloidal CBTS NCs for optoelectronic application. We explore hole transport and electron blocking properties of our CBTS NCs in

OPDs. Thin film ($<1\mu\text{m}$) OPDs are now emerging as a key technology of next-generation image sensors because of direct band, along with flexibility, and transparency of organic semiconductors.^{35,36} HTL in an OPD plays an important role to extract holes to anode but also to prevent injection of unwanted electron from anode to active layer to simultaneously decrease the dark current and increase the external quantum efficiency (EQE) of the OPD. So far PEDOT:PSS is the most widely used HTL in OPDs. However, hygroscopicity and acidic surface condition of PEDOT:PSS is known to cause poor driving stability as well as low devices stability.^{37,38} Furthermore, semi-metallic property with deep LUMO level bring about recombination loss in OPD.^{39,40} Hence, it is desired to develop new HTL materials. Since, CBTS can transport holes at low temperature, and our solution processed CBTS NC films can be formed at low temperatures, we explored the HTL properties of CBTS NC films in OPDs. In order to utilize the CBTS NCs as a hole transport layer, it is necessary to have appropriate electrical and optical properties between the electrode and the photoactive layer. In order to comparatively study out-of-plane charge transport behavior of both HTLs, hole-only-device architecture of Au/CBTS(PEDOT:PSS)/Au is employed and charge carrier mobility is extracted by means of conventional space charge limited current (SCLC) analyses.^{41,42} The obtained hole mobility values of CBTS NCs and PEDOT:PSS are 1.64×10^{-3} and 9.72×10^{-4} $\text{cm}^2 \text{V}^{-2} \text{s}^{-1}$, respectively. Considering that SCLC mobility of PEDOT:PSS in previous reports were in the range of $5 \times 10^{-8} - 1.57 \times 10^{-4}$ $\text{cm}^2 \text{V}^{-2} \text{s}^{-1}$, we can conclude that room temperature processed CBTS NCs can possess high enough hole mobility for HTL application. Also, the transmittance of CBTS NCs film with 40 nm thickness is above 90% in the visible range. The energy band diagram of the CBTS NCs film in the Figure 4a is determined by ultraviolet photoelectron spectroscopy (UPS) in Figure A.7b and c. HOMO level and Fermi level of the CBTS NCs were calculated by using onset of secondary electron cut-off region and the low binding energy region of UPS spectra in comparison to PEDOT:PSS. As such, HOMO and

LUMO levels of CBTS NCs are optimal for both hole transport and electron blocking, respectively, the most important properties of a HTL.

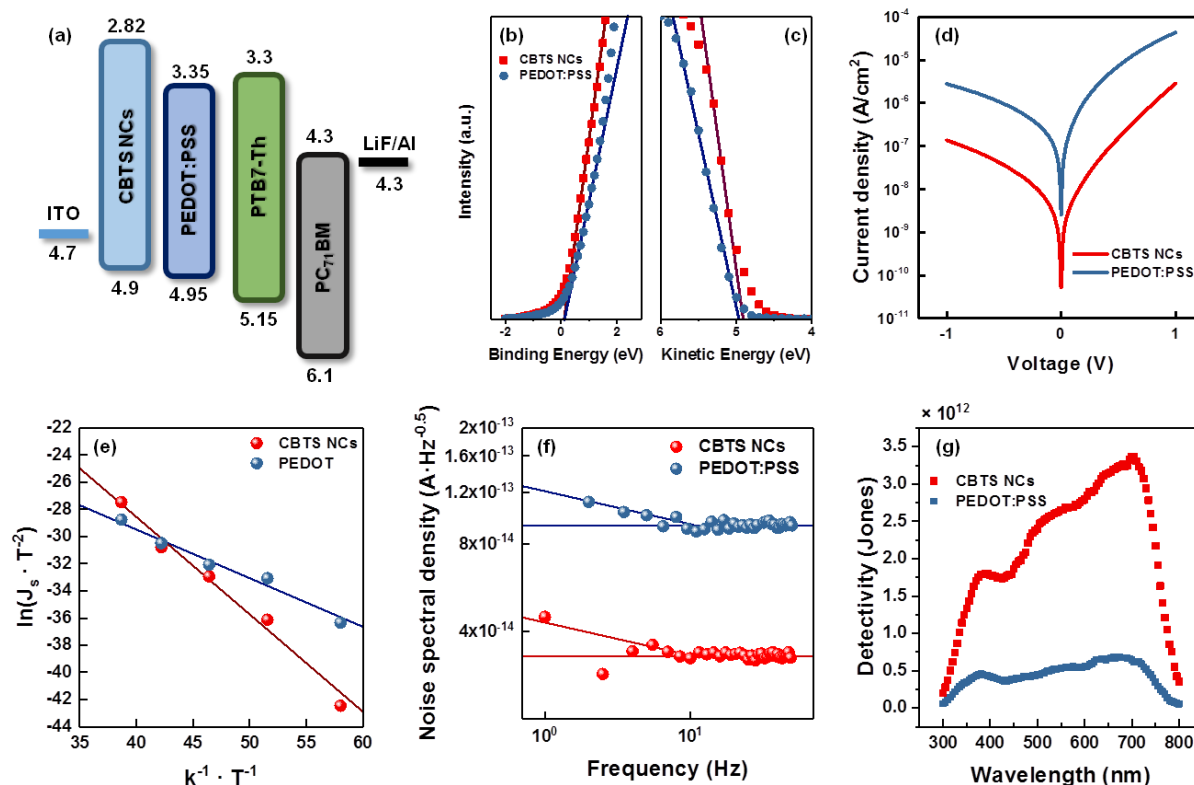


Figure A.7: The HTL performances of CBTS NCs. (a) Energy diagram for layered OPD structure. PTB7-Th: poly([2,6'-4,8-di(5-ethylhexylthienyl)benzo[1,2-b;3,3-b]dithiophene][3-fluoro-2[(2-ethylhexyl)carbonyl]thieno[3,4-b]thiophenediyl)); PC₇₁BM: [6,6]-Phenyl-C71-butyric acid methyl ester. (b-c) UPS spectra of (b) the low binding energy region to calculate the energy distance from HOMO edge to Fermi level and (c) the low kinetic energy region to define work function. (d) J_d - V characteristics, (e) $\ln(J_s T^{-2})$ versus $k^{-1}T^{-1}$ plots to calculate effective barrier height, (f) noise spectral density and (g) specific detectivity (D^*) of each OPDs with CBTS NCs and PEDOT:PSS as a HTL. Data acquisition, analysis and discussion by K. M. Sim and D. S. Chung from DGIST, Republic of Korea.

In order to test the feasibility of CBTS NCs as HTL of OPDs, ITO/HTL (PEDOT:PSS or CBTS NCs)/PCE10:PC₇₀BM/LiF/Al structure was employed. Especially, to test noise suppression role of CBTS NCs, thin organic active layer thickness of 150 nm was used, which usually leads to high dark current and thus noise current. Note that in this case, overall OPD thickness can be maintained less than 500 nm, which can realize genuine merits of OPDs. Dark J_d - V relation in Figure A.7d show apparent difference between PEDOT:PSS and CBTS HTL measured at room temperature, with an order of lower dark current density throughout whole the reverse

bias regime in the case of CBTS NCs HTL. This can be attributed to higher injection barrier of electron from ITO to photo-active layer as speculated by energy level diagram (Figure A.7a). To quantitatively measure the effect of CBTS NCs on suppressing dark current injection, effective Schottky barrier height was measured by means of temperature-dependent dark J_d - V analyses of both PEDOT:PSS- and CBTS NCs-OPDs in the temperature range from 293 K to 173 K. The resulting J_d - V characteristics were analyzed using a typical diode equation:

$$J_d = J_s \left[\exp \left(\frac{q(V - J_d R_s)}{\eta k T} \right) - 1 \right] \quad \text{Eq.(A.5)}$$

where J_s is the dark saturation current density, V is the applied voltage, R_s is the series resistance, k is the Boltzmann's constant, T is the temperature, and η is the ideality factor.⁴³ With the assumption that the electron injection from ITO can be described by Schottky injection, the dark saturation current can be described by thermionic emission theory:

$$J_s = A^* T^2 \exp \left(\frac{-\phi_B}{k T} \right) \quad \text{Eq.(A.6)}$$

where A^* is the Richardson constant, and ϕ_B is the effective barrier height. Therefore, the slope of $\ln(J_s T^2)$ versus $(kT)^{-1}$ plot can provide ϕ_B .²⁰ In Figure A.7e, $\ln(J_s T^2)$ vs. $(k_B T)^{-1}$ plots are summarized. The obtained effective barrier height of CBTS NCs-OPD was found to be 0.8 eV, which is significantly higher than 0.4 eV of PEDOT:PSS-OPD, supporting the abovementioned dark current suppressing effect of CBTS NCs as HTL. Assisted by the deeply suppressed dark current, low noise current density could be obtained for CBTS NCs-OPD as summarized in Figure A.7f, and thus high detectivity OPD could be realized as shown in Figure A.7g. A low noise equivalent power of $9.20 \times 10^{-14} \text{ W Hz}^{0.5}$ and a high peak specific detectivity (D^*) over 3.2×10^{12} Jones could be obtained from CBTS NCs-OPD despite of thin film active layer thickness ($\sim 150 \text{ nm}$), revealing the ideal HTL role of CBTS NCs.

A.4 Conclusions

In conclusion, colloidal CBTS NCs are synthesized for the first time. The reaction condition is designed rationally overcoming the problem of dissolution Ba and other precursors, and at the same time providing colloidal stability of organic capped CBTS NCs. The organic capped NCs disperse in nonpolar solvents like chloroform, toluene and hexane. The same NCs, after replacing organic ligands with S^{2-} , form colloidal dispersion in polar solvents like DMSO, DMF and formamide. To test the quality of colloidal CBTS NCs for low-temperature solution processed optoelectronic applications, we used NCs film (~ 40 nm) as HTL in OPD. The results show CBTS NCs exhibit better hole transport and electron blocking capabilities, compared to popular PEDOT:PSS HTL. Low noise equivalent power of 9.20×10^{-14} W $\text{Hz}^{0.5}$ and a high peak specific detectivity (D^*) over 3.2×10^{12} Jones are obtained using thin (~ 150 nm) active layer. These results suggest CBTS NCs-OPD are promising for photodetector. Overall, the novel synthesis, optical properties, and HTL application of colloidal CBTS NCs will help to develop solution processed and earth-abundant semiconductors.

A.5 References

- (1) Katagiri, H.; Sasaguchi, N.; Hando, S.; Hoshino, S.; Ohashi, J.; Yokota, T. Preparation and Evaluation of $\text{Cu}_2\text{ZnSnS}_4$ Thin Films by Sulfurization of E-B Evaporated Precursors. *Sol. Energy Mater. Sol. Cells* **1997**, *49*, 407-414.
- (2) Wang, W.; Winkler, M. T.; Gunawan, O.; Gokmen, T.; Todorov, T. K.; Zhu, Y.; Mitzi, D. B. Device Characteristics of CZTSSe Thin-Film Solar Cells with 12.6% Efficiency. *Adv. Energy Mater.* **2014**, *4*, 1301465.
- (3) Wallace, S. K.; Mitzi, D. B.; Walsh, A. The Steady Rise of Kesterite Solar Cells. *ACS Energy Lett.* **2017**, *2*, 776-779.

- (4) Steinhagen, C.; Panthani, M. G.; Akhavan, V.; Goodfellow, B.; Koo, B.; Korgel, B. A. Synthesis of $\text{Cu}_2\text{ZnSnS}_4$ Nanocrystals for Use in Low-Cost Photovoltaics. *J. Am. Chem. Soc.* **2009**, *131*, 12554-12555.
- (5) Zhou, H. P.; Hsu, W. C.; Duan, H. S.; Bob, B.; Yang, W. B.; Song, T. B.; Hsu, C. J.; Yang, Y. CZTS Nanocrystals: A Promising Approach for Next Generation Thin Film Photovoltaics. *Energy Environ. Sci.* **2013**, *6*, 2822-2838.
- (6) Liu, Y.; Yao, D.; Shen, L.; Zhang, H.; Zhang, X. D.; Yang, B. Alkylthiol-Enabled Se Powder Dissolution in Oleylamine at Room Temperature for the Phosphine-Free Synthesis of Copper-Based Quaternary Selenide Nanocrystals. *J. Am. Chem. Soc.* **2012**, *134*, 7207-7210.
- (7) Larramona, G.; Bourdais, S.; Jacob, A.; Chone, C.; Muto, T.; Cuccaro, Y.; Delatouche, B.; Moisan, C.; Pere, D.; Dennler, G. 8.6% Efficient CZTSSe Solar Cells Sprayed from Water-Ethanol CZTS Colloidal Solutions. *J. Phys. Chem. Lett.* **2014**, *5*, 3763-3767.
- (8) Chen, S. Y.; Walsh, A.; Gong, X. G.; Wei, S. H. Classification of Lattice Defects in the Kesterite $\text{Cu}_2\text{ZnSnS}_4$ and $\text{Cu}_2\text{ZnSnSe}_4$ Earth-Abundant Solar Cell Absorbers. *Adv. Mater.* **2013**, *25*, 1522-1539.
- (9) Shannon, R. D. Revised Effective Ionic-Radii and Systematic Studies of Interatomic Distances in Halides and Chalcogenides. *Acta Crystallogr. A* **1976**, *32*, 751-767.
- (10) Shin, D.; Saporov, B.; Zhu, T.; Huhn, W. P.; Blum, V.; Mitzi, D. B. $\text{BaCu}_2\text{Sn}(\text{S},\text{Se})_4$: Earth-Abundant Chalcogenides for Thin-Film Photovoltaics. *Chem. Mater.* **2016**, *28*, 4771-4780.
- (11) Hong, F.; Lin, W. J.; Meng, W. W.; Yan, Y. F. Trigonal $\text{Cu}_2\text{-II-Sn-VI}_4$ (II = Ba, Sr and VI = S, Se) Quaternary Compounds for Earth-Abundant Photovoltaics. *Phys. Chem. Chem. Phys.* **2016**, *18*, 4828-4834.
- (12) Ge, J.; Koirala, P.; Grice, C. R.; Roland, P. J.; Yu, Y.; Tan, X. X.; Ellingson, R. J.; Collins, R. W.; Yan, Y. F. Oxygenated CdS Buffer Layers Enabling High Open-Circuit

Voltages in Earth-Abundant $\text{Cu}_2\text{BaSnS}_4$ Thin-Film Solar Cells. *Adv. Energy Mater.* **2017**, 7,1601803.

(13) Zhou, Y. H.; Shin, D.; Ngaboyamahina, E.; Han, Q. W.; Parker, C. B.; Mitzi, D. B.; Glass, J. T. Efficient and Stable $\text{Pt}/\text{TiO}_2/\text{CdS}/\text{Cu}_2\text{BaSn}(\text{S},\text{Se})_4$ Photocathode for Water Electrolysis Applications. *ACS Energy Lett.* **2018**, 3, 177-183.

(14) Ge, J.; Yu, Y.; Yan, Y. F. Earth-Abundant Trigonal $\text{BaCu}_2\text{Sn}(\text{Se}_x\text{S}_{1-x})_4$ ($x=0-0.55$) Thin Films with Tunable Band Gaps for Solar Water Splitting. *J. Mater. Chem. A* **2016**, 4, 18885-18891.

(15) Ge, J.; Grice, C. R.; Yan, Y. F. Cu-based Quaternary Chalcogenide $\text{Cu}_2\text{BaSnS}_4$ Thin Films Acting as Hole Transport Layers in Inverted Perovskite $\text{CH}_3\text{NH}_3\text{PbI}_3$ Solar Cells. *J. Mater. Chem. A* **2017**, 5, 2920-2928.

(16) McCarthy, C. L.; Brutchey, R. L. Solution Deposited $\text{Cu}_2\text{BaSnS}_{4-x}\text{Se}_x$ from a Thiol-Amine Solvent Mixture. *Chem. Mater.* **2018**, 30, 304-308.

(17) Teymur, B.; Zhou, Y. H.; Ngaboyamahina, E.; Glass, J. T.; Mitzi, D. B. Solution-Processed Earth-Abundant $\text{Cu}_2\text{BaSn}(\text{S},\text{Se})_4$ Solar Absorber Using a Low-Toxicity Solvent. *Chem. Mater.* **2018**, 30, 6116-6123.

(18) Ge, J.; Roland, P. J.; Koirala, P.; Meng, W. W.; Young, J. L.; Petersen, R.; Deutsch, T. G.; Teeter, G.; Ellingson, R. J.; Collins, R. W.; Yan, Y. F. Employing Overlayers To Improve the Performance of $\text{Cu}_2\text{BaSnS}_4$ Thin Film based Photoelectrochemical Water Reduction Devices. *Chem. Mater.* **2017**, 29, 916-920.

(19) Dou, L.; Yang, Y.; You, J.; Hong, Z.; Chang, W.-H.; Li, G.; Yang, Y. Solution-Processed Hybrid Perovskite Photodetectors with High Detectivity. *Nat. Commun.* **2014**, 5, 5404.

(20) Qi, B.; Zhou, Q.; Wang, J. Exploring the Open-Circuit Voltage of Organic Solar Cells under Low Temperature. *Sci. Rep.* **2015**, 5, 11363.

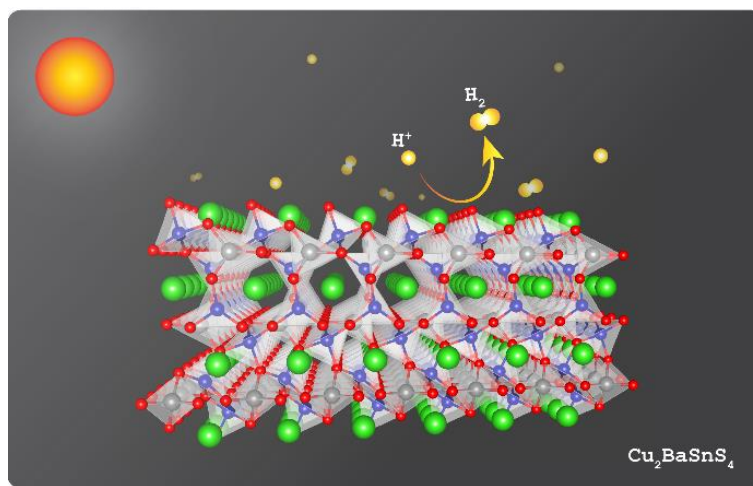
- (21) Sim, K. M.; Yoon, S.; Cho, J.; Jang, M. S.; Chung, D. S. Facile Tuning the Detection Spectrum of Organic Thin Film Photodiode via Selective Exciton Activation. *ACS Appl. Mater. Interfaces* **2018**, *10*, 8405-8410.
- (22) Pierre, A.; Deckman, I.; Lechêne, P. B.; Arias, A. C. High Detectivity All-Printed Organic Photodiodes. *Adv. Mater.* **2015**, *27*, 6411-6417.
- (23) Rafique, S.; Abdullah, S. M.; Shahid, M. M.; Ansari, M. O.; Sulaiman, K. Significantly Improved Photovoltaic Performance in Polymer Bulk Heterojunction Solar Cells with Graphene Oxide /PEDOT:PSS Double Decked Hole Transport Layer. *Sci. Rep.* **2017**, *7*, 39555.
- (24) Street, R. A.; Mulato, M.; Lau, R.; Ho, J.; Graham, J.; Popovic, Z.; Hor, J. Image Capture Array with an Organic Light Sensor. *Appl. Phys. Lett.* **2001**, *78*, 4193-4195.
- (25) Yoon, S.; Ha, J.; Cho, J.; Chung, D. S. Nonabsorbing Acceptor-Based Planar Heterojunction for Color-Selective and High-Detectivity Polymer Photodiodes. *Adv. Opt. Mater.* **2016**, *4*, 1933-1938.
- (26) Sung, M. J.; Yoon, S.; Kwon, S. K.; Kim, Y. H.; Chung, D. S. Synthesis of Phenanthro 1,10,9,8-cdefg carbazole-Based Conjugated Polymers for Green-Selective Organic Photodiodes. *ACS Appl. Mater. Interfaces* **2016**, *8*, 31172-31178.
- (27) Webber, D. H.; Brutchey, R. L. Alkahest for V_2VI_3 Chalcogenides: Dissolution of Nine Bulk Semiconductors in a Diamine-Dithiol Solvent Mixture. *J. Am. Chem. Soc.* **2013**, *135*, 15722-15725.
- (28) Yang, Y. C.; Wang, G.; Zhao, W. G.; Tian, Q. W.; Huang, L. J.; Pan, D. C. Solution-Processed Highly Efficient $\text{Cu}_2\text{ZnSnSe}_4$ Thin Film Solar Cells by Dissolution of Elemental Cu, Zn, Sn, and Se Powders. *ACS Appl. Mater. Interfaces* **2015**, *7*, 460-464.
- (29) McCarthy, C. L.; Webber, D. H.; Schueller, E. C.; Brutchey, R. L. Solution-Phase Conversion of Bulk Metal Oxides to Metal Chalcogenides Using a Simple Thiol-Amine Solvent Mixture. *Angew. Chem. Int. Ed.* **2015**, *54*, 8378-8381.

- (30) Zhao, X.; Lu, M. X.; Koeper, M. J.; Agrawal, R. Solution-Processed Sulfur Depleted Cu(In, Ga)Se₂ Solar Cells Synthesized from a Monoamine Dithiol Solvent Mixture. *J. Mater. Chem. A* **2016**, *4*, 7390-7397.
- (31) Zhou, Y.; Itoh, H.; Uemura, T.; Naka, K.; Chujo, Y. Preparation, Optical Spectroscopy, and Electrochemical Studies of Novel Pi-Conjugated Polymer-Protected Stable PbS Colloidal Nanoparticles in a Nonaqueous Solution. *Langmuir* **2002**, *18*, 5287-5292.
- (32) Nag, A.; Kovalenko, M. V.; Lee, J. S.; Liu, W. Y.; Spokoyny, B.; Talapin, D. V. Metal-free Inorganic Ligands for Colloidal Nanocrystals: S²⁻, HS⁻, Se²⁻, HSe⁻, Te²⁻, HTe⁻, TeS₃²⁻, OH⁻, and NH₂⁻ as Surface Ligands. *J. Am. Chem. Soc.* **2011**, *133*, 10612-10620.
- (33) Nag, A.; Zhang, H.; Janke, E.; Talapin, D. V. Inorganic Surface Ligands for Colloidal Nanomaterials. *Z. Phys. Chemie-Int. J. Res. Phys. Chem. Chem. Phys.* **2015**, *229*, 85-107.
- (34) Swarnkar, A.; Shanker, G. S.; Nag, A. Organic-Free Colloidal Semiconductor Nanocrystals as Luminescent Sensors for Metal Ions and Nitroaromatic Explosives. *Chem. Commun.* **2014**, *50*, 4743-4746.
- (35) Baeg, K. J.; Binda, M.; Natali, D.; Caironi, M.; Noh, Y. Y. Organic Light Detectors: Photodiodes and Phototransistors. *Adv. Mater.* **2013**, *25*, 4267-4295.
- (36) Jansen-van Vuuren, R. D.; Armin, A.; Pandey, A. K.; Burn, P. L.; Meredith, P. Organic Photodiodes: The Future of Full Color Detection and Image Sensing. *Adv. Mater.* **2016**, *28*, 4766-4802.
- (37) Park, H.; Kong, J. An Alternative Hole Transport Layer for Both ITO- and Graphene-Based Organic Solar Cells. *Adv. Energy Mater.* **2014**, *4*, 1301280.
- (38) Wang, Y. P.; Zhu, H. L.; Shi, Z. Z.; Wang, F. Z.; Zhang, B.; Dai, S. Y.; Tan, Z. A. Engineering the Vertical Concentration Distribution within the Polymer: Fullerene Blends for High Performance Inverted Polymer Solar Cells. *J. Mater. Chem. A* **2017**, *5*, 2319-2327.

- (39) Lenz, A.; Kariis, H.; Pohl, A.; Persson, P.; Ojamae, L. The Electronic Structure and Reflectivity of PEDOT:PSS from Density Functional Theory. *Chem. Phys.* **2011**, *384*, 44-51.
- (40) Bubnova, O.; Khan, Z. U.; Wang, H.; Braun, S.; Evans, D. R.; Fabretto, M.; Hojati-Talemi, P.; Dagnelund, D.; Arlin, J. B.; Geerts, Y. H. et al. Semi-Metallic Polymers. *Nat. Mater.* **2014**, *13*, 190-194.
- (41) Xu, H.; Fu, X.; Cheng, X.; Huang, L.; Zhou, D.; Chen, L.; Chen, Y. Highly and Homogeneously Conductive Conjugated Polyelectrolyte Hole Transport Layers for Efficient Organic Solar Cells. *J. Mater. Chem. A* **2017**, *5*, 14689-14696.
- (42) Niu, J.; Yang, D.; Ren, X.; Yang, Z.; Liu, Y.; Zhu, X.; Zhao, W.; Liu, S. Graphene-Oxide Doped PEDOT:PSS as a Superior Hole Transport Material for High-Efficiency Perovskite Solar Cell. *Org. Electron.* **2017**, *48*, 165-171.
- (43) Dou, L. T.; Yang, Y.; You, J. B.; Hong, Z. R.; Chang, W. H.; Li, G. Solution-Processed Hybrid Perovskite Photodetectors with High Detectivity. *Nat. Commun.* **2014**, *5*, 5404.

Appendix B

Mechanistic Insights of Hydrogen Evolution Reaction on $\text{Cu}_2\text{BaSnS}_4$ (CBTS) from First Principles



The work presented in this chapter has led to the following publication:

Chakraborty, R.; Ghosh, P. Mechanistic Insights of Hydrogen Evolution Reaction on Quaternary Earth-abundant Chalcogenide $\text{Cu}_2\text{BaSnS}_4$ from First Principles. *Appl. Surf. Sci.* **2021**, 570, 151049. Copyright permission has been taken from Elsevier publication for full paper.

Abstract

Photocatalytic conversion of water to produce hydrogen is an environment-friendly way of converting solar energy to chemical energy. In the last two decades, the quaternary chalcogenide family of semiconductors has become a potentially important class of materials for this purpose. Amongst them, earth-abundant and non-toxic $\text{Cu}_2\text{BaSnS}_4$ (CBTS) is emerging as a promising candidate for photocathode where the Hydrogen evolution reaction (HER) takes place. In this work, using first-principles DFT-based calculations, we have provided mechanistic insights into (photo-)electrochemical HER on low-indexed (001) and (110) CBTS surfaces. Our study suggests that amongst the different surfaces considered in this work, the metal-rich (110) termination will be the most efficient one for HER reaction. We believe our result will be beneficial for the future development of HER photocathodes employing this group of materials.

B.1 Introduction

With the rising concern regarding the negative impact of fossil fuels on the environment, the research to find alternate "green" energy sources has intensified. Hydrogen (H_2) obtained from photoelectrochemical (PEC) splitting of water is one source where the solar energy is converted and stored in chemical bonds.^{1,2} Further conversion of H_2 to its oxidized products releases this energy without negatively impacting the environment. PEC water splitting consists of two half-cell reactions: (a) reduction of H^+ ions at the cathode to produce H_2 (hydrogen evolution reaction, HER), and (b) oxidation of water at the anode to release oxygen (oxygen evolution reaction, OER). Of these two, OER is more sluggish, thereby reducing the overall Faradaic efficiency to a great extent.³ Additionally, the catalysts used for these reactions are typically expensive noble metals and their compounds, viz. Pt for HER and IrO_2 for OER.⁴ Hence there is much effort to find cheap and efficient catalysts for HER and OER as replacements for the existing ones.⁴⁻⁹ Usually, there have been two approaches, either to design a catalyst that is efficient for both the reactions or two separate catalysts for the two reactions.^{10, 11} This work focuses on exploring materials as possible catalysts for HER reaction only. Such a photocatalyst should satisfy the following criteria: (a) it should be an efficient photo absorber that absorbs a broad region of the solar spectrum, (b) the conduction and valence band of the photocatalyst should cradle the oxidation and reduction potentials of water splitting, (c) the reactants and products should have optimum binding strength on the catalyst such that they have sufficient stability on the catalyst surface during the occurrence of the reaction and the products can be easily desorbed.

The first criterion in the above list points to a semiconductor with a direct bandgap in the 1.5-2.0 eV range. The success of Kesterite $\text{Cu}_2\text{ZnSn}(\text{S}, \text{Se})_4$ (CZTSSe) as a photo absorber achieving ~12% photovoltaic efficiency is worth mentioning in this regard.¹² While it has a tunable direct bandgap in the prescribed range, the similarity in the atomic radius of Zn^{2+} and Sn^{4+} in these systems results in anti-site defects.¹³ In this premise, a few years ago, several

computational studies predicted a different class of materials where the small Zn^{2+} was substituted with larger sized Ba^{2+} or Sr^{2+} , to prevent the formation of anti-site disorders while retaining the bandgap similar to CZTSSe.^{14,15} One of these materials, trigonal Copper-Barium-thiostannate, $\text{Cu}_2\text{BaSnS}_4$ (CBTS), is emerging as a promising low-cost material for photovoltaic energy conversion and PEC.¹⁶⁻¹⁹ Bulk CBTS has a bandgap of ~ 2 eV.^{20, 21} Additionally, CBTS exhibits superior semiconducting properties like band-edge emission at room temperature, high carrier mobility, and good photovoltaic efficiency due to the absence of deep traps.²²⁻²⁴ Moreover, Mott-Schottky analysis by Ge *et al.* showed that the conduction and valence band edges of CBTS cradle the oxidation and reduction potentials^{16, 18, 25}, which is the second criterion for a good photocatalyst. Multiple reports have emerged in the last five years employing CBTS in photocathodes (where the Hydrogen evolution reaction occurs) for water electrolysis.^{26, 27} In a notable work, thin films of this material were used as a cocatalyst in photoelectrochemical water splitting.²⁸ Considerable efficiency was recorded from a near-stoichiometric composition. Further, the authors noticed that increasing or decreasing the presence of Cu has a detrimental effect on the catalytic performance. In a more recent study by Xie *et al.*, the authors obtained a significant photocurrent response of $4 \text{ mA}\cdot\text{cm}^{-2}$ for HER using large-grained CBTS films without using any cocatalysts.²⁹ However, to the best of our knowledge, in all these studies, no effort was directed to grow preferential facets selectively. As a result, the observed efficiencies were an averaged effect from multiple different crystal terminations.

Despite the multiple experimental studies reported in the literature, we observe no reports on the mechanistic aspect of HER on CBTS. For example, since this reaction occurs on the surface and CBTS has a complex structure, an important question would be which surface compositions would be efficient for HER on CBTS? Also, what is the preferred mechanism? The answers to these questions would help experimental researchers to tune the catalytic

performance by varying experimental conditions. This method has previously been observed to successfully enhance the catalytic activity of multiple chalcogenide HER catalysts like MoS_2 , FeS_2 , and NiS_2 .^{5, 30, 31}

The present work, to the best of our knowledge, is the first effort to understand the correlation between the structural and electronic properties of surfaces of CBTS with its HER activity. Specifically, using first-principles DFT calculations, we have studied the HER reaction on different terminations of (001) and (110) surfaces. Of these, we note that the (110) facets were found in large-grained thin films studied by Xie et al.²⁹ The rest of the chapter is organized as follows. First, we provide details of our DFT calculations and discuss the computational models used to study the bulk crystal and different surfaces in Section B.2. The structure and electronic properties of the surfaces are discussed in Section B.3.1. In Section B.3.2, we correlate these electronic properties with the adsorption energy of hydrogen on these surfaces. The HER mechanism on these surfaces is probed in Section B.3.3. A conclusion is drawn in Section B.4.

B.2 Computational Details

B.2.1 Details of DFT calculations.

All the calculations were performed using the open-source Quantum Espresso (QE) package, a plane wave implementation of DFT.³² The spin-polarized version of DFT was implemented for all calculations. The exchange and correlation functionals were described by the generalized gradient approximation (GGA) of Perdew–Burke–Ernzerhof (PBE).³³ Since Cu contains *d*-electrons, electron-electron correlation effects are important. However, these are not correctly captured by conventional GGA-PBE functionals. Hence, we have performed PBE+U calculations to determine the structure, electronic properties, and interactions of the different surface terminations with H. Based on the literature report by Hong et al., we have applied $U=8.5$ eV on Cu 3d orbitals.¹⁴ We note that previous computational work on this material, U has also been applied on Sn-*d* states. However, these states are occupied and lie deep in energy.

Consequently, they do not affect the CBTS band structure, as is evident from the plot of the bulk band structure with and without U on the Sn-d states (Figure B.1). Hence, we have not applied U on Sn-*d* orbitals.

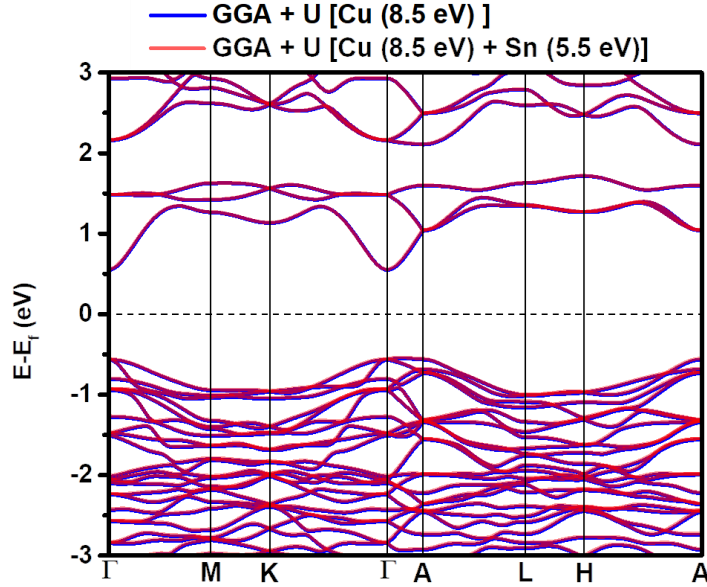


Figure B.1: Comparison of computed electronic bandstructure of bulk $\text{Cu}_2\text{BaSnS}_4$ (CBTS) using GGA+U on Cu and Sn d-orbitals, and only Cu d-orbitals.

Further, for bulk CBTS, we have also performed the band structure calculations with GAU-PBE hybrid functional.³⁴ A detailed discussion on the effect of GGA+U and GAU-PBE functionals on the band structure and the bandgap is described in Section B.2.2. Electron-ion interactions were described by Optimized Norm-Conserving Vanderbilt Pseudopotential (ONCVSP).³⁵ The pseudopotentials have valence configurations of $3s^23p^63d^{10}4s^1$, $5s^25p^66s^2$, $4d^{10}5s^25p^2$, $3s^23p^4$, and $1s^1$ for Cu, Ba, Sn, S, and H respectively. We have used kinetic energy cut-offs of 100 and 400 Ry for the wave function and charge density. To speed up the converge, we have used the gaussian smearing with a smearing width of 0.002 Ry. $7 \times 7 \times 5$ unshifted Monkhorst-Pack (MP) k-point mesh was used to sample the Brillouin zone (BZ).³⁶

B.2.2 Bulk crystal.

Bulk CBTS can either exist in a tetragonal ($\bar{4}$ space group) or trigonal ($P3_1$ space group) crystal structure. Since it is well known that the trigonal phase is more stable than the tetragonal

one, in this study, we have restricted ourselves to the former crystal structure.¹⁴ The optimized structure (Figure B.2a) is non-magnetic. We find that our computed lattice parameters (reported in Table B.1) are in excellent agreement with the experimental values as well as with those previously obtained with GGA (PBE) and GGA (PBE) + U.^{14,37} The trigonal form consists of a tetrahedral network of alternating Cu and Sn atoms linked by S. The Ba sits comfortably in a cavity of 8 coordination from sulfur. The S-tetrahedra containing the Cu ions is distorted with Cu-S bond lengths varying between 2.36 to 2.42 Å. In contrast, in the S-tetrahedra containing the Sn atom, we find the four Sn-S bonds to have almost identical bond lengths; 2 Sn-S bonds of 2.44 Å each, and the other two bonds are only 0.01 Å longer. These results suggest a stronger interaction between Cu and S than that between Sn and S. We note that our computed bond lengths are in good agreement with experimental reports.³⁷ The labeled dashed lines in Figure B.1a show the possibilities of terminating the crystal in the 001-direction. Figure B.2b shows the same structure viewed perpendicular to the 110-growth direction. This structure is later used to model the 110-surface terminations.

Table B.1: Comparison of lattice parameters of $\text{Cu}_2\text{BaSnS}_4$ (CBTS).

	a (Å)	b (Å)	c (Å)
This work (PBE + U)	6.47	6.47	16.01
This work (PBE)	6.45	6.45	15.85
Experimental²⁷	6.37	6.37	15.83

The computed band structure (Figure B.2c) using PBE+U shows a direct bandgap of 1.1 eV at the Γ -point of the BZ, which, though larger than that obtained from PBE, is still less the experimentally observed value of ~ 2 eV.²² Since PBE and PBE+U underestimate the bandgap,³⁸ we have computed the band structure with Gau-PBE hybrid functionals using the PBE+U optimized structure (Figure B.3). This results in a bandgap of 1.6 eV, closer to the experimentally observed value. Our results are in reasonably good agreement with Hong et al., where they have used the HSE functional and obtained a bandgap of 1.79 eV.¹⁴ Further

comparison of the band structure obtained from GGA+U and Gau-PBE functional shows that though the band gaps are different, the band dispersions for both the cases are similar.

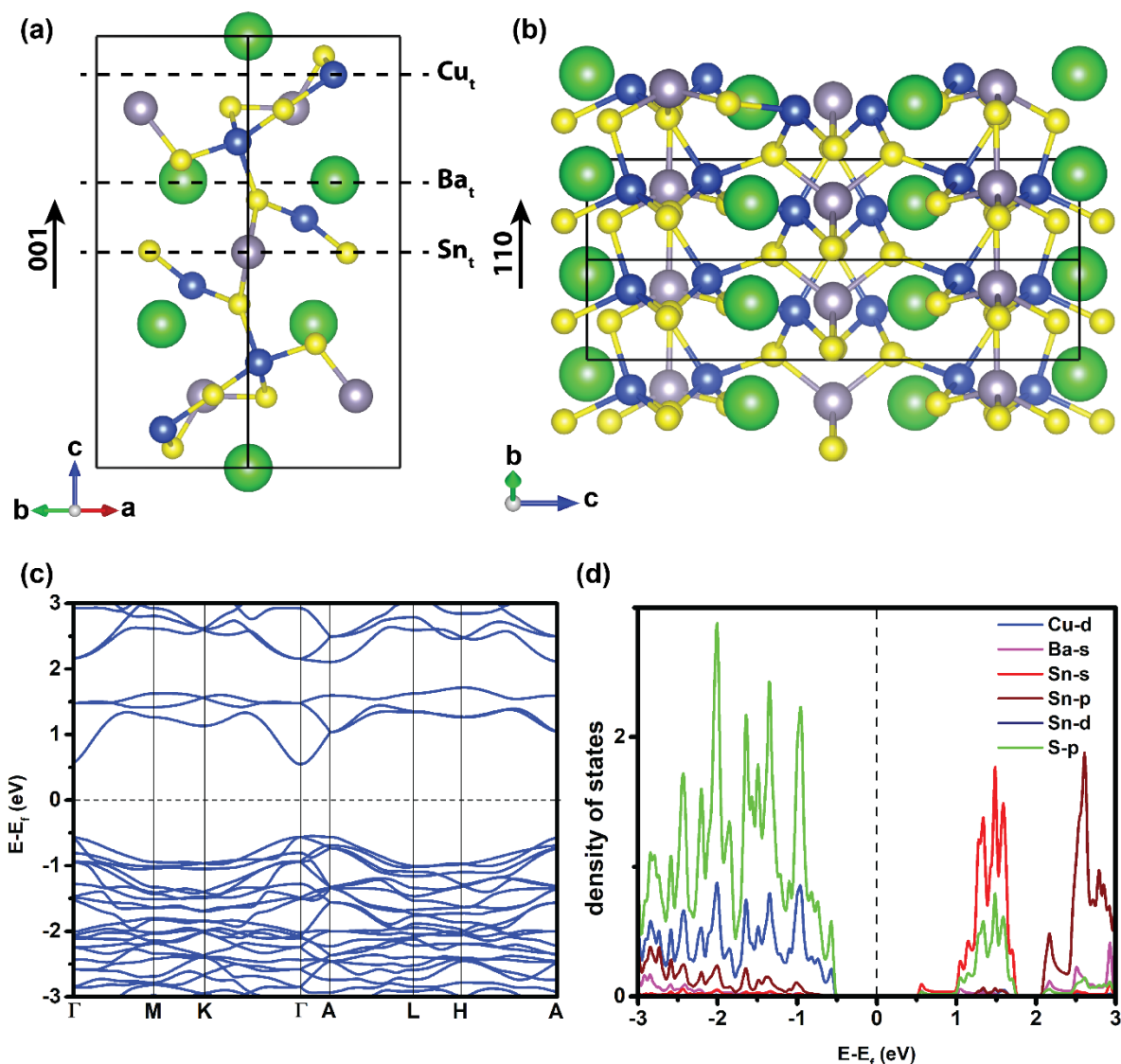


Figure B.2: (a) The optimized structure of $\text{Cu}_2\text{BaSnS}_4$ (CBTS) in the 001-lattice direction. The dashed lines labeled as Cu_t , Ba_t , and Sn_t indicate possible Cu, Ba, and Sn terminated surfaces, respectively. (b) The optimized structure of $\text{Cu}_2\text{BaSnS}_4$ (CBTS) in the 110-lattice direction (c) Band structure of CBTS using PBE+U with $U = 8.5$ eV on the Cu d-orbitals. The black dashed line marks the Fermi level, chosen to be at the middle of the gap. (d) The projected density of states. Atom color code: Cu (blue), Ba (green), Sn (grey), S (yellow).

Since, for the surfaces, performing calculations with hybrid functionals are expensive, and we are interested in the interactions of H with surfaces that depend on the band dispersion, we have moved forward with the calculations with GGA+U. The projections of the total density of

states on the atomic orbitals (PDOS) are shown in Figure B.2d. We observe that the valence band is entirely composed of Cu-d and S-p states. The conduction band (between 0 – 2 eV) has contributions from Sn-s and S-p orbitals. This is corroborated by observing almost parabolic dispersion of the conduction band edge in the band structure. The Sn-p states contribute to the bands lying above 2 eV. From the Bader charge analysis³⁹, we find the partial charges on the constituent atoms: Sn (+1.44), Cu (+0.38), Ba (+1.5), S (-0.91). It can be seen that Ba is close to its ideal ionic +2 state, suggesting minimal orbital interaction with sulfur. This also gets reflected in the PDOS. We do not observe Ba state hybridizing with other atomic orbitals at either of the band edges. On the other hand, both Sn and Cu hybridize strongly with the S atoms, reducing the expected ionic charge from their nominal values of +4 and +1.

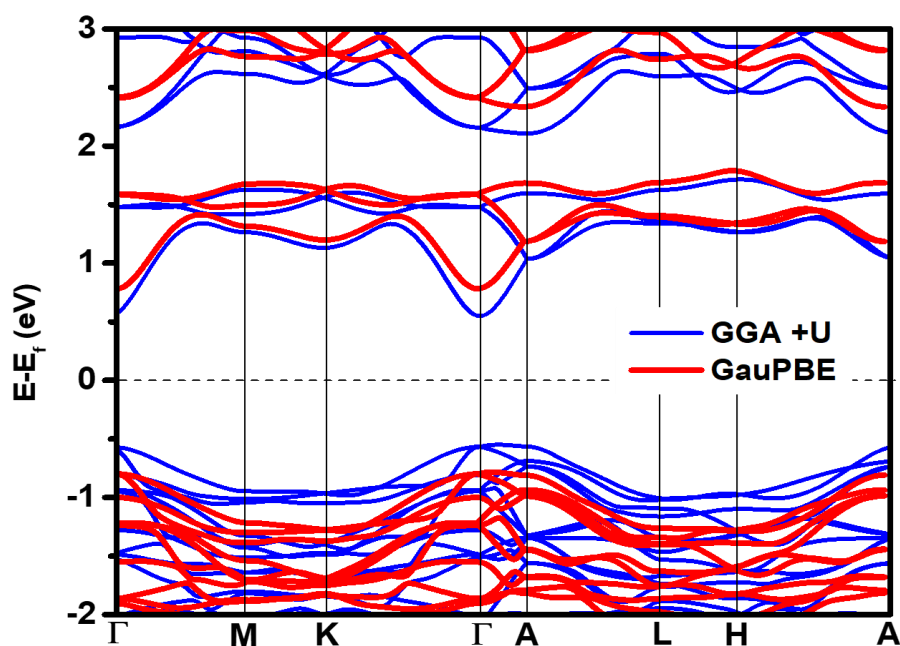


Figure B.3: Comparison of electronic bandstructure using GGA (PBE)+U and Gau-PBE for bulk CBTS.

The good agreement of our computed structure and electronic properties of bulk CBTS with literature (both experimental and computed) suggests that our choice of computational parameters reported in Section B.2.1 correctly describes CBTS.

B.2.3 The surface models.

Lower index terminations are usually a good starting point for the investigation of adsorption because they are typically more stable and comprise most of the surface of synthesized samples. As for CBTS, although no experimental effort has been directed towards growing preferential facets, lower index terminations were shown to be dominant in films grown using sputtering-based deposition techniques, as well as in solution-processed films and nanocrystalline forms.^{24, 29, 40} Therefore, in this work, we have chosen two low indexed surfaces, a) the (001) surface and b) the (110) surface. Both the surfaces have been modeled with slabs of finite thickness, details of which are given below.

B.2.3.1 (001) Surface

The (001) surface can be created by cleaving the crystal perpendicular to the (001) direction, thereby exposing the (001) surface. In the bulk lattice, the unit cell can be thought of growing in the [001] direction with alternating repetition of Sn-S, Cu-S, and Ba layers. Based on this, we identified three possible ways to terminate the (001) surface – (a) Sn-termination, (b) Cu-termination, and (c) Ba-termination (See Figure B.2a). These are named after the most exposed metal atom on the surface. For all these cases, the surface has been modeled with a symmetric slab. We have used slabs that are thick enough such that at the middle of the slab, the interplanar distances are the same as those observed in bulk. To minimize the spurious interactions between the periodic images, a vacuum was used (Figure B.4). For each of the terminations, the vacuum and slab thicknesses are reported in Table B.2. The BZ integrations are done using a $7 \times 7 \times 1$ k-point mesh.

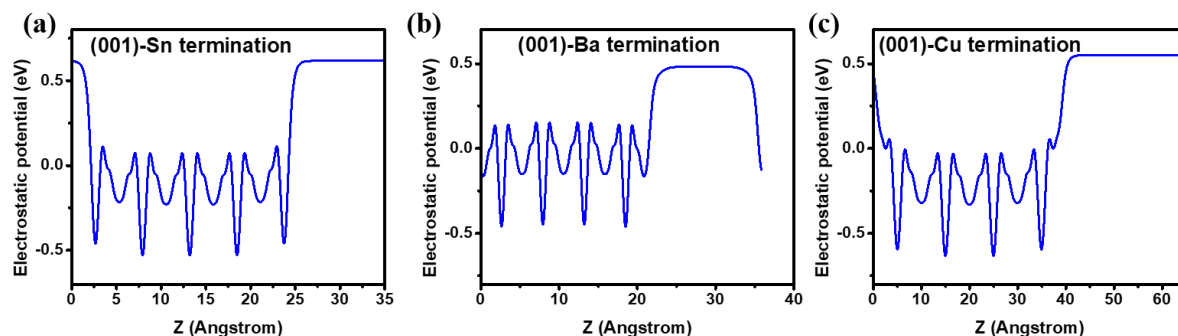


Figure B.4: Planar average of the electrostatic potential along the stacking direction (z) of 001 slabs of CBTS. (a) for Sn termination, (b) for Ba-termination, and (c) for Cu-termination.

Table B.2: Optimized parameters for modelled CBTS slabs with (001) surface terminations (shown in Figure B.6).

	Sn-termination	Ba-termination	Cu-termination
No of layers	17	17	19
Bulk-truncated slab thickness (\AA)	21	20	25
Vacuum thickness (\AA)	15	16	11

B.2.3.2 (110) Surface:

The (110) surface has been modeled with an asymmetric slab consisting of 4 layers (96 atoms). We have found that for this slab, after relaxation, the middle layers have interplanar distances similar to that of bulk, thereby suggesting that our slab is sufficiently thick. In this slab model, the top and bottom surfaces are different. One side has a larger number of metal atoms (we named it M-surface), while the other has a larger number of S atoms (S-surface). Since both sides of the slab have different charge densities, they result in a spurious but strong dipole moment between the periodic images. To nullify the dipole moment, we have applied an electric field in the opposite direction of the dipole (Figure B.5). Additionally, we have used a vacuum of 14 \AA in the direction perpendicular to the surface. Further, we have used a $3 \times 3 \times 1$ ($5 \times 5 \times 1$) k-point grid to perform the BZ integrations for the relaxation (DOS and Bader charges) calculations.

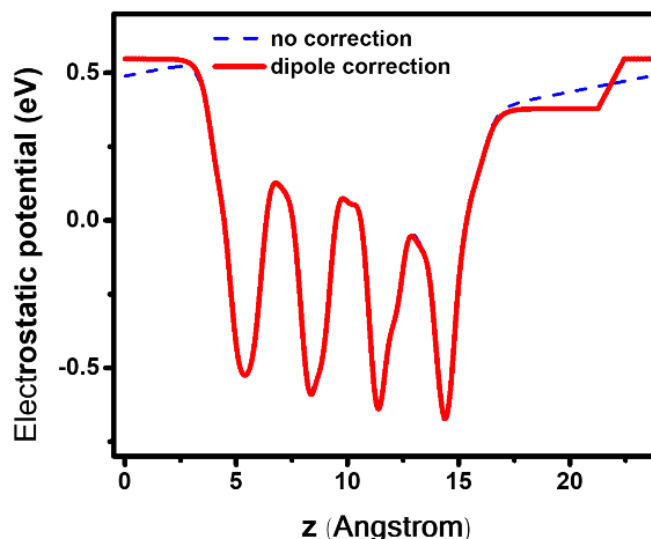


Figure B.5: Planar average of the electrostatic position (with and without dipole correction) along the direction perpendicular to the (110) CBTS surface (z).

B.3 Results and Discussion

B.3.1 Surface structures and electronic properties.

B.3.1.1 (001) termination

The relaxed geometries of the different (001) terminations are shown in Figure B.6. For the case of Sn-termination and Cu-termination, the tetravalency of Sn and Cu, respectively, are not fulfilled on the surface. Instead, each of the metal atoms is coordinated with only three sulfur atoms. In bulk truncated Sn-termination, two S atoms are almost in the same plane as the Sn atoms. The third S atom is in the layer below the one containing the Sn and S atoms. In contrast, in Cu-termination, out of the three S atoms, one is about 1.11 Å above the layer of the Cu atoms, while the other two are about 0.79 and 0.85 Å below the Cu layer (Figure B.6c-d). In Ba-termination, the Ba and S atoms form the surface atoms (Figure B.6e-f). Thus, all the surfaces possess intrinsic S-vacancies. This kind of under-saturated metal atoms on the surface was linked with the high HER performance of chalcogenide catalysts.⁴¹

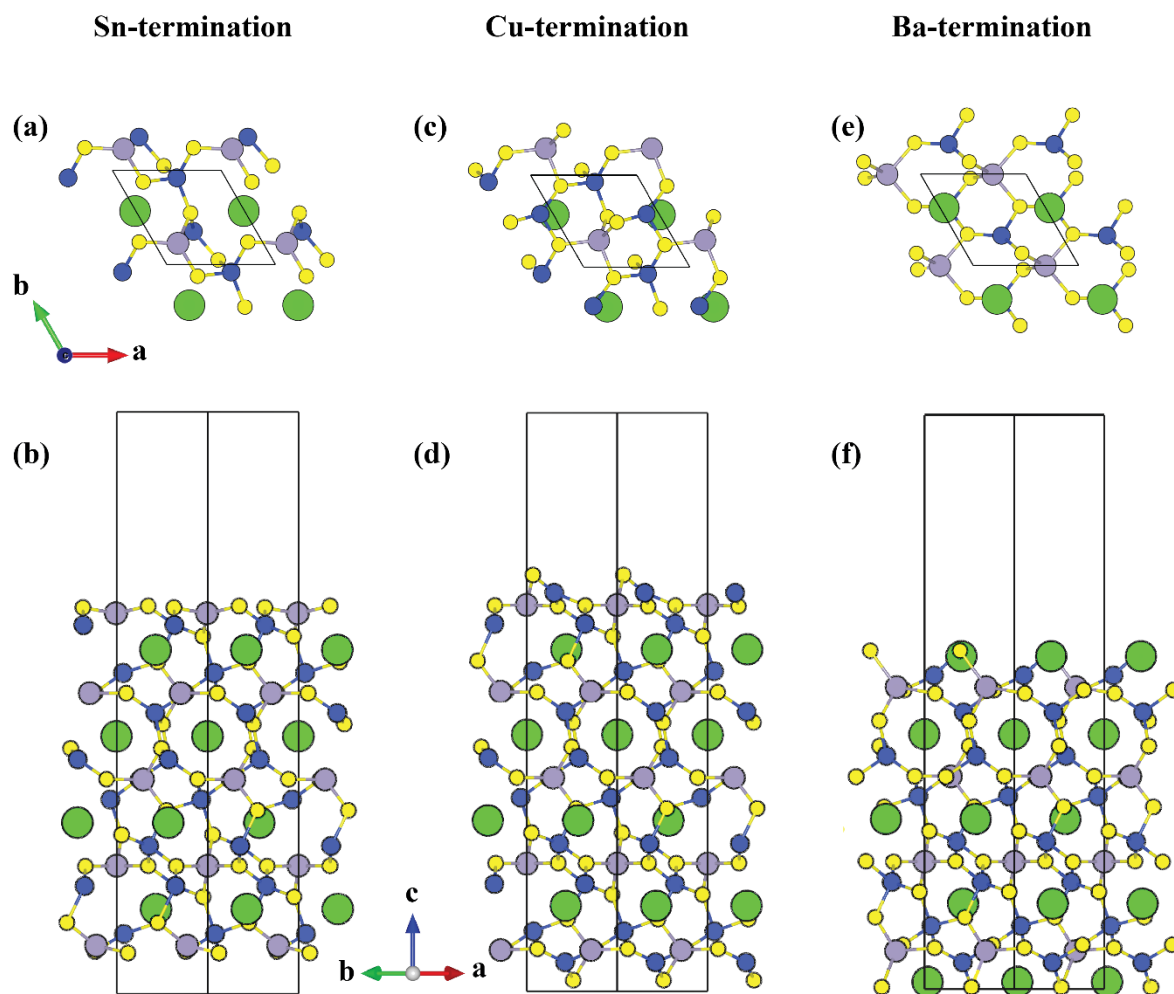


Figure B.6: Relaxed structures of the different terminations of (001) surfaces. The top panel shows the top view, while the bottom panel shows the side view. (a-b) show the structure of the Sn-termination, (c-d) the Cu-termination and (e-f) the Ba-termination. For clarity, only the surface atoms are shown in (a), (c), and (e). Atom color code: Cu (blue), Ba (green), Sn (grey), S (yellow).

After relaxation, we observe an overall shortening of the bond lengths between the atoms on the surface. For example, for Sn-termination, the surface Sn-S bond lengths are reduced to about 2.32 Å compared to 2.45 Å in the bulk-truncated surface. In contrast, the Sn-S bond length between the surface Sn and subsurface S is about 2.41 Å (2.44 Å in the bulk truncated case). The subsurface Cu-S bond lengths in the CuS_4 tetrahedron are also significantly altered. The Cu-S (with the exposed S atoms) bond lengths are shortened to about 2.31 and 2.33 Å (a contraction of about 4.1 % with respect to that in bulk). The other two Cu-S bond lengths are also shortened; however, the contraction is smaller than the two above-mentioned bond lengths.

Similar to the Sn terminated case, for the Cu terminated surface, also we find that the surface Cu-S bonds are shortened to 2.19 Å (for the S atom above the Cu layer) and 2.29 Å (for the S atom below the Cu layer). Further, the Cu-S bond length between the surface Cu and the S atom in the subsurface Sn layer is also shortened to 2.33 Å. For the Ba-termination, the bond between the S atom and the Cu atom below it is reduced to 2.26 Å (vs. 2.42 Å in bulk terminated one). The Ba-S distance is also reduced from 3.29 Å in bulk to 3.27 Å. For all these cases, as we move towards the bulk of the slab, we see that the bond length elongates and finally reaches its bulk value.

A similar observation can be made for the bond angles as well. In the bulk crystal, the Cu-S-Cu and Cu-S-Sn bond angles are about 132° and 104.5° , respectively. The Cu-S-Cu bond angle involving the surface atoms varies by about $1-2^\circ$ and mostly retains its bulk value of 132° . In contrast, we observe that the Cu-S-Sn bond angle is contracted by about 10° compared to that observed in bulk on the surface. This is caused by the undersaturation of the bridging Sulphur atom. When the under-coordinated surface Sulphur atoms have a fewer number of covalent bonds, thereby increasing the electronic density on its non-bonding orbitals (also known as lone-pair orbitals). Consequently, the bond-pair lone-pair electronic repulsion dominates the repulsion between two bonds, decreasing the bond angle.

The projected-DOS of the (001) surfaces for all of the terminations are shown in Figure B.7. For each of the cases, the vacuum energy is set to zero. The energy eigenvalues of the Kohn-Sham states are scaled with respect to the vacuum energy. Hence, the position of the Fermi energy, E_F (for metallic systems), or the position of the valence band maxima (for systems with a bandgap) corresponds to the work function ($\bar{\phi}$). From this calculation, we find $\bar{\phi}$ to be 5.50 eV for the Sn-termination, 6.19 eV for Cu-termination and 2.79 eV for the Ba-termination. Usually, surfaces with low values of work functions act as good electron donors. This suggests that the Ba-termination will act as the best electron donor with the smallest value of work

function. We note that this value is less than that of about 5 eV observed for MoS_2 , which is one of the best chalcogenide HER catalysts ever reported.⁴² The DOS plots for the three terminations show states corresponding to the surface dangling bonds around the band edges. For the Sn termination, the surface dangling bond states are entirely empty (Figure B.7a). As a result, the surface remains semiconducting. Conversely, these states are partially filled for Cu and Ba terminations, giving rise to a non-zero density of states at the Fermi level (Figure B.7b and B.7c, respectively). In the Sn-termination, we observe that the occupied surface states have a contribution from S-p and Cu-d. The empty surface state (between -5 to -4 eV in Figure B.7a) has contributions primarily from the surface Sn (p and s) and S-p states. For Cu and Ba terminations, the states at the Fermi level have contributions primarily from S-p orbitals. Moreover, for the Cu (Ba)-termination, we also observe that the Cu-d (Sn-p and s) states have significant contributions at the Fermi energy. Like the bulk electronic structure, Ba does not contribute to valence and conduction band edges on the surfaces. This suggests that just like the bulk, Ba remains electronically inert on the surfaces.

To check which surface site is more probable towards accepting an H^+ , we calculated the Fukui functions⁴³ of these slabs: $f_+(r) = \rho_N(r) - \rho_{N-1}(r)$. Here, $\rho_N(r), \rho_{N-1}(r)$ are the electron density of the neutral and the positively charged system at a position coordinate r , respectively. The positively charged system is in the same geometry as that of the neutral one. $f_+(r)$ is the Fukui electron density at r . The positive value of the function tells us which sites will be more likely to donate an electron to an incoming H^+ ion. The isosurfaces of $f_+(r)$ are shown in Figure B.7(d-f). We find that the positive lobes of the isosurfaces are localized on the surface Sulphur atoms for all the cases, suggesting that these are the probable sites where an incoming H atom would like to bind. This is expected given sulfur's more electronegative nature than other atoms.

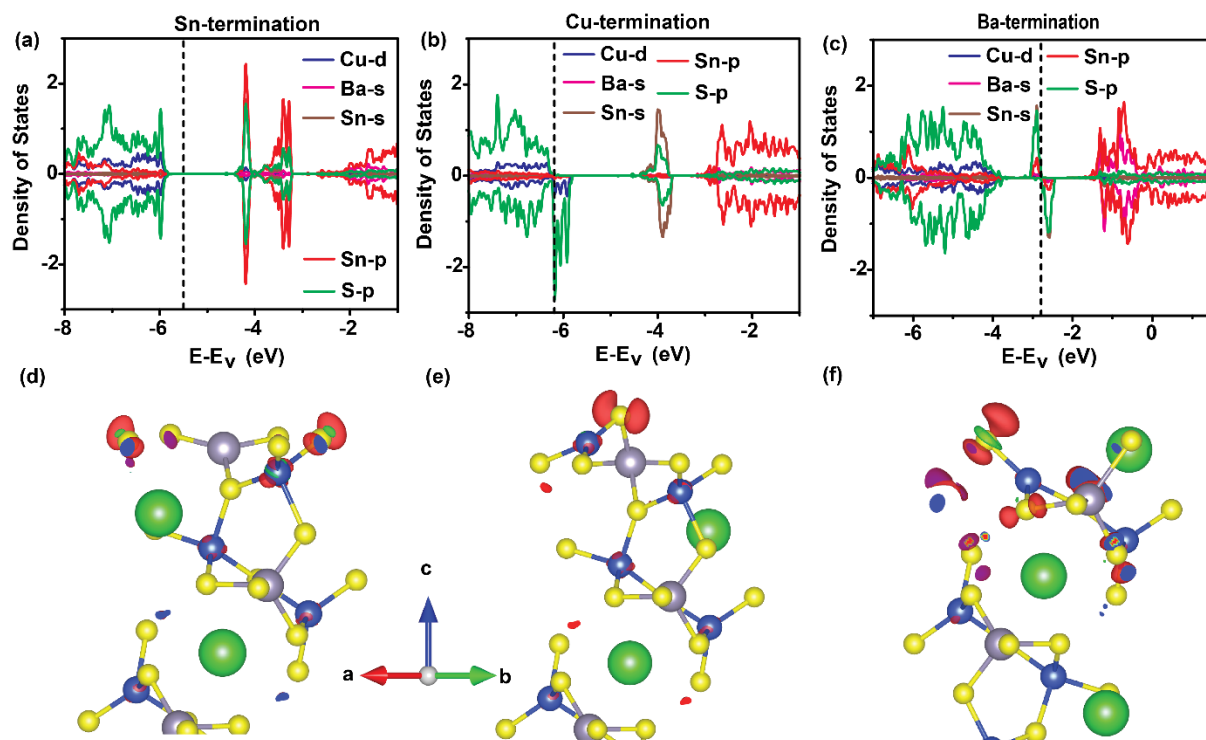


Figure B.7: (a-c) The density of states (DOS) projected on the atomic orbitals of the surface atoms of three terminations. The electronic states are shifted with respect to vacuum energy. The black dashed line marks the Fermi level. (d-f) Isosurfaces of positive electron density (red lobes) calculated using the Fukui function, for isovalues of $\pm 0.0015 \text{ e}/\text{\AA}^3$. The lobes indicate the most probable sites for H-adsorption. Atom color code: Cu (blue), Ba (green), Sn (grey), S (yellow).

Further, we have carried out the Bader charge analysis to determine the difference in the electronic charges on the surface atoms compared to their bulk analogs. The Bader charges are tabulated in Table B.3. We see that, for all the terminations, the charges on the atoms in the bulk region of the slab are precisely the same as that observed in bulk crystal, reflecting the adequacy of the slab thickness. On the surface atoms, we see the deviation of the partial charges from their bulk values. We observe that the negative charge on the surface S atoms is significantly reduced from their corresponding bulk values on the Sn-terminated surface. Similarly, on the Cu-terminated surface, we observe a slight enhancement of the positive charge on the surface Cu atoms and a significant reduction of the negative charge on the surface S atom. This suggests that after relaxation, the surface charge density is redistributed. The overall surface charge is reduced, resulting in the stabilization of the surfaces. In contrast, we see a significant reduction of the positive charge on the surface Sn and enhancement of the

negative charge on the surface S atoms for the Ba-termination. These results indicate that the Ba terminated surface becomes electron-rich compared to its other two counterparts. Overall, we see that the Bader charges support the calculated work functions and Fukui densities of different surfaces.

Table B.3: Bader charges on different sites of the (001)-surface terminations. The suffix "sur" implies the atom is on the surface, while "b" implies it is positioned in the bulk or the middle of the slab.

	Cu-termination	Ba-termination	Sn-termination
Cu_{sur}	0.42	0.29	0.38
Cu_{b}	0.38	0.38	0.38
Sn_{sur}	1.47	1.10	1.34
Sn_{b}	1.47	1.47	1.47
Ba_{sur}	1.50	1.46	1.49
Ba_{b}	1.50	1.50	1.51
S_{sur}	-0.54	-1.07	-0.8
S_{b}	-0.94	-0.92	-0.94

B.3.1.2 (110) termination

From the optimized structure (Figure B.8a), we see that Sulphur vacancy is typical for all the metal tetrahedra on the M-surface termination. All the exposed metal atoms are under-coordinated due to the cleavage of one or two metal sulfide bonds on the surface. The trends in the change in surface bond distances for the M- and S-terminated surfaces remain similar to that observed for (001) termination. However, the behavior of the bond angles is slightly different. Here, we observe that the Sn-S-Cu bond angle gets contracted on the M-surface while the Cu-S-Cu angle remains unchanged. The bottom S-surface, on the other hand, shows different behavior. The absence of the Sn atom results in the dimerization of two S atoms belonging to two neighboring Cu-S units. The S-S bond distance (1.99\AA) is similar to those observed in disulfide compounds. This reduction in the S-S length results in the formation of a

Cu-S-S-Cu bridge (Figure B.8e). Also, the Sn-S and Cu-S bond distances are reduced to 2.40 Å and 2.25 Å due to this bridge formation.

Like the (001) surface, we have calculated the Fukui electron density for the (110) slab, the isosurfaces of which are plotted in Figure B.8a. On the M-surface, we do not notice any atom having positive isovalues of the Fukui function. This contrasts with that observed for the (001) surfaces, where significant electron density was found on S atoms on all surfaces. This is perhaps expected since the S-atoms are relatively deeper inside the surface. The absence of sulfur dangling bonds gets reflected in the projected-DOS (Figure B.8b) as well. We observe no contribution of the surface atomic orbitals at the Fermi level, similar to what we have observed for the 001-Sn termination. The M-surface is semiconducting, having a bandgap of ~ 0.1 eV. This might help in light-driven carrier formation on the surface and electron injection to any adsorbed proton. This cuts back the requirement of having mobile carriers from the bulk of the material, which often results in a loss of catalytic efficiency. The positive Bader charges on the Cu and Sn are reduced compared to the bulk values (Figure B.8d). Also, the charge on the Ba atoms remains unchanged. The overall larger reduction in the magnitude of positive charges compared to that of the negative charges on the surface atoms indicates that there is a spillover of electrons on the surface.

In contrast to this, the S-terminated surface is metallic (Figure B.8c), the states at the Fermi energy have contributions from both Cu and S. Bader charge analysis shows that there is an overall loss of electrons from the surface Sn, Cu, and S atoms (they become slightly more positive) is compensated by the gain in electrons of the atoms on the M-terminated surface (Figure B.8d). Additionally, the surface has non-zero spin polarization. The nature of the magnetic moment (spin up or down) is schematically shown in Figure B.8e. We note that the magnetic moments on the Cu-S-S-Cu complex are antiferromagnetically aligned with respect

to the magnetic moments on the other atoms. The magnitude of the magnetic moments on different surface atoms varies between 0.02 to 0.58 μ_B .

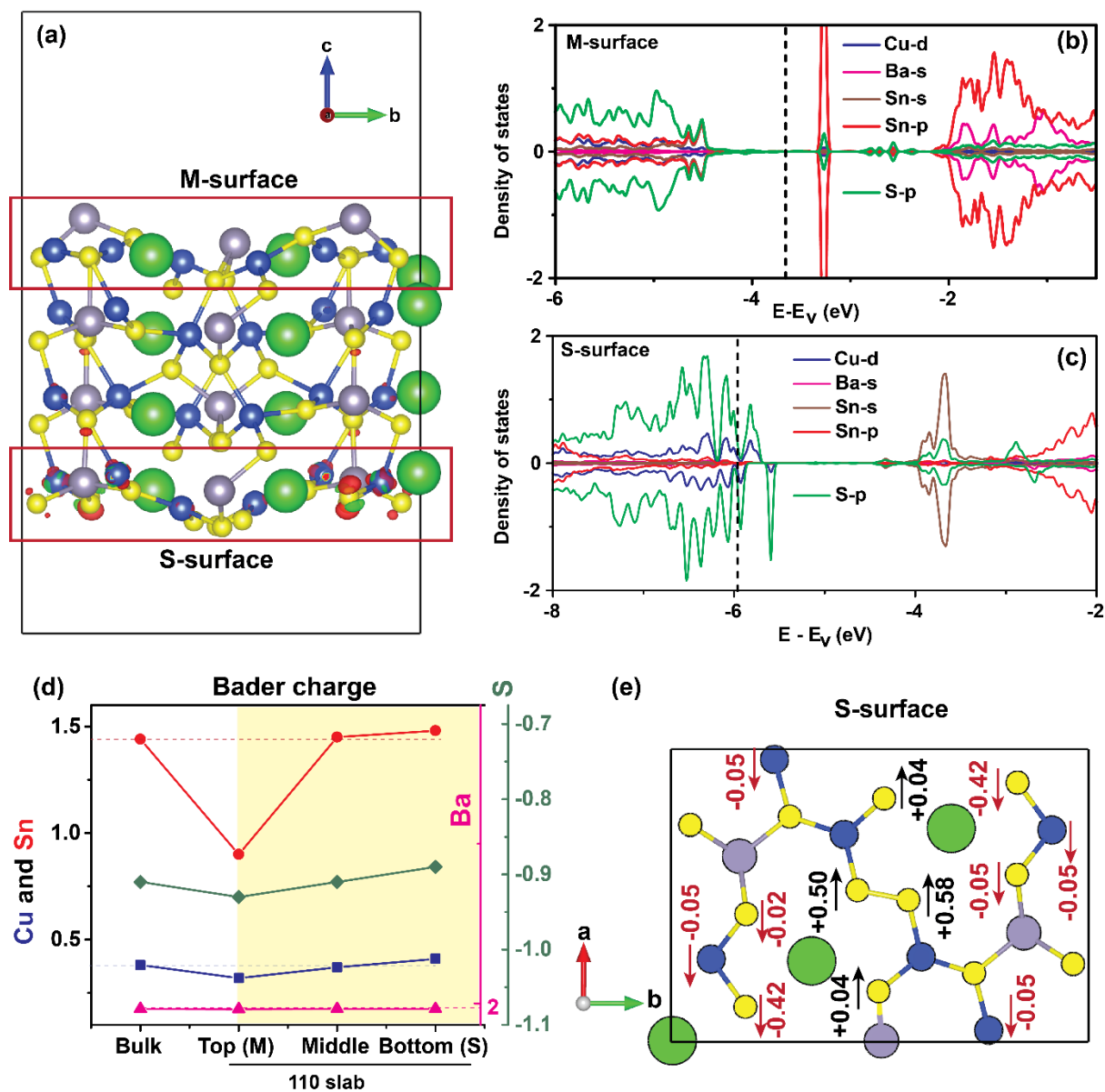


Figure B.8: Electronic properties of 110 slab. (a) The Fukui function calculated on the optimized slab. The charge densities are plotted with an isovalue of $\pm 0.0015 \text{ e}/\text{\AA}^3$. The red boxes mark the two different terminations, denoted by M-surface and S-surface. (b-c) Projected DOS of the M (b) and S (c) terminations, energy scaled with respect to the vacuum energy. The black dashed line marks the Fermi level. (d) Comparison of Bader charges in the bulk system and on the different surface atoms. (e) The spin polarization on the S-surface. Black arrows indicate spin up, and red arrows indicate spin down. Atom color code: Cu (blue), Ba (green), Sn (grey), S (yellow).

The work function, $\bar{\phi}$ for both of these surfaces were calculated similarly to that of the (001) termination. The S-terminated surface has a work function of 5.96 eV, while it is 3.66 eV for

the M-surface. These values suggest that charge injection to an adsorbate through a catalytic site from the M-surface would be easier compared to that of the S-surface.

B.3.2 Thermodynamics of H-adsorption on the surfaces.

To study the adsorption of hydrogen (both atomic and molecular) on these surfaces, we have calculated the binding energies for the same. In brief, we have put H-atoms/H₂ molecules at sites on the surfaces and relaxed those geometries. The binding energies (ΔE_H) were calculated using the formula,

$$\Delta E_H = \frac{E(CBTS+nX) - E(CBTS) - \frac{n}{z}E(H_2)}{n} \quad \text{Eq. (B.1)}$$

In equation B.1, n , $E(i)$ are the number of bound H-atoms/molecules and energy of the i^{th} system, respectively. Here i represents the surface with n H atoms/molecules (denoted by X in the above equation) bound to the surface ($CBTS+nX$), the corresponding clean surface ($CBTS$), and molecular hydrogen in vacuum (H_2). $z=1$ if X corresponds to Hydrogen molecule and $Z=2$ if X represents an H atom. For the adsorption of molecular hydrogen, we find that irrespective of the initial orientation of the H₂ molecule (that is, horizontal or vertical), after relaxation, they have similar desorption energies. In the following sections, we discuss the adsorption energies for different surfaces.

B.3.2.1 001-Surfaces

Figure B.9 summarizes the adsorption energies of one ($n = 1$ in equation B.1) and two ($n = 2$ in equation B.1) atomic H and one H₂ molecule on the different terminations of the (001) surface. The right panel shows the surface sites and their combinations that were considered for H-adsorption at different terminations. We observe that the adsorption energies lie between -1.2 to 0.6 eV. They are primarily exothermic for the single H-adsorption. For the majority of the structures, incorporating a second Hydrogen causes the energies to become comparably endothermic, except when the surface undergoes a considerable amount of reorganization.

Here, we will only discuss the most exothermic scenarios for H-adsorption on individual surfaces, since those are the most probable ones towards showing catalytic activity.

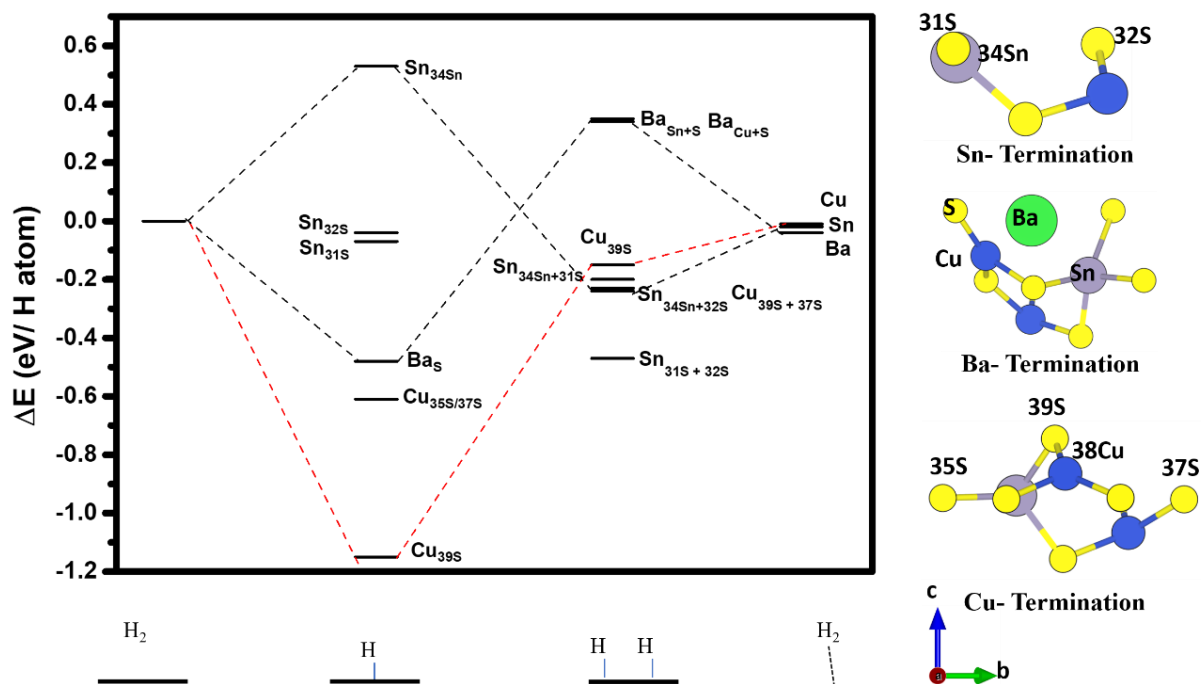


Figure B.9: Calculated adsorption energies of one and two Hydrogen atoms and H₂ molecules at different sites. The sites are named in the following notation, A_{xb}, where A is the name of the termination, and xb is the site's name where Hydrogen is adsorbed in the final relaxed geometry. The site labels are shown in the figure on the right-hand side. Atom color code: Cu (blue), Ba (green), Sn (grey), S (yellow).

Figure B.10 shows the clean surface structures and the most exothermic H-adsorbed structures. For all of the studied surfaces, the sulfur atoms provide the most exothermic adsorption site. Amongst all the 001-surfaces, the strongest binding with sulfur happens on the 001-Cu termination. The sulfur atom labeled as 39S (Figure B.10b) has the H-adsorption energy of -1.15 eV with a sulfur hydrogen distance of 1.35 Å. The addition of the second hydrogen on the surface saturates the other sulfur dangling bond marked 37S (Figure B.10c) and reduces the adsorption energy to -0.24 eV. At this configuration, both sulfur hydrogen bonds have bond lengths of 1.35 Å. In contrast, on the Sn-terminated 001-surface, we see the opposite behavior on increasing hydrogen concentration on the surface. The adsorption energy increases from -0.07 eV (Figure B.9e) to -0.47 eV (Figure B.10f) on introducing the second hydrogen.

Although the sulfur hydrogen bond length remains the same as 1.35 Å, the Cu-S bond length increases from 2.31 (saturated 31S) and 2.29 (unsaturated 32S) Å to 2.36 Å. The reorganization of electron density from the Cu-S bond to the S-H bond might be the reason for the more exothermic adsorption of the second hydrogen on the surface. Similar to the 001-Cu terminated surface, on the Ba-terminated 001-surface, the adsorption becomes less energetically favorable when introducing a second Hydrogen (Figure B.10h and B.10i). In this case, the adsorption energy increases from -0.48 eV to 0.34 eV. The endothermic adsorption is attributed to the formation of a Cu-H surface bond due to the unavailability of a second sulfur atom on this surface. Thus, it appears that the 001-Ba termination would favor the adsorption of one single hydrogen on the unit cell surface and will hinder the adsorption of a second one.

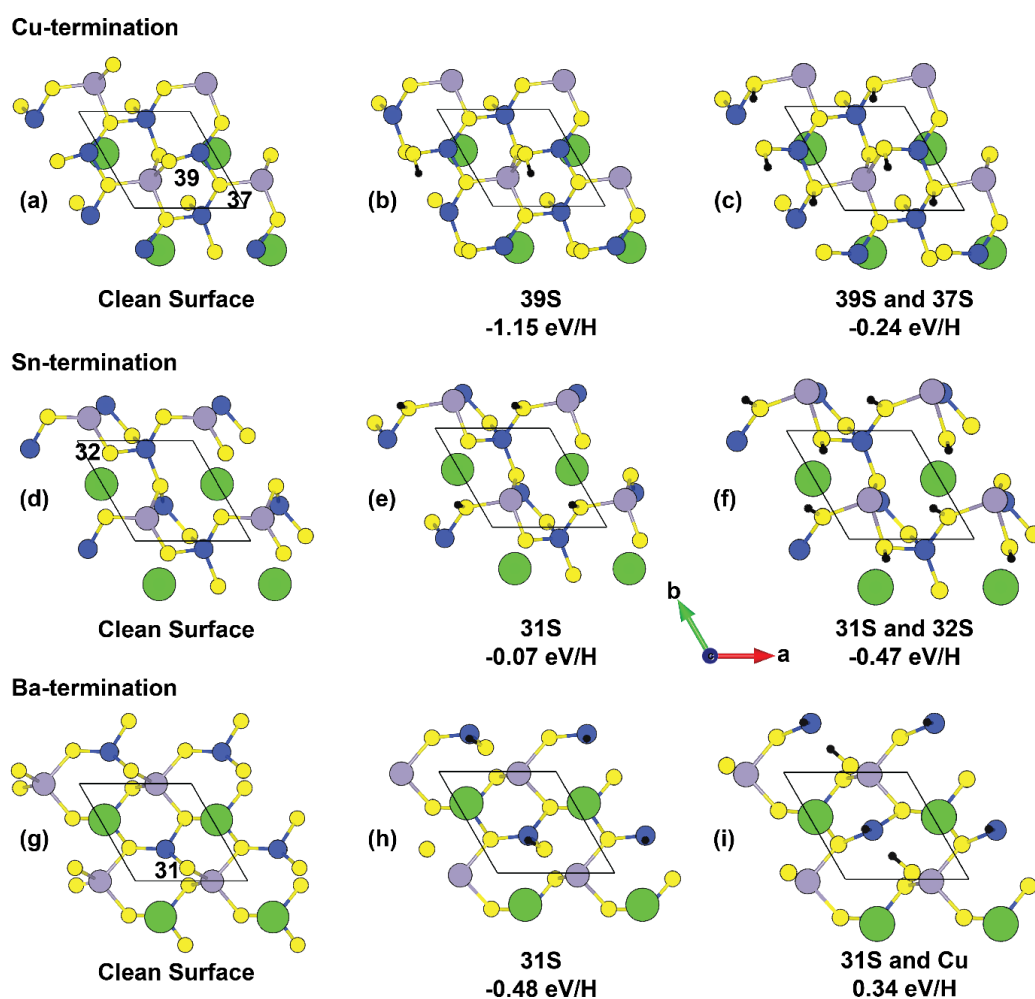


Figure B.10: Surface structures of the clean surfaces and the most probable adsorption sites on the 001 terminations. The corresponding names mark the adsorption site of the hydrogen. Atom color code: Cu (blue), Ba (green), Sn (grey), S (yellow), H (black).

B.3.2.2 110-Surfaces

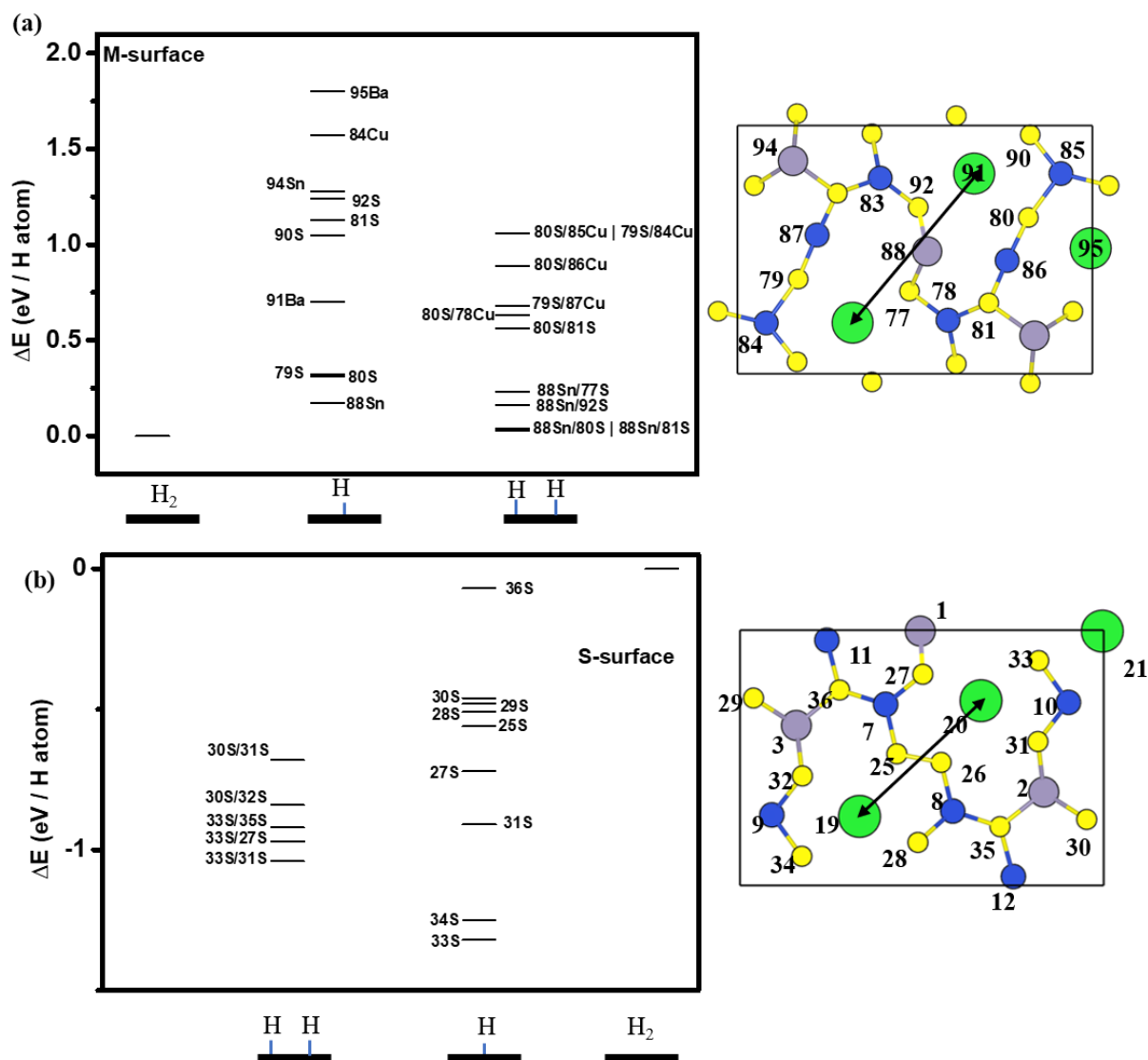


Figure B.11. Hydrogen adsorption energies for single and two Hydrogen atoms on (a) M-terminated and (b) S-terminated (110) surfaces. The right panel shows the atom indices. The double-headed arrows highlight the symmetry relationships. Atom color code: Cu (blue), Ba (green), Sn (grey), S (yellow).

The (110) surface has a comparatively larger surface area than the (001) terminations and, thus, more sites. The right panels in Figure B.11 show the considered surface sites. Here we find that on both surfaces (M and S), there is a symmetric arrangement of atoms. For example, on the M-termination, the symmetric pairs of atoms are 85Cu and 84Cu, 79S and 80S, etc. On the S-termination, they are 19Ba and 20Ba, 33S and 34S, etc. The same symmetric relationship is maintained for polarization (see Figure B.8e). So, for both of the sites, we performed the

adsorption energy calculations only on one of the symmetric partners of the pair. As a one-time check whether the same symmetric relationship gets reflected in the adsorption energy or not, we calculated adsorption energies for 79S and 80S on the M-surface. We observed that the adsorption energy differs only slightly (by about 0.06 eV) with no significant changes in the surface structure. This symmetric positioning of atoms helps us to reduce the number of calculations.

Figure B.11 (a-b) summarizes the adsorption energies for all considered cases. Figure B.12 shows the clean surface and the most exothermic structures. In contrast to the (001)-surfaces, the (110) M-terminated surface (Figure B.12a) contains more metal dangling bonds than sulfur ones. Moreover, the sulfur atoms, in this case, are at a lower elevation than the protruding metal atoms. Consequently, all adsorption of hydrogen on this surface is endothermic in nature. Amongst these, the smallest endothermic adsorption energy is found to be on the 88Sn site (Figure B.12b) with an adsorption energy of 0.17 eV/H atom. 88Sn is the most exposed and undersaturated atom on this surface. The Sn-H bond length is 1.77 Å. Adsorption of incoming second hydrogen is a downhill process with the second H binding to the 81S site (Figure B.12c). This results in adsorption energy of 0.03 eV/H atom of the two H atoms co-adsorbed on this surface. We observe slight reorganization of the surface structure with Sn-H and S-H bond lengths of 1.77 and 1.35 Å, respectively. As opposed to the M-termination, the (110) S-termination (Figure B.12d) has an abundance of exposed sulfur atoms that helps in the favorable adsorption of hydrogen atoms. Therefore, the adsorption of hydrogen on this surface is exothermic in nature. The strongest adsorption is provided by the 33S site (Figure B.12e), with an S-H bond length of 1.35 Å. The second hydrogen adsorbs at the adjacent 31S site. The adsorption of the second H is an uphill process, and the adsorption energy is slightly reduced from -1.32 eV/H atom to -1.04 eV/H atom (Figure B.12f). Both of the 33S-H and 31S-H bond lengths in this configuration are 1.35 Å.

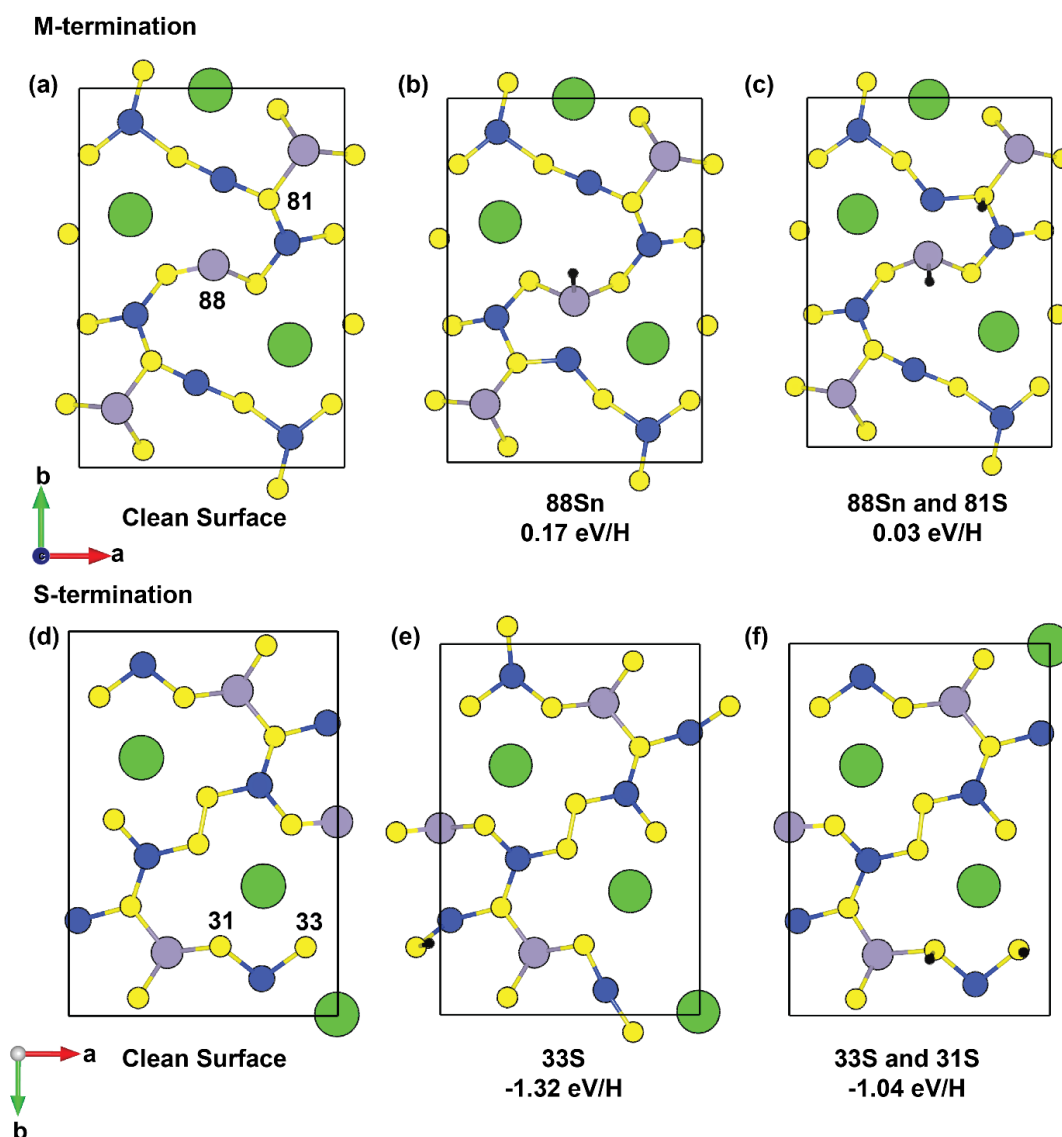


Figure B.12: Surface structures of the most probable adsorption sites on the 110 terminations. Atom color code: Cu (blue), Ba (green), Sn (grey), S (yellow), H (black).

B.3.3 HER mechanism.

After studying the adsorption of a single H atom, two H atoms, and an H_2 molecule on the different surface terminations of the (001) and (110) surfaces of CBTS, we discuss the plausible HER reaction mechanisms on these surfaces.

The first step of HER on the photocathode involves the adsorption of a proton from the solvent to the catalyst (Volmer mechanism). Following this, the HER reaction can occur in two ways: two protons bound to the surface form H_2 , which then desorbs (Tafel mechanism), or a second proton from the solvent attacks the proton bound to the catalyst to form H_2 (Heyrovsky

mechanism). The favorable pathway will depend on the adsorption energy of the proton and the Gibbs free energy change ($|\Delta G|$) for each reaction step. According to our definition of adsorption energy, the adsorption energy should be sufficiently negative, implying that the adsorbates remain bound to the surface when the reaction occurs on the surface; moreover, as shown recently by Peterson and others ΔG of the reaction should be positive.⁴⁴⁻⁴⁷ Since the above-mentioned reaction steps involve a solvated proton and an electron whose energy is not possible to compute, we consider the computational H electrode (CHE) model proposed by Norskov and coworkers.⁴⁸ In this model, the energies of proton and electron are not explicitly calculated but use the fact that under standard conditions, the free energy of ($H^+ + e^-$) is equal to half the free energy of H₂. The change in ΔG is given by:

$$\Delta G = \Delta E_{X^*} + \Delta E_{ZPE} - T\Delta S_X \quad \text{Eq.(B.2)}$$

where X^* can be adsorbed H atom or molecule. Δ Denotes the difference of a physical quantity between reactants and products; E , ZPE , T , and S denote energy, zero-point energy corrections, temperature, and entropy. We neglect the vibrational entropy at the adsorbed state because it is small. Hence, $\Delta S_{X^*} \cong -\frac{n}{2}S_{H_2}^0$, where n denotes the number of H atoms and $S_{H_2}^0$ is the entropy of H₂ in the gas phase at the standard condition and is given by 0.4 eV.⁸ Further, previous studies have shown that out of the last two terms in the right-hand side of equation B.2, the contribution of ΔE_{ZPE} is typically an order of magnitude smaller than the entropy correction.³¹ Hence in our calculations, we have only considered the entropy correction for the computation of ΔG .

Figure B.13 shows the computed ΔG values for the most probable adsorption sites on different surfaces. A comparison of ΔG amongst the different surfaces for the Volmer-Heyrovsky mechanism shows that only for the M-terminated (110) and Sn-terminated (001) surfaces $\Delta G > 0$, suggesting that on these surfaces, the Volmer-Heyrovsky mechanism will be favorable. In the Volmer-Tafel mechanism, there is an intermediate step involving co-adsorption of two H⁺.

This is followed by the formation and desorption of H_2 . Our calculations show that the adsorption of the second H^+ is a downhill step only for the (001)-Sn termination and the (110)-S termination. However, for both these cases, the ΔG is strongly negative, suggesting that it might be difficult to desorb the H atoms bound to the surface to form H_2 . Amongst the other terminations, on the (110)-M termination, (001)-Cu termination and the (001)-Ba termination, the ΔG between a single H^+ adsorption and two H^+ adsorption is positive. On the (001)-Ba termination, it is about 1.36 eV, which is significantly large. Similarly, for the (001)-Cu termination, a large value of ΔG is observed between a single H^+ adsorption and two H^+ adsorption. Hence, we anticipate that these two terminations will not participate in the HER reaction through the Volmer-Tafel mechanism. In contrast, on the (110)-M termination, the change in free energy for the second H adsorption with respect to the first H adsorption is only 0.09 eV uphill. The ΔG for this reaction intermediate is 0.46 eV, i.e., it is slightly endergonic. Moreover, for this termination, the adsorption of the second H^+ is the potential determining step in the Volmer-Tafel mechanism.

A comparison of the two competing mechanisms considered above suggests that Sn-terminated (001) and M-terminated (110) surfaces are the best candidates for HER through the Volmer-Heyrovsky mechanism. However, on the Sn-terminated surface, a second incoming H binds too strongly. A consequence of this might be that before H_2 is formed through the Volmer-Heyrovsky mechanism, a second H^+ ion will come and bind to the surface, provided that this is kinetically more favorable than H_2 formation and desorption. However, $\Delta G < 0$ for this reaction mechanism suggests that the thermodynamics does not favor the Tafel-Heyrovsky mechanism on the surface. In contrast, on the M-terminated surface, the adsorption of the second H^+ , which is a prerequisite for the Volmer-Tafel mechanism, is thermodynamically unfavorable. Thus, we envisage that the (110)-M terminated surface will be the best candidate as a (photo-)electrocatalyst for the HER. The reaction might proceed either according to the

Volmer-Heyrovsky mechanism or Volmer-Tafel mechanism, depending on the kinetics of the process. The reason for this can be attributed to the unique structure of this termination where the S atoms, to which the H atoms are more prone to bound, are slightly below the protruding metal atoms. As a consequence, incoming proton binds to the Sn atoms, whose p-orbitals contribute to the surface states, with weaker binding energy. Hence the incoming H atoms have the optimal binding strength that is suitable for HER reaction.

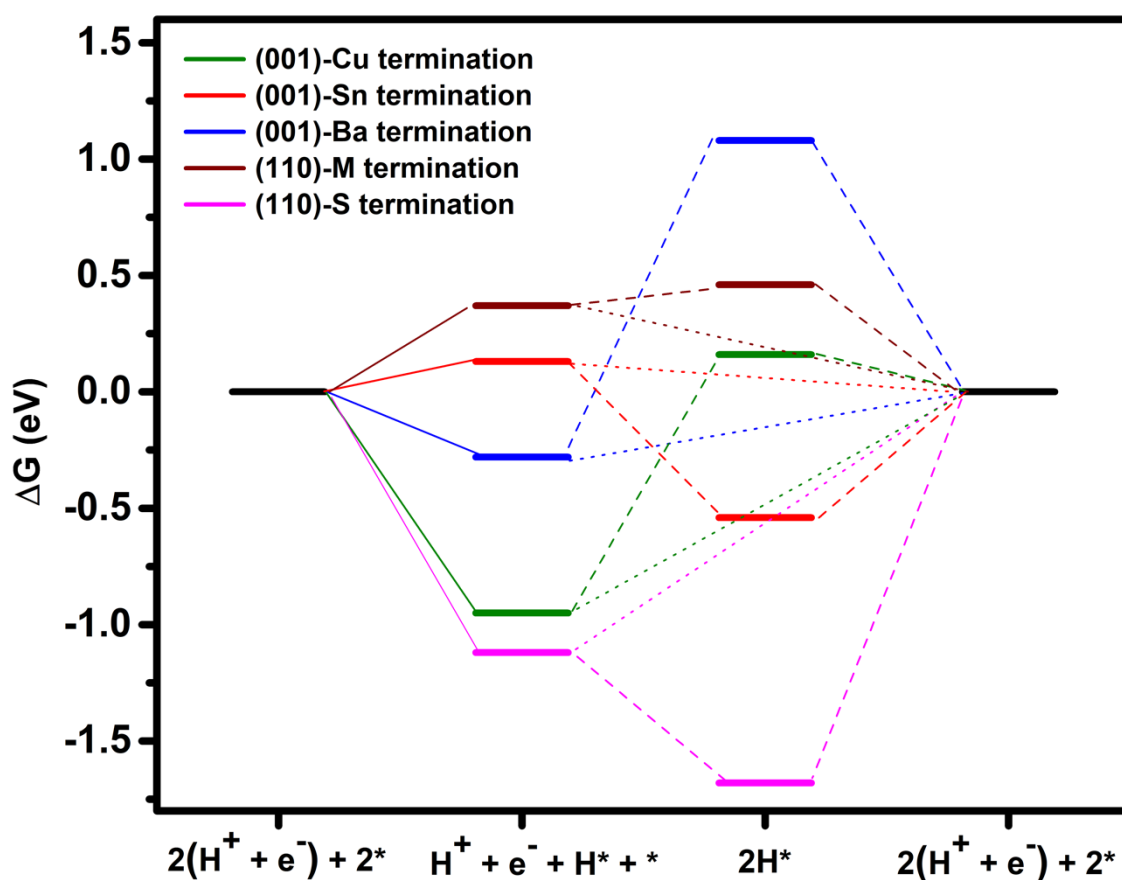


Figure B.13: Free energy change of the most stable configurations of Hydrogen adsorption on the different terminations of the (001) and (110) CBTS surfaces. The solid lines show the Volmer step. Dashed lines indicate the Tafel mechanism, while dotted lines indicate the Heyrovsky mechanism.

B.4 Conclusions

We have systematically investigated the thermodynamics of HER activity on five terminations of two CBTS surfaces, namely the (001) and (110), using first-principles calculations. We have considered both the Volmer-Heyrovsky and Volmer-Tafel mechanisms. Based on our

thermodynamic considerations, we find that the (110)-M terminated surface to be the best candidate for HER on this surface. However, to concretely comment on the preferred mechanism, i.e., Volmer-Heyrovsky or Volmer-Tafel, one needs to study the kinetics of the reaction steps. We believe our result will be beneficial for the future development of HER photocathodes employing this group of materials.

B.5 References

- (1) Li, J.; Güttinger, R.; Moré, R.; Song, F.; Wan, W.; Patzke, G. R. Frontiers of Water Oxidation: The Quest for True Catalysts. *Chem. Soc. Rev.* **2017**, *46*, 6124-6147.
- (2) Ursua, A.; Gandia, L. M.; Sanchis, P. Hydrogen Production from Water Electrolysis: Current Status and Future Trends. *Proc. IEEE* **2012**, *100*, 410-426.
- (3) Divanis, S.; Kutlusoy, T.; Ingmer Boye, I. M.; Man, I. C.; Rossmeisl, J. Oxygen Evolution Reaction: A Perspective on a Decade of Atomic Scale Simulations. *Chem. Sci.* **2020**, *11*, 2943-2950.
- (4) Osterloh, F. E. Inorganic Materials as Catalysts for Photochemical Splitting of Water. *Chem. Mater.* **2008**, *20*, 35-54
- (5) Yan, Y.; Xia, B.; Xu, Z.; Wang, X. Recent Development of Molybdenum Sulfides as Advanced Electrocatalysts for Hydrogen Evolution Reaction. *ACS Catal.* **2014**, *4*, 1693-1705.
- (6) Sun, L.; Wu, Z.; Xiang, S.; Yu, J.; Wang, Y.; Lin, C.; Lin, Z. High-efficiency Photoelectrochemical Hydrogen Generation Enabled by p-Type Semiconductor Nanoparticle-Decorated n-Type Nanotube Arrays. *RSC Adv.* **2017**, *7*, 17551-17558.
- (7) Shu, X.; Zhao, C.; Zhang, X.; Liu, X.; Xing, Z.; Fang, D.; Wang, J.; Song, Y. Highly Efficient Near-Infrared Light Photocatalytic Hydrogen Evolution over MoS₂ Supported Ta₂O₅ Combined with an Up-Conversion Luminescence Agent (β -Tm³⁺, Yb³⁺:NaYF₄/MoS₂-Ta₂O₅ Nanocomposite), *New J. Chem.* **2018**, *42*, 6134-6143.

- (8) Gao, Y.; Li, H.; Wang, J.; Ma, J.; Ren, H. New Insight on Hydrogen Evolution Reaction Activity of MoP₂ from Theoretical Perspective. *Nanomaterials (Basel)* **2019**, *9*, 1270.
- (9) Bhat, K. S.; Nagaraja, H. S. Performance Evaluation of Molybdenum Dichalcogenide (MoX₂; X= S, Se, Te) Nanostructures for Hydrogen Evolution Reaction. *Int. J. Hydrog. Energy* **2019**, *44*, 17878-17886.
- (10) Wang, H.; Chen, Z.-n.; Wu, D.; Cao, M.; Sun, F.; Zhang, H.; You, H.; Zhuang, W.; Cao, R. Significantly Enhanced Overall Water Splitting Performance by Partial Oxidation of Ir through Au Modification in Core–Shell Alloy Structure. *J. Am. Chem. Soc.* **2021**, *143*, 4639-4645.
- (11) Zhang, G.; Lan, Z.-A.; Lin, L.; Lin, S.; Wang, X. Overall Water Splitting by Pt/g-C₃N₄ Photocatalysts without using Sacrificial Agents. *Chem. Sci.* **2016**, *7*, 3062-3066.
- (12) Wang, W.; Winkler, M. T.; Gunawan, O.; Gokmen, T.; Todorov, T. K.; Zhu, Y.; Mitzi, D. B. Device Characteristics of CZTSSe Thin-Film Solar Cells with 12.6% Efficiency. *Adv. Energy Mater.* **2014**, *4*, 1301465.
- (13) Chen, S.; Walsh, A.; Gong, X.-G.; Wei, S.-H. Classification of Lattice Defects in the Kesterite Cu₂ZnSnS₄ and Cu₂ZnSnSe₄ Earth-Abundant Solar Cell Absorbers. *Adv. Mater.* **2013**, *25*, 1522-1539.
- (14) Hong, F.; Lin, W.; Meng, W.; Yan, Y. Trigonal Cu₂-II-Sn-VI₄ (II = Ba, Sr and VI = S, Se) Quaternary Compounds for Earth-Abundant Photovoltaics. *Phys. Chem. Chem. Phys.* **2016**, *18*, 4828-4834.
- (15) Xiao, Z.; Meng, W.; Li, J. V.; Yan, Y. Distant-Atom Mutation for Better Earth-Abundant Light Absorbers: A Case Study of Cu₂BaSnSe₄. *ACS Energy Lett.* **2017**, *2*, 29-35.
- (16) Ge, J.; Yu, Y.; Yan, Y. Earth-Abundant Trigonal BaCu₂Sn(Se_xS_{1-x})₄ (x = 0–0.55) Thin Films with Tunable Band Gaps for Solar Water Splitting. *J. Mater. Chem. A* **2016**, *4*, 18885-18891.

- (17) Shin, D.; Saparov, B.; Zhu, T.; Huhn, W. P.; Blum, V.; Mitzi, D. B. $\text{BaCu}_2\text{Sn}(\text{S},\text{Se})_4$: Earth-Abundant Chalcogenides for Thin-Film Photovoltaics. *Chem. Mater.* **2016**, *28*, 4771-4780.
- (18) Ge, J.; Koirala, P.; Grice, C. R.; Roland, P. J.; Yu, Y.; Tan, X.; Ellingson, R. J.; Collins, R. W.; Yan, Y. Oxygenated CdS Buffer Layers Enabling High Open-Circuit Voltages in Earth-Abundant $\text{Cu}_2\text{BaSnS}_4$ Thin-Film Solar Cells. *Adv. Energy Mater.* **2017**, *7*, 1601803.
- (19) Ge, J.; Roland, P. J.; Koirala, P.; Meng, W.; Young, J. L.; Petersen, R.; Deutsch, T. G.; Teeter, G.; Ellingson, R. J.; Collins, R. W.; Yan, Y. Employing Overlayers to Improve the Performance of $\text{Cu}_2\text{BaSnS}_4$ Thin Film based Photoelectrochemical Water Reduction Devices. *Chem. Mater.* **2017**, *29*, 916-920.
- (20) Shin, D.; Ngaboyamahina, E.; Zhou, Y.; Glass, J. T.; Mitzi, D. B. Synthesis and Characterization of an Earth-Abundant $\text{Cu}_2\text{BaSn}(\text{S},\text{Se})_4$ Chalcogenide for Photoelectrochemical Cell Application. *J. Phys. Chem. Lett.* **2016**, *7*, 4554-4561.
- (21) Zhu, T.; Huhn, W. P.; Wessler, G. C.; Shin, D.; Saparov, B.; Mitzi, D. B.; Blum, V. $\text{I}_2\text{-II-IV-VI}_4$ (I = Cu, Ag; II = Sr, Ba; IV = Ge, Sn; VI = S, Se): Chalcogenides for Thin-Film Photovoltaics. *Chem. Mater.* **2017**, *29*, 7868-7879.
- (22) Shin, D.; Zhu, T.; Huang, X.; Gunawan, O.; Blum, V.; Mitzi, D. B. Earth-Abundant Chalcogenide Photovoltaic Devices with over 5% Efficiency Based on a $\text{Cu}_2\text{BaSn}(\text{S},\text{Se})_4$ Absorber. *Adv. Mater.* **2017**, *29*, 1606945.
- (23) Chen, Z.; Sun, K.; Su, Z.; Liu, F.; Tang, D.; Xiao, H.; Shi, L.; Jiang, L.; Hao, X.; Lai, Y. Solution-Processed Trigonal $\text{Cu}_2\text{BaSnS}_4$ Thin-Film Solar Cells. *ACS Appl. Energy Mater.* **2018**, *1*, 3420-3427.
- (24) Chakraborty, R.; Sim, K. M.; Shrivastava, M.; Adarsh, K. V.; Chung, D. S.; Nag, A. Colloidal Synthesis, Optical Properties, and Hole Transport Layer Applications of $\text{Cu}_2\text{BaSnS}_4$ (CBTS) Nanocrystals. *ACS Appl. Energy Mater.* **2019**, *2*, 3049-3055.

- (25) Ge, J.; Grice, C. R.; Yan, Y. Cu-Based Quaternary Chalcogenide Cu₂BaSnS₄ Thin Films Acting as Hole Transport Layers in Inverted Perovskite CH₃NH₃PbI₃ Solar Cells. *J. Mater. Chem. A* **2017**, *5*, 2920-2928.
- (26) Zhou, Y.; Shin, D.; Ngaboyamahina, E.; Han, Q.; Parker, C. B.; Mitzi, D. B.; Glass, J. T. Efficient and Stable Pt/TiO₂/CdS/Cu₂BaSn(S,Se)₄ Photocathode for Water Electrolysis Applications. *ACS Energy Lett.* **2018**, *3*, 177-183.
- (27) Teymur, B.; Zhou, Y.; Ngaboyamahina, E.; Glass, J. T.; Mitzi, D. B. Solution-Processed Earth-Abundant Cu₂BaSn(S,Se)₄ Solar Absorber using a Low-Toxicity Solvent. *Chem. Mater.* **2018**, *30*, 6116-6123.
- (28) Ge, J.; Yan, Y. Synthesis and Characterization of Photoelectrochemical and Photovoltaic Cu₂BaSnS₄ Thin Films and Solar Cells. *J. Mater. Chem. C* **2017**, *5*, 6406-6419.
- (29) Xie, J.; Yi, Q.; Zhang, F.; Bagheri, R.; Zheng, F.; Zou, G. Large-Grained Cu₂BaSnS₄ Films for Photocathodes. *ACS Appl. Mater. Interfaces* **2019**, *11*, 33102-33108.
- (30) Jaramillo, T. F.; Jørgensen, K. P.; Bonde, J.; Nielsen, J. H.; Horch, S.; Chorkendorff, I. Identification of Active Edge Sites for Electrochemical H₂ Evolution from MoS₂ Nanocatalysts. *Science* **2007**, *317*, 100-102.
- (31) Wu, M.-H.; Chou, W.-J.; Huang, J.-S.; Putungan, D. B.; Lin, S.-H. First-Principles Investigation of the Hydrogen Evolution Reaction on Different Surfaces Of Pyrites MnS₂, FeS₂, CoS₂, NiS₂. *Phys. Chem. Chem. Phys.* **2019**, *21*, 21561-21567.
- (32) Giannozzi, P.; Baroni, S.; Bonini, N.; Calandra, M.; Car, R.; Cavazzoni, C.; Ceresoli, D.; Chiarotti, G. L.; Cococcioni, M.; Dabo, I.; Dal Corso, A. et al. QUANTUM ESPRESSO: a Modular and Open-Source Software Project for Quantum Simulations of Materials. *J. Phys. Condens. Matter* **2009**, *21*, 395502.
- (33) Perdew, J. P.; Burke, K.; Ernzerhof, M. Generalized Gradient Approximation Made Simple [Phys. Rev. Lett. *77*, 3865 (1996)]. *Phys. Rev. Lett.* **1997**, *78*, 1396-1396.

- (34) Song, J.-W.; Yamashita, K.; Hirao, K. Communication: A New Hybrid Exchange Correlation Functional for Band-Gap Calculations Using a Short-Range Gaussian Attenuation (Gaussian-Perdue–Burke–Ernzerhof). *J. Chem. Phys.* **2011**, *135*, 071103.
- (35) Hamann, D. R. Optimized Norm-Conserving Vanderbilt Pseudopotentials. *Phys. Rev. B* **2013**, *88*, 085117
- (36) Monkhorst, H. J.; Pack, J. D. Special Points for Brillouin-Zone Integrations. *Phys. Rev. B* **1976**, *13*, 5188-5192.
- (37) Teske, C. L.; Vetter, O. Preparative and X-Ray Investigations of the Copper Silver Barium Tin Sulfide (Cu_{2-x}Ag_xBaSnS₄) System. *Z. Anorg. Allg. Chem.* **1976**, *426*, 281-287.
- (38) Assoud, A.; Soheilnia, N.; Kleinke, H. New Quaternary Barium Copper/Silver Selenostannates: Different Coordination Spheres, Metal–Metal Interactions, and Physical Properties. *Chem. Mater.* **2005**, *17*, 2255-2261.
- (39) Tang, W.; Sanville, E.; Henkelman, G. A Grid-Based Bader Analysis Algorithm without Lattice Bias. *J. Condens. Matter Phys.* **2009**, *21*, 084204.
- (40) Ge, J.; Yan, Y. Synthesis and Characterization of Photoelectrochemical and Photovoltaic Cu₂BaSnS₄ Thin Films and Solar Cells. *J. Mater. Chem. C* **2017**, *5*, 6406-6419.
- (41) Yin, Y.; Han, J.; Zhang, Y.; Zhang, X.; Xu, P.; Yuan, Q.; Samad, L.; Wang, X.; Wang, Y.; Zhang, Z. et al. Contributions of Phase, Sulfur Vacancies, and Edges to the Hydrogen Evolution Reaction Catalytic Activity of Porous Molybdenum Disulfide Nanosheets. *J. Am. Chem. Soc.* **2016**, *138*, 7965-7972.
- (42) Andersen, A.; Kathmann, S. M.; Lilga, M. A.; Albrecht, K. O.; Hallen, R. T.; Mei, D. Adsorption of Potassium on MoS₂(100) Surface: A First-Principles Investigation. *J. Phys. Chem. C* **2011**, *115*, 9025-9040.
- (43) Ayers, P. W.; Yang, W.; Bartolotti, L. J. *Chemical Reactivity Theory: A DFT View*. **2010**.

(44) Exner, K. S. Does a Thermoneutral Electrocatalyst Correspond to the Apex of a Volcano Plot for a Simple Two-Electron Process? *Angew. Chem. Int. Ed.* **2020**, *59*, 10236-10240.

(45) Lindgren, P.; Kastlunger, G.; Peterson, A. A. A Challenge to the $G \sim 0$ Interpretation of Hydrogen Evolution. *ACS Catal.* **2020**, *10*, 121-128.

(46) Exner, K. S., Paradigm change in hydrogen electrocatalysis: The volcano's apex is located at weak bonding of the reaction intermediate. *Int. J. Hydrog. Energy* **2020**, *45*, 27221-27229.

(47) Ooka, H.; Nakamura, R. Shift of the Optimum Binding Energy at Higher Rates of Catalysis, *J. Phys. Chem. Lett.* **2019**, *10*, 6706-6713.

(48) Nørskov, J. K.; Rossmeisl, J.; Logadottir, A.; Lindqvist, L.; Kitchin, J. R.; Bligaard, T.; Jónsson, H. Origin of the Overpotential for Oxygen Reduction at a Fuel-Cell Cathode. *J. Phys. Chem. B* **2004**, *108*, 17886-17892.

Thesis Summary and Future Directions

Thesis Summary

This thesis discussed the excitonic properties like binding energy, emission energy, trapping and a strategy for decreasing spectroscopic data acquisition time for 2D layered hybrid perovskites. These semiconductors have emerged as potentially exciting material for optoelectronic applications because of easy tunability of their properties by varying composition. However, the vast compositional space makes composition-property relationship difficult to map. This thesis is devoted on understanding how A-site and X-site ions modify excitonic properties for $A_n\text{PbX}_4$ (A = organic ammonium cation, $n = 1$ or 2 , $X = \text{Cl, Br, I}$). The outcome of the thesis work is expected to help in rational designing of compositions for targeted optoelectronic applications. Thereafter, in the thesis appendix section, a different semiconductor material, chalcogenide colloidal $\text{Cu}_2\text{BaSnS}_4$ nanocrystals are introduced for optoelectronic application, and the bulk surfaces of this material is investigated for photocatalytic applications by computational methods.

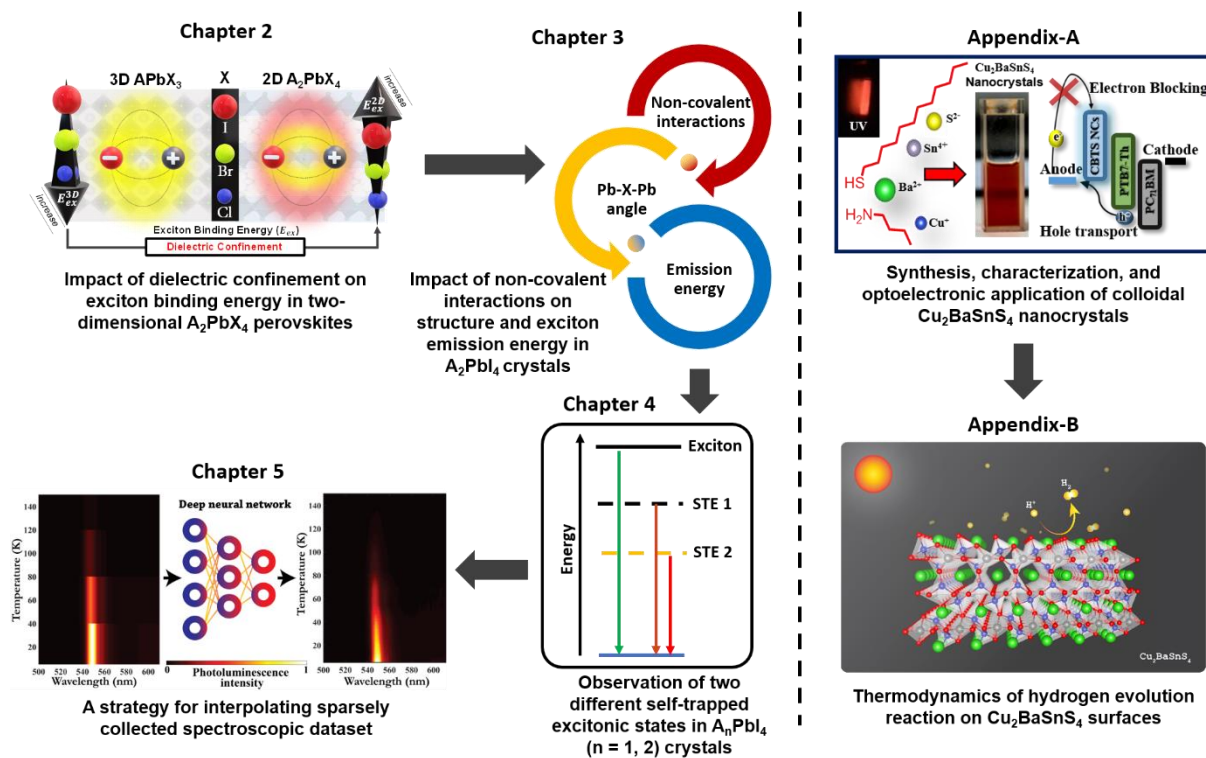


Figure F.1: Graphical summary of the thesis, Chapter 2 to Chapter 5, and Appendix.

Figure F.1 summarizes the work conducted in different chapters of this thesis. The following is the summary of the conclusions drawn in different chapters.

At first, we showed that by tuning the dielectric constants of the A and Pb-X layers in A_2PbX_4 hybrid perovskites, the exciton binding energy can be tuned in the range of 50-450 meV. This tunability potentially allows utilization of layered hybrid perovskites in a range of different optoelectronic applications. Then, functionalized A-site organic cations like $I-(CH_2)_n-NH_3^+$ ($n = 2-6$) were used to bring in halogen-halogen interaction between the organic cation and the inorganic Pb-I layer in A_2PbI_4 perovskites. $(I-(CH_2)_n-NH_3)_2PbI_4$ ($n = 2 - 6$) perovskites were found to undergo minimal temperature-dependent structural changes and show stable emission energy in the 10-300 K temperature range. The introduction of new non-covalent interaction sites was proven to be an effective strategy for enhancing the structural and optical stability of layered hybrid perovskite compositions. Then we focused on the luminescence originating from the trapped excitons in hybrid iodide perovskite single crystals. Two broadband emissive centres were observed at low temperatures (<100 K) from these materials. The excitation and emission mechanism probed by PL excitation and decay measurements suggested that the emissive centres are very different from each other, and possibly located at different crystal environments. Then, in the last chapter of this thesis, we developed a method for reducing time of temperature-dependent PL measurements. Typically, such measurements take long time. Machine-learning the non-linear trends in a sparsely collected dataset and then predicting PL spectra at different temperatures was found to be an effective strategy for reducing time of the experiment. The method was successful in quantifying exciton binding energy, emission energy, and width of emission peak for multiple layered hybrid perovskites.

In the appendix section, synthesis and surface modification of colloidal Cu_2BaSnS_4 (CBTS) nanocrystals were discussed. The nanocrystals were also utilized in a hole transport layer in an organic photodiode showing improved performance compared to typically used organic hole

transport materials. Then, DFT-based calculations were used to probe the thermodynamics of hydrogen evolution reaction on five different surfaces of CBTS. Among the studied surfaces, metal-rich (110) surface was found to have very favourable electronic properties and thermodynamic barriers for hydrogen evolution reaction.

Future Directions

Efficient dissociation of excitons to free carriers is required for high photovoltaic efficiency. A material like (phenylethylammonium)₂PbI₄ has high exciton binding energy (>300 meV), and thus, exciton dissociation is inefficient, reducing the overall photovoltaic efficiency.¹ Increasing the dielectric constant of the organic layer is one way of reducing the exciton binding energy in layered hybrid perovskites, as was shown in Chapter 2 of this thesis.

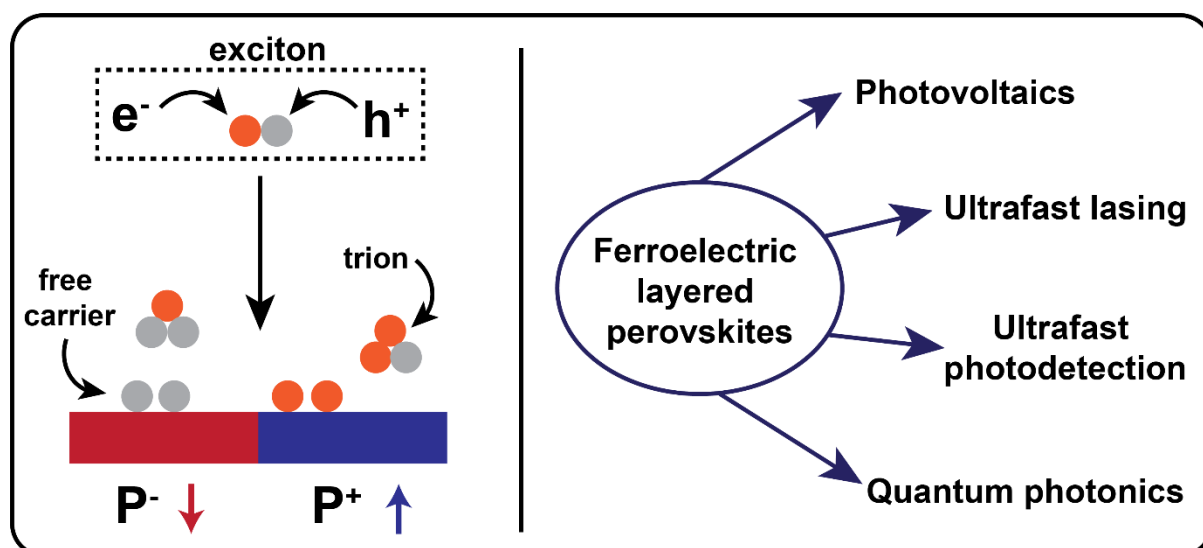


Figure F.2: Left panel: fate of exciton near a ferroelectric surface. P⁻ and P⁺ indicate opposing polarization directions. Right panel: potential applications based on exciton's behaviour in ferroelectric perovskites.

Another approach could be designing compositions such that the material generates internal ferroelectric domains.²⁻⁴ Ferroelectric materials possess spontaneous electrical polarizations and can inherently generate very large local electric field that is not possible to employ externally.⁵ Also, the direction of the field can be modulated by external perturbations like mechanical stress or heat, and internal perturbations like doping.⁶ The electric field facilitates exciton dissociation, formation of charged excitons (trions), and provide long carrier diffusion

lengths.^{6, 7} For these reasons, ferroelectric materials with direct band gap in the visible range, are very appealing for photovoltaic applications.⁸ Also, they can find applications as waveguides, ultrafast lasers, photodetectors, and photocatalysts.⁹⁻¹⁴

Ferroelectric and dielectric modulation of excitons in 2D materials have been realized on transition metal dichalcogenides (MY_2 with $M = Mo, W$; $Y = S, Se$) placed on different surfaces.^{7, 10, 15-19} Layered hybrid perovskites like A_2PbX_4 retain important excitonic properties like tunable direct bandgap in the visible range, high exciton binding energy of MY_2 .²⁰ Additionally, offer an advantage that ferroelectric compositions can be designed by tuning A-site cations.²¹⁻²³ In these materials, ferroelectric modulation of excitons is expected to be realized without the need of the sample to be transferred on different ferroelectric substrates. While a few ferroelectric A_2PbX_4 perovskites have been reported, not much is known about the excitonic properties of these materials.²⁴ There remains a lot of potential in designing new ferroelectric layered perovskite compositions, and studying their excitonic energy landscape.

References

- (1) Smith, I. C.; Hoke, E. T.; Solis-Ibarra, D.; McGehee, M. D.; Karunadasa, H. I. A Layered Hybrid Perovskite Solar-Cell Absorber with Enhanced Moisture Stability. *Angew. Chem. Int. Ed.* **2014**, *53*, 11232-11235.
- (2) Guo, W.; Liu, X.; Han, S.; Liu, Y.; Xu, Z.; Hong, M.; Luo, J.; Sun, Z. Room-Temperature Ferroelectric Material Composed of a Two-Dimensional Metal Halide Double Perovskite for X-ray Detection. *Angew. Chem. Int. Ed.* **2020**, *59*, 13879-13884.
- (3) Kutes, Y.; Ye, L.; Zhou, Y.; Pang, S.; Huey, B. D.; Padture, N. P. Direct Observation of Ferroelectric Domains in Solution-Processed $CH_3NH_3PbI_3$ Perovskite Thin Films. *J. Phys. Chem. Lett.* **2014**, *5*, 3335-3339.

- (4) Chen, X.-G.; Song, X.-J.; Zhang, Z.-X.; Zhang, H.-Y.; Pan, Q.; Yao, J.; You, Y.-M.; Xiong, R.-G. Confinement-Driven Ferroelectricity in a Two-Dimensional Hybrid Lead Iodide Perovskite. *J. Am. Chem. Soc.* **2020**, *142*, 10212-10218.
- (5) Cherifi-Hertel, S.; Bulou, H.; Hertel, R.; Taupier, G.; Dorkenoo, K. D.; Andreas, C.; Guyonnet, J.; Gaponenko, I.; Gallo, K.; Paruch, P. Non-Ising and Chiral Ferroelectric Domain Walls Revealed by Nonlinear Optical Microscopy. *Nat. Commun.* **2017**, *8*, 15768.
- (6) Wen, B.; Zhu, Y.; Yudistira, D.; Boes, A.; Zhang, L.; Yidirim, T.; Liu, B.; Yan, H.; Sun, X.; Zhou, Y.; Xue, Y.; Zhang, Y.; Fu, L.; Mitchell, A.; Zhang, H.; Lu, Y. Ferroelectric-Driven Exciton and Trion Modulation in Monolayer Molybdenum and Tungsten Diselenides. *ACS Nano* **2019**, *13*, 5335-5343.
- (7) Soubelet, P.; Klein, J.; Wierzbowski, J.; Silvioli, R.; Sigger, F.; Stier, A. V.; Gallo, K.; Finley, J. J. Charged Exciton Kinetics in Monolayer MoSe₂ near Ferroelectric Domain Walls in Periodically Poled LiNbO₃. *Nano Lett.* **2021**, *21*, 959-966.
- (8) Huang, H. Ferroelectric Photovoltaics. *Nat. Photonics* **2010**, *4*, 134-135.
- (9) He, M.; Xu, M.; Ren, Y.; Jian, J.; Ruan, Z.; Xu, Y.; Gao, S.; Sun, S.; Wen, X.; Zhou, L.; Liu, L.; Guo, C.; Chen, H.; Yu, S.; Liu, L.; Cai, X. High-Performance Hybrid Silicon and Lithium Niobate Mach-Zehnder Modulators For 100 Gbit s⁻¹ and Beyond. *Nat. Photonics* **2019**, *13*, 359-364.
- (10) Li, D.; Huang, X.; Xiao, Z.; Chen, H.; Zhang, L.; Hao, Y.; Song, J.; Shao, D.-F.; Tsybal, E. Y.; Lu, Y.; Hong, X. Polar Coupling Enabled Nonlinear Optical Filtering at MoS₂/Ferroelectric Heterointerfaces. *Nat. Commun.* **2020**, *11*, 1422.
- (11) Lv, L.; Zhuge, F.; Xie, F.; Xiong, X.; Zhang, Q.; Zhang, N.; Huang, Y.; Zhai, T. Reconfigurable Two-Dimensional Optoelectronic Devices Enabled by Local Ferroelectric Polarization. *Nat. Commun.* **2019**, *10*, 3331.

- (12) Wang, C.; Zhang, M.; Chen, X.; Bertrand, M.; Shams-Ansari, A.; Chandrasekhar, S.; Winzer, P.; Lončar, M. Integrated Lithium Niobate Electro-Optic Modulators Operating at CMOS-Compatible Voltages. *Nature* **2018**, *562*, 101-104.
- (13) Abalmasov, V. A. Ultrafast Reversal of the Ferroelectric Polarization by a Midinfrared Pulse. *Phys. Rev. B* **2020**, *101*, 014102.
- (14) Kumar, V.; O'Donnell, S.; Zoellner, B.; Martinez, J.; Wang, G.; Maggard, P. A. Interfacing Plasmonic Nanoparticles with Ferroelectrics for Hot-Carrier-Driven Photocatalysis: Impact of Schottky Barrier Height. *ACS Appl. Energy Mater.* **2019**, *2*, 7690-7699.
- (15) Lau, K. W.; Calvin; Gong, Z.; Yu, H.; Yao, W. Interface excitons at lateral heterojunctions in monolayer semiconductors. *Phys. Rev. B* **2018**, *98*, 115427.
- (16) Wang, Q. H.; Kalantar-Zadeh, K.; Kis, A.; Coleman, J. N.; Strano, M. S. Electronics and Optoelectronics of Two-Dimensional Transition Metal Dichalcogenides. *Nat. Nanotechnol.* **2012**, *7*, 699-712.
- (17) Xu, Y.; Horn, C.; Zhu, J.; Tang, Y.; Ma, L.; Li, L.; Liu, S.; Watanabe, K.; Taniguchi, T.; Hone, J. C.; Shan, J.; Mak, K. F. Creation Of Moiré Bands in a Monolayer Semiconductor by Spatially Periodic Dielectric Screening. *Nat. Mater.* **2021**, *20*, 645-649.
- (18) Li, C. H.; McCreary, K. M.; Jonker, B. T. Spatial Control of Photoluminescence at Room Temperature by Ferroelectric Domains in Monolayer WS₂/PZT Hybrid Structures. *ACS Omega* **2016**, *1*, 1075-1080.
- (19) Wang, K.; De Greve, K.; Jauregui, L. A.; Sushko, A.; High, A.; Zhou, Y.; Scuri, G.; Taniguchi, T.; Watanabe, K.; Lukin, M. D.; Park, H.; Kim, P. Electrical Control of Charged Carriers and Excitons in Atomically Thin Materials. *Nat. Nanotechnol.* **2018**, *13*, 128-132.
- (20) Goryca, M.; Li, J.; Stier, A. V.; Taniguchi, T.; Watanabe, K.; Courtade, E.; Shree, S.; Robert, C.; Urbaszek, B.; Marie, X.; Crooker, S. A. Revealing Exciton Masses and Dielectric

Properties of Monolayer Semiconductors with High Magnetic Fields. *Nat. Commun.* **2019**, *10*, 4172.

(21) Yang, C.-K.; Chen, W.-N.; Ding, Y.-T.; Wang, J.; Rao, Y.; Liao, W.-Q.; Tang, Y.-Y.; Li, P.-F.; Wang, Z.-X.; Xiong, R.-G. The First 2D Homochiral Lead Iodide Perovskite Ferroelectrics: [R- and S-1-(4-Chlorophenyl)ethylammonium]₂PbI₄. *Adv. Mater.* **2019**, *31*, 1808088.

(22) Shi, P.-P.; Lu, S.-Q.; Song, X.-J.; Chen, X.-G.; Liao, W.-Q.; Li, P.-F.; Tang, Y.-Y.; Xiong, R.-G. Two-Dimensional Organic–Inorganic Perovskite Ferroelectric Semiconductors with Fluorinated Aromatic Spacers. *J. Am. Chem. Soc.* **2019**, *141*, 18334-18340.

(23) Wu, Z.; Liu, X.; Ji, C.; Li, L.; Wang, S.; Peng, Y.; Tao, K.; Sun, Z.; Hong, M.; Luo, J. Discovery of an Above-Room-Temperature Antiferroelectric in Two-Dimensional Hybrid Perovskite. *J. Am. Chem. Soc.* **2019**, *141*, 3812-3816.

(24) Shahrokhi, S.; Gao, W.; Wang, Y.; Anandan, P. R.; Rahaman, M. Z.; Singh, S.; Wang, D.; Cazorla, C.; Yuan, G.; Liu, J. M.; Wu, T. Emergence of Ferroelectricity in Halide Perovskites. *Small Methods* **2020**, *4*, 2000149.

List of Publications

Included in this thesis:

1. Chakraborty, R.; Sim, K. M.; Shrivastava, M.; Adarsh, K. V.; Chung, D. S.; Nag, A. Colloidal Synthesis, Optical Properties, and Hole Transport Layer Applications of $\text{Cu}_2\text{BaSnS}_4$ (CBTS) Nanocrystals. *ACS Appl. Energy Mater.* **2019**, *2*, 3049–3055.
2. Chakraborty, R.; Nag, A. Correlation of Dielectric Confinement and Excitonic Binding Energy in 2D Layered Hybrid Perovskites Using Temperature Dependent Photoluminescence. *J. Phys. Chem. C* **2020**, *124*, 16177–16185.
3. Chakraborty, R.; Nag, A. Dielectric confinement for designing compositions and optoelectronic properties of 2D layered hybrid perovskites. *Phys.Chem.Chem.Phys.* **2021**, *23*,82.
4. Chakraborty, R.; Sheikh, T.; Ghosh, P.; Nag, A. Neural Networks for Analysis of Optical Properties in 2D Layered Hybrid Lead Halide Perovskites. *J. Phys. Chem. C* **2021**, *125*, 5251-5259.
5. Chakraborty, R.; Ghosh, P. Mechanistic Insights of Hydrogen Evolution Reaction on Quaternary Earth-abundant Chalcogenide $\text{Cu}_2\text{BaSnS}_4$ from First Principles. *Appl. Surf. Sci.* **2021**, *570*, 151049.
6. Chakraborty, R.; Sheikh, T.; Nag, A. Iodine-Iodine Interactions Suppressing Phase Transitions of 2D Layered Hybrid $(\text{I}-(\text{CH}_2)_n-\text{NH}_3)_2\text{PbI}_4$ ($n = 2-6$) Perovskites. *Chem. Mater.* **2022**, *34*, 288–296.
7. Chakraborty, R.; Nag, A. Two Self Trapped Excitons in 2D Layered Lead Iodide Perovskite Single Crystals. *Manuscript under preparation.*

Not included in this thesis:

1. Singhal, N.; Chakraborty, R.; Ghosh, P.; Nag, A. Low-Bandgap Cs₄CuSb₂Cl₁₂ Layered Double Perovskite: Synthesis, Reversible Thermal Changes, and Magnetic Interaction. *Chem. Asian J.* **2018**, *13*, 2085-2092.
2. Swarnkar, A.; Mir, W. J.; Chakraborty, R.; Jagadeeswararao, M.; Sheikh, T.; Nag, A. Are Chalcogenide Perovskites an Emerging Class of Semiconductors for Optoelectronic Properties and Solar Cell? *Chem. Mater.* **2019**, *31*, 565–575.
3. Ravi, V. K.; Swarnkar, A.; Chakraborty, R.; Nag, A. Excellent green but less impressive blue luminescence from CsPbBr₃ perovskite nanocubes and nanoplatelets. *Nanotechnology* **2016**, *27*, 325708.

Copyrights and Permissions

1. Physical chemistry chemical physics : PCCP

0.00 USD

Article: Dielectric Confinement for Designing Compositions and Optoelectronic Properties of 2D Layered Hybrid Perovskite

Order License ID	Pending	Publisher	ROYAL SOCIETY OF CHEMISTRY
ISSN	1463-9076		Page
Type of Use	Republish in a thesis/dissertation	Portion	

LICENSED CONTENT

Publication Title	Physical chemistry chemical physics : PCCP	Rightsholder	Royal Society of Chemistry
Article Title	Dielectric Confinement for Designing Compositions and Optoelectronic Properties of 2D Layered Hybrid Perovskite	Publication Type	Journal
		Start Page	82
		End Page	93
		Issue	1
		Volume	23
Author/Editor	Royal Society of Chemistry (Great Britain), Deutsche Bunsen-Gesellschaft für Physikalische Chemie., Koninklijke Nederlandse Chemische Vereniging., Società chimica italiana.		
Date	01/01/1999		
Language	English		
Country	United Kingdom of Great Britain and Northern Ireland		

REQUEST DETAILS

Portion Type	Page	Rights Requested	Main product
Page range(s)	82-93	Distribution	Worldwide
Total number of pages	11	Translation	Original language of publication
Format (select all that apply)	Print, Electronic	Copies for the disabled?	Yes
Who will republish the content?	Academic institution	Minor editing privileges?	Yes
Duration of Use	Life of current edition	Incidental promotional use?	No
Lifetime Unit Quantity	Up to 499	Currency	USD

NEW WORK DETAILS

Title	Dielectric Confinement, Structure, and Luminescence of 2D Layered Hybrid Halide Perovskites	Institution name	IISER Pune
		Expected presentation date	2022-01-31
Instructor name	Angshuman Nag		

ADDITIONAL DETAILS

Order reference number	N/A	The requesting person / organization to appear on the license	Rayan Chakraborty
------------------------	-----	---	-------------------

REUSE CONTENT DETAILS

Title, description or numeric reference of the portion(s)	Dielectric Confinement for Designing Compositions and Optoelectronic Properties of 2D Layered Hybrid Perovskite	Title of the article/chapter the portion is from	Dielectric Confinement for Designing Compositions and Optoelectronic Properties of 2D Layered Hybrid Perovskite
Editor of portion(s)	Chakraborty, Rayan; Nag, Angshuman	Author of portion(s)	Chakraborty, Rayan; Nag, Angshuman
Volume of serial or monograph	23	Issue, if republishing an article from a serial	1
Page or page range of portion	82-93	Publication date of portion	2021-01-06

Total Items: 1

Total Due: 0.00 USD

Accepted: All Publisher and CCC Terms and Conditions



Correlation of Dielectric Confinement and Excitonic Binding Energy in 2D Layered Hybrid Perovskites Using Temperature Dependent Photoluminescence

Author: Rayan Chakraborty, Angshuman Nag

Publication: The Journal of Physical Chemistry C

Publisher: American Chemical Society

Date: Jul 1, 2020

Copyright © 2020, American Chemical Society

PERMISSION/LICENSE IS GRANTED FOR YOUR ORDER AT NO CHARGE

This type of permission/license, instead of the standard Terms and Conditions, is sent to you because no fee is being charged for your order. Please note the following:

- Permission is granted for your request in both print and electronic formats, and translations.
- If figures and/or tables were requested, they may be adapted or used in part.
- Please print this page for your records and send a copy of it to your publisher/graduate school.
- Appropriate credit for the requested material should be given as follows: "Reprinted (adapted) with permission from {COMPLETE REFERENCE CITATION}. Copyright {YEAR} American Chemical Society." Insert appropriate information in place of the capitalized words.
- One-time permission is granted only for the use specified in your RightsLink request. No additional uses are granted (such as derivative works or other editions). For any uses, please submit a new request.

If credit is given to another source for the material you requested from RightsLink, permission must be obtained from that source.

BACK

CLOSE WINDOW

Iodine-Iodine Interactions Suppressing Phase Transitions of 2D Layered Hybrid $(I-(CH_2)_n-NH_3)_2PbI_4$ ($n = 2-6$) Perovskites



Author: Rayan Chakraborty, Tariq Sheikh, Angshuman Nag

Publication: Chemistry of Materials

Publisher: American Chemical Society

Date: Jan 1, 2022

Copyright © 2022, American Chemical Society

PERMISSION/LICENSE IS GRANTED FOR YOUR ORDER AT NO CHARGE

This type of permission/license, instead of the standard Terms and Conditions, is sent to you because no fee is being charged for your order. Please note the following:

- Permission is granted for your request in both print and electronic formats, and translations.
- If figures and/or tables were requested, they may be adapted or used in part.
- Please print this page for your records and send a copy of it to your publisher/graduate school.
- Appropriate credit for the requested material should be given as follows: "Reprinted (adapted) with permission from {COMPLETE REFERENCE CITATION}. Copyright {YEAR} American Chemical Society." Insert appropriate information in place of the capitalized words.
- One-time permission is granted only for the use specified in your RightsLink request. No additional uses are granted (such as derivative works or other editions). For any uses, please submit a new request.

If credit is given to another source for the material you requested from RightsLink, permission must be obtained from that source.

[BACK](#)

[CLOSE WINDOW](#)

Neural Networks for Analysis of Optical Properties in 2D Layered Hybrid Lead Halide Perovskites



Author: Rayan Chakraborty, Tariq Sheikh, Prasenjit Ghosh, et al

Publication: The Journal of Physical Chemistry C

Publisher: American Chemical Society

Date: Mar 1, 2021

Copyright © 2021, American Chemical Society

PERMISSION/LICENSE IS GRANTED FOR YOUR ORDER AT NO CHARGE

This type of permission/license, instead of the standard Terms and Conditions, is sent to you because no fee is being charged for your order. Please note the following:

- Permission is granted for your request in both print and electronic formats, and translations.
- If figures and/or tables were requested, they may be adapted or used in part.
- Please print this page for your records and send a copy of it to your publisher/graduate school.
- Appropriate credit for the requested material should be given as follows: "Reprinted (adapted) with permission from {COMPLETE REFERENCE CITATION}. Copyright {YEAR} American Chemical Society." Insert appropriate information in place of the capitalized words.
- One-time permission is granted only for the use specified in your RightsLink request. No additional uses are granted (such as derivative works or other editions). For any uses, please submit a new request.

If credit is given to another source for the material you requested from RightsLink, permission must be obtained from that source.

BACK

CLOSE WINDOW

Colloidal Synthesis, Optical Properties, and Hole Transport Layer Applications of Cu₂BaSnS₄ (CBTS) Nanocrystals



Author: Rayan Chakraborty, Kyu Min Sim, Megha Shrivastava, et al

Publication: ACS Applied Energy Materials

Publisher: American Chemical Society

Date: May 1, 2019

Copyright © 2019, American Chemical Society

PERMISSION/LICENSE IS GRANTED FOR YOUR ORDER AT NO CHARGE

This type of permission/license, instead of the standard Terms and Conditions, is sent to you because no fee is being charged for your order. Please note the following:

- Permission is granted for your request in both print and electronic formats, and translations.
- If figures and/or tables were requested, they may be adapted or used in part.
- Please print this page for your records and send a copy of it to your publisher/graduate school.
- Appropriate credit for the requested material should be given as follows: "Reprinted (adapted) with permission from {COMPLETE REFERENCE CITATION}. Copyright {YEAR} American Chemical Society." Insert appropriate information in place of the capitalized words.
- One-time permission is granted only for the use specified in your RightsLink request. No additional uses are granted (such as derivative works or other editions). For any uses, please submit a new request.

If credit is given to another source for the material you requested from RightsLink, permission must be obtained from that source.

BACK

CLOSE WINDOW



Mechanistic insights of hydrogen evolution reaction on quaternary earth-abundant chalcogenide $\text{Cu}_2\text{BaSnS}_4$ from first principles

Author: Rayan Chakraborty, Prasenjit Ghosh

Publication: Applied Surface Science

Publisher: Elsevier

Date: 30 December 2021

© 2021 Elsevier B.V. All rights reserved.

Journal Author Rights

Please note that, as the author of this Elsevier article, you retain the right to include it in a thesis or dissertation, provided it is not published commercially. Permission is not required, but please ensure that you reference the journal as the original source. For more information on this and on your other retained rights, please visit: <https://www.elsevier.com/about/our-business/policies/copyright#Author-rights>

BACK

CLOSE WINDOW

Scaling law for excitons in 2D perovskite quantum wells

SPRINGER NATURE

Author: J.-C. Blancon et al
Publication: Nature Communications
Publisher: Springer Nature
Date: Jun 8, 2018

Copyright © 2018, The Author(s)

Creative Commons

This is an open access article distributed under the terms of the [Creative Commons CC BY](#) license, which permits unrestricted use, distribution, and reproduction in any medium, provided the original work is properly cited.

You are not required to obtain permission to reuse this article.

To request permission for a type of use not listed, please contact [Springer Nature](#)

Tuning the Band Gap in Hybrid Tin Iodide Perovskite Semiconductors Using Structural Templating

 **ACS Publications**
Most Trusted. Most Cited. Most Read.

Author: Jeremy L. Knutson, James D. Martin, David B. Mitzi
Publication: Inorganic Chemistry
Publisher: American Chemical Society
Date: Jun 1, 2005

Copyright © 2005, American Chemical Society

PERMISSION/LICENSE IS GRANTED FOR YOUR ORDER AT NO CHARGE

This type of permission/license, instead of the standard Terms and Conditions, is sent to you because no fee is being charged for your order. Please note the following:

- Permission is granted for your request in both print and electronic formats, and translations.
- If figures and/or tables were requested, they may be adapted or used in part.
- Please print this page for your records and send a copy of it to your publisher/graduate school.
- Appropriate credit for the requested material should be given as follows: "Reprinted (adapted) with permission from {COMPLETE REFERENCE CITATION}. Copyright {YEAR} American Chemical Society." Insert appropriate information in place of the capitalized words.
- One-time permission is granted only for the use specified in your RightsLink request. No additional uses are granted (such as derivative works or other editions). For any uses, please submit a new request.

If credit is given to another source for the material you requested from RightsLink, permission must be obtained from that source.

BACK

CLOSE WINDOW

White-Light Emission from Layered Halide Perovskites



Author: Matthew D. Smith, Hemamala I. Karunadasa

Publication: Accounts of Chemical Research

Publisher: American Chemical Society

Date: Mar 1, 2018

Copyright © 2018, American Chemical Society

PERMISSION/LICENSE IS GRANTED FOR YOUR ORDER AT NO CHARGE

This type of permission/license, instead of the standard Terms and Conditions, is sent to you because no fee is being charged for your order. Please note the following:

- Permission is granted for your request in both print and electronic formats, and translations.
- If figures and/or tables were requested, they may be adapted or used in part.
- Please print this page for your records and send a copy of it to your publisher/graduate school.
- Appropriate credit for the requested material should be given as follows: "Reprinted (adapted) with permission from {COMPLETE REFERENCE CITATION}. Copyright {YEAR} American Chemical Society." Insert appropriate information in place of the capitalized words.
- One-time permission is granted only for the use specified in your RightsLink request. No additional uses are granted (such as derivative works or other editions). For any uses, please submit a new request.

If credit is given to another source for the material you requested from RightsLink, permission must be obtained from that source.

[BACK](#)

[CLOSE WINDOW](#)

Trap States in Lead Iodide Perovskites



Author: Xiaoxi Wu, M. Tuan Trinh, Daniel Niesner, et al

Publication: Journal of the American Chemical Society

Publisher: American Chemical Society

Date: Feb 1, 2015

Copyright © 2015, American Chemical Society

PERMISSION/LICENSE IS GRANTED FOR YOUR ORDER AT NO CHARGE

This type of permission/license, instead of the standard Terms and Conditions, is sent to you because no fee is being charged for your order. Please note the following:

- Permission is granted for your request in both print and electronic formats, and translations.
- If figures and/or tables were requested, they may be adapted or used in part.
- Please print this page for your records and send a copy of it to your publisher/graduate school.
- Appropriate credit for the requested material should be given as follows: "Reprinted (adapted) with permission from {COMPLETE REFERENCE CITATION}. Copyright {YEAR} American Chemical Society." Insert appropriate information in place of the capitalized words.
- One-time permission is granted only for the use specified in your RightsLink request. No additional uses are granted (such as derivative works or other editions). For any uses, please submit a new request.

If credit is given to another source for the material you requested from RightsLink, permission must be obtained from that source.

[BACK](#)

[CLOSE WINDOW](#)

Advances and Promises of Layered Halide Hybrid Perovskite Semiconductors



Author: Laurent Pedesseau, Daniel Sapori, Boubacar Traore, et al

Publication: ACS Nano

Publisher: American Chemical Society

Date: Nov 1, 2016

Copyright © 2016, American Chemical Society

PERMISSION/LICENSE IS GRANTED FOR YOUR ORDER AT NO CHARGE

This type of permission/license, instead of the standard Terms and Conditions, is sent to you because no fee is being charged for your order. Please note the following:

- Permission is granted for your request in both print and electronic formats, and translations.
- If figures and/or tables were requested, they may be adapted or used in part.
- Please print this page for your records and send a copy of it to your publisher/graduate school.
- Appropriate credit for the requested material should be given as follows: "Reprinted (adapted) with permission from {COMPLETE REFERENCE CITATION}. Copyright {YEAR} American Chemical Society." Insert appropriate information in place of the capitalized words.
- One-time permission is granted only for the use specified in your RightsLink request. No additional uses are granted (such as derivative works or other editions). For any uses, please submit a new request.

If credit is given to another source for the material you requested from RightsLink, permission must be obtained from that source.

BACK

CLOSE WINDOW

